Distribution Category UC-20

UCRL--53480-Vol.2

DE85 001728

UCRL-53480

MARS

MIRROR ADVANCED REACTOR STUDY

July 1984

Final Report
Volume 2
Commercial Fusion Synfuels Plant

Lawrence Livermore National Laboratory
TRW Energy Development Group
University of Wisconsin–Madison
General Dynamics/Convair Division
University of Washington
Grumman Aerospace Corporation
EBASCO Services, Inc.
Science Applications, Inc.
G. A. Technologies
Energy Technology Engineering Center (ETEC)
University of California–Los Angeles
Ontario Hydro

Acknowledgments

The preparation of a technical report of this magnitude is a major undertaking that involves the work of many people. In addition to the contributions from the participating authors, the process of preparing and publishing these volumes required the talents and participation of members of the LLNL Technical Information Department: editors Maureen L. Donohue and M. Elaine Price; and LLNL's M-Division administrative support personnel: Martelle G. Mays, Karma D. Thomas, and Ruth A. Porth, who provided word processing and layout expertise. Maureen Donohue, in particular, deserves special mention for the large commitment of her time and skills, which were devoted to editing and organizing this report from the individual manuscript contributions to the final printing.

Contributing Authors

Lawrence Livermore National Laboratory

B. G. Logan, C. D. Henning, G. A. Carlson, R. W. Werner

D. E. Baldwin
W. L. Barr
R. H. Bulmer
D. E. Christiansen
R. S. Devoto
D. W. Dorn
G. W. Hamilton
M. A. Hoffman[a]
B. M. Johnston
O. H. Krikorian
W. N. Kumal
R. C. Maninger
W. S. Neef
P. D. Stroud[b]

TRW Energy Development Group

J. D. Gordon

D. H. Berwald
R. B. Campbell
B. A. Flanders
S. A. Freije
J. K. Garner
D. M. Goebel
W. Y. Lim
S. C. Mortenson
E. P. Motley
Y. Saito

University of Wisconsin—Madison

G. L. Kulcinski, L. J. Perkins[c]

H. M Attaya
K. R. Audenaerde
M. L. Corradini
G. A. Emmert
L. A. ElGuebaly
J.H. Huang[d]
E. M. Larsen
Y.-T. Li[d]
C. W. Maynard
E. Montalvo[e]
K. E. Plute
R. A. Sanders
J. F. Santarius
M. E. Sawan
D. C. Schluderberg[f]
I. N. Sviatoslavsky
D.-K. Sze[g]
W. F. Vogelsang
A. M. White
L. J. Wittenberg

General Dynamics/Convair Division

J. F. Parmer

K. L. Agarwal
H. G. Arrendale
R. W. Baldi
R. Dharmarajan
M. W. Liggett
D. W. Magnuson
C. A. Sink
J. D. Sutliff
R. A. Sutton
D. J. Tait
J. C. Yu

University of Washington

F. L. Ribe
D. Rowe[h]
G. L. Woodruff

Grumman Aerospace Corp.

R. Botwin, R. J. Herbermann

R. H. Bullis
V. S. Calia
I. R. Clarkson
L. A. Deutsch
J. L. Erickson
S. Z. Fixler
T. E. Luzzi
R. G. Micich
M. L. Rossi
D. W. Sedgley
M. C. Stauber

Ebasco Services, Inc.

J. R. Bilton

H. H. Audi
S. P. Balaes
J. A. Cohen
P. R. Grimm
F. J. Kuo
R. W. Lohf
G. E. Mahoney
G. C. Pan
I. Romero
N. E. Young

Science Applications, Inc.

H. Gurol, J. E. Glancy

A. E. Dabiri
R. C. Erickson
B. E. Kirstein
G. W. Shuy

GA Technologies

L. C. Brown

Energy Technology Engineering Center (ETEC)

N. J. Hoffman

University of California—Los Angeles

R. W. Conn

S. P. Grotz
N. M. Ghoniem
F. Najmabadi
K. Raghavi

Ontario Hydro—Fusion Fuels Technology Project

T. Drolet
O. K. Kveton
S. K. Sood

---

[a] University of California—Davis, Davis, CA
[b] University of Illinois, Urbana, IL
[c] Present address: Lawrence Livermore National Laboratory, Livermore, CA.
[d] Southwestern Institute of Physics, Leshan, Peoples Republic of China.
[e] Present address: University of Texas, Austin, TX.
[f] Babcock and Wilcox, Lynchburg, VA.
[g] Present address: Argonne National Laboratory, Argonne, IL.
[h] Rowe & Associates, Bellevue, WA.

Contents

1 MARS and Synfuels—Producing Thermochemical Hydrogen

1. MARS and Synfuels—Producing Thermochemical Hydrogen

1.1 INTRODUCTION

Because the world is rapidly depleting its supplies of nonrenewable fuels and also because of the unstable political climates in many of the major oil-producing nations, the U.S. must have abundant domestic sources of energy to supply fuel for residential and commercial electricity, transportation, and heating. Energy self-sufficiency is vital to our country's well-being and we must work to that end as a national goal. We believe that in the long term this energy will be best provided by the fusion reactor, not only by producing electricity, but also by serving as the heat source for synthetic fuel production.

As part of the Mirror Advanced Reactor Study (MARS), we have examined ways to use fusion energy to produce synthetic fuel. Specifically, we studied the combination of Lawrence Livermore National Laboratory's (LLNL) tandem mirror reactor (TMR) with the MARS physics base (see Table 1-1) and GA Technologies' sulfur-iodine cycle (see Sec. 1.4) to produce hydrogen.

Table 1-1. Selected design parameters for the MARS as a driver for the thermochemical plant.

Parameter	Value
Fusion power (MW_f)	3500
Neutron power (MW_f)	2800
Blanket energy multiplication M	1.2
Blanket thermal power (MW_t)	3360
First wall loading, average (MW/m^2)	5
Reactor Q	33
Central cell length (m)	150
Direct converter power available to thermochemical plant (MW_e)	173
Direct converter thermal available to thermochemical plant (MW_t)	320
Fraction of blanket thermal available at high temperature (1273 K)	0.46
Fraction of blanket thermal available at low temperature (773 K)	0.54

The hydrogen is then used as a feedstock to produce methanol, a portable fuel with a complex molecular structure. Alternatively, other fuels such as methane or gasoline could be produced or the hydrogen itself could be used as a portable fuel. Methanol was selected because it can replace gasoline and heating oil and because there is a well established technology for its production and distribution in existing pipelines.

The cost of methanol produced in the MARS synfuel plant would be about $1.70 per gallon in 1983 dollars with a production rate of 1.6 million gallons per day. Whereas this cost is somewhat above the present price in the United States, it is significantly below the present price in Japan and Europe. By the time fusion is capable of producing methanol in the early 21st century, the real cost of natural fuel is expected to rise to a point where fusion would be competitive. For this reason, we believe it is imperative to develop methods now for producing synthetic fuels. Moreover, we believe that the fusion/synfuels program has tremendous potential in this area and as such it should continue to be an integral part of the national fusion program.

Figure 1-1 shows the postulated U.S. energy flow and consumption for the year 2000. It illustrates the extreme economic importance of synthesizing these portable fuels. Note that on the input side, 35 quads of energy are used to produce electricity via central station power, 4 quads are used to produce electricity through hydro and geothermal plants, and 53 quads--the largest part--are used as portable fuels. On the output side, we can see that portable fuels are even more important because industrial use of fuels is much more efficient than residential use. As the nonrenewable supplies of oil, coal, and gas that constitute the input flow predictably diminish, they must be replaced by the renewables: fusion is one of these.*

Synthetic fuel production should be studied in conjunction with the fusion reactor for the following reasons:

1. These studies will form the foundation that demonstrates fusion's applicability to our future national overall energy needs.

2. Synfuel studies will be important because fusion's availability and the need for synfuels may coincide. At the same time that fusion energy sources become available for commercial use, many analysts predict that synthetic fuels will be needed to bolster the waning supplies of nonrenewable fuels. Thus, fusion and synfuels would be mutually supportive.

3. Fusion reactor studies will receive wider exposure as a direct result of synfuel reactor studies. For example, different scientific disciplines will become involved; different industrial partners will be made aware of fusion; more advanced reactor designs will be created.

*There are only three renewable sources of energy: solar, the breeder, and fusion.

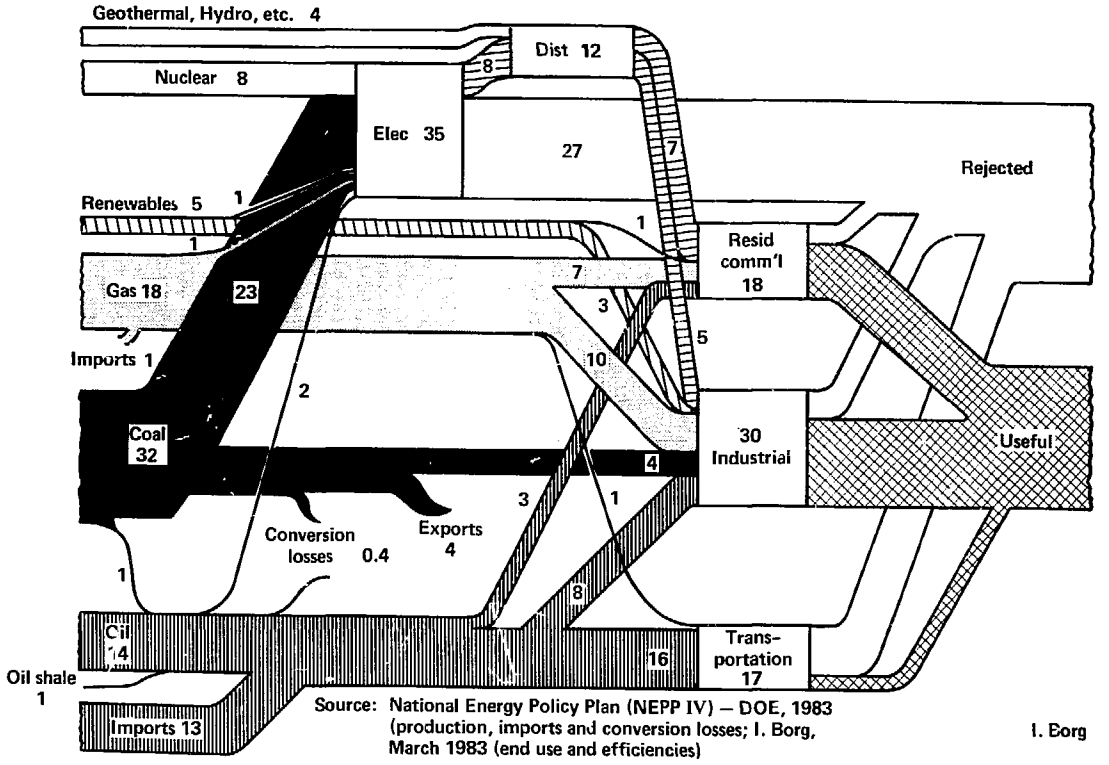

Fig. 1-1. Postulated U.S. energy flow and consumption for the year 2000. The net primary resource consumption is 92 quads.

4. Fusion/synfuels studies will foster a better understanding of tritium control, tritium adsorption in various materials, structural and moderator materials selection, operation in higher than "conventional" temperatures, economies of scale, comparisons of fusion electric vs fusion synfuel, and finally even the possibility of cogeneration.

1.2 THE MARS REACTOR

As we have stated, the MARS/synfuel physics is the basis for our study and the plasma and engineering parameters have been selected specifically for the thermochemical production of hydrogen in what we believe to be a reasonable commercial thermochemical plant size. The reactor produces a nominal 3500 MW of fusion power at a Q of 33. With this power, after the necessary conversion, 5223 moles of hydrogen are produced per second equal to 4.2×10^8 liters per hour of saleable product. This, with the addition of 1000 tons per day of bituminous coal input, results in the production of 38,000 barrels (42 U.S. gallons)/day of methanol.

This TMR, with its linear topology and output of both thermal energy and high-voltage dc electrical energy, has advantages for synfuel applications, which will be enumerated in Sec. 6 of this volume. However, one intrinsic advantage of using fusion/synfuels with either a mirror or a tokamak reactor is that of siting and sizing. Large plants can be constructed in remote sites and the fuels produced can then be transported by pipeline to their destinations.

An artist's view of the MARS reactor is shown in Fig. 1-2. The physics base for this reactor is discussed in Sec. 2 of this volume.

1.3 THE HIGH-TEMPERATURE TWO-ZONE BLANKET

Energy to drive the thermochemical process is provided by TRW's MARS blanket. It is a two-temperature-zone blanket containing a helium-cooled high-temperature (1000°C) zone and a Li-Pb-cooled low-temperature (500°C) zone. All blanket structural material is HT-9 ferritic steel. The Li-Pb low-temperature coolant, always in direct contact with the HT-9 structure, keeps this material at 520°C or less throughout the blanket.

Through good neutronic design, varied compositions, etc., we have achieved a blanket in which 46% of the energy is produced in the high temperature zone. The bulk of the tritium breeding is done in the high temperature zone using SiC spheres impregnated with 2% $LiAlO_2$. The Li-Pb provides the n-2n reactions for a more than adequate tritium breeding level of 1.15.

The high temperature zone of the blanket is quite adequate for thermochemical plant applications. The low temperature zone of the blanket is limited in maximum operating temperature by corrosion because the Li-Pb attacks the HT-9. At 500°C, with simple coupon static testing, weight losses in the steel were found to be significant. The need to limit corrosion to acceptable levels requires operating the low temperature zone of this blanket at lesser temperatures than are desirable for a thermochemical plant. Our overall plant efficiency would improve if operating temperatures could be

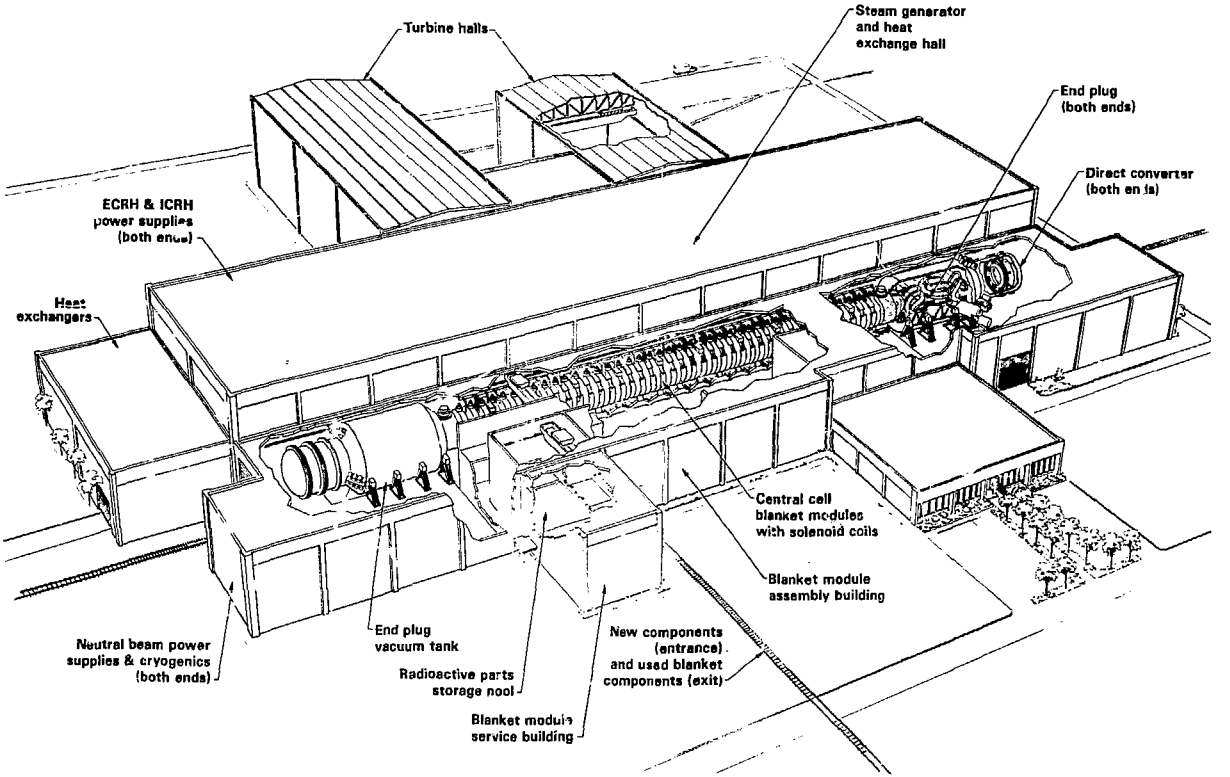

Fig. 1-2. General view of the MARS tandem mirror reactor.
NOTE: 1 quad = 10^{18} Btu = 1 x 10^{21} joules = 2.78 x 10^{14} kW/hr.

higher. This higher temperature may be possible by doping the Li-Pb coolant with a corrosion inhibitor or treating the HT-9 with a protective coating.

This blanket, in its early stages of development, requires much more study, particularly in the area of magnetohydrodynamic (MHD) effects and their influence on pumping, pressure drop, and heat transfer in the Li-Pb loop.

1.4 GA TECHNOLOGIES' THERMOCHEMICAL CYCLE

Our thermochemical process uses GA Technologies' sulfur-iodine cycle to thermochemically decompose water to make hydrogen and oxygen, using only water as the feedstock fluid (see Fig. 1-3). The chemical reagents, sulfur and iodine, are continuously recycled and reused with essentially no loss of material. This cycle is one of three that has been demonstrated at the laboratory level.

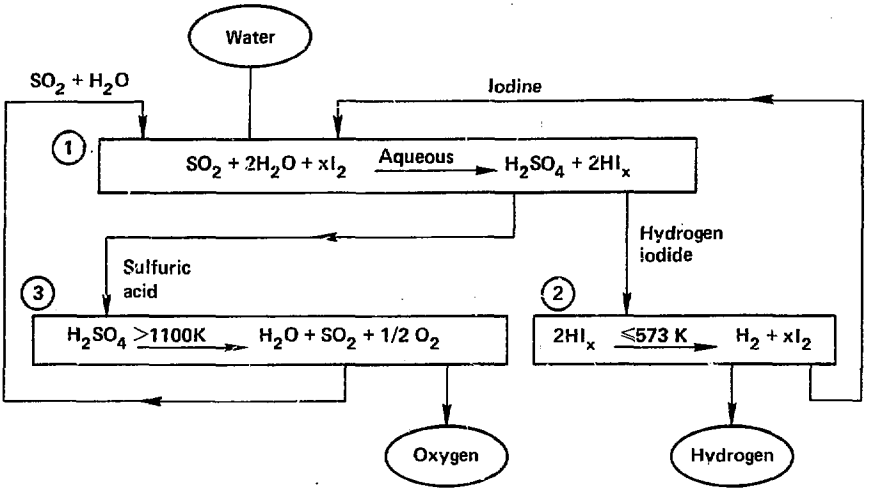

Fig. 1-3. GA Technologies' sulfur-iodine cycle to thermochemically decompose water to make hydrogen and oxygen, using water as the feedstock fluid.

The next stage of development in thermochemical hydrogen production, a "technological circuit" so-called because it uses actual plant operating pressures, temperatures, and materials, is about to come on line in Italy, using another of the three promising cycles. This circuit, called "Christine," will produce 10,000 liters of hydrogen per hour. The location of the experiment is the Joint Research Centre of the Commission of European Communities at Ispra. The hydrogen produced is a token amount, but it is nevertheless an impressive beginning. In comparison, as we have just noted, the plant that forms the basis of our reference design is large enough to produce approximately 5000 moles of hydrogen per second, roughly a 4 x 10^4 extension of the technological circuit. The overall plant efficiency for this commercial size unit is substantial, 35 to 40% (37% ref). Given good development, experiments, and further study, it seems reasonable that

thermochemical plants can attain efficiencies in the forties, perhaps as high as 50%.

1.5 INTERFACING THE REACTOR TO THE THERMOCHEMICAL PLANT

During the course of our studies, we have developed and systematized an effective interface algorithm for use between the TMR energy supply and the thermochemical plant energy demand. Helium is used as the high-temperature energy transport medium and Li-Pb is used at the lower temperature end in this particular study. The chemical plant then uses helium and steam internally. No intermediate heat exchangers have been used for isolation purposes. Instead, we rely on the use of duplex tubing. This avoids some of the temperature degradation inherent in heat exchangers, particularly gas/gas heat exchangers, but retains the isolation required to keep tritium out of the thermochemical plant and particularly out of the hydrogen product. Our design goal in this area is not more than one part of tritium in 10^{12} parts of hydrogen. Using all barriers to fullest advantage, this goal may be achievable, but tritium control warrants serious attention and study irrespective of whether it is in the context of synfuel or electricity production. Tritium and its control are discussed in Sec. 7 of this volume. The power temperature diagram for the MARS/synfuel produced by our interface algorithm is shown in Fig. 1-4.

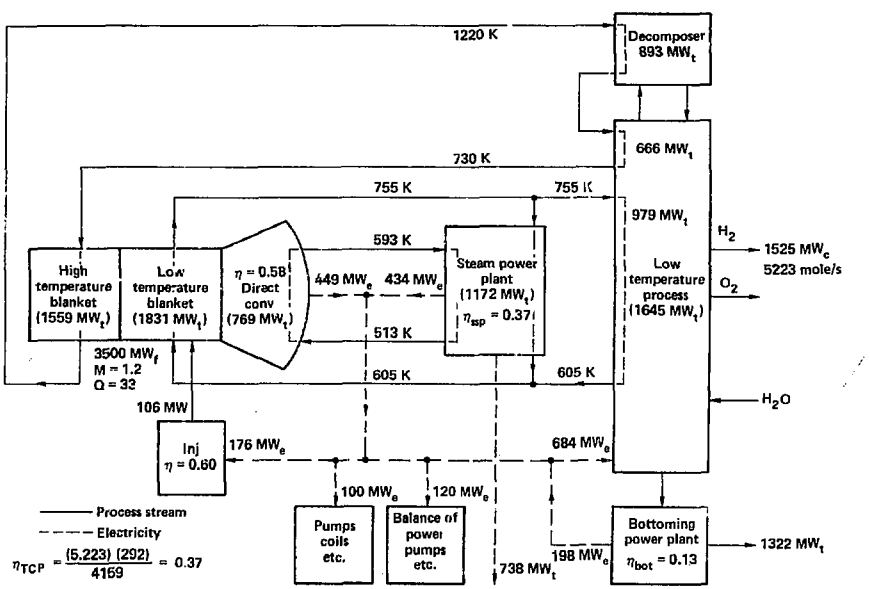

Fig. 1-4. The power temperature diagram for the MARS/synfuel produced by the interface algorithm.

1.6 PLANT LAYOUT

We have developed a preliminary plot plan for a synfuel plant. The area required for this plant will be comparable to that required for a nuclear power plant of the same relative output, about 0.36 mi^2 in our case. The plant layout is illustrated in Fig. 1-5.

We have used both an appropriate degree of process unit redundancy and the operation of like units in parallel (six units is typical) in the thermochemical design and we can thus predict a high combined TMR/chemical plant availability of ∿74% determined by the reactor.

1.7 MATERIALS FOR THE REACTOR AND THE CHEMICAL PLANT

There are enough options and choices for materials for the reactor and the chemical plant to provide a credible material base using reasonable extrapolations from existing data. However, there is a lack of long-term creep data on the high-temperature materials as well as a lack of experimental property data on SiC and its tritium solubility. Experimental corrosion data on H_2SO_4, in both liquid and gaseous states, are also required. For the chemical plant, Table 1-2 illustrates our candidate materials for the sulfuric acid section of the thermochemical process. We judge this to be the most difficult materials area in the chemical plant because it contains corrosive fluids and vapors ranging in temperature from ∿400 to 1125 K. The materials listed in this table have been successfully tested in this hostile environment.

1.8 THE MULTI-STAGED FLUIDIZED-BED DECOMPOSER

The highest temperature heat in GA Technologies' sulfur-iodine cycle is required to decompose SO_3 to SO_2. This decomposition temperature, 1100 K for our reference case, occurs in the last stage of a newly developed four-stage fluidized-bed decomposer. We developed this concept as a direct consequence of our basic fusion/synfuel study program and then further detailed it in this MARS/synfuel collaboration. We believe that this new unit is a very significant contribution to the thermochemical process. The staged decomposer performs two very important functions: (1) with its multiple stages, each of which is isothermal, it can track energy demand to energy supply, as suggested by the temperature enthalpy curve in Fig. 1-6; (2) it diminishes the quantity of energy needed at the highest temperature in inverse proportion to the number of stages used.

We found four stages to be a practical, economic choice. The temperatures of the four stages were equi-partitioned at 875, 950, 1025, and 1100 K. This decomposer, using Waspaloy with an aluminide coating as the structural material, operates satisfactorily in the high-differential-pressure corrosive environment. This decomposer is fully discussed in Sec. 8 of this volume, and it warrants further study and refinement. We highlight some of its features in Table 1-3.

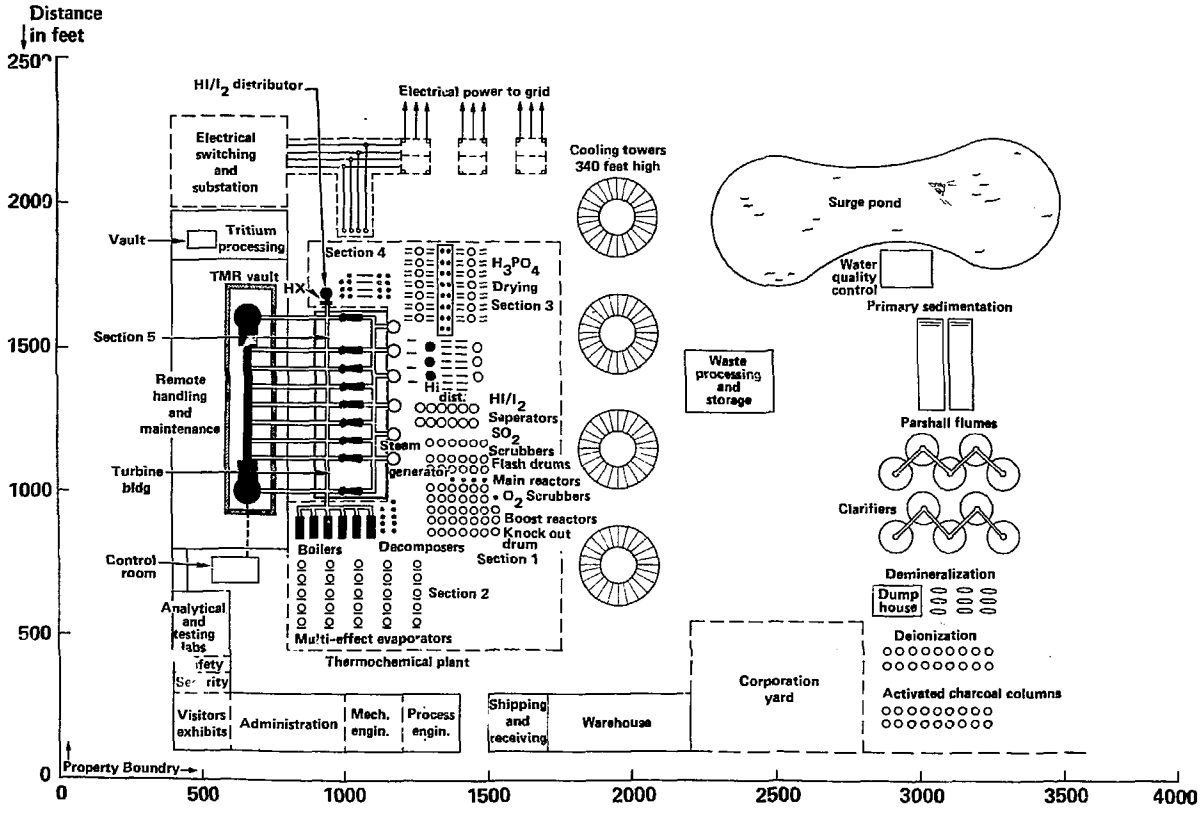

Fig. 1-5. TMR-synfuels thermochemical hydrogen-production-plant plot plan, 1981 version.

Table 1-2. Candidate construction materials for H_2SO_4.

Principal unit operation	Fluids	Approximate fluid tempertures °C	Approximate fluid tempertures K	Material candidates for heat exchangers, vessels, pumps, and other hardware	
Main solution reaction	$SO_2 + I_2 + H_2O \rightarrow$ $HI_x + H_2SO_4$ (55 wt%)	125	398	Glass-lined steel	Ceramics-SiC, Al_2O_3, carbon
				Fluorocarbon plastics and elastomers	Impervious graphite tantalum
Concentration	H_2SO_4 55-65 wt%	95-150	368-423	Hastelloys B-2 or C-276 Impervious graphite	Glass or brick-lined steel
Concentration	H_2SO_4 65-75 wt%	150-180	423-453	Hastelloys B-2 or C-276 Impervious graphite	Glass or brick-lined steel
Concentration	H_2SO_4 75-98 wt%	180-420	453-693	Brick-lined steel; cast Fe-14 wt% Si	
Vapor formation and decomposition	$H_2SO_4 \rightarrow H_2O + SO_3$	330-600	603-873	Brick-lined steel; cast Fe-14 wt% Si Silicide coatings on steel; Hastelloy G	
Vapor decomposition	$SO_3 + H_2O \rightarrow$ $H_2O + SO_2 + \frac{1}{2} O_2$	600-850	873-1123	Incoloy 800H with aluminide coating Waspaloy with coating	

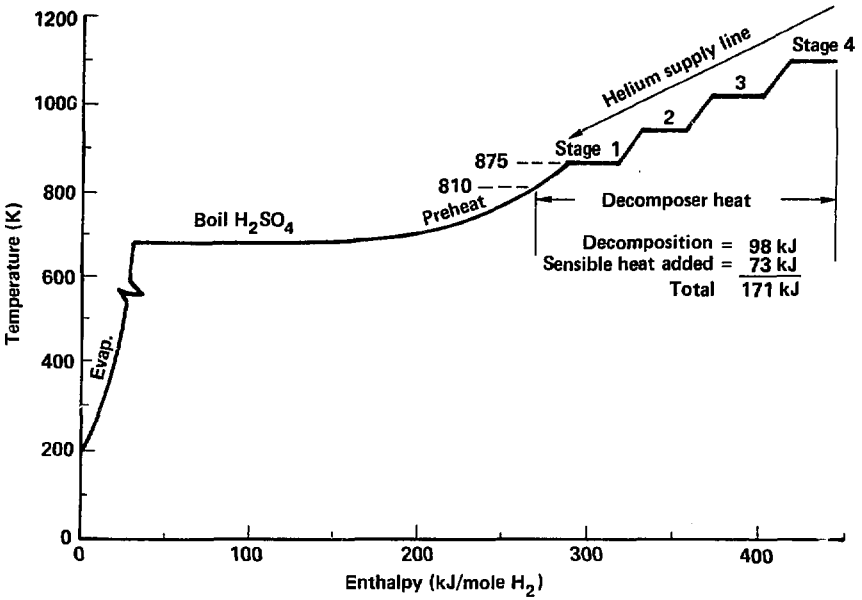

Fig. 1-6. The temperature enthalpy curve tracked by the multi-staged fluidized-bed decomposer.

1.9 FUELS BEYOND HYDROGEN

Hydrogen is a fuel in its own right. Whether we can ever progress to a total hydrogen economy is doubtful. As we have stated, in the long view hydrogen may better serve as a feedstock to produce more complex fuels such as methanol. We do not yet know what the best fuel or product might be; we have chosen methanol to illustrate that it is a reasonable next step to synthesize this fuel from hydrogen through fusion and thermochemical cycles, particularly in a transition period when a fusion economy is just emerging and our coal resources have not yet been depleted. The virtue of methanol synthesis from fusion is twofold: less coal is used in the process because fusion replaces the otherwise necessary coal combustion and less carbon dioxide is vented to the atmosphere precisely because coal is not burned. The production of methanol is discussed in Sec. 10 of this volume.

Table 1-3. Multi-stage fluidized-bed SO_3 decomposer.

Highlights

- 1100 K last stage operating temperature gives 63% decomposition, 1200 K maximum structure temperature.
- Four-stage decomposer matches blanket heat output efficiently and relieves energy requirements on hottest stage as 1/n, where n is the number of stages.
- Waspaloy has good properties at 1200 K and does not require a major development effort.
- As a fluidized bed concept, each stage is isothermal and temperature gradients are minimal between the bed and the coolant.

Data on the fourth stage (only) using Waspaloy double-walled (duplex) tubes--preliminary figures[a]

Parameter	Value
Maximum operating temperature (K)	1202.5
Heat flux through tube walls (W/cm^2)	2.5
Primary circumferential stress:	
Outer tube (MPa/psi)	12.1/1750
Inner tube (MPa/psi)	12.1/1750
Allowable stress, 1% creep at 10^5 hour (MPa)	25
Inside diameter (cm)	1.1
Outside diameter (cm)	1.58
Wall thickness, double wall (cm)	0.24
Number of decomposers required	9
Energy per decomposer (MW)	104
Decomposer diameter (m)	3.14
Decomposer stage height (m)	2.2
Decomposer overall height (m)	∿9
Tube side	Helium at 50 atm
Shell side	SO_3 - SO_2 at 7 atm

[a] $\approx 10^5$ tubes total in all stages.

CONTENTS

1.10 TRITIUM CONTROL

As we have implied previously, we believe that the study of fusion/synfuels will continue to have a very positive impact on generic fusion reactor designs, bringing into the fold as it does new technical disciplines with different perspectives and bringing to attention those areas that may have had less than sufficient study. A case in point is tritium control: tracing the triton as it migrates through the system from its birth in the blanket as a result of a neutron-lithium reaction to its desired destination as a fuel to drive the reactor. For synfuels this tracking is of paramount importance because the hydrogen product that we wish to sell must be essentially tritium-free. However, keeping track of the tritons is not limited to our special application of fusion but is a problem for the scientific community as a whole, since the way the tritium is dispersed and held up throughout the reactor system in different materials at different temperatures has a strong impact on the success or failure of a particular design concept.

To reduce the tritium inventories in the high temperature zone of the blanket to acceptable levels, we emphasized material selection and utilization. The piping, shroud, and support panels were constructed of $MgAl_2O_4$. Our first design used SiC. This was necessary because the tritium inventory in SiC was calculated to be extremely high, i.e., approximately 160 kg in alpha SiC or 800 kg in beta SiC, the usual form of the carbide. These high inventories occur mainly below 1100 K. Table 1-4 summarizes the tritium inventory in the overall reactor system. The 4.2-kg inventory is considered to be a reasonable amount.

Finally, we have calculated the atomic fraction of tritium in the hydrogen product to be 5.4×10^{-12}, quite close to our design goal.

The question of tritium control is fully discussed in Sec. 7 of this volume.

Table 1-4. Summary of the tritium inventory in the MARS/synfuel system.

Item	Tritium inventory (gms)
Blanket high temperature zone	2256
Blanket low temperature zone	79
Coolant handling system	1363
Storage unit (1 day fuel supply)	500
Total	4200

2 Physics Base and Parameters for the Tandem Mirror Reactor

CONTENTS

2. Physics Base and Parameters for the Tandem Mirror Reactor

2.1 GENERAL DESCRIPTION OF THE REACTOR AND ITS PHYSICS

The MARS TMR that is coupled to the synfuel production plant has a new axicell design. In this design an additional yin-yang pair is introduced into each end-plug region to provide MHD stability and reduce neoclassical radial transport. Continuous injection of neutral beams and electron-cyclotron resonant heating (ECRH) are required to maintain the plug's electrostatic confining potential. The thermal barrier located between the central cell and the plug creates a potential drop at the plug entrance, whereby plug electrons become thermally insulated from central cell and axicell electrons. This allows an increase of end-plug ion confining potential (ϕ_c in Fig. 2-1) by heating plug electrons locally rather than heating all the electrons in the machine.

The MARS TMR is ignited and confines 10% α-particle plasma density in addition to the DT plasma. Power is derived separately from an α-particle halo, which also serves the purpose of isolating the DT plasma from wall impurities. The loss of reactor gain from the α-particle plasma fraction is made up in the present design by replacing the charge-exchange thermal barrier pumps of the previous design[1] with a low-power drift pump to remove cold ions and α particles in the thermal barrier region. This can be accomplished with only a few MW instead of more than 100 MW used by neutral-beam pumping. The Q value is thus increased significantly even though thermalized α particles from the ignited plasma are retained.

Figure 2-2 shows the magnet set for the MARS axicell design. The components are described as follows:

1. The central cell is a 150-m-long solenoid in which a power-producing high-beta DT plasma is confined by straight magnetic field lines using simple, circular, NbTi superconducting coil modules. The magnetic field in the central cell is 4.7 T at the conductor.

2. The axicell is formed by two circular, high-magnetic-field coils. Each coil has a copper insert inside the Nb_3Sn superconducting coils to achieve a maximum magnetic field of 24 T. This high field provides high central-cell plasma density relative to the plug density. Neutral beams injected between the two axicell hybrid coils (point c) generate a small ion confining potential at this point and fuel the central cell (since the lowest axicell mirror magnetic field is toward the central cell, as can be seen from the magnetic field plot of Fig. 2-1a). Figure 2-1b shows the axial electrostatic potential profile.

3. The transition coil is a C-type coil. It transforms the plasma shape leaving the axicell from a circular cross section into an elliptical cross section necessary for the yin-yang anchor.

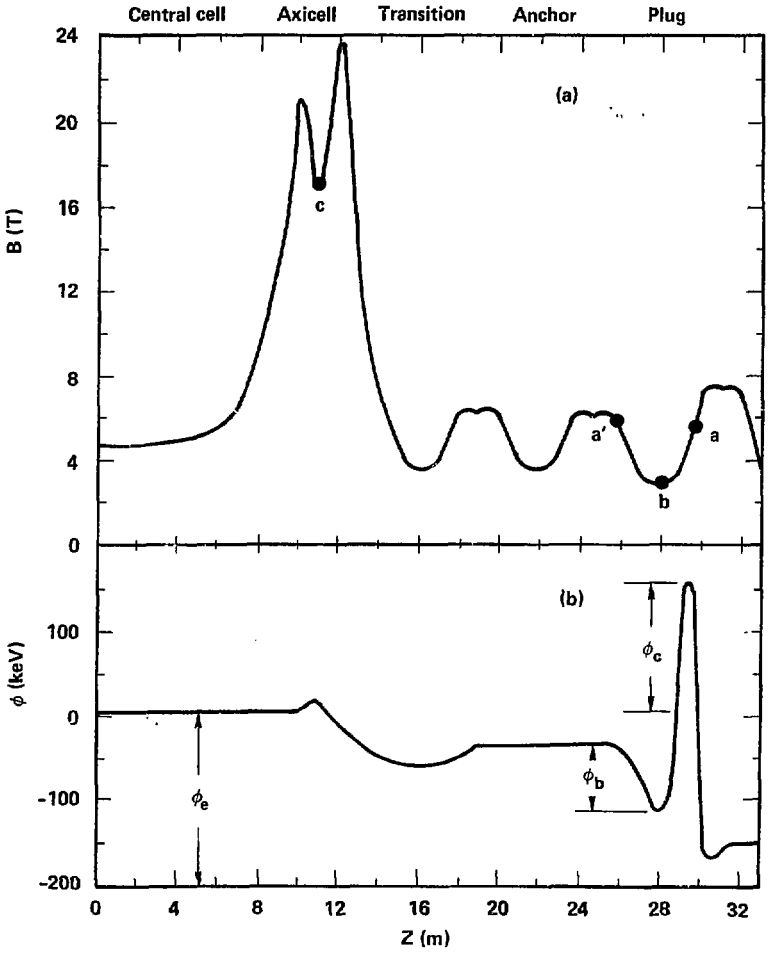

Fig. 2-1. Axial plots of magnetic field and electrostatic potential in the MARS TMR end region.

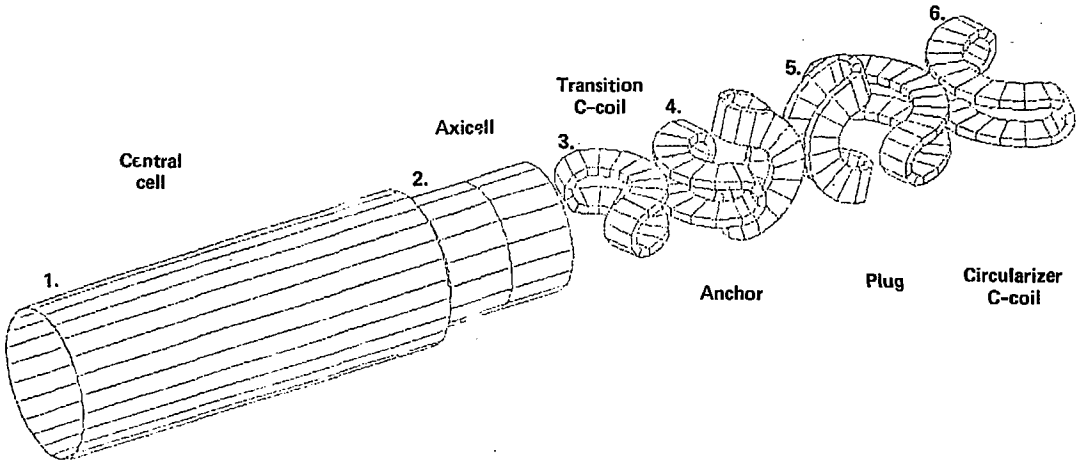

Fig. 2-2. Magnet coils for the MARS axicell TMR.

4. The anchor and the plug are both yin-yang pairs. In the transition to the anchor the ions are heated by ion-cyclotron resonant heating (ICRH) at 55 MHz, and a 5-keV neutral beam is injected. In the plug, a 475-keV neutral beam is injected off midplane (at point a') to provide sloshing ions that create density maxima near their turning points. ECRH at the thermal barrier minimum (point b) provides mirror-trapped electrons that reduce the fraction of cold central-cell electrons passing into this region. This further deepens the thermal barrier potential well.

   The anchor and the plug provide MHD stability for the whole configuration. They form the confining potential ϕ_c and the potential barrier ϕ_b, which separates the central cell and yin-yang electrons, as shown in Fig. 2-1b. The back-to-back anchor-plug combination also cancels the geodesic (twisting) curvatures of the B lines to provide improved radial transport.

5. The axicell magnet (rather than a a yin-yang) is necessary on economic grounds to provide the strong mirror field that separates the central cell and anchor-plug regions. It also regulates the small fraction of passing plasma density in the end region to stabilize trapped-particle modes.

2.2 PHYSICS PARAMETERS FOR A 3500-MW_f REACTOR

Table 2-1 shows the optimized reactor parameters for P_{FUS} = 3500 MW_f appropriate for coupling to the synfuel plant at a hydrogen chemical equivalent power of 1437 MW. A key parameter is Q = 33, corresponding to a central cell length of 150 m. The wall loading Γ = 5 MW/m^2, and the first wall radius is 0.6 m.

A general view of the MARS TMR plant for electrical production is shown in Fig. 1-2. The tanks at the ends contain circular direct converters of plasma end-loss energy to electricity.

2.3 TANDEM MIRROR REACTOR POWER BALANCE FOR PRODUCING HYDROGEN

Figure 2-3 is a power-flow diagram of the parameters shown in Table 2-1 for the MARS TMR synfuel case where we have a fusion power of 3500 MW and a reactor Q of 33. The five contributors to the TMR-injected power of 106 MW_e are shown, as well as losses of 180 MW_e to the copper coils and auxiliary systems. The blanket power of 3282 MW_t supplies the synfuel plant, which has a hydrogen output of 5024 mole/s (1437 MW). The synfuel plant also requires 468 MW_e of electric input. This synfuel electrical requirement and the TMR recirculating power of 348 MW_e are furnished by 452 MW_e from a steam power plant operating on synfuel plant heat, plus 364 MW_e from the direct converter.

Table 2-1. MARS physics parameters for coupling to the synfuel plant.

Parameter	Value
Central cell	
Ion density, n_c (cm^{-3})	3.7×10^{14}
Ion temperature, T_c (keV)	26
Electron temperature, T_{ec} (keV)	22
Vacuum magnetic field, $B_{c,vac}$ (T)	4.7
Beta (average)	0.28
Central cell potential, ϕ_e (keV)	161
Central cell length (m)	150
First wall radius, r_{FE} (m)	0.60
Hot plasma radius, r_c (m)	0.49
Neutron wall loading, Γ_{fw} (MW/m^2)	5.0
Fusion gain Q	33
Axicell	
Total ion density (cm^{-3})	6.8×10^{15}
Hot ion density (cm^{-3})	4.7×10^{14}
Average confined ion energy (keV)	300
Midplane plasma radius (m)	0.27
Plasma length (m)	2.0
Beta (m)	0.2
Transition/anchor region	
Passing ion density at B minimum (cm^{-3})	1.9×10^{13}
Passing ion density at geodesic curvature peaks (cm^{-3})	3.9×10^{13}
Hot ion density (cm^{-3})	4.2×10^{13}
Average confined-ion energy (keV)	690
Beta (average)	0.5
Length (m)	15.5
Yin-yang plug	
Passing ion density at barrier (cm^{-3})	5.3×10^{12}
Sloshing ion density at barrier (cm^{-3})	1.1×10^{13}
Hot electron energy at barrier (keV)	730
Warm electron temperature at potential peak (keV)	120
Length (m)	6.6
Beta (average)	0.5
Ion confining potential, ϕ_c (keV)	142
Barrier potential depth, ϕ_b (keV)	113

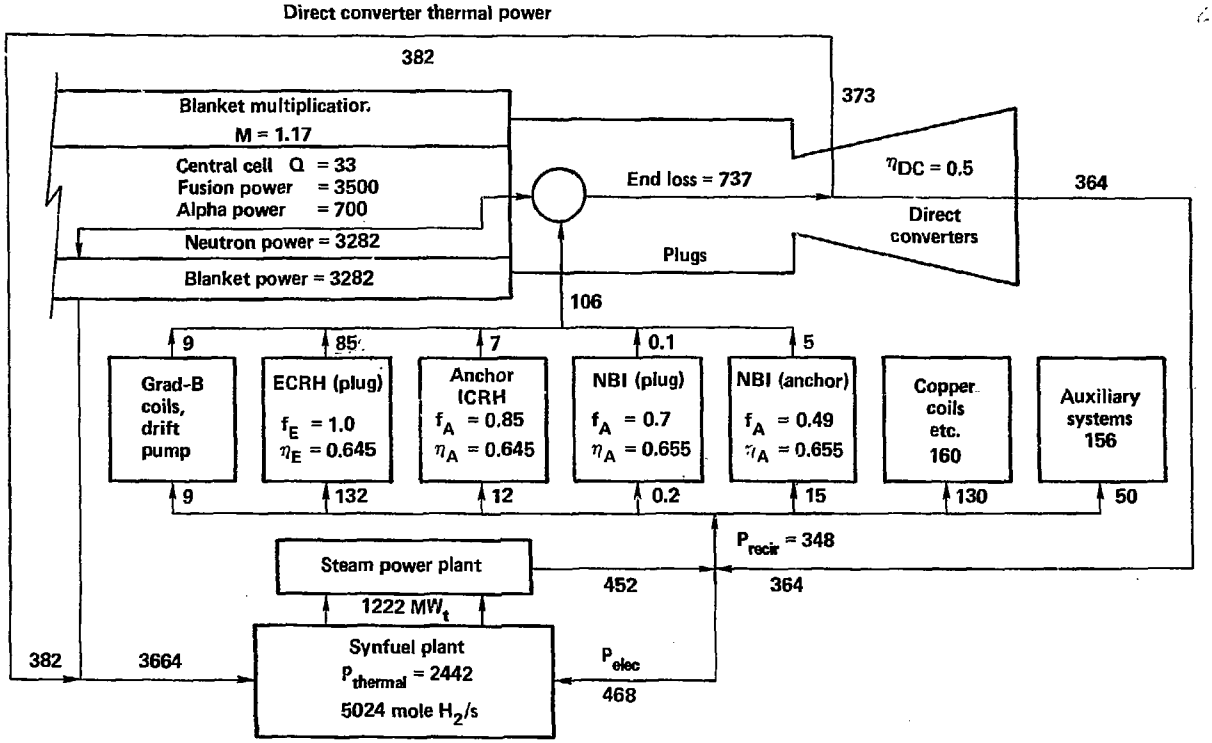

Fig. 2-3. Power-flow diagram for the MARS TMR for hydrogen production.

2.4 SYNFUEL INFLUENCE ON THE MARS DESIGN

In contrast to the TMR parameters in Table 2-1 and Fig. 2-3, the MARS reactor for electrical application, discussed in Volume 1 of this report, has a smaller fusion power of 2547 MW, which provides an electrical output of 1200 MW_e, an output constrained by the present maximum size criteria of power stations on an electrical power grid.

This arbitrarily reduced power for electrical use yields a lower Q value of 26 (33 for the synfuel case) brought about primarily by a reduced reactor length of 129 m (150 m for the synfuel case) and a reduced wall loading of 4.3 MW/m^2 (5.0 MW/m^2 for synfuels).

The synfuel plant allows a higher TMR Q value, and a more nearly optimal use of the TMR principle. Because a synfuel plant can stand alone with its own fusion power plant, it can accommodate greater power without the requirement of electrical grid conformity.

REFERENCE

1. R. W. Werner, T. H. Zerguini, and F. L. Ribe, Synfuels from Fusion Using the Tandem Mirror Reactor and a Thermochemical Cycle to Produce Hydrogen, Lawrence Livermore National Laboratory, Livermore, CA, UCID-19609 (1982).

3 High-Temperature Two-Temperature-Zone Blanket System for Synfuel Application

CONTENTS

3. High-Temperature Two-Temperature-Zone Blanket System for Synfuel Application

3.1 GENERAL DESCRIPTION OF THE BLANKET MODULE

The MARS high temperature blanket has two temperature zones: a helium-cooled high-temperature zone (950°C) and a Li-Pb-cooled low-temperature zone (500°C). The blanket structural material is HT-9 ferritic steel kept at or below 520°C by the Li-Pb coolant. Each blanket module is composed of a cylindrical first wall structure and two Li-Pb end-closure plena. A set of 12 pods (submodules) suspended within the Li-Pb forms the high temperature zone. The entire blanket mass plus the weight of the magnets are supported by the shield structure (see Fig. 3-1).

3.2 GOAL OF THE HIGH TEMPERATURE BLANKET

The principal goal of the MARS high temperature blanket design effort is to produce high temperature heat for synthetic fuel or electricity production. The blanket has been integrated with the thermochemical process for synthetic fuel production (see Sec. 6 of this volume) to yield efficient conversion of fusion energy to hydrogen fuel. Our conversion efficiency is 37%. Additional goals that have had a significant effect on the design are manufacturability, low tritium inventory, no reactive liquid metals, no exotic materials, and a maintenance concept that allows all central-cell components to be replaced as part of normal operations.

3.3 PERFORMANCE SUMMARY

Neutronics analyses show that the high temperature blanket has an energy multiplication (M) of 1.15, a tritium breeding ratio (TBR) of 1.13 and a deposited fraction of high temperature heat (FHT) of 0.48. Thermal losses from the high temperature zone to the low temperature zone reduced the FHT to 46%. displacement per atom/full power year (dpa/FPY). (First wall damage is 69 dpa/FPY.) A maximum structural steel temperature of 520°C is expected, with a 24°C maximum ΔT through the first wall. Silicon carbide temperatures are expected to remain below 1050°C with the 950°C helium exit temperature. The helium pumping power in the blanket is calculated to be 1.6 MW. Helium inlet/outlet temperatures are 457 and 947°C, and Li-Pb inlet/outlet temperatures are 332 and 482°C. The 3- to 4-calendar year lifetime at 80% availability corresponds to 12 to 16 MW year/m^2 at the first wall. Fusion blanket lifetime studies remain speculative; however, we consider 3 to 4 calendar years reasonable at a 5-MW/m^2 wall loading.

Most of the tritium is bred in the high temperature zone to simultaneously achieve tritium self-sufficiency while maximizing the fraction of the blanket operating at high temperature. We use a small amount (2% by volume) of $LiAlO_2$ in the SiC spheres to achieve the tritium breeding and maximum heat fraction goals. The tritium inventory in the solid breeder is predicted to be about 2300 g.

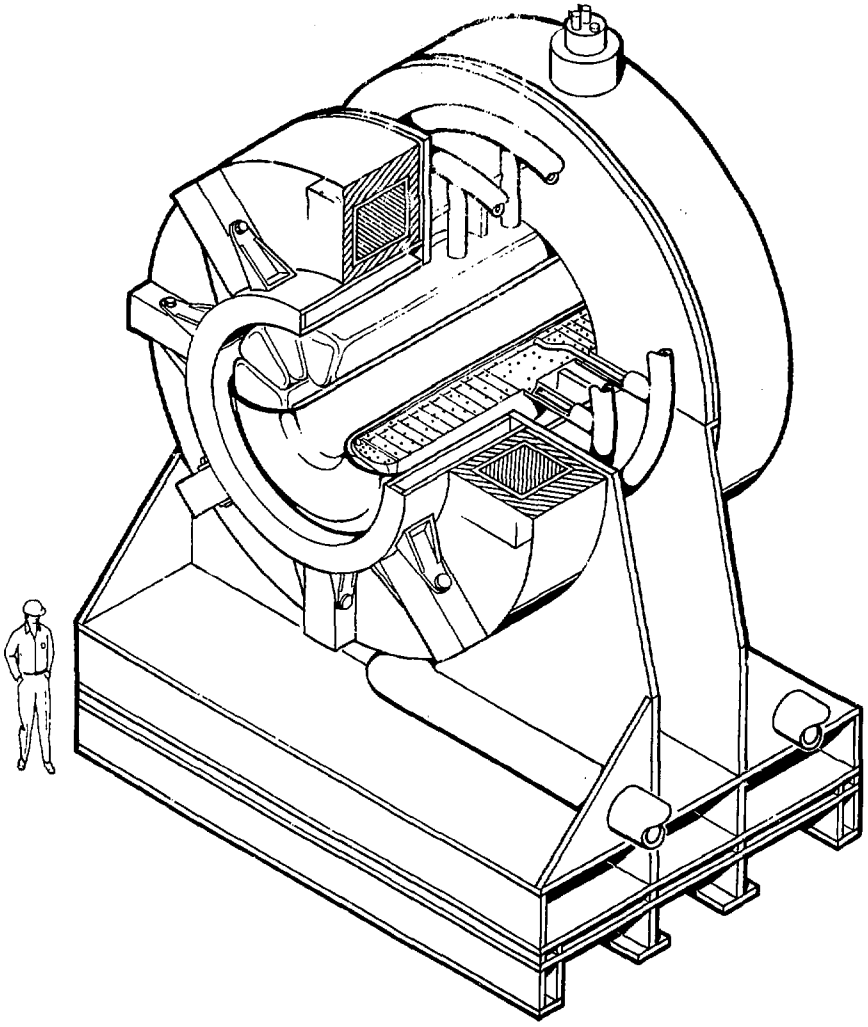

Fig. 3-1. High-temperature blanket module.

At this time we can only estimate the effects of swelling, embrittlement, and creep on the lifetime of structural steels as a result of fusion neutron fluences and energies. We have only recently begun studies of the combined effects of these phenomena. The blanket has been designed to tolerate swelling by allowing room for expansion. Predicted swelling, creep rates, and neutron effects on ductile-to-brittle transition temperatures are given in Sec. 9 of this volume.

Activation is minimized by selecting specialized materials. The most activated materials in the blanket are alloys added to the steel, such as molybdenum, nickel, and manganese. HT-9 with isotopically tailored molybdenum may be a feasible low-activation structural material. Minimizing the steel in the blanket also reduces the amount of activated material. We have not analyzed loss of coolant or lose of fusion accidents, but the two coolant blanket designs may prove advantageous if one of the coolants is lost.

The major issues associated with the high temperature blanket design are: Li-Pb corrosion, structural lifetime, MHD effects on liquid metal cooling, and tritium inventory in the solid breeder. The fusion community is currently investigating Li-Pb corrosion of HT-9. Relevant experimental results are presently available. We can only roughly estimate the lifetime of structures in the fusion environment, and this will remain an open issue for all fusion reactors until better analytical tools and experimental results are available. Tritium hold-up in the porous SiC and the $LiAlO_2$ solid breeder, ceramic pipe blanket liners, and metal pipe walls has been calculated to be 4200 g. However, neutronic effects on sintering, radio chemical effects on solubility, and precise rates of diffusion and removal are not well known.

3.4 BLANKET DESIGN

The MARS high temperature blanket concept is pictured in Figs. 3-1 through 3-3. All structural steel (HT-9) is in direct contact with $Li_{17}Pb_{83}$ for cooling and to minimize neutron capture in the steel. The high temperature zone consists of pods containing SiC pebbles doped with 2% $LiAlO_2$ for breeding tritium and cooled with 50 atm helium exiting at 950°C. It is necessary to breed tritium in the high temperature zone to obtain enough of the blanket heat at high temperature to match the thermochemical process requirements.

Performance goals include a high-temperature (900 to 1000°C) heat fraction greater than 40%, tritium self sufficiency (TBR > 1.05), and a 3- to 4-year first-wall/blanket lifetime. Major safety goals are low tritium inventory (less than 5 kg), no reactive liquid metals, minimum long-term activation, and a passive loss-of-coolant-flow safety system. Other design goals are the elimination of exotic materials (because of limited resources and costs), a blanket and shield thickness less than 1.85 m to reduce central-cell magnet costs, and easily removable magnets to simplify module change-out and magnet replacement.

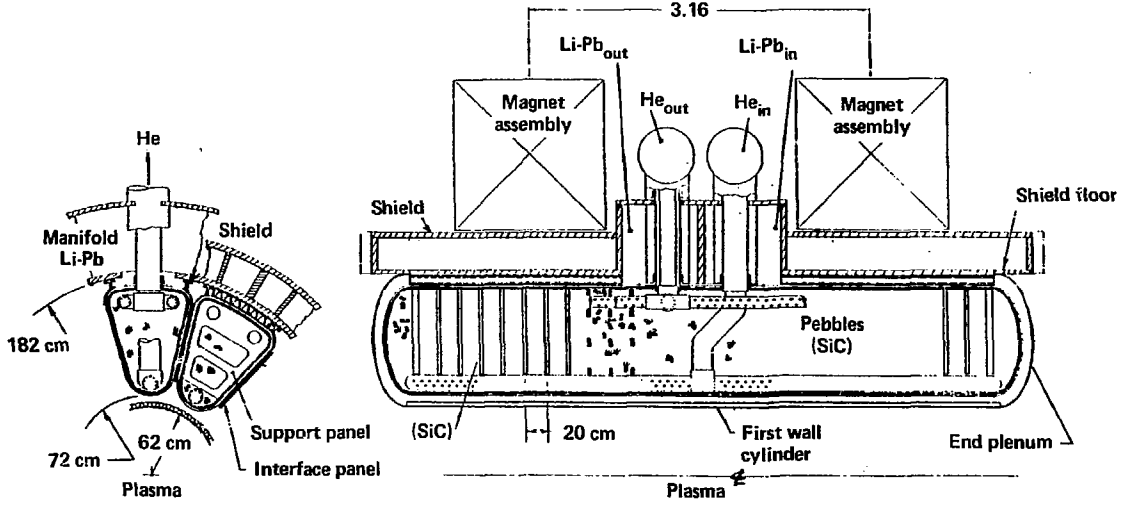

Fig. 3-2. High-temperature blanket structure.

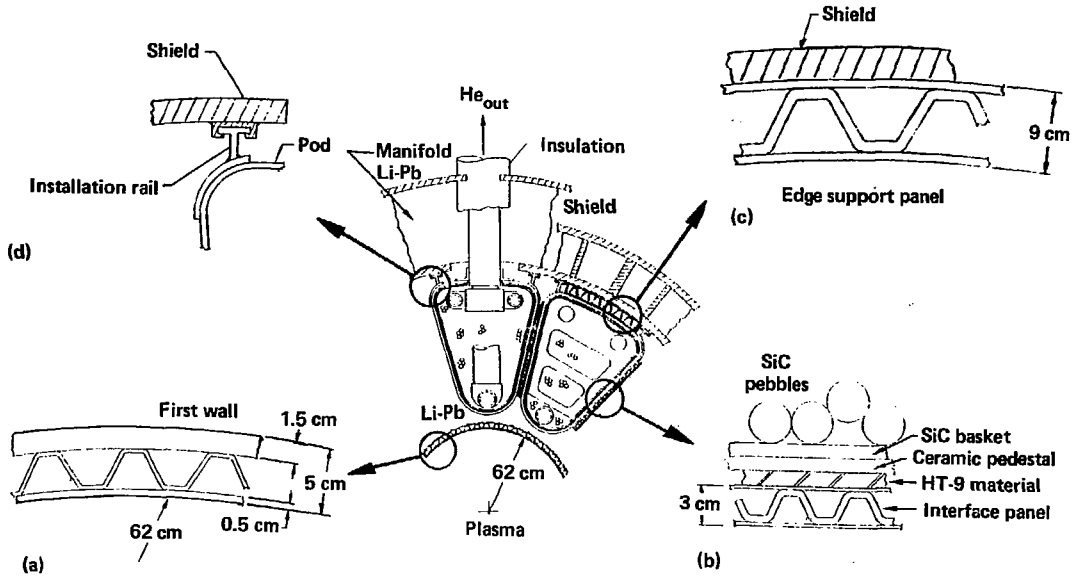

Fig. 3-3. Blanket first-wall and interface structure.

3.4.1 Low-Temperature Zone Structure

The low temperature structure is cooled by axially flowing Li-Pb enveloping the pods. All steel components are kept below 520°C. This region consists of: (1) the first wall structure, (2) interface panels between pods, (3) an edge support panel between the shield and back of the pods, (4) the pod support rails, and (5) the end plenum closures. These are shown in Figs. 3-2 and 3-3.

The first wall consists of a cylindrical, corrugated sandwich wall of HT-9. The composite wall is 5 cm thick, with a 0.5-cm first wall and a 1.5-cm second wall. The corrugation stabilizes the structure and provides flow direction for the Li-Pb (see Fig. 3-3a). Corrugated steel interface panels are placed between adjacent pods to provide Li-Pb flow passages for cooling and structural support for the pod sidewalls (see Fig. 3-3b). The edge support panels are similar to the interface panel, and they consist of corrugated sandwich-steel panels placed between the back wall of the pods and the shield to provide Li-Pb flow passages for cooling, as well as to transfer the helium pressure load from the pods into the shield structure (see Fig. 3-3c). The pod support system is a T-section support rail of HT-9 attached to each back corner of the pods. The support rails are mounted on the shield structure for support during assembly (see Fig. 3-3). The end plena consist of an annular end closure cap (5 mm thick) welded to each end of the first wall and the blanket shield (see Fig. 3-2).

3.4.2 High-Temperature Zone Structure

The high temperature pod is a 30-deg sector of a circular-shaped pressure vessel constructed of HT-9. The vessel is 592 cm long and 100 cm high with a nose radius of 23 cm. The vessel wall is 1.1 cm thick with a 2.1-cm-thick semi-elliptical dome welded to each end, as shown in Fig. 3-4. The steel vessel wall is maintained at or below 520°C by circulating Li-Pb on the outside of the pod.

Silicon carbide spherical pebbles 3.5 cm in diameter and SiC support panels 3 cm thick are supported on a 1-cm-thick SiC basket. The pebbles contain 2 at.% $LiAlO_2$. The basket supports the pebbles and panels and separates them from the steel vessel. Thermal insulation (a low-density alumina-silica mat) fills a 1-cm gap between the steel vessel wall and SiC basket. The gap is provided by 1-cm-high ceramic spacing pedestals placed between the steel vessel wall and the basket in alignment with the support panels (see Fig. 3-4). Each pod has 23 support panels, spaced at 20-cm intervals, except in the central helium inlet/outlet area (Fig. 3-2). The support panels resist a domino failure in which a sudden loss of pressure in one pod would cause adjacent pods to burst in series.

3.4.3 Module Structures

The shield is the main structural skeleton of the high temperature blanket. The end plena and high temperture pods are attached to and supported by the shield. Because the shield, magnet supports, piping structures, and module support have been integrally designed with the blanket, these structures are described here.

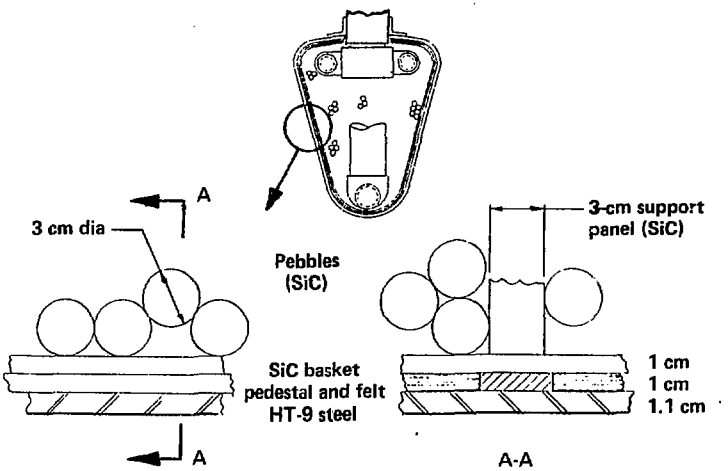

Fig. 3-4. Helium pod.

3.4.4 Magnet Support

The shield structure acts as an integrated box beam and as such is designed to transmit loads resulting from the magnet weight (200 tons) and critical failure condition (13,000 tons axially). The magnet loads are transmitted to the shield via the eight pin-joint-attach fittings (shown in Fig. 3-5), which are secured to a continuous circumferential-structural ring that attaches through bolt patterns to the shield.

This type of support has several unique design advantages. For example, only a minimum of effort is needed to remove the magnets; paths are restricted to minimize magnet heat loss; and magnet failure loads can be accommodated. Magnets can be separated from the module by removing the shear bolts used to secure the structural ring to the shield. Enough stiffeners are provided to ensure minimum out-of-round deflection of the ring. Conduction heat paths are intercepted at the pin joint by a 2.5-cm polyimide insulating collar. Active liquid-nitrogen cooling can be introduced within the pin (by providing a 1.5-in.-diameter hole) to increase the collar's effectiveness. Additional intercepts can be provided by isolating the magnet support arms with a pin/truss type of structure.

The superconductor will contract during chilldown by approximately 2 cm. This contraction as well as vertical alignment tolerances are accommodated by incorporating vertical translation slots into the support fitting. Because of the geometry of the magnet support structure, this also defines a single predictable load path for the magnet weight; the magnet is essentially hung from the top pin. Because the support pins are sized for the failure load, they provide a simple method of supporting the weight while relieving tolerance requirements.

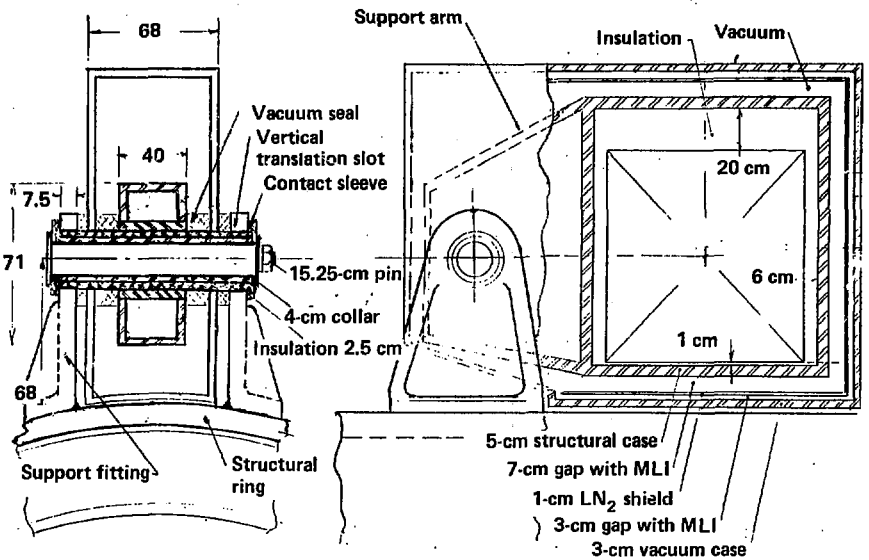

Fig. 3-5. Magnet support structure.

The liquid-nitrogen magnet heat shield is attached directly to the magnet vacuum case by spacers, whereas the vacuum case itself is directly supported on the pin and is therefore free from physical contact with the superconductor. The vacuum is isolated at the pin joint by insulating vacuum seals.

3.4.5 Lithium-Lead and Helium Piping Structure

Figures 3-6 and 3-7 show the flow paths for the Li-Pb and helium coolants. The relatively low temperature and pressure requirements for the Li-Pb allow the use of rectangular flow paths with conventional steel plate construction. The shield construction geometry allows the water and Li-Pb flow paths to be separated from each other by double wall construction. It also allows the separation of any interface weld joints. The high-temperature, high-pressure helium pipes are lined with insulation.

3.4.6 Assembly Structural Support

The module weight and magnet loads are carried to the floor with conventional plate steel construction. This support structure uses box-type construction to maximize rigidity and redundancy. Loads can be reacted in the floor through grips and/or bolt tie downs.

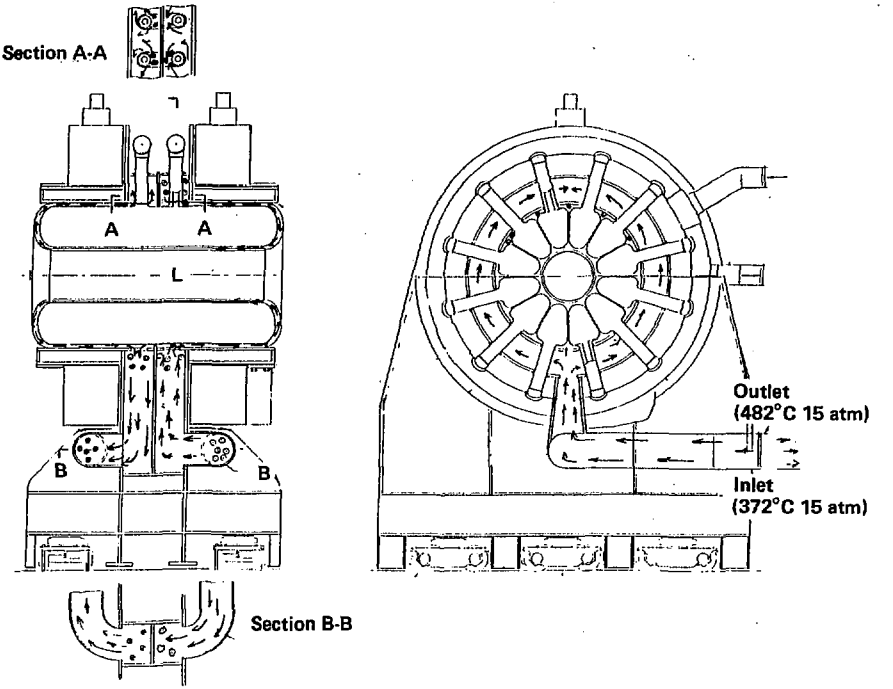

Fig. 3-6. Lithium-Lead coolant flow paths.

Reactor alignment is provided by module-mounted jacks. Transhaulers are used to move the modules into the reactor for positioning and alignment. Six of these rail-type movers are required to move a module. They are remotely operated, permit ±60-deg module movement, and incorporate a vertical lift stroke of 19 cm.

3.5 STRUCTURAL ANALYSIS

3.5.1 Approach

The fusion reactor will have to be tested to determine how the fusion environment affects the material properties of steel. We have designed to tolerate swelling and thermal expansion by allowing the structures to move. We have also performed a simplified analysis to ensure that beginning-of-life stress levels are tolerable; the results are presented below.

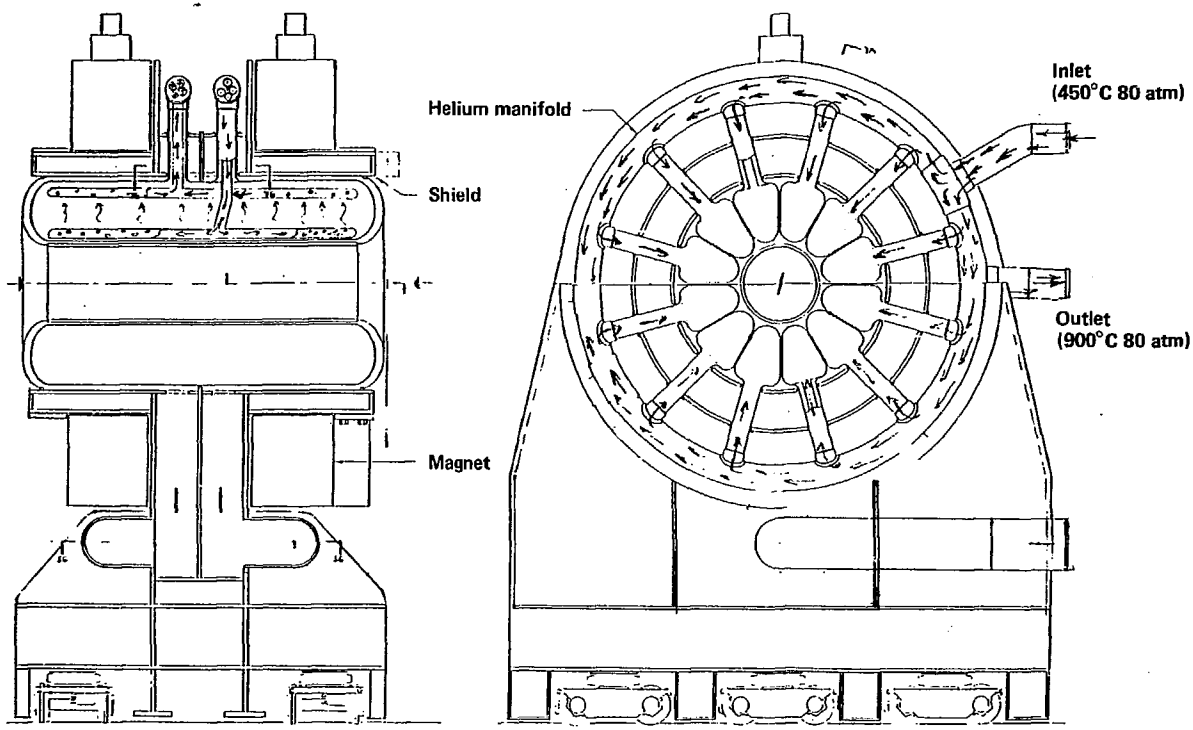

Fig. 3-7. Helium coolant flow paths.

3.5.2 Allowable Design Stress for HT-9

We have estimated the allowable design stress as a function of temperature for HT-9 based on experimental data. Figure 3-8 shows the result of plotting the lowest value of two-thirds yield strength at room temperature, one-third ultimate tensile strength at temperature, or two-thirds the creep rupture strength at temperature for a 3-calendar-year lifetime (at 80% availability). Design stress for a 3-year lifetime is limited by the ultimate tensile strength below temperatures of 540°C and by creep rupture strength above this temperature. The MARS high temperature blanket does not appear to be limited by creep at the 520°C operating temperature for 4 full power years.

It is possible to attain higher strengths by heat treating HT-9, but we did not choose to do this because it would aggravate embrittlement problems, both neutron-induced and lead embrittlement. Several allowable design strengths for HT-9 have been reported because of variations in interpretating the data, allowable strength criteria, and heat treatment and manufacturing techniques. The allowable stresses presented in Fig. 3-8 are conservative and are reasonably close to values used by others.[1,2]

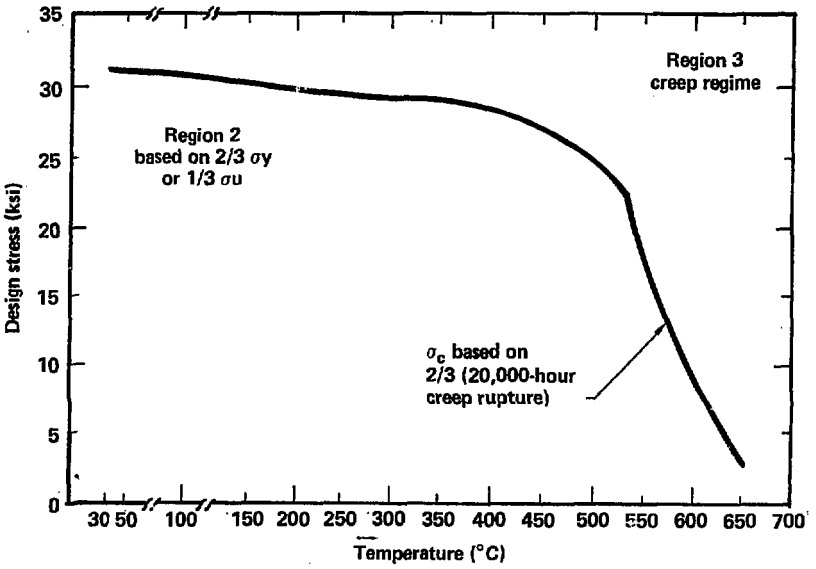

Fig. 3-8. Allowable design stress vs temperature for HT-9.

3.5.3 First Wall

The first wall is a cylindrical shell of corrugated sandwich construction with the corrugations oriented in the axial direction. This shell is subjected to an external pressure load from the Li-Pb. To use the design procedures of the ASME boiler code,[3] we derived an equivalent cylinder thickness based on the sandwich shell having equal stiffness in both the hoop and axial directions for a 5-cm-thick sandwich construction, with the outer facing 1.5 cm thick and inner facing 0.5 cm thick. The equivalent thickness is computed to be 4.05 cm. The allowable pressure is not currently available in the boiler code for HT-9. We used the allowable pressure for the nickel-iron-chromium alloy Incoloy 800 because the mechanical properties for this alloy are close to those of HT-9. The design, based on this analysis, is rated for 200-psi allowable external pressure, which produces a hoop stress of 5.9 ksi. This is well below the design strength for HT-9. Hence, we have concluded that the chosen geometry satisfies the design requirements.

3.5.4 Pod Analysis

The pods are basically a single-wall HT-9 construction under an internal pressure of 50 atm. A corrugated sandwich panel is inserted between the side walls of the adjacent pods to reduce the bending stress on the flat portion of the pods. The nose section of the pods is cylindrical. The minimum thickness of the nose section was obtained using Boiler Code Equation-VG-27(C) (1).[3] Using an allowble stress of 23 ksi (see Fig. 3-8), we computed the minimum thickness of the pod nose section to be 0.7 cm.

Each pod contains 23 SiC panels each 3 cm thick. These panels are of nonuniform width to accommodate the pod section and allow for cutouts. If the pressure in a pod drops to zero, the pressure from the pods on either side has to be resisted to avoid a propagating failure. The side wall resists these forces by acting as a beam in bending and transferring the load to the SiC panels, which act as plate columns in compression and bending. A preliminary analysis showed that these panels do not have a problem resisting the bending and compressive loads.

The side walls of the pods can be treated as flat rectangular sandwich plates supported by SiC panels. Other considerations dictate a maximum spacing of 100 cm between the SiC panels near the helium entrance piping. Treating this 100-x-70-cm panel as a simply supported sandwich plate and using the procedure outlined in Ref. 4, we computed that a pressure of 850 psi produces a maximum bending stress of 42 ksi. In bending, the boiler code allows the stress level to reach as high as the room temperature yield stress (σ_y = 45 ksi at room temperature for HT-9). This means that the sidewalls of the pods can withstand a pressure drop of 850 psi as a fault condition. Analysis has shown that an 8-in.-diameter hole in a pod would cause a maximum pressure drop of 350 psi between adjacent pods because of the common header pressure coupling.

3.5.5 End Closure Analysis

There are two types of end closures: individual pod end closures of approximately semi-elliptical dome shape under an internal pressure of 50 atm,

and a toroidal ring end plenum under an internal pressure of 200 psi. For the purposes of doing a preliminary analysis, both end closures may be approximated as ellipsoidal heads with a ratio of 2:1. We used boiler code equation VG-32d to determine the minimum thickness, which resulted in a minimum thickness of 1.6 cm for the pod end closure and 0.5 cm for the end plenum.[3]

3.5.6 Magnet Support Analysis

The magnet support consists of eight double-shear-pin assemblies that transfer magnetic and gravitational forces from the magnet into the support structure. The support structure then transfers these forces to the ground. The gravitational forces are produced by the weight of the magnet and the structure. The magnetic forces are caused by a fault condition where one magnet de-energizes but the others keep functioning. This results in a 2.7×10^7 lb load applied axially on the magnet center line.

We have analyzed the key areas of high stress (the support pins and the magnet mounting bolts). A von Mises failure criterion is assumed for a biaxial state of stress with a safety factor of 1.5. We analyzed the pin as two short cantilevers rigidly fixed at the center section. Because of the shear and bending, the 10-in.-diameter pin material needs to have a yield stress of ~149 ksi (e.g., SS-304LN). When the actual material is selected, a fracture analysis will be performed to avoid catastropic brittle failure. The bolts mounting the magnet assembly to the module support structure require a shear yield strength of 80 ksi (e.g., heat-treated SS-316). A total of 20 2-in.-diameter bolts is required for each pin support assembly (10 per side).

3.5.7 Module Structural Support Analysis

The critical section for the module occurs where a simple box structure resists the bending moment and shear. At this section, assuming 2-in.-thick inner walls and 4-in.-chick outer walls, the material yield stress would be ~64 ksi. The base section for transferring the loads to the ground would have a yield stress of 78 ksi. Because high-strength heat-treated materials are impractical for the large support structures, these areas will be reinforced. We have reported the strength requirements for this first-cut design because they show that the stresses are within reason, requiring less than a factor of two reduction to allow the use of any of several steels.

3.6 NEUTRONICS

Our neutronics analyses have concentrated on the module lifetime, tritium self-sufficiency, and the fraction of energy deposition in the form of high temperature heat. We have covered the following areas:

1. Blanket ceramics (other than graphite) to overcome swelling problems (lifetime constraint).

2. Addition of lithium-bearing compounds to the solid breeder (tritium production and FHT constraint).

3. Addition of a thick, frontal Li-Pb zone to enhance breeding and reduce parasitics in the solid breeder (tritium production constraint).

4. Dimensional adjustment to balance tritium production, energy multiplication, and FHT.

5. Three-dimensional calculations to fine-tune the design.

6. Burnup calculation to verify adequate module lifetime and demonstrate adequate module performance over that lifetime.

3.6.1 One-Dimensional Neutronics Analyses

Table 3-1 presents selected results from a series of one-dimensional calculations to evaluate the thickness of the front Li-Pb zone and thickness of the SiC "breeder" region. The Li-Pb uses natural lithium, whereas the breeder has 2 vol% $LiAlO_2$ (90% enriched in ^6Li) in SiC. Earlier neutronics results indicated that tritium production in the breeder was clearly dominated by the ^6Li (n,T) reaction; to reduce sintering, the volume fraction of the lithium-bearing compound was minimized by ^6Li enrichment. We selected $LiAlO_2$ as the lithium-beating compound because of its chemical compatibility with SiC.

Table 3-1. Blanket thickness analysis.

Thickness of front Li-Pb (cm)	Thickness of breeder region (cm)	Blanket energy mult. (M)	Tritium breeding ratio (TBR)	Fraction of blanket energy at high temperature (FHT)	First wall damage (dpa/year)	Leakage
10	100	1.25	1.31	0.54	71	9.3×10^{-4}
14	148	1.26	1.38	0.62	74	4.5×10^{-5}
14	60	1.29	1.23	0.45	73	6.6×10^{-3}
5	148	1.22	1.25	0.74	68	8.6×10^{-5}
5	60	1.25	1.04	0.53	66	1.1×10^{-2}

Tables 3-1 and 3-2 present the results of selected calculations of Li-Pb lithium enrichment and the volume fraction of $LiAlO_2$ for fixed blanket dimensions corresponding to a frontal Li-Pb zone of 5 cm and a breeder zone of 1 m.

Table 3-2. Lithium enrichment analysis.

^6Li enrichment in Li-Pb (%)	Fraction $LiAlO_2$ in SiC breeder	M	TBR	FHT	First wall damage (dpa/yr)	Energy deposition (W/cm^3)
7.6 (natural)	0.01	1.24	1.21	0.35-0.53	69.0	38.0
7.6	0.02	1.23	1.24	0.39-0.54	69.0	37.8
1	0.01	1.26	1.13	0.41-0.54	69.4	39.2
1	0.02	1.24	1.19	0.44-0.56	69.4	38.7

Table 3-3 shows the spatial energy deposition for the one-dimensional model in Fig. 3-8: the FHT is equal to the higher of the bracketing values given in Table 3-2. The FHT bracketing calculations are done by first assuming that the Li-Pb at the pod edge is to be ignored (generating the lower limit) and by then assuming that the Li-Pb at the edge is uniformly distributed throughout the pod (generating the upper limit). As input to the thermal analysis, the upper limit on the FHT is the most conservative.

3.6.2 Three Dimensional Neutronics

Figure 3-9 shows the cross-sectional equivalence between one- and three-dimensional neutronics models; not shown are the axial zones corresponding to Li-Pb plena and module ends. The three-dimensional model was deemed necessary to adequately assess the axial competition for neutrons between SiC regions without Li-Pb and the Li-Pb-filled regions between adjacent pods and at the module ends. Because the Li-Pb regions are not intimately dispersed within the breeder material, one-dimensional analysis will tend to over-predict tritium production and under-predict parasitic capture. FHT is also difficult to treat adequately in one-dimensional analysis. (Table 3-2 shows the bounds.)

Table 3-3. Blanket energy deposition.

Zone	Inner radius (cm)	Material	Energy deposition (MeV/source neutron)
1	62	Steel	0.569
2	62.5	Li-Pb	2.498
3	65.0	Steel	1.695
4	67.0	Li-Pb	2.361
5	72.0	Li-Pb	0.267
6	72.75	Breeder + steel + Li-Pb	1.345
7	77.5	Breeder + steel + Li-Pb	0.092
8	82.5	Breeder + steel + Li-Pb	0.874
9	87.5	Breeder + steel + Li-Pb	1.462
10	92.5	Breeder + steel + Li-Pb	1.143
11	102.5	Breeder + steel + Li-Pb	1.543
12	112.5	Breeder + steel + Li-Pb	0.948
13	132.5	Breeder + steel + Li-Pb	0.449
14	152.5	Breeder + steel + Li-Pb	0.013
15	171	Steel	0.107
16	172	Li-Pb	0.107
17	182	Shield	0.241
		Total	1622
		FHT	0.46

The three-dimensional performance parameters are seen to be a tritium breeding reactor of 1.13, a blanket energy multiplication M of 1.15, and 0.48 for the FHT. These compare to the one-dimensional parameters of 1.24, 1.19, and 0.44 to 0.56. It is worth noting that the depletion of ^{6}Li in the Li-Pb diminishes the disparity between the one-dimensional homogenized zone descriptions and the three-dimensional system they model.

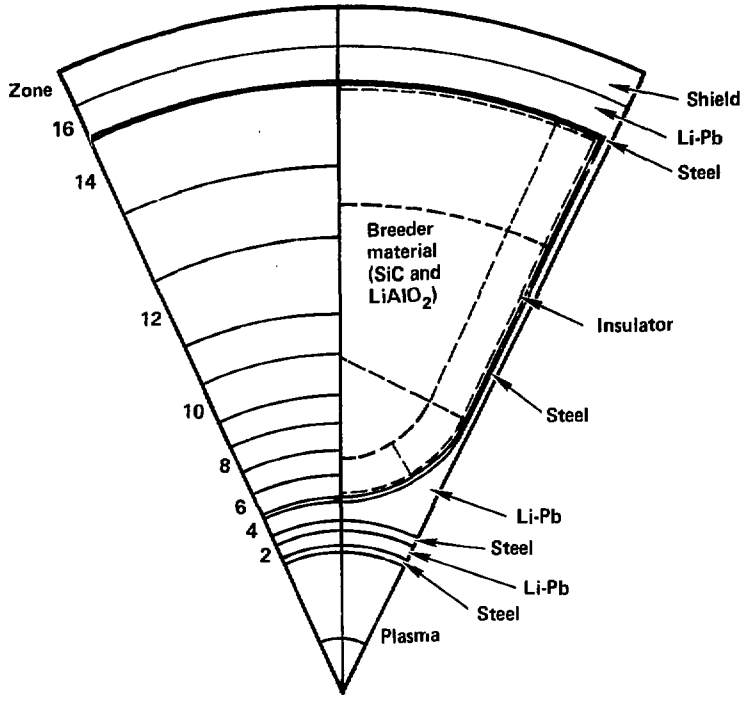

Fig. 3-9. One- and three-dimensional neutronics models (axial details not depicted).

3.6.3 Burnup Calculations

Using a solid breeder for both tritium breeding and high-temperature heat production requires a time-dependent calculation to evaluate the effects of burnup. Lithium burnup is particularly important since the neutronics performance is affected by the size of the regions and the distribution of ^{6}Li and ^{7}Li. The Li-Pb, which is distributed among all the modules and mixed, is assumed to be maintained at a constant concentration. The principal effect of neutron interactions with $LiAlO_2$ is a reduction in lithium concentration. The ^{7}Li burnup is almost three orders of magnitude less than the ^{6}Li burnup and will be less than 1% over the life of the module. Therefore, only ^{6}Li burnup is explicitly calculated. An average burnup rate for each zone is calculated from the three-dimensional TART run by

$$K = \frac{RF}{L} \quad ,$$

where

K is the burnup per atom of ^6Li per year,

R is the reactions per source neutron (TART output),

F is the source neutrons per module-year (for a wall loading of 4.9 MW/m^2), and

L is the ^6Li atoms per zone.

The ^6Li is then depleted at this rate for one year by $Li\ (T + 1) = L\ (T)\ e^{-K}$, and a new three-dimensional TART run is performed. One-year time steps can allow burnup of 30% of the ^6Li in the front zone, which changes the burnup rate by 15%, but has at most a few percent effect on performance. TART is a Monte Carlo calculation; results for individual zones have standard deviations of about 1%; performance summary results, combining several zones, have correspondingly better statistics.

The module performance as a function of full power years (FPY) is summarized in Table 3-4 and in Fig. 3-10. In the top portion of Fig. 3-10, tritium breeding is shown for four regions. The middle, front, and back refer to the radial position in the solid breeder and liquid refers to the Li-Pb. In the lower portion, low- and high-temperature zone energy depositions are shown. Energy multiplication is the sum of the two divided by 14.1, whereas FHT is their ratio. As ^6Li is depleted (particularly in the front), tritium breeding and energy deposition shift back in the breeder and out to the Li-Pb. The increase in M is primarily caused by increased neutron capture in lead.

Table 3-4. Burnup summary.

Time (FPY)	M	FHT	Tritium breeding ratio		
			Total	$LiAlO_2$	Li-Pb
0	1.153	0.481	1.126	1.056	0.070
1	1.155	0.474	1.104	1.029	0.075
2	1.162	0.465	1.092	1.009	0.083
3	1.173	0.457	1.087	0.997	0.090
4	1.162	0.448	1.030	0.932	0.098

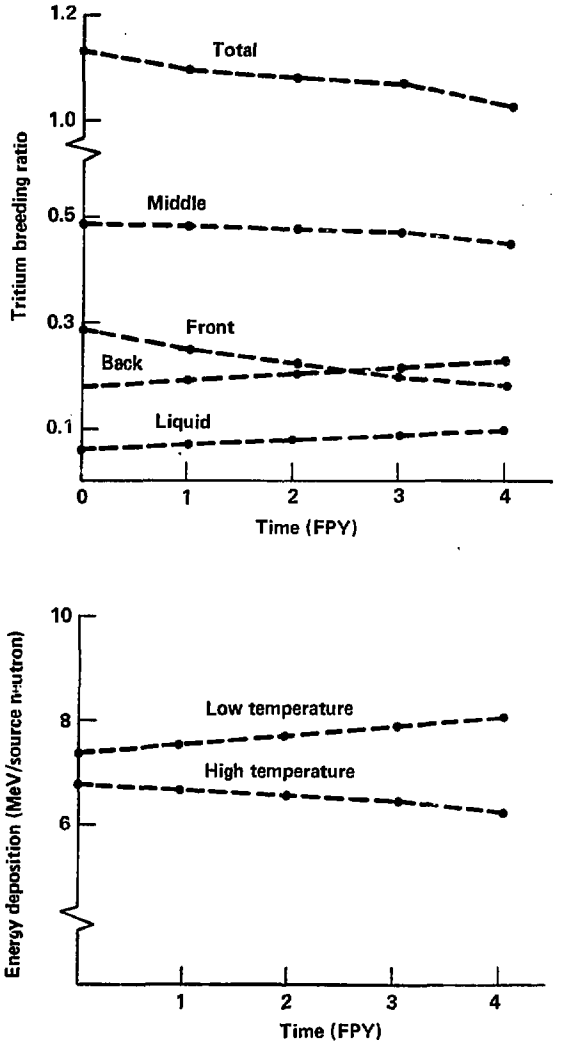

Fig. 3-10. Blanket lithium burnup.

These results demonstrate the neutronic viability of the solid breeder concept. Tritium breeding, based on average breeding from modules of different ages, is sufficient beyond 4 FPY. In the first 3 FPY, performance changes only slightly. The TBR drops only 4% while FHT drops 3% for an individual module. The change in TBR and FHT averaged over the central cell is a factor of two lower.

3.6.4 First Wall Damage

Damage calculations were performed with the one-dimensional code ONEDANT. The neutron flux was normalized to 4.9 MW/m^2 at the first wall. The results presented in Table 3-5 show the highest damage in the first wall of about 70 dpa/year.

Table 3-5. Neutron damage.

	Radius (cm)	dpa/FPY
First wall	62.125	69.3
	62.375	66.4
Corrugation	62.75	63.3
	63.25	60.2
	63.75	57.3
	64.25	54.6
	64.75	52.1
Second wall	65.5	47.8
	66.5	42.3
Pod wall	72.375	27.3
	73.542	24.9
	64.125	22.3
	76.708	19.9
	78.333	17.7
	80.0	15.9

3.7 MONTE CARLO CALCULATIONS OF NEUTRONICS EFFECTS ON MAGNETS AND INSULATORS

3.7.1 Introduction

This section describes a set of Monte Carlo calculations performed for the MARS synfuel blanket module by the University of Washington. Most of the neutronics results needed for the performance of the MARS synfuel blanket have been obtained at TRW using ONEDANT,[5] a one-dimensional discrete-ordinate neutron-gamma-coupled transport code. This code can compute essentially all the neutronics results needed for such a study, such as tritium breeding, power densities, and radiation damage parameters. However, the limitation of one-dimension is fairly significant for a blanket of this type. The blanket is very heterogeneous and contains numerous gas volumes in the form of structural spaces and helium coolant pipes and manifolds. The TRW group has also performed Monte Carlo calculations using the TARTNP code,[6] but only in a limited fashion. The objective of the TARTNP calculations was primarily to determine the tritium breeding ratio, and only the breeding regions were included in the modeling of the input.

The primary purpose of the calculations reported here is to determine the energy deposition in the central cell magnet. Three important criteria must be considered in these calculations: (1) the total energy deposition in the magnet, which relates to the capital and operating costs of the refrigeration system; (2) the maximum dose rate delivered to the insulation for the superconductor, which determines how long the magnet can operate before it fails; and (3) the displacement rate in the stabilizer for the superconductor, which determines the rate at which the resistance increases and how long the magnet can be operated until annealing must be performed. It was not possible to calculate the displacement rate because displacement cross sections are not included in the libraries available for use with the MCNP code,[7] which was used here.

3.7.2 Description of Module

The model of the MARS central cell module used for the MCNP calculations is shown in Fig. 3-11. The z-axis shown corresponds to the axis of the plasma. The illustrated plane is a slice that includes the helium inlet and outlet pipes. The module does not have azimuthal symmetry, and these pipes would not appear in slices taken at other locations. The numbers shown are the identifying cell numbers used for the calculations. It is particularly relevant to note cell numbers 129 through 132, which are located in the lower left side of the right superconducting coil. These cell locations were defined with the expectation that the radiation dose to the superconducting insulation would have a maximum in this vicinity. Unlike the total energy deposition in the magnet, which is a global parameter, the maximum permissible insulation dose is a constraint that cannot be exceeded at any location.

The helium inlet pipe is shown as a straight segment in Fig. 3-11. In fact, in the current TRW design the pipe has a double bend, one bend located in the blanket pod and the other just outside the pod. It is not clear which is the more conservative design. In general, bends in helium piping are preferable to minimize radiation streaming, and this may well be true in the

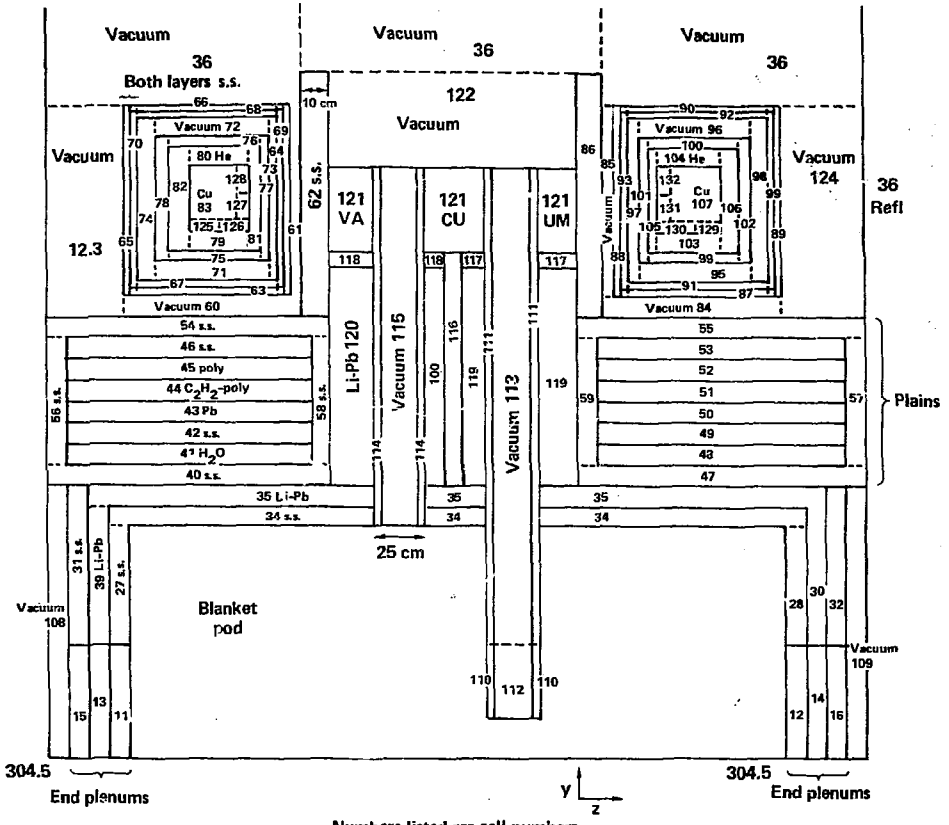

Fig. 3-11. MCNP model of MARS synfuel module.

present case. On the other hand, the bend in the current design has a segment that is aimed at the magnet on the right side. In any case, the results described here are relevant to the configuration in Fig. 3-11, and additional results will be obtained for the double-bend case.

There are 12 blanket pods arranged azimuthally around the blanket. The details of a pod are illustrated in Fig. 3-12. The plane on the left side of Fig. 3-12 is a plane of symmetry of the pod. We used a reflecting boundary condition for both of the side planes, since this pod geometry is repeated around the circular cross section of the module.

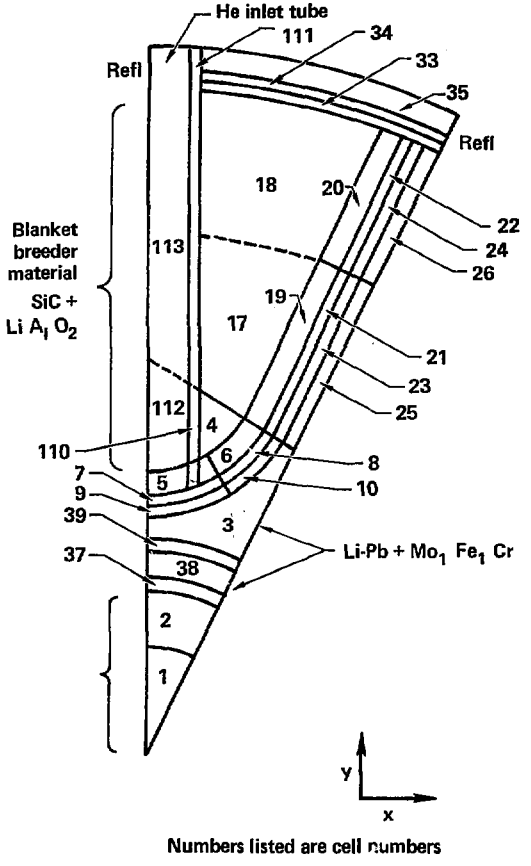

Fig. 3-12. MCNP model of MARS synfuel blanket pod.

Some additional detail of the shield design is given in Fig. 3-13, and a larger sketch of the superconducting magnet is shown in Fig. 3-14. There are two such coils for each module and the cell numbers in Fig. 3-14 correspond to the left-hand coil.

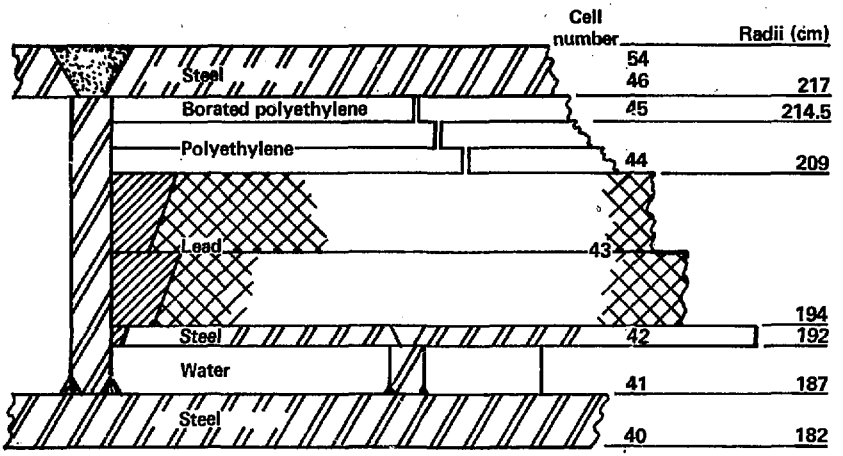

Fig. 3-13. MARS synfuel module shield geometry.

The composition of the magnet is listed in Table 3-6. The distribution of the materials in the magnet, the stabilizer, superconductor, support, and insulation are consistent with those reported in the STARFIRE report.[8]

3.7.3 Results

3.7.3.1 Tritium Breeding. Although it was not the primary purpose of these calculations, we felt it was worthwhile to calculate the tritium breeding ratio at the same time that we obtained the other results. It was necessary to accurately model the tritium breeding regions to obtain accurate results for the magnets, and not much additional computing time was required to tally the tritium-producing reactions.

Both the ^{6}Li and ^{7}Li tritium breeding results are given in Table 3-7 for three different combinations of cells. The overall breeding ratio of 1.14 is in good agreement with earlier results reported both at TRW and by Abrams at LLNL.[9]

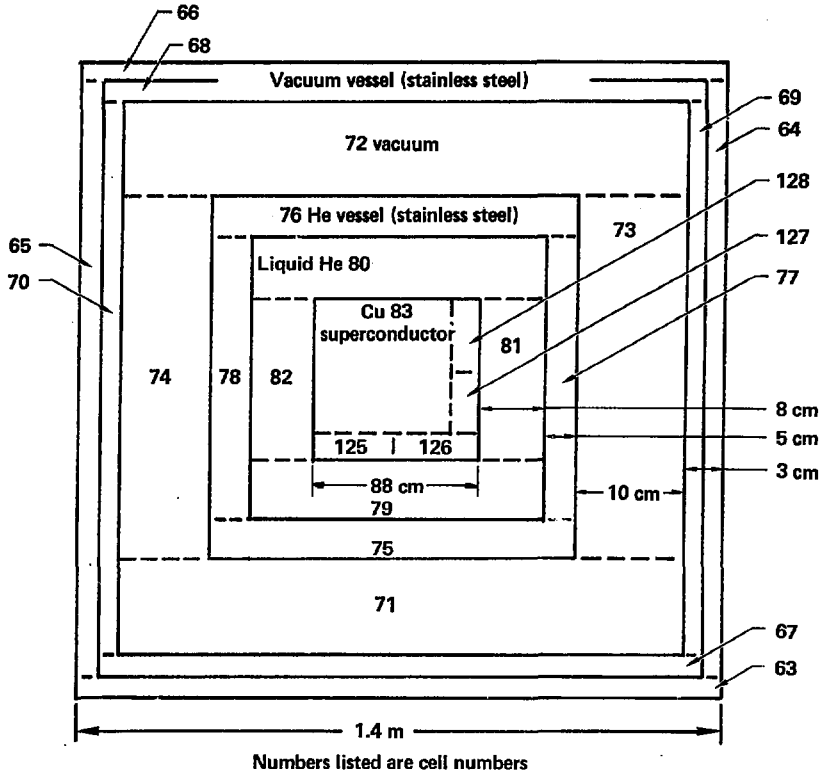

Fig. 3-14. MCNP model of central cell magnet for MARS synfuel module.

Table 3-6. Magnet composition.

Material	Weight fraction	Cross-section area fraction (%)[a]
Conductor-Cu/NbTi	0.4343	22.7
Support (SS)	0.5511	32.0
Insulation (G-10)	0.0146	3.8
He vessel	---	15.6
He	---	25.9

Element[b,c]	Weight fraction in magnet[d]
Fe	0.5332
Cr	0.01239
Mo	0.00548
Nb	0.02868
Ti	0.02647
C	0.01066
O	0.002795
H	0.00114
Cn	0.37914

[a]Based on magnet composition in Ref. 8.

[b]Area ratio NbTi/Cu assumed = 1.5.

[c]Atom fraction in insulation: C = 0.4, H = 0.52, O = 0.08

[d]Magnet cell nos.: 83, 107, 125-132.

Table 3-7. Tritium breeding results.

Cell Nos.	Vol (cm^3)	t_6[a]	t_7[b]	T_6[b]	T_7[b]
(3,13,14,29, 30,119,120)	5.705(+5)[c]	0.563(-8) (0.0410)[d]	1.784(-8) (0.0215)	0.0546	0.0102
(4-6,15,17-20)	1.521(+6)	0.891(-7) (0.0205)	5.132(-11) (0.0391)	1.0485	7.808(-5)
(25,26,35,38)	3.498(+5)	5.233(-8)	1.894(-8)	0.01831	0.00602
				1.1214±0.0225	0.0169±0.0002
				TBR = 1.138 ± 0.0252	

[a] Tritium atoms/cm^3 source neutron.

[b] Tritium atoms/source neutron.

[c] 5.704(+5) represents 5.705 x 10^5.

[d] (0.0410) represents statistical std. dev. of 4.1%.

3.7.3.2 Total Energy Desposition. The total energy deposition in the magnet is listed by cell in Table 3-8. The breakdown between neutron and gamma heating is included, and it is clear that gamma heating is the dominant contributor.

The total value of 1.02 x 10^{-3} MeV per source neutron corresponds to the fraction of 6.05 x 10^{-5} of the total energy produced in the module, assuming that the blanket energy multiplication is 1.2. The most commonly used limit is 10^{-6}, which is exceeded in the present case by a factor of about 60.

3.7.3.3 Insulation Dose. The neutron and gamma energy deposition in each of the components of the superconducting insulation (which is assumed to be G-10) is given in Table 3-9 for each relevant cell. For dose calculations, the energy deposition per unit volume must be converted to energy per unit mass, and the totals for each cell are given in Table 3-10. The dose rate, in rad/year (10^{-2} Gy/year), is obtained by normalizing to the wall loading. The values given in the last column of Table 3-10 correspond to 1 MW/m^2. The higher dose rate occurs, as might be expected, in cells 127 and 131. The latter is the highest of all at 1.58 x 10^8 rad/year at a wall loading of 1 MW/m^2.

Table 3-8. Nuclear heating in central cell magnet.

Cell Nos.	Nuclear heating (MeV/gr) Neutron	Photon	Cell mass (gr)	Total heating (MeV)
79	1.19(-10)[a](0.2551)[b]	1.45(-10) (0.14[illegible]	7.[illegible]0 (+3)	1.88(-6) (0.1441)
80	1.94(-11) (0.3017)	4.94(-11) (0.1781)	9.73(+3)	6.80(-6) (0.1536)
81	1.79(-10) (0.2830)	3.58(-10) (0.1490)	7.12(+3)	3.83(-6) (0.1371)
82	6.49(-11) (0.4888)	6.20(-11) (0.2346)	7.12(+3)	9.05(-7) (0.2750)
83	9.18(-13) (0.1566)	4.89(-11) (0.1432)	4.54(+6)	2.71(-4) (0.1410)
103	1.16(-10) (0.2381)	2.35(-10) (0.1593)	7.10(+3)	2.49(-6) (0.1325)
104	3.06(-11) (0.3038)	6.76(-11) (0.1575)	9.73(+3)	9.57(-7) (0.1440)
105	2.71(-10) (0.3385)	3.63(-10) (0.1501)	7.12(+3)	4.52(-6) (0.1683)
106	8.48(-11) (0.4890)	9.20(-11) (0.2466)	7.12(+3)	1.26(-6) (0.2673)
107	1.07(-12) (0.1636)	6.62(-11) (0.1278)	4.54(+6)	3.06(-4) (0.1258)
125	3.73(-12) (0.2079)	1.34(-10) (0.1758)	1.24(+5)	1.72(-5) (0.1711)
126	6.08(-12) (0.2185)	2.56(-10) (0.1651)	1.24(+5)	3.27(-5) (0.1609)
127	1.31(-11) (0.1841)	5.77(-10) (0.1618)	1.19(+5)	7.05(-5) (0.1583)
128	1.07(-11) (0.2017)	4.53(-10) (0.1791)	1.54(+5)	7.15(-5) (0.1750)
129	3.84(-12) (0.1803)	1.88(-10) (0.1936)	1.24(+5)	2.39(-5) (0.1898)
130	9.67(-12) (0.1936)	4.41(-10) (0.1621)	1.24(+5)	6.61(-5) (0.1587)
131	1.78(-11) (0.2045)	7.26(-10) (0.1685)	1.19(+5)	8.89(-5) (0.1645)
132	9.23(-12) (0.1988)	4.35(-10) (0.1501)	1.54(+5)	6.85(-5) (0.1470)
			Total	1.02(-3) (0.0459)

[a] 1.19(-10) represents 1.19×10^{-10}.

[b] (0.2551) represents statistical standard deviation of 25.5%.

Table 3-9. Neutron and photon heating in superconductor insulation.

Cell Nos.	Neutron heating (MeV/cm^3)			Photon heating (MeV/cm^3)		
	Carbon	Hydrogen	Oxygen	Carbon	Hydrogen	Oxygen
83	2.57(-13)[a] (0.2098)	3.13(-12) (0.1942)[b]	4.39(-14) (0.2236)	3.06(-14) (0.1437)	1.88(-16) (0.1437)	1.47(-14) (0.1437)
107	3.21(-13) (0.2262)	3.67(-12) (0.2132)	5.68(-14) (0.2362)	3.41(-14) (0.1279)	2.10(-16) (0.1279)	1.64(-14) (0.1279)
125	1.40(-12) (0.2544)	1.65(-11) (0.2401)	2.44(-11) (0.2634)	7.24(-13) (0.1786)	4.45(-16) (0.1786)	3.49(-14) (0.1785)
126	2.48(-12) (0.2252)	3.01(-11) (0.2543)	4.22(-13) (0.2843)	1.32(-13) (0.1664)	8.15(-16) (0.1664)	6.40(-14) (0.1664)
127	4.26(-12) (0.2345)	5.37(-11) (0.2208)	6.94(-13) (0.2423)	3.01(-13) (0.1623)	1.85(-15) (0.1623)	1.45(-13) (0.1623)
128	3.42(-12) (0.2629)	4.34(-11) (0.2412)	5.59(-13) (0.2832)	2.62(-13) (0.1804)	1.44(-15) (0.1804)	1.13(-13) (0.1804)
129	1.18(-12) (0.2371)	1.43(-11) (0.2198)	1.94(-13) (0.2485)	1.00(-13) (0.1981)	6.19(-16) (0.1981)	4.82(-14) (0.1981)
130	3.15(-12) (0.2582)	3.86(-11) (0.2416)	5.22(-13) (0.2716)	2.31(-13) (0.1631)	1.41(-15) (0.1631)	1.11(-13) (0.1631)
131	6.54(-12) (0.2724)	7.61(-11) (0.2498)	1.13(-12) (0.2880)	3.79(-13) (0.1723)	2.33(-15) (0.1723)	1.83(-13) (0.1723)
132	3.00(-12) (0.2899)	3.61(-11) (0.2621)	5.01(-13) (0.3027)	2.24(-13) (0.1520)	1.37(-15) (0.1531)	1.08(-13) (0.1531)

[a] 2.59(-13) represents 2.59×10^{-13}.
[b] (0.2098) represents statistical standard deviation of 20.98%.

Table 3-10. Total nuclear heating in superconductor insulation.

Cell Nos.	Total neutron (MeV/gr)	Total photon (MeV/gr)	Total heating (MeV/gr)	Dose rate (rad/year) (w = 1 MW/m^2)
83	2.89(-11)[a]	3.83(-13)	2.93(-11)	6.52(+6)
107	3.40(-11)	4.28(-13)	3.45(-11)	7.68(+6)
125	1.53(-10)	9.08(-13)	1.54(-10)	3.42(+7)
126	2.77(-10)	1.66(-12)	2.79(-10)	6.22(+7)
127	4.94(-10)	3.77(-12)	4.97(-10)	1.10(+8)
128	3.98(-10)	2.93(-12)	4.01(-10)	8.94(+7)
129	1.32(-10)	1.26(-12)	1.33(-10)	2.96(+7)
130	3.56(-10)	2.89(-12)	3.59(-10)	7.99(+7)
131	7.05(-10)	4.75(-12)	7.10(-10)	1.58(+8)
132	3.34(-10)	2.80(-12)	3.36(-10)	7.50(+7)

[a] 2.89(-11) represents 2.89×10^{-11}.

The limiting dose rate to the superconductor insulation is not a well-established parameter. The most commonly used value is a lifetime limit of 5×10^9 rad (5×10^7 Gy). Based on a wall loading of 5 MW/m^2, the lifetime of the magnet would be limited to approximately 6.3 years.

As noted earlier, it may well be that replacing the straight helium inlet pipe with one having a double bend will significantly improve both the total energy deposition in the magnet and the radiation dose to the insulation.

3.8 THERMAL HYDRAULICS

3.8.1 High Temperature Zone

Helium is the high-temperature working fluid that carries away the heat absorbed in the SiC and spherical pebbles. The heat transfer coeffcient in the packed bed is calculated using a Stanton number correlation[10]

$$St = 0.40\ Re^{-0.437}\ Pr^{-2/3} ,$$

where

St = Stanton number = h/GC_p,

Re = Reynolds number,

Pr = Prandtl number,

C_p = specific heat,

G = fluid mass velocity based on the unpacked tube, and

h = heat transfer coefficient.

The film temperature drop between the surface of the sphere and the surrounding helium can then be calculated, knowing both the local energy density from the neutronic calculation and the diameter of the sphere.

The temperature distribution in the packed bed varies significantly with sphere radius. Figure 3-15 depicts the relationship between the sphere diameter and the film drop profile through the bed. At small pebble diameters, the larger surface area keeps the film drop low, causing a large front-to-back temperature gradient in the surface temperature of the pebbles, side wall, and support blocks. A radius exists that produces a nearly flat sphere-surface temperature profile throughout the bed, with a large film drop in the front of the bed and a smaller film drop in the back of the bed. This optimum radius is about 1.9 cm, as is shown in Fig. 3-15. At this radius, the structural blocks and sidewalls will not be subjected to large front-to-back temperature gradients. The maximum film drop temperature of 455°C occurs in the front of the bed, and the maximum SiC sphere surface temperature is 960°C. The maximum sphere centerline temperature is 1000°C.

3.8.2 Helium Fluid Hydraulics

One consideration in using helium as the high-temperature working fluid is the pumping power needed to flow large volumes of the gas through the system. The pressure drop through the module has been calculated for the flow paths shown in Figs. 3-2 and 3-7. The coolant operates at 50 atm with T_{in} at 457°C and T_{out} at 947°C. A simplified flow schematic of the helium piping system is shown in Fig. 3-16, illustrating the detail of the pressure drop calculation. The total pressure drop is a summation of the pressure drops through inlet/outlet manifold straight pipes and manifold tees, pod distribution and collector pipes, and packed bed.

To estimate the pressure drop through the pipes, we used a conservative value of friction factor for concrete pipe to account for high-temperature piping insulating material. This value may be relatively rough. We calculated the pressure drop in the manifold and pod entrance/exit tees using the equivalent length of straight pipe that would cause the same frictional pressure drop as flow through a standard tee.

We estimated the pressure drop in the pod distribution entrance pipe and the pod collector pipe according to the procedure outlined in Ref. 11. The method provides empirical data for calculating the pressure change through holes of 90-deg turns of flow into and out of the branch side duct.

We calculated the pressure drop in an incompressible packed bed composed of nearly spherical particles, as described and developed in Ref. 10. The continuity equation was our basis for calculating the bulk velocity of the helium in the packed bed. The total pressure drop through the module helium

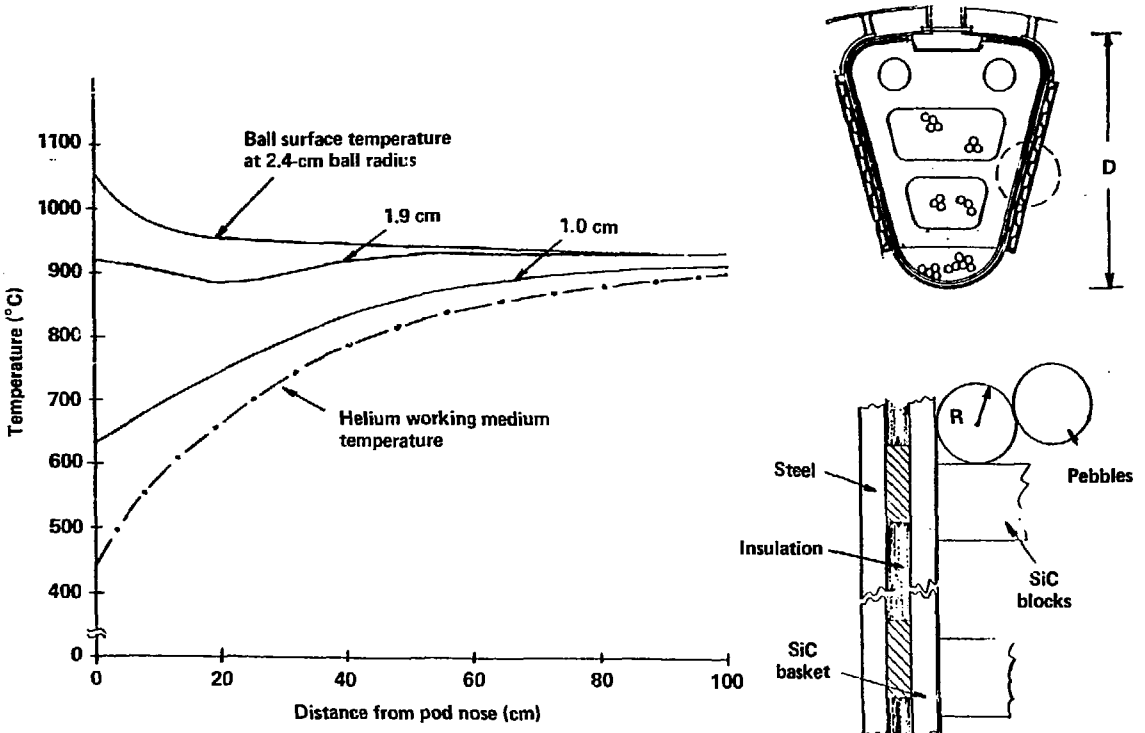

Fig. 3-15. Effect of pebble size on bed temperature.

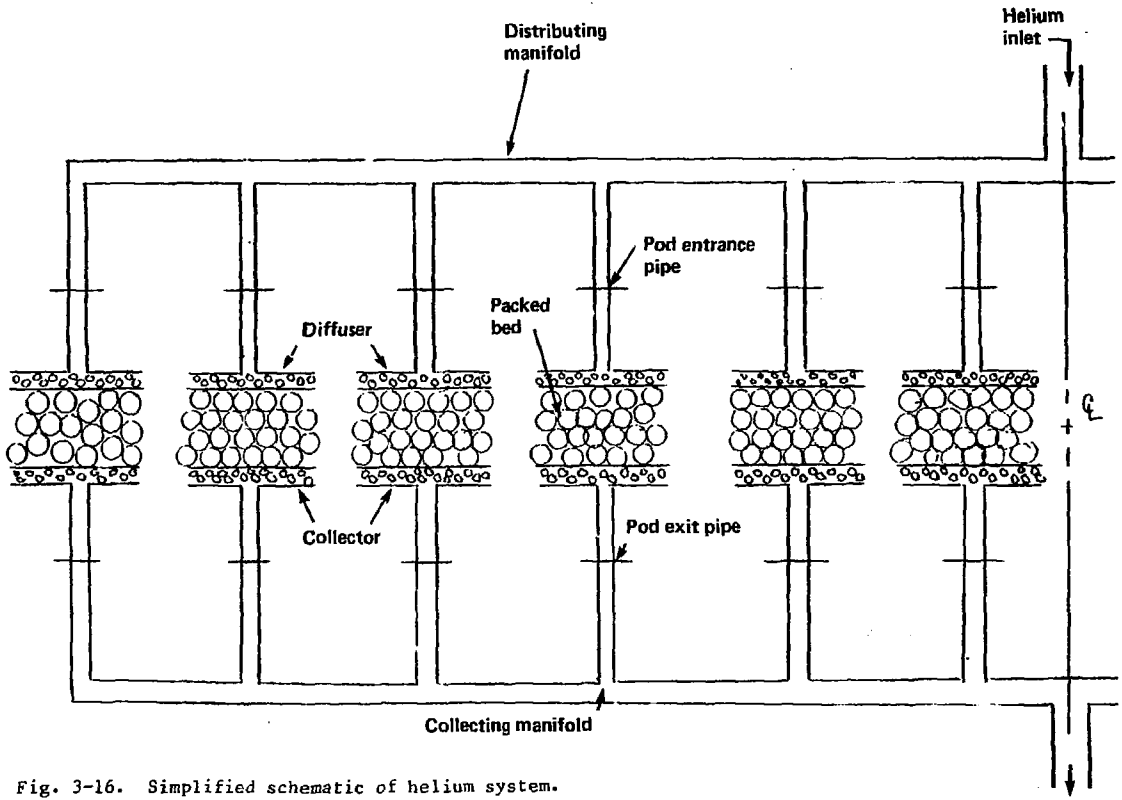

Fig. 3-16. Simplified schematic of helium system.

piping system is 18 psi. The pumping power requirement is 0.31 MW_e per 6.3-m module. Each module handles 62 MW in the helium so that the pumping power percentage is 0.5.

Holes in the pod diffuser and collector must be sized for proper distribution of the flow through the pod. Also, flow orifices will be needed in the large feed manifold. These will require a detailed design effort.

3.8.3 Low Temperature Zone

The first wall coolant, Li-Pb, is a conducting liquid metal; the effect of the strong magnetic field on the heat transfer capacity of the coolant must be considered. Not only is the Reynold's number (Re) used to describe the fluid flow in the first wall, but an additional parameter, the Hartman number (Ha), is used to describe the flow regime

$$Ha = a\,B\left(\frac{\sigma_L}{\mu}\right)^{1/2} ,$$

where

a = channel half-width,

B = field strength,

σ_L = fluid electrical conductivity, and

μ = dynamic viscosity.

The factor Re/Ha, which represents the ratio of inertia to electromagnetic forces, is used as a measure of the importance of the magnetic field effects on the flow of the fluid. Turbulent flow will be dampened at Re/Ha < 60 for flow parallel to the magnetic field.[12] Since Re/Ha for our design is approximately 200, no significant dampening effect is expected to occur. Thus, we used the turbulent, liquid-metal Nusselt-number (Nu) empirical correlation[12]

$$Nu = 6.5 + 0.025\,(RePr)^{0.8} ,$$

where Pr = Prandtl number.

Entrance effects in the magnetic field may be significant and have not been accounted for here.

The main objective in cooling the first wall is to maintain a maximum temperature in the steel below 520°C. The Li-Pb enters the module at 332°C and exits at 482°C; thus, a total Li-Pb mass flow of 2600 kg/s is needed to cool the low temperature region. The maximum heat deposition of 28 W/cm^3 occurs in the first wall. Figure 3-17 shows the temperature profile at the maximum temperature locations of the first and second walls. The film drops for the first and second walls are 12 and 8°C, respectively; the conduction temperature drops in the first and second steel walls are 24 and 18°C, respectively. The maximum temperature that the steel reaches in the first wall region is about 515°C.

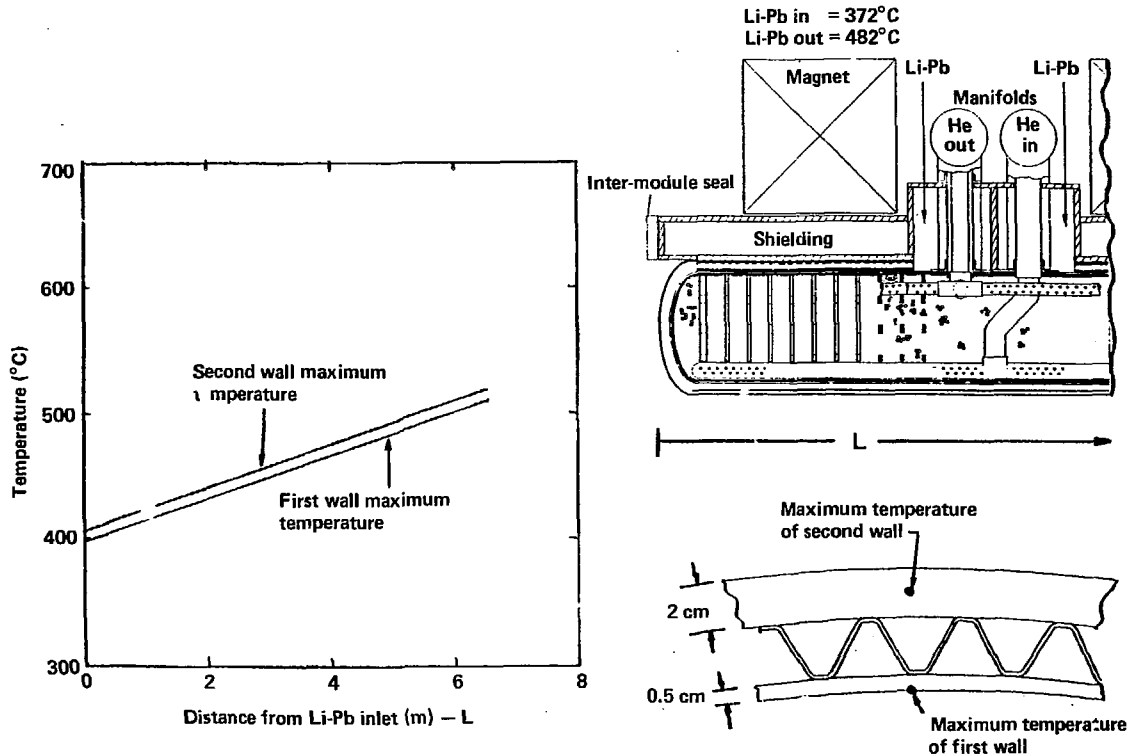

Fig. 3-17. First- and second-wall temperature maxima.

3.8.4 Thermal Interface

To maximize FHT, the heat transfer between high and low temperature zones must be kept as low as possible. As the number of pods increases or the inner radius of the module increases, the heat leak from the high to low temperature zone increases as a result of the increase in surface area between the two regions. This was one reason for selecting a small number of pods and the small inner radius of the module. The operating conditions of the module also affect the performance of the blanket: the larger the temperature difference between the two regions, the more heat that is lost.

It is necessary to insulate the two regions from one another. The following properties of the insulation are essential: (1) high resistance to radiation damage; (2) the ability to maintain the structural integrity of the blanket; (3) low density to minimize internal heat generation; and (4) low effective thermal conductivity. Table 3-11 shows the experimental values of thermal conductivity for some low-density fibrous insulators at high temperatures in stagnant gas.[13] The effective thermal conductivity can approach that of the conductivity of the stagnant gas.

Table 3-11. Conductivity of fiber insulation.

Insulation	W/m (K)							
	Air		Argon		Helium		Steam	
	300	1000	300	1000	300	1000	300	1000
Alumina-silica material ($8\ lb/ft^3$)	0.06	0.22	0.07	0.28	0.24	0.54	0.17	0.36
Carbon felt ($5\ lb/ft^3$)	--	NA	0.11	0.29	0.24	0.51	--	--
Graphite felt ($4\ lb/ft^3$)	--	NA	0.11	0.27	0.26	0.51	0.17	0.36
Zirconia fibrous board ($24\ lb/ft^3$)	0.07	0.14	0.07	0.14	0.15	0.49	0.13	0.17
Zirconia felt ($14\ lb/ft^3$)	0.08	0.17	0.08	0.17	0.18	0.40	--	0.23

As Fig. 3-18 shows, the MARS baseline insulation design consists of ceramic (MgO) pedestals separating the pebble basket and the pod wall, and a fibrous alumina-silica mat between pedestals with stagnant helium filling the voids. As determined by the structural analysis, the ceramic pedestals are assumed to cover 2% of the total surface area of the interface between the high and low temperature regions. Also shown in Fig. 3-18 is the relationship between the amount of heat lost to the low temperature region, the thickness

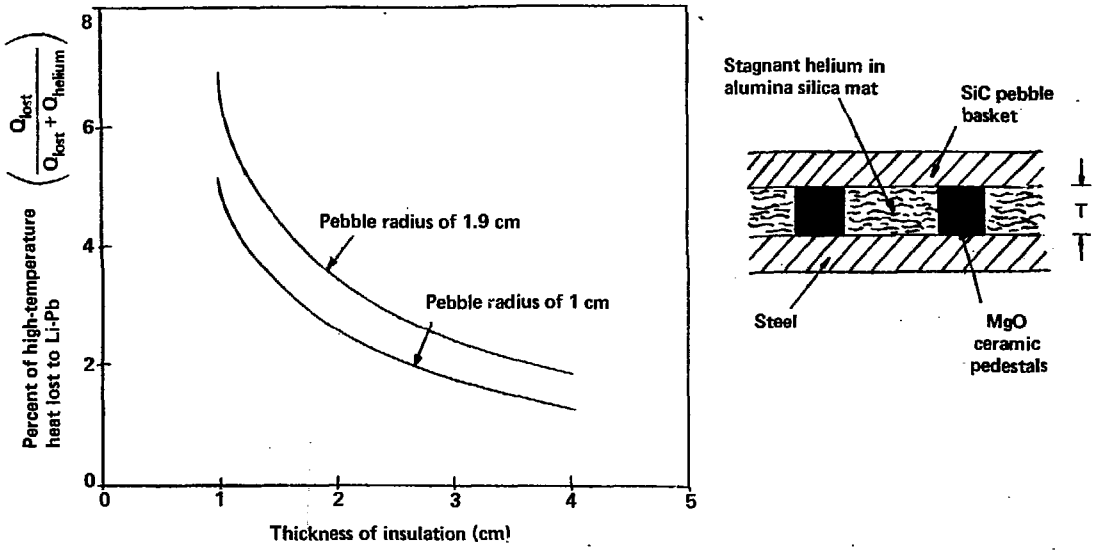

Fig. 3-18. Performance of insulation at various pebble radii and thicknesses.

of insulation, and the pebble radius. As the insulation thickness increases, the heat leak decreases. At the larger pebble radius (1.9 cm), the heat leak is larger because the SiC surface temperature increases at the front of the blanket. For the baseline design of a 1.9-cm pebble radius and 2-cm insulation thickness, the heat loss to the low temperature zone is only 3.4% of the total high temperature heat.

3.8.5 Magnetohydrodynamic Pressure Drop

Magnetohydrodynamic effects dominate pressure, pumping, and heat transfer in the Li-Pb loop. Magnetohydrodynamic pumping power is high enough (15 MW thermal) to noticeably affect net plant efficiency, and MHD pressure strongly affects the structural design and lifetime of the first wall. High pressures are more easily handled in piping as well as toward the back of the blanket where thicker structures can be used and where these structures are not under buckling loads.

As discussed in the preceding section, magnetic fields affect heat transfer by changing the transition velocity of the laminar/turbulent flow.[14] Magnetic fields have also been shown to cause concentrations of flow streamlines in the vicinity of changes in magnetic field strength or direction.[15] Our knowledge of liquid-metal MHD flow is limited because few experiments have been performed in this area and because possible current paths are very complex in changing flow situations.[16] Experiments have been performed for flow in straight pipes and between conducting plates in uniform magnetic fields.[17-21] However, the flow paths in the MARS high temperature blanket are considerably more complex than those verified experimentally, making the calculational results somewhat uncertain.

Our approach has been to determine the problem areas and to apply a simplified analysis to derive approximate values for pressure drops and pumping power. An alternate blanket design concept, presented in Sec. 3.18 of this volume, reduces the requirements for flow control and electrically insulated baffles in the blanket. This blanket is expected to perform similarly to the MARS high temperature blanket, but it is mechanically quite different and has not been studied in detail. We do not perceive any feasibility issues with flow control in the current blanket concept, but MHD flow problems increase the blanket's complexity and will require a comprehensive development program.

3.8.6 Calculations

The Hartman and end-of-loop pressure drops and radial inflow pressure drops were calculated using

$$\Delta P_H = \frac{VB^2 \sigma_w t_w L}{a(1+c)} \quad , \quad c = \sigma_w t_w / \sigma a \tag{3-1}$$

$$\Delta P_E = 0.062\, \sigma a V B^2 \quad , \tag{3-2}$$

$$\Delta P_R = VB_\perp^2 \sigma \Delta R \quad , \tag{3-3}$$

where

V = fluid velocity,

$B_\perp$ = magnetic field strength perpendicular to the flow,

σ_w = electrical conductivity of wall,

t_w = wall thickness,

a = channel half width in the B field direction,

σ = electrical conductivity of fluid,

L = flow path length perpendicular to the B field, and

ΔR = flow path length, change in radius.

Equation (3-1) was used for flow perpendicular to the magnetic field and Eq. (3-2) for turns and flow into and out of the field.[1]

Figure 3-19 and Tables 3-12 and 3-13 show the materials' properties, locations, and magnitudes of the field strengths used, as well as the calculated MHD pressure drops. The maximum first wall pressure is 1.0 MPa (150 psi) including the static head. Pressure increases for temperature and pressure control will raise this to ~1.3 MPa (200 psi).

3.8.7 Discussion of Issues

Electrically insulated duct walls of sandwich construction are required in the toroidal flow channels at the back of the blanket. A layer of insulating material is placed between the thick steel duct wall, and a 0.5-mm steel sheet separates the insulation from the Li-Pb. Using Eq. (3-1), the pressure drop in the inlet or outlet header would be 2750 kPa with 2-cm-thick uninsulated wall, and is reduced to 91.1 kPa with the 0.5-mm sandwich wall. The 2750-kPa figure is unacceptably high because of the resulting high pressure at the first wall. The average velocity in the toroidal header was used because Eq. (3-1) is linear in velocity. The channel sizes assumed were two 78-cm x 30.5-cm channels, one on each side of the helium pipes (see Fig. 3-19), for both the inlet and outlet headers.

Electrically insulated sandwich flow baffles are also desirable in the toroidal end caps (6 and 10 in Fig. 3-19). Without baffles, the pressure drop in the end caps is given approximately by Eq. (3-3); with baffles, the pressure drop is given approximately by Eq. (3-1), with L replaced by ΔR. These equations differ by the factor $C/(1 + C)$, where C is given in Eq. (3-1). Taking t_w as the thickest wall in contact with the flow (the 1.6-cm helium pod end cap), the pressure drop without baffles is 3.8 times higher than with baffles, or 1900 kPa vs 500 kPa. We have assumed the use of baffles in the MARS high-temperature blanket design. The 500-kPa pressure drop at the ends of the modules is the highest single drop in the blanket.

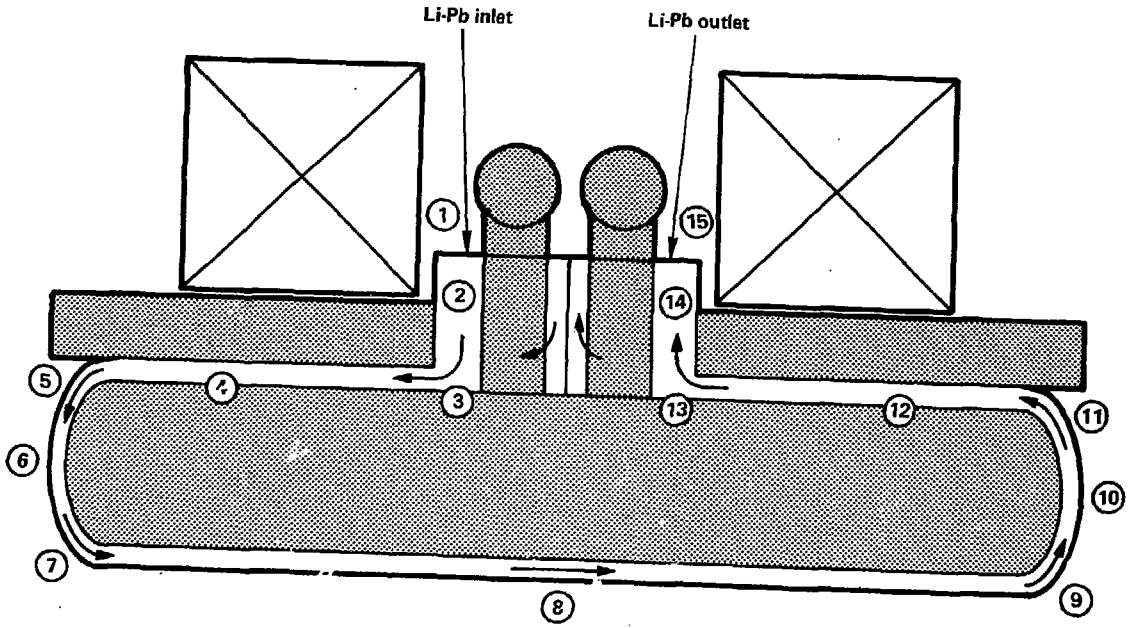

Fig. 3-19. Lithium-lead flow.

Table 3-12. Properties used in MHD calculations.

Electrical conductivity of steel (mho/m)	2.0×10^{6}
Electrical conductivity of Li-Pb (mho/m)	8.0×10^{5}
Viscosity of Li-Pb (kg/ms)	1.9×10^{-3}
Density of Li-Pb (kg/m^3)	9400
Heat capacity of Li-Pb (J/kg C^{o})	170

Table 3-13. MHD pressure drop.

Position[a]	B(T)	V(m/s)	Flow analyzed	ΔP(kPa)
1	3.0	0.135	Inlet/outlet	50.5
2[b]	3.5	0.172	Field	91.1
3	4.0	0.213	Turn	20.3
4	5.4	0.213	Viscous	0.15
5	4.1	0.213	Turn	61.4
6	4.3	0.117	Field	500
7	4.5	0.175	Turn	26.4
8	4.5	0.741	Viscous	10.6
9	4.5	0.175	Turn	26.4
10	4.3	0.117	Field	500
11	4.1	0.213	Turn	61.4
12	5.4	0.213	Viscous	0.15
13	4.0	0.213	Turn	20.3
14[b]	3.5	0.172	Field	91.1
15	3.0	0.135	Inlet/outlet	50.5
				1510.0

[a]See Fig. 3-19.

[b]Average velocity of toroidal flow around module.

The flow path to the first wall has the longest legs perpendicular to the magnetic field (legs 5 and 10 in Fig. 3-19). Consequently, there will be a tendency for the flow to "short-circuit" through regions of lower pressure drop near the back of the modules unless baffles and orifices can be engineered very carefully into the design.

To quantify this problem, consider the ratio of the Δp_{FW} (for the flow cooling the first wall) to Δp_{BW} (for the flow cooling the back wall behind the pods for no-flow baffling), using the values in Table 3-13. Thus,

$$\left(\frac{\Delta p_{FW}}{\Delta p_{BW}}\right) \approx \frac{1287 \text{ kPa}}{287 \text{ kPa}} \times \frac{u_{FW}}{u_{BW}} = 4.5 \frac{u_{FW}}{u_{BW}} \quad .$$

Tc obtain the same rise in the Li-Pb bulk temperature ΔT_B for both flow paths, we require that (based on the neutronics analysis presented above)

$$\frac{\dot{m}_{FW}}{\dot{m}_{BW}} = \frac{\dot{Q}_{FW}}{\dot{Q}_{BW}} \approx 25 \quad .$$

This leads to a velocity ratio of

$$\frac{u_{FW}}{u_{BW}} = \frac{\dot{m}_{FW}}{\dot{m}_{BW}} \times \left(\frac{A_{BW}}{A_{FW}}\right) \approx 25 \left(\frac{A_{BW}}{A_{FW}}\right) \quad .$$

If the ratio of the flow area at the back wall to the flow area at the first wall is on the order of unity, we find the unbaffled pressure drop ratio for equal ΔT_B rise would be

$$\left(\frac{\Delta p_{FW}}{\Delta p_{BW}}\right) \approx 4.5 \times 25 = 113 \quad .$$

This large ratio of pressure drops indicates the amount by which the backwall pressure must be increased to achieve both the maximum mixed bulk temperature at the exit (for a uniform inlet bulk temperature) and the same Δp across each flow path. This increase can be achieved by routing all the flow to the first wall area and then around the pod and/or by increasing the perpendicular component of the B field to the flow path by redirecting the flow at the back of the blanket.

Other potential problems are associated with the large variations in the pressure gradient along a typical flow path. Table 3-13 shows that the pressure drop for flow path 6 perpendicular to the B field is estimated at 500 kPa, whereas the pressure drop for flow path 8 along the first wall parallel to the B field is only 10.4 kPa. Engineering the flow distribution is subject to large uncertainties because of these large differences in pressure drop as the flow goes back and forth about four times from a path perpendicular to the B field to one parallel to the B field. These uncertainties arise because of many factors, such as manufacturing tolerances, thermal deformations, swelling, and deformation due to neutron irradiation, changes in flow and orifice areas due to erosion, corrosion, and mass

transport. Increasing the pressure drop to ~100 kPa in the parallel flow zones by increasing the component of flow perpendicular to the B field (e.g., spiralling corrugations between the first and second walls) will reduce or eliminate the uncertainties without greatly affecting the first wall pressure or the pumping power.

Stagnant or near-stagnant regions in the Li-Pb can be created whenever the flow makes a turn relative to the magnetic field or when the flow goes through an orifice or around a baffle plate. The flow patterns due to the MHD interaction are rather complex and often counter to our intuition. Reference 15 contains an interesting account of some of the possible flow patterns. The flow along the first wall (flow path 8 in Fig. 3-19) is the most critical because of the higher heat fluxes. The first wall structure is made up of front and back walls that are welded to a corrugated inner sheet, as illustrated in Fig. 3-3. As the flow turns corner 7 in Fig. 3-19, it will tend to follow the path of least resistance. Because of the axial B field, all the flow will try to follow along the back wall of the first wall structure to avoid crossing the B field. Viscous forces (in the turbulent regime of the first wall channels) will tend to cancel this effect. Turbulent flow is expected in the first wall channels (Ref. 12) when end effects are neglected, but velocity profiles in the region of the turn are unknown and entrance effects may persist for a significant distance down the channels.[12] Stagnant layers in contact with the first wall more than a few millimeters cannot be tolerated because of the large ΔTs across such layers and the resulting high first wall temperature. Directing the flow so that it has a component perpendicular to the B field, as mentioned above for pressure control, should greatly alleviate this problem because the flow will be transitioning from Hartmann or laminar plug flow to turbulent viscous flow. In addition, both regimes should be tolerable, especially since the flow will be developing turbulence as it moves down the channel and becomes hotter (i.e., the worst problems occur at the cooler entrance side of the module). An alternative suggestion for increasing the heat transfer coefficient and eliminating stagnant regions would be to use flow turbulators. However, turbulator performance in magnetic fields has not been assessed, and the additional pressure drops are unknown.

Much development is still needed to overcome the MHD flow uncertainties in heat transfer coefficients and pressure/temperature balancing. Increasing the flow component perpendicular to the B field seems to be the most attractive and effective way of dealing with these problems, although the results have not been analyzed in detail for this design. An alternative possibility is to design the blanket with all flow perpendicular to the B field, eliminating turns in and out of the field and reducing the analysis to relatively well-known Hartmann flow. An alternate blanket concept that began with this idea is presented in Sec. 3.18 of this volume.

3.9 MATERIALS AND THEIR INTERACTIONS

3.9.1 Lithium-Lead Compatibility

The upper temperature for Li-Pb will be limited by either the creep rupture strength of the structure or by corrosion of the structure, or both. Static tests of HT-9 in Li-Pb have been performed,[22] but are not directly

applicable to the flowing conditions and the 150°C temperature difference from inlet to outlet of the flow circuit. Dynamic tests of HT-9 in flowing Li-Pb are being performed at ORNL and ANL. Until these data become available, the maximum Li-Pb interface temperatures cannot be chosen with confidence. The maximum Li-Pb/HT-9 interface temperature is 490°C, corresponding to a corrosion rate of 5.9 mg/m^2-hour based on the 1000-hour static test data presented in Fig. 3-20. These data indicate that the Li-Pb reached saturation by 3000 hours at all three temperatures. At 500°C the corrosion rate had apparently already begun to level off at the 1000-hour test. Figure 3-21 shows the corrosion rates for the 3000- and 1000-hour tests. The points plotted are weight lost at the end of each static test. The data at 1000 hours may be closer to flowing conditions because saturation has not affected the results as much as in the 3000-hour data, as indicated by the curved lines in Fig. 3-20. On the other hand, short-term surface effects may dominate the 1000-hour tests. We believe that more experimental results are needed. As mentioned above, these data are not directly applicable to flowing conditions. The static tests almost certainly understate the problem because they do not consider mass transfer or velocity effects. The temperature dependence indicated by the 1000-hour results in Fig. 3-20 may be significant.

Temperature dependence of the corrosion rate may make it desirable to lower the Li-Pb outlet temperature. Lowering the Li-Pb maximum operating temperature would increase Li-Pb pumping power and decrease thermal-to-electrical efficiency, therefore decreasing the thermochemical conversion efficiency of the plant. Too low a temperature would make it difficult to supply enough heat to the process, particularly the H_2SO_4 boiler (see Sec. 6 of this volume). A Li-Pb outlet temperature below about 450°C would be difficult to accommodate.

At the corrosion rates expected in MARS, the major problems will occur on the cold side of the loop where material precipitates out of the coolant, possibly clogging the valves and steam generator tubes.

3.9.2 Radiation Effects on Structural Materials

3.9.2.1 Brittle-to-Ductile Transition Temperature Behavior. As we stated previously, we have chosen ferritic steels for the blanket because of their excellent physical and mechanical properties and their resistance to neutron-induced void swelling and helium embrittlement. Ferritic steels (HT-9 and 9 Cr-2 Mo) have been shown to reach a state of magnetic saturation at relatively low field strengths (1 to 2 T), indicating that ferromagnetism will not present a problem in the tandem mirror.[23] We considered using HT-9 (12 Cr - 1 Mo) and 2-1/4 Cr - 1 Mo for the MARS high temperature blanket. These steels are limited in their useful lifetimes by irradiation embrittlement at low temperatures, by swelling, and by creep rupture and liquid-metal corrosion at high temperatures. We have updated and used already developed[24] design equations for the shift in ductile-to-brittle transition temperature (ΔDBTT), swelling, and creep rupture time.

Figure 3-22 shows the estimated ΔDBTT for HT-9 during irradiation. The ΔDBTT is calculated for the worst case--the minimum structure temperature (348°C). The shift is shown to saturate after only a few months of operation at ~100°C. After operation for about 1 year, the plant is

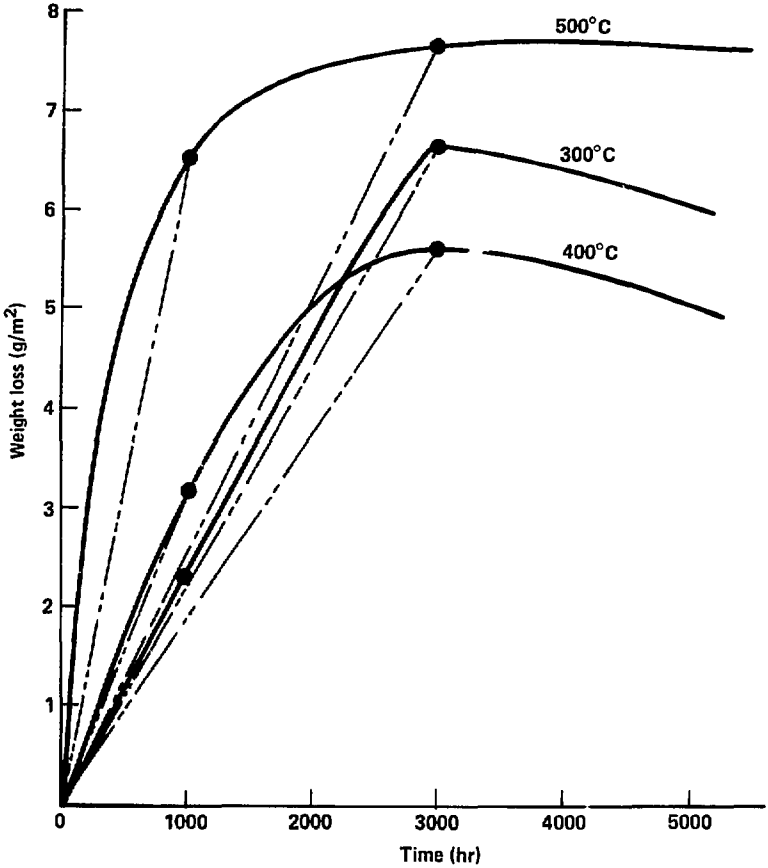

Fig. 3-20. Results of static corrosion test of HT-9 in lead-lithium.

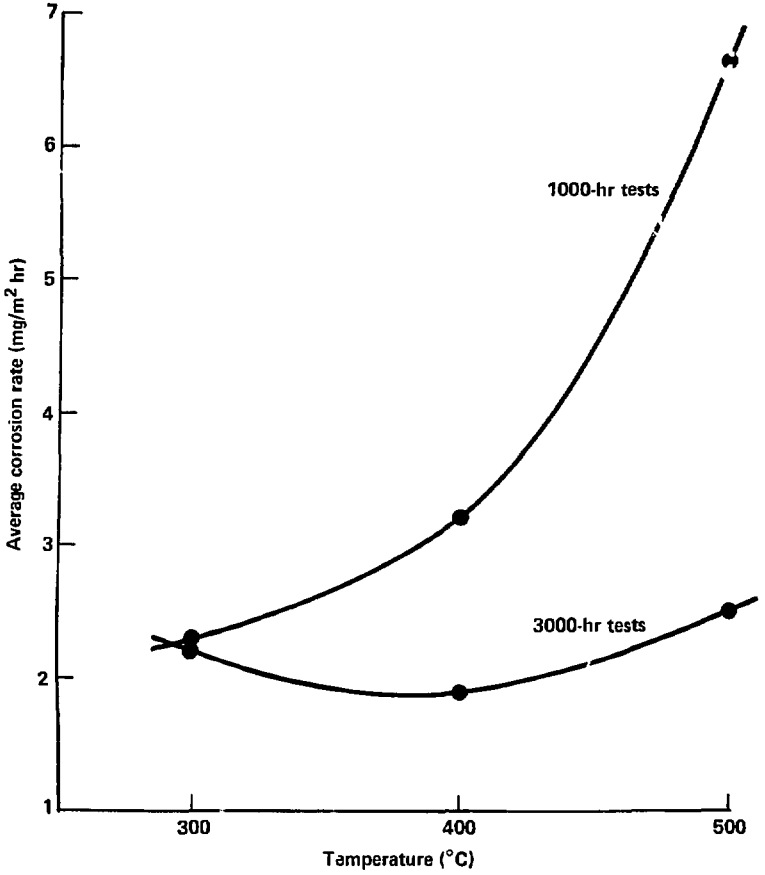

Fig. 3-21. Lithium-lead/HT-9 corrosion data.

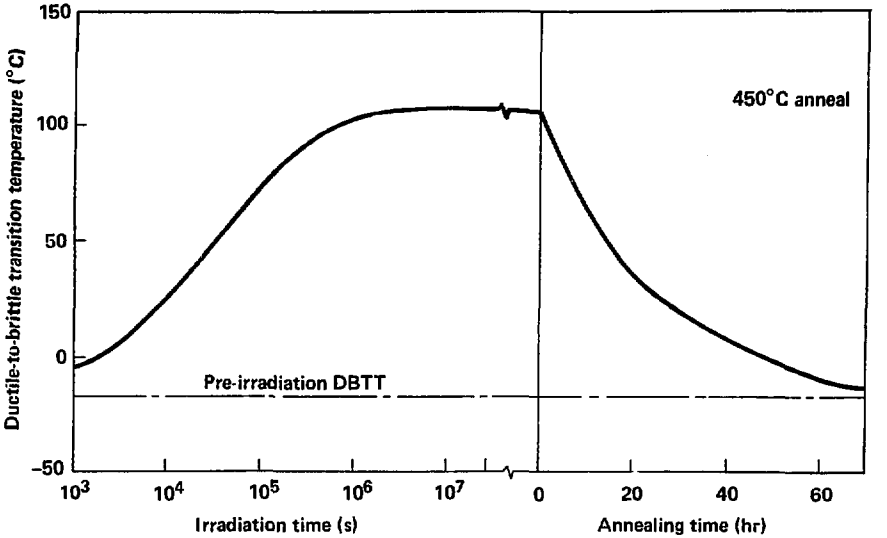

Fig. 3-22. Ductile-to-brittle transition temperature vs radiation and annealing time.

shut down for scheduled maintenance and the structure temperature is held constant at 450°C for approximately 60 hours. This allows an almost full recovery of the ΔDBTT as shown in Fig. 3-22. The procedure is repeated once every scheduled maintenance (approximately every year). The annealing procedure is calculated according to a functional fit to the results of the RANEL annealing computer model.[25]

3.9.2.2 Swelling of Ferritic Steels. Neutron-induced swelling of ferritic steels depends on the displacement per atom, irradiation temperature, and chromium content.[24,26] Iron-chromium-carbon alloys exhibit a systematic dependence on chromium content, as shown in Fig. 3-23. Unfortunately, the peak swelling temperature for HT-9 and 2-1/4 Cr-1 Mo is approximately 426°C, occurring within the expected operating temperature range. The predicted first-wall volumetric swelling after three calendar years (80% availability) is 4.0 and 1.8% (ΔV/V%) for HT-9 and 2-1/4 Cr-1 Mo, respectively. This extrapolation is for similar heat treatment of steel assuming a predominantly bainitic microstructure.

The reduced swelling of 2-1/4 Cr-1 Mo, as compared with HT-9, is the primary reason for considering it in the MARS design. However, the high yield and thermal creep strength of HT-9 mean that less material will be required (thinner sections), resulting in lower costs, less activated material to dispose of, and possibly decreased swelling-induced stresses. These stresses can depend on the thickness of structural members when temperature (and

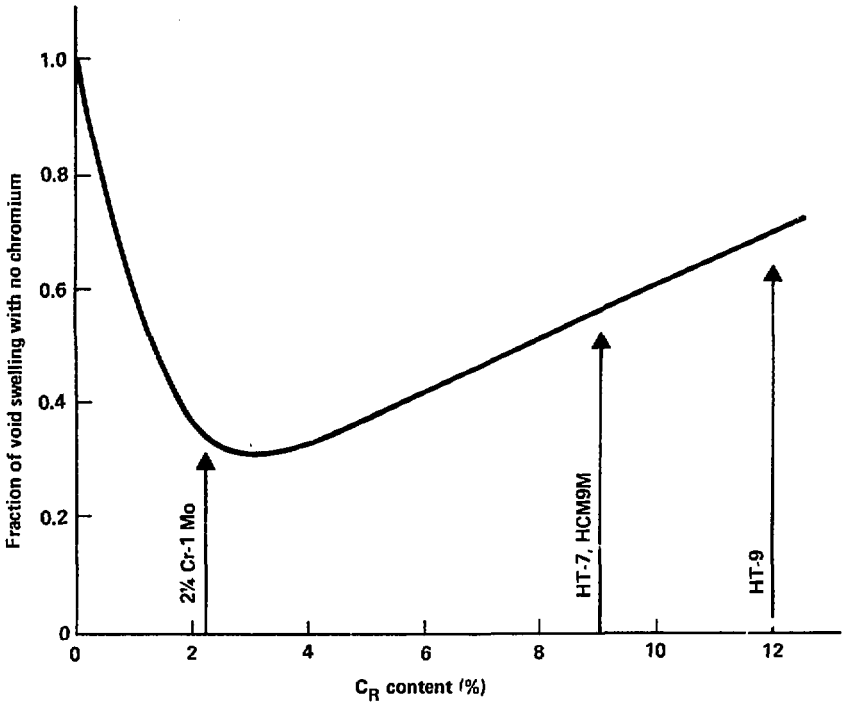

Fig. 3-23. Effect of chromium content on swelling of ferritic steels.

therefore swelling) differentials depend on thickness, and when swelling strains are taken up in bending. The temperature drop through the first wall causes differential swelling across the wall, inducing stress in the section. Table 3-14 compares the two alloys in this respect. The first wall thickness is assumed to vary inversely with yield strength, the peak swelling temperature (426°C) is assumed to occur on the inside surface of the first wall, and the section is assumed to be constrained. Stress relief due to creep is ignored. The stress in HT-9 is 82% of its yield strength and the stress in the 2-1/4 Cr-1 Mo is 86% of yield.

Swelling strain (elongation) of the first wall parallel to the plasma axis is taken up in bending the toroidal end caps. Because the stronger HT-9 will allow thinner end caps than 2-1/4 Cr-1 Mo, lower stress would be induced in the HT-9 by the same amount of bending. The HT-9 will, of course, swell more and therefore bend more, but the thinner section and higher working strength will tend to cancel the higher swelling.

Table 3-14. Temperature-dependent swelling-induced stress in the first wall.[a]

	HT-9	2 1/4 Cr - 1 Mo
Yield strength (MPa at 400°C)	290	218
Thickness (cm)	0.50	0.67
Thermal conductivity (W/MK)	29	34
ΔT (°C)	24	32
Swelling difference (%)	0.61	0.46
Young's modulus (GPa at 400°C)	175	183
Induced stress (MPa)	238	187
Percent of yield	82	86

It has been shown that irradiation creep significantly relaxes the swelling-induced stresses.[27] As shown above, the stresses generated by swelling differentials will not lead to plastic deformation at the end of life (3 years) for either HT-9 or 2-1/4 Cr-1 Mo. The fractional stress is slightly higher in 2-1/4 Cr-1 Mo than in HT-9. When irradiation creep is included, the stress in the first wall will be a function of irradiation time. The magnitude of the stress is determined as a balance between swelling and irradiation creep. Watson[27] has shown that for a clamped plate, the steady-state residual stress is proportional to the ratio of swelling to creep compliance. Even though the swelling is a factor of two smaller in 2-1/4 Cr-1 Mo than in HT-9, the magnitude of creep compliance is uncertain. It is premature, therefore, to make a final selection without a complete analysis.

The slow creep deformation of structures at high temperature under applied stress will eventually lead to failure. Creep will also tend to relieve swelling and thermal stress. In some areas creep and swelling can combine to cause excessive elongation. For example, swelling and creep will cause the first wall of the MARS high-temperature blanket to grow in axial length because of the tension caused by the Li-Pb pressure acting on the toroidal end caps. Creep can therefore limit lifetime by creep rupture or by contributing to excessive deformation. Thus, total deformation at end of life as well as the time to rupture should be quantified. Ghoniem and Conn[24,26] have developed a method to calculate time to rupture. It appears that HT-9 will not be limited by creep rupture below about 520°C. Swelling elongation of the first wall is predicted to be 1.3%, or 8 cm over the 630-cm length of the module (3-year lifetime). We have not calculated creep elongation, but we expect it to be small compared with swelling elongation because the stress in this direction is low.

We have chosen HT-9 over 2-1/4 Cr-1 Mo because its strength advantages outweigh the problems associated with swelling. The higher yield strength and creep strength of HT-9 allow the use of less structural material. This affects cost both by reducing the amount of material and by making it easier to manufacture and handle the thinner sections. Less material also results in less activated material. The HT-9 contains 1/2% nickel, whereas 2-1/4 Cr-1 Mo does not, but long-term activation of both steels is dominated by molybdenum. Isotopic separation of molybdenum or substitution of molybdenum with vanadium would greatly reduce activation, making it desirable to reconsider using 2-1/4 Cr-1 Mo to eliminate the nickel in HT-9.[26]

The study of fusion blanket lifetimes is in its infancy. Analyses of the combined effects of swelling, creep, embrittlement, and thermal stresses have been performed in only a few cases.[27] A finite-element code that includes radiation effects would be a very useful tool in this type of study.

3.10 LABORATORY TEST PERFORMANCE OF SOLID BREEDERS

One of our major concerns is the chemical compatibility of the solid breeder materials, including possible chemical reactions between a breeding material and the SiC carrier. Sintering of these materials is also a concern. Although many lithium compounds have been considered as breeding materials, only a few are suitable for the MARS blanket because of its relatively high operating temperature (1000°C). We reviewed the literature on solid breeders and selected potential candidates for the MARS high temperature blanket. Because there is a scarcity of data on solid breeders in the temperature range of interest, some preliminary screening tests were performed as a part of a TRW research project.

Potential lithium compounds have been categorized and discussed by many authors.[2,28,29] These compounds were put into several groups including liquid metals (e.g., Li, $Li_{17}Pb_{83}$), intermetallics (e.g., LiAl, Li_7Pb_2) binary compounds (e.g., Li_2O, Li_2C_2, LiF, Li_3N, Li_4Si), and ternary oxides (e.g., $LiAlO_2$, Li_2SiO_3, Li_2TiO_3, $LiFeO_2$, Li_4SiO_4, Li_2ZrO_8). All compounds that melted or decomposed at less than 900°C were rejected. Any material that was believed to react with oxygen or SiC was eliminated. The most promising compounds remaining were Li_2O and the ternary oxides.

Lithium oxide has a high melting point, high lithium-atom density, good tritium extraction, and relatively low chemical reactivity. However, formation of LiOT from Li_2O can cause serious problems, such as an acceleration of sintering and corrosion of structural materials. Therefore, we turned our attention to the ternary oxides. One of the disadvantages of the ternary oxides is their low lithium density; thus, a neutron multiplier is required. In the MARS high temperature blanket, however, the $Li_{17}Pb_{83}$ coolant provides adequate multiplication. The remaining concern was high temperature operation because of self-sintering or sintering to the SiC carrier. Based on melting point and neutronics, we selected $LiAlO_2$ and Li_2TiO_3 for testing.

3.10.1 Lithium Titanate and Silicon Carbide Heated Separately

We conducted separate tests for possible self-sintering of Li_2TiO_3 and SiC powder. The tests took place in the BREW furnace at 1100°C and 1×10^{-5} Torr for 5 hours. The SiC did not show any sign of self-sintering; the Li_2TiO_3 sintered and its color changed from white to bluish gray. This color change may be caused by trace impurities. Based on the x-ray diffraction pattern, no chemical reaction occurred. The scanning electron microscope (SEM) micrograph (Fig. 3-24) shows a self-sintering of Li_2TiO_3.

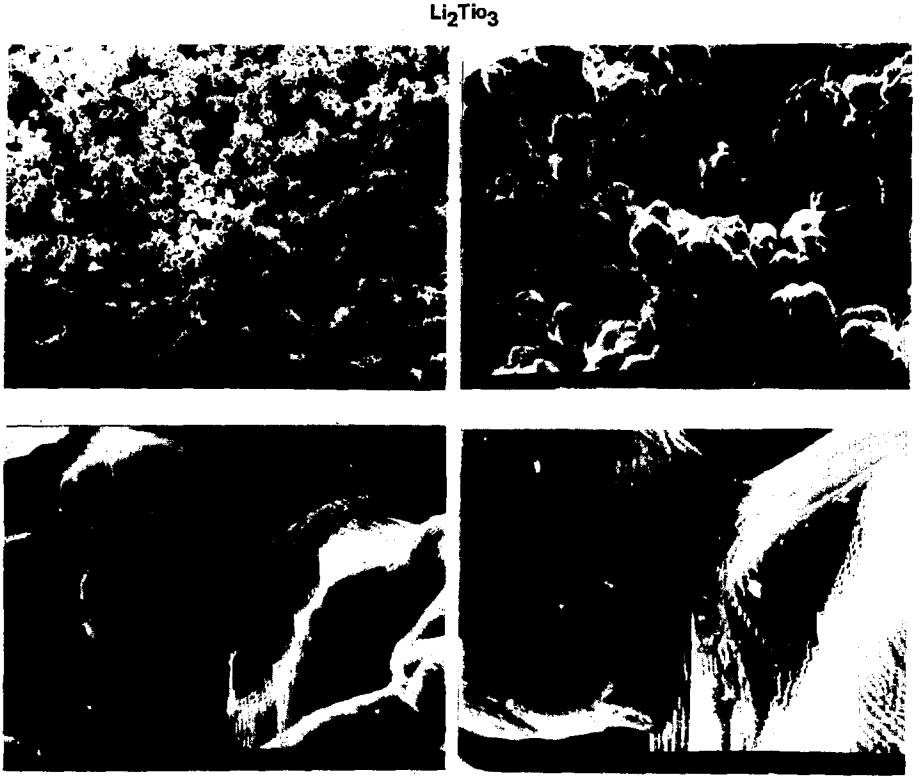

Fig. 3-24. Lithium titanate after 4-hour vacuum exposure at 1100°C.

3.10.2 Mixtures of Lithium Titanate and Silicon Carbide

The test conditions were identical to those in the previous experiment. Two mixture ratios were tested; both mixtures (1:1 and 1:6) sintered during heating. The shape of the particles, determined by SEM, seem to indicate both self-sintering of Li_2TiO_3 and Li_2TiO_3-SiC sintering. The x-ray diffraction shown in Fig. 3-25 gives some evidence of a chemical reaction between Li_2TiO_3 and SiC. The Li_2TiO_3 seemed to disappear and new peaks that appeared after heating corresponded to Li_2SiO_3. Unfortunately, TiC and SiC have identical x-ray diffraction spectra, and the formation of TiC cannot be confirmed by x-ray diffraction analysis. Thermodynamically, the following reaction should occur:

$$Li_2TiO_3 + SiC \rightarrow Li_2SiO_3 + TiC$$

$$\Delta G^0_{reaction} = -20.305 \text{ kcal} \quad .$$

Although definitive evidence is lacking, it appears that the above reaction took place during the heating at 1100°C. From this result and based on the thermodynamics, it is also likely that lithium zirconate (Li_2ZrO_3) another solid breeder candidate, will react with SiC to form lithium silicate and zirconium carbide.

3.10.3 Lithium Aluminate and Silicon Carbide

Mixtures of $LiAlO_2$ and SiC (1:1 and 1:5) were heated to 1100°C in a similar manner as in the previous case. When the furnace was opened, we found that most of the sample powders spilled all over the furnace. An excessive outgassing must have occurred at approximately 300°C. Because of this problem, we carried out a degassing using a laboratory box furnace. The $LiAlO_2$ powder (100 μm) was heated from 750 to 800°C for 4 hours. The weight loss by heating was approximately 25%. Additional heating at 800°C for 4 hours did not change the weight appreciably. The x-ray diffraction spectra (Fig. 3-26) showed that the commercial $LiAlO_2$ contains a hydrated $LiAlO_2$ and some Li_2CO_3.

A thermal gravimetric analysis of $LiAlO_2$ indicated a weight loss of 21% at 200 to 300°C and 4% at 550 to 650°C. The first weight loss is due to dehydration of $LiAlO_2 \times H_2O$ and the second weight loss seems to be due to a decomposition of Li_2CO_3. The hydration number is calculated to be 1.

We again blended SiC and the preheated $LiAlO_2$ to make 1:1 and 1:5 ratios. We then conducted the compatibility test in a similar manner as in the previous case. This time, we did not see an excessive pressure rise as the temperature was increased to 500°C in the vacuum. The weight change was only 1.7 and 0.8% for the 1:1 and 1:5 mixtures, respectively. The x-ray diffraction spectra did not indicate a significant change except for the change of a α-$LiAlO_2$ to γ-$LiAlO_2$ during the heating at 1100°C, as shown in Fig. 3-27. This phase change was also reported by Johnson et al.[30] The irreversibility of the phase change is reconfirmed by the present work.

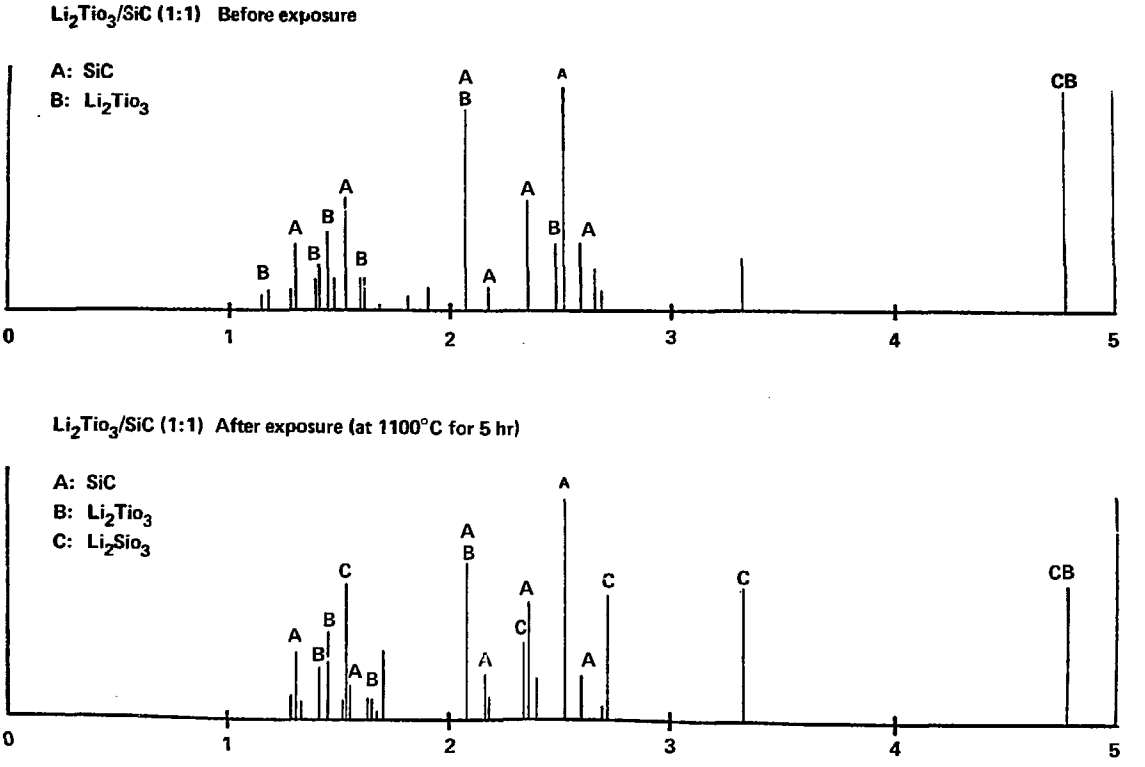

Fig. 3-25. X-ray diffraction pattern of Li_2Tio_3/SiC (1:1).

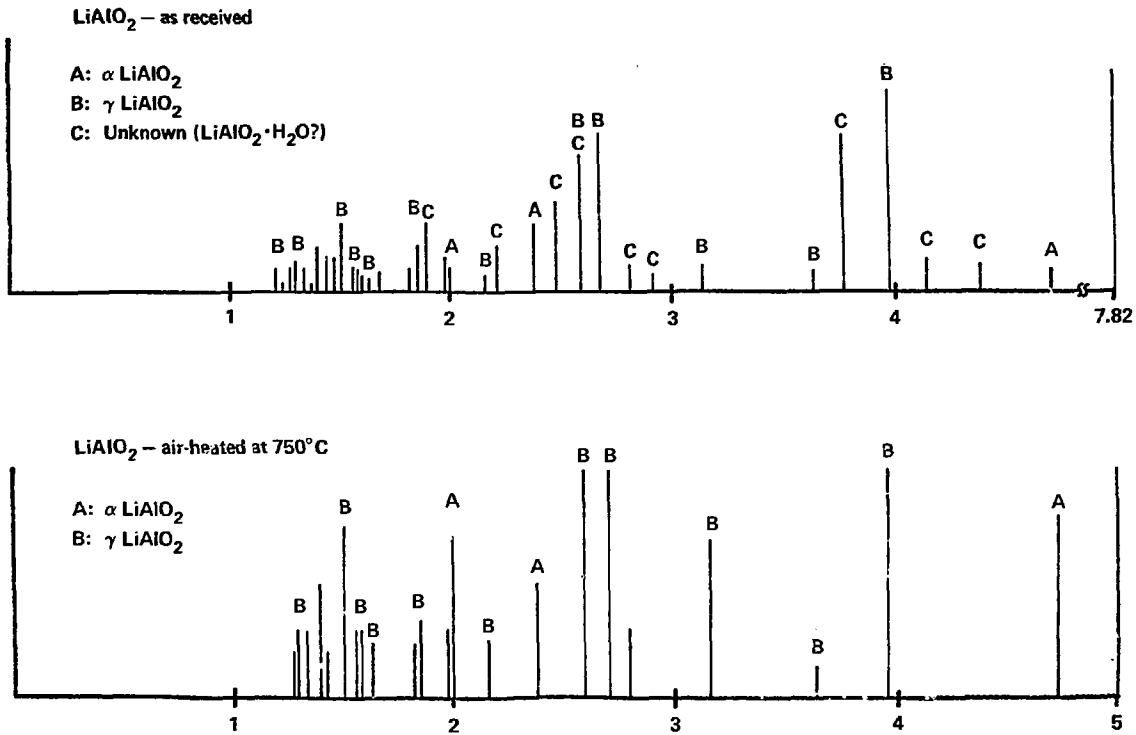

Fig. 3-26. X-ray diffraction pattern of $LiAlO_2$.

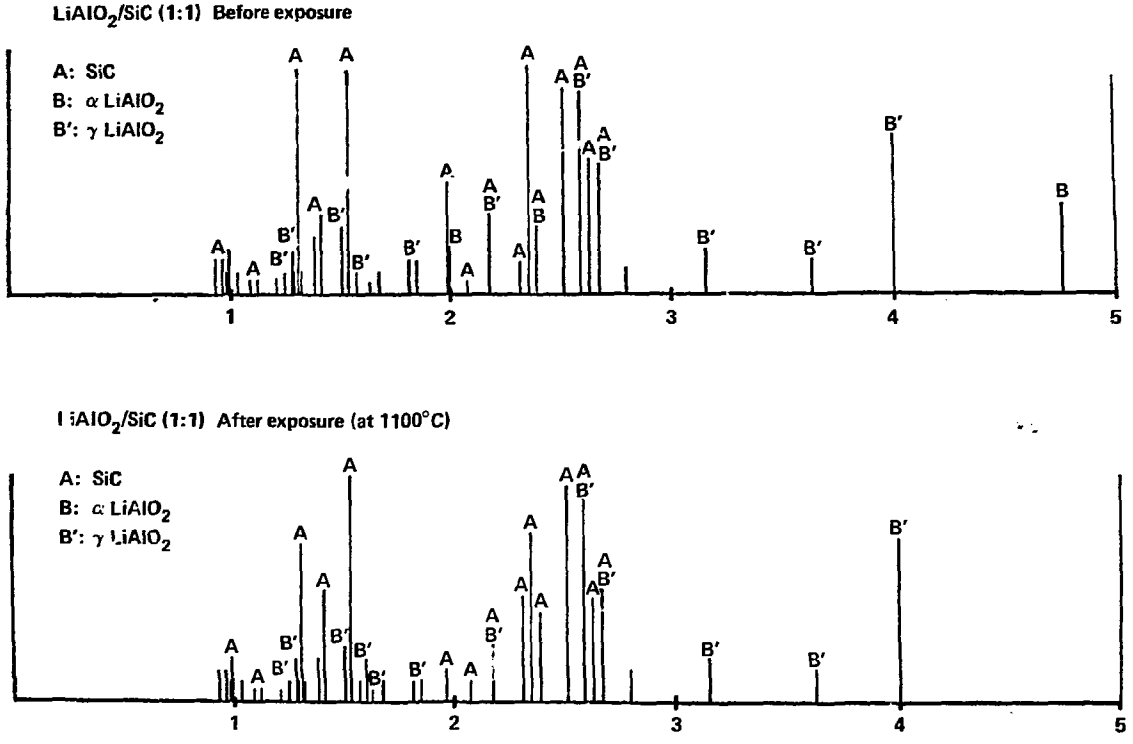

Fig. 3-27. X-ray diffraction pattern of $LiAlO_2$/SiC (1:1).

Table 3-15 summarizes the chemical compatibility test of a lithium compound with SiC. The following conclusions may be drawn from the present study:

1. Li_2TiO_3 reacted with SiC and formed Li_2SiO_3 at 1100°C after 5 hours.
2. Li_2TiO_3 showed self-sintering during heating at 1100°C for 5 hours.
3. Based on the preliminary test results, $LiAlO_2$ is compatible with SiC at 1100°C for 5 hours; no evidence of chemical reaction or sintering was detected.

Table 3-15. A summary of chemical compatibility tests of lithium compounds and SiC.

	Weight change (g)	X-ray diffraction	SEM	Observation
SiC	0.472/3.682	No change in the spectra	--	No sintering
Li_2TiO_3	0.444/2.767	No change in the spectra	Self-sintering	Color change--white to bluish gray--self sintering
$LiAlO_2$[a]	5.256/20.351	Substantial change in the spectra--clear peaks of α and γ $LiAlO_2$	--	No sintering
Li_2TiO_3/SiC	0.200/6.146	Disappearance of Li_2TiO_3 peaks--appearance of Li_2SiO_3 peaks	Shows sintering	Color change gray to black sintering
$LiAlO_2$/SiC	0.056/3.2239	Disappearance of α $LiAlO_2$--no new peaks	--	No sintering

[a]Air heated at approximately 750°C for 4 hours.

3.11 POD RUPTURE ANALYSIS

During steady-state operation, the pressure in all 12 pods should be identical so that there are no unbalanced stresses in the pod walls. We performed a preliminary analysis to determine the magnitude of the maximum pressure differentials between any two pods in the event of a pod rupture and the subsequent blowdown.

If a pod ruptures, a transient blowdown will occur. During this process all module helium supply and return lines must be closed to prevent additional helium from escaping. All helium in the pods and manifolds will exit to the plasma region through the failure point. Figure 3-28 shows the 12-pod arrangement and also indicates helium flow directions during a failure blowdown.

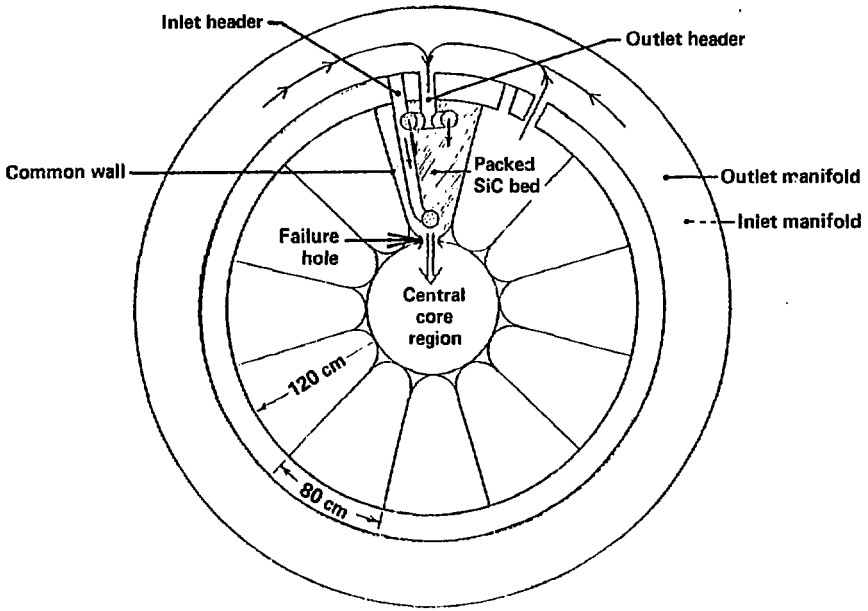

Fig. 3-28. Pod rupture flowdown paths.

A worst case analysis has shown that the maximum pressure differential between pods across the common wall regions will be 24 atm for an 8-in.-diameter hole and 80-atm operating pressure. Analysis of the pod structure shows that it can withstand a 58-atm differential. The maximum pressure drop occurs near the inner radius of the power blanket across the common pod wall. The maximum ΔP exists only at the instant of failure and then decreases very rapidly as the blowdown proceeds. Figure 3-29 shows the maximum and average pressure differentials as a funtion of hole size for 50- and 80-atm operating pressures.

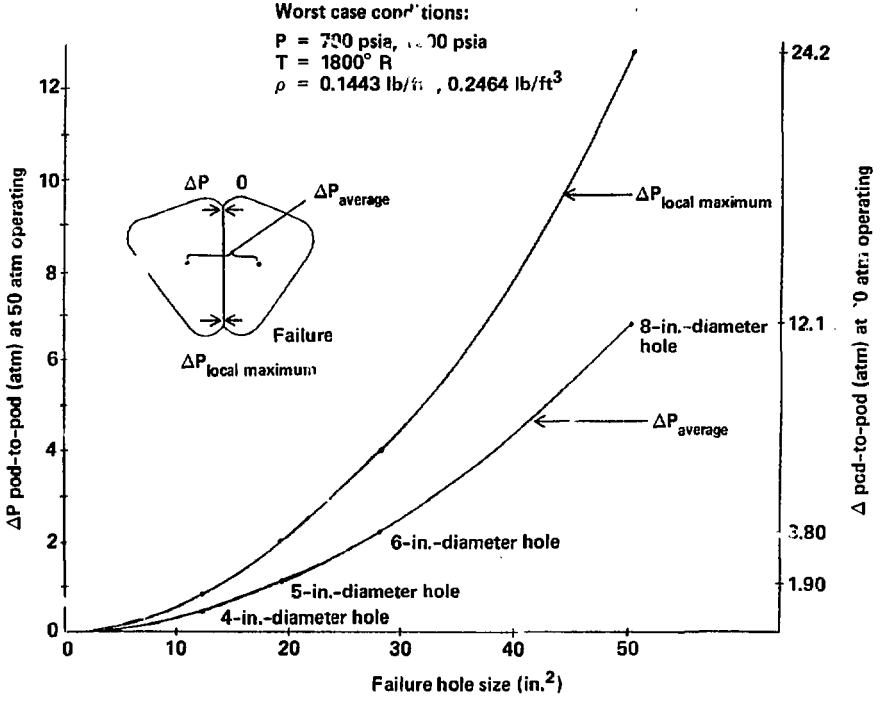

Fig. 3-29. Pod-to-pod pressure differentials vs failure hole size.

The approach used to determine the pressure differential between adjacent pods involves calculating the pressure drop through a pod for a given rupture hole diameter and the corresponding mass flow rate. The total pressure drop through a failed pod consists of three parts. The first pressure drop is from flow through the helium outlet ducting. This is the sum of losses in the straight header section, the perforated manifold, and numerous perforations in the manifold. The second major pressure drop is from flow through the SiC-packed bed. The third major pressure drop is from losses through the inlet header and its perforated manifold.

The largest failure size investigated, which is not shown in Fig. 3-29, was a tear along the length of the pod 0.5 in. wide and 13.0 ft long, simulating a separation or stress crack failure. The local maximum and average pressure differentials for such a failure at a 50-atm operating pressure are 30.8 and 15.9 atm, respectively. For an 80-atm operating pressure, these values are 50.4 and 29.1 atm, respectively. Thus, even in the case of a split down two-thirds of the length of a pod, the pressure differential is below the 58-atm limit for the structure. We believe that the pod design is strong enough to preclude a domino failure.

3.12 SCOPING THE SHIELD DESIGN

The shield design has only been scoped at this time to show that it is feasible to meet the requirements for the shield. Further design iterations will refine and optimize the concept. The function of this shield is to protect the superconducting magnets from radiation and to protect workers in the reactor area during maintenance. The MARS high-temperature blanket shield uses steel as the shielding and main structural material. It also provides structural support for the blanket and magnets. Figure 3-30 shows the shield materials and thicknesses used in the neutronics and thermal hydraulics scoping analyses described below. Further optimization is expected to result in a thinner shield.

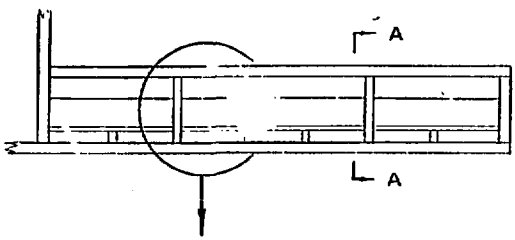

Section A-A

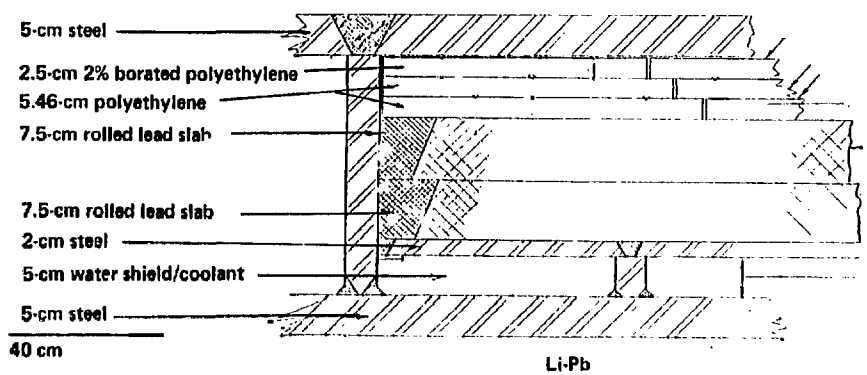

Fig. 3-30. Shield.

3.12.1 Shield Design Criteria

The principal design consideration for the shield is to protect the superconducting magnets from neutron and gamma radiation. Three values characterize the central-cell shield requirements: (1) 2.2×10^{-5} dpa/FPY in the Cu stabilizer to allow 5 FPY before the first anneal; (2) 2.0×10^{8} rad (insulator)/FPY to ensure a lifetime dose less than 5×10^{9} rad; and (3) 0.06 mW/cm^3 peak heat load in the winding to minimize cryogenic costs.

3.12.2 General Structural Description

The primary purpose of the cylindrical shield is to provide radiation protection for the central cell magnets during reactor operation. In addition, the shield has been structurally integrated into and forms a part of the module support structure and, therefore, provides support for the magnets and blanket.

The shield is a box structure supporting the blanket and magnet. It encloses circulating borated water for cooling and lead and polyethylene slabs to attenuate neutron and gamma radiation. The 5-cm steel-box floor (inner radius) interfaces with the blanket Li-Pb coolant (maximum temperature ~500°C) and pods on one side and with the borated water coolant in the shield (maximum tempeature ~100°C) on the other. An insulation layer is required in this region. The water coolant is enclosed with 2 cm of steel, which also acts as a support for the two 7.5-cm lead slabs. The three polyethylene slabs are capped by a 5-cm steel cover. Channels located on the shield floor at the Li-Pb interface are designed to accept the pod support rails.

3.12.3 Shield Neutronics

We have demonstrated the feasibility of the shield for the MARS high-temperture blanket, and although the final design of the shield has not been completed, it presents little conceptual difficulty. We still need to address the shield design in the vicinity of the module-to-module interfaces.

We performed a one-dimensional neutronics analysis of the shield using the ONEDANT code. Its performance against our criteria is given in Table 3-16, and the energy deposition as a function of position is given in Table 3-17.

Table 3-16. Shield performance.

	Criteria	Performance
Stabilizer damage (dpa/FPY)	$<2.2 \times 10^{-5}$	3.5×10^{-5}
Insulator dose (rad/FPY)	$<2.0 \times 10^{8}$	3.6×10^{6}
Peak conductor heat deposition (mW/cm^3)	<0.06	0.053

Table 3-17. Energy deposition profile.

Material	Radius (cm)	Energy deposition	
		Neutrons (mW/cm^3)	Gammas (mW/cm^3)
Steel	182.8	2.37	256
	184.5	1.74	301
	186.2	1.19	304
Water	187.8	9.50	34.1
	189.5	4.52	33.0
	191.2	3.25	32.2
Steel	193.0	0.33	212
Lead	195.5	0.039	134
	198.5	0.035	9.6
	201.5	0.029	2.5
	204.5	0.024	1.3
	207.5	0.020	1.7
Polyethylene	210.4	0.346	0.17
	213.1	0.168	0.20
Borated polyethylene	215.1	5.58	0.18
	216.4	0.507	0.17
Steel	218.3	0 0115	0.87
	220.8	0.0092	0.31

Although the proposed shield fails to satisfy the first criterion, it appears that compliance can be achieved by trading some lead for polyethylene Future work will address optimization and model plumbing penetrations (e.g., helium and Li-Pb pipes).

3.12.4 Shield Thermal Hydraulics

The thermal-analyzer finite-element computer model[31] was used to predict temperature profiles in the shield. One requirement is to maintain a maximum temperature in the polyethylene below 120°C.[32] Also, the heat leak from the Li-Pb region should be low because the heat carried out by the water will be at a low temperature. It is necessary to keep thermal gradients in the shield low to maintain structural integrity.

Insulation will be required between the Li-Pb in the back wall region and the shield. Without this insulation, two design problems exist: (1) a large temperature differential on the order of 300 to 400°C will occur through the first 5 cm of the shield, and (2) a large heat leak on the order of 16 W/cm^2 will occur between the Li-Pb region to the water-cooled shield, causing intolerable film drop temperatures in the water cooling system.

To keep the water pressure at 100 to 150 psi, the inner shell must be insulated from the Li-Pb so that the maximum temperature of the inner shell is about 150 to 200°C. This decreases the heat leak and reduces the film drop on the inner shell side to a reasonable value. If the inner shell of the shield is constrained at 165°C and the maximum water temperature is 56°C, polyethylene reaches a temperture of 120°C, which just meets the maximum service temperature. Thus, trace cooling will not be needed at the outer shell of the shield. The film drop temperatures are 53°C on the shield side and 84°C on the blanket side.

The 6.32-m-long shield module section must accommodate about 1.9 MW of heating, not including the heat leak from the Li-Pb region. Assuming an inlet water temperature of 40°C and a temperature rise of 16°C, a water flow rate of 28 kg/s is required. The water velocity of 0.146 m/s will cause a very low pressure drop through the channels, requiring only 0.14 W of pumping power per module.

3.13 SEALS

3.13.1 Vacuum Seals

The modules interface with each other through module-to-module seals designed both to maintain the reactor vacuum and allow the joint to be sealed and disconnected by remote operation for safety. Studies indicate that the seal can be brazed. Each joint seal can be verified without requiring a reactor vacuum. The seal is flexible enough to permit deflections resulting from module temperature expansions. Figure 3-31 shows a schematic of the intermodule seal concept.

The flat seal plate is closed against the grooved seal plate on the adjacent module by pressurizing the bellows. The bellows chamber contains a steel plug for shielding. Backing plates guide and support the movable bellows, seal plate, and shield plug assembly. The seal is formed by allowing a molten brazing alloy to flow into the grooves in the stationary seal plate surface. Resistance heating melts the alloy and warms the flow paths. This allows a relatively low pressure in the bellows to position the seal. Two seal grooves allow the seal's integrity to be tested through a port between the grooves.

3.13.2 Remote-Actuated Lithium-Lead Pipe Connections

For protection against potential tritium residue and to minimize disengagement time, the Li-Pb pipe connections are also designed to be operated remotely. Because of the relatively low operating temperatures, the Li-Pb joint can be brazed with a design similar to that used in the module vacuum seal. The joints are brazed using metal that is allowed to flow into two areas located between the two surfaces to be joined. Heating coils in the joint areas ensure continuous flow of the brazing material. Cooling jackets, if required, are provided to ensure that the brazing compound remains confined while the seal hardens. The chamber between the two joints has a test port that allows the integrity of the seal to be verified. The concept is shown in Fig. 3-32.

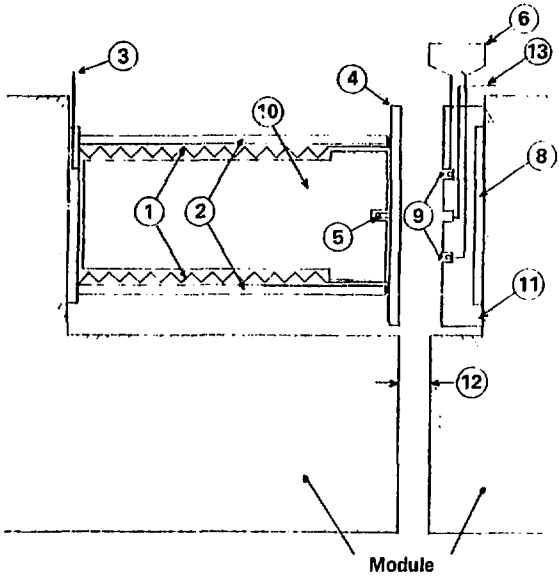

Features

Metal sealing
Remote coupling/decoupling
Seal verification

1. Bellows
2. Backing plate
3. Pressurization feed
4. Seal plate
5. Shield plug attach
6. Brazing alloy reservoir
7. Alloy drain
8. Insulation
9. Alloy distribution groove
10. Shield plug
11. Seal base
12. Module clearance
13. Test connection

Fig. 3-31. Module-to-module interface seal.

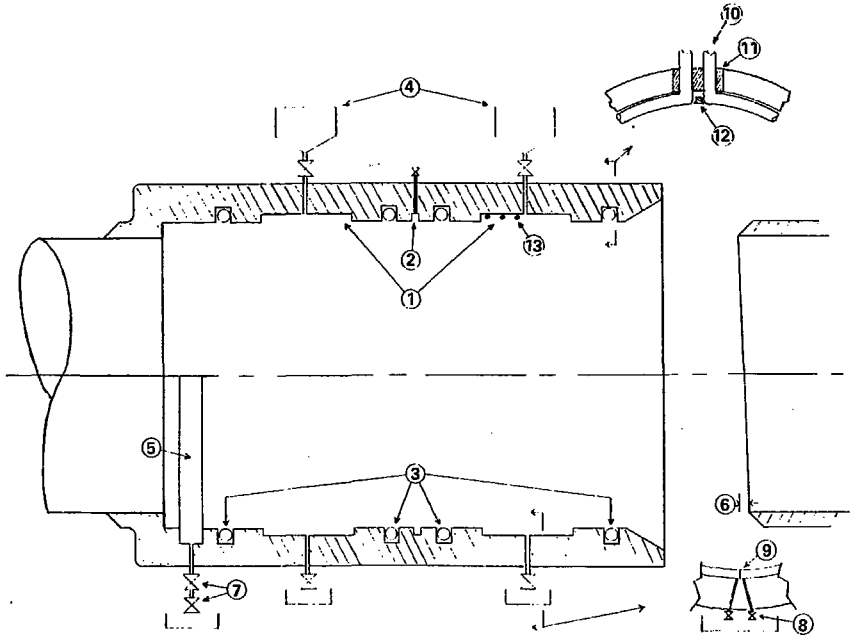

Features

Metal seal
Remote operation
Seal verification

1. Joint area
2. Test connection
3. Cooling tubes
4. Braze alloy reservoir
5. Drip grove
6. 1-cm offset
7. Li-Pb drain
8. Braze alloy drain
9. Baffle
10. Cooling tubes
11. Bushing
12. Thermal bridge
13. Heating coil

Fig. 3-32. Lithium-lead pipe coupling.

3.14 TRITIUM AND ITS CONTROL

Tritium and its control are discussed primarily in Sec. 7 of this volume, and the reader is therefore referred to that section for a more complete discussion of this subject. Some additional details that apply to fuel design and tritium process equipment costs are covered below.

3.14.1 Tritium Removal

Tritium is produced in the high temperature blanket at a rate of ~450 g/day. The tritium is bred in a solid lithium-containing material ($LiAlO_2$) and diffuses into the helium coolant. Tritium inventory in the solid breeder, excluding the blanket structural components, is estimated at less than 100 g based on a diffusional tritium holdup argument. A partial pressure of oxygen on the order of 1 Torr in the helium maintains the tritium primarily as T_2O. By maintaining the chemical form of tritium as T_2O, the containment of tritium is believed to be easier than containment in a system that contains molecular tritium (T_2). This is because T_2O does not permeate metals that have a surface oxide scale as readily as does T_2.

The tritium path through the high-temperature helium loop begins in the breeding blanket, then passes through the recirculating helium (which supplies process heat to the chemical plant), and finally to recovery from the helium by physical adsorption. A small amount of tritium, on the order of 50 g/day, is bred in the Li-Pb. It is recovered by a flash unit operation.

Tritium is lost by leakage and permeation from the process system mainly in the high-temperature loop through the process heat exchanger, piping, and compressors. Additional tritium is lost by leakage and permeation from the Li-Pb loop. An accidental release of a fraction of the tritium in these loops is possible, and the fraction released provides a basis for sizing the tritium control equipment for the reactor hall.

3.14.2 Solid Breeder Tritium Inventory

We have estimated the portion of the tritium inventory resulting from diffusional holdup and the rate of T_2O formation in the high-temperature solid breeder. Diffusional holdup of the tritium depends on the particle size of the breeder compound and is estimated at about 65 g for the reactor if the particle diameter is 100 μm. This estimate is strongly influenced by the tritium diffusivity value, which is poorly known and little understood in the lithium compounds of interest. Assuming for calculational purposes that the helium stream contains 1 ppm oxygen at 1000 °C, our calculations indicate that the rate of T_2O formation is controlled by tritium diffusion through the solid breeder compound, and that tritium will react with oxygen as soon as it reaches a solid surface that contains adsorbed oxygen.

The tritium inventory in a breeder blanket has been estimated based on the following assumptions:

1. The lithium compound particles are spherical.

2. Tritium is swept away by the coolant gas (containing 1 ppm O_2) as soon as T_2O is formed.

Under these assumptions, the tritium inventory in each particle, S, is *the volume integral of the tritium concentration, i.e.,*

$$S = \int_0^{r_0} C_T(r)\, 4\rho r^2 dr \quad ,$$

which is

$$S = \frac{4\rho R_T}{45\, D}\, r_0^5 \quad ,$$

where

R_T = tritium generation rate in (atoms/cm^3-s),

D = tritium diffusivity in the breeder compound (cm^2/s), and

r_0 = radius of particle sphere (cm).

The total tritium inventory is obtained by using the total generation rate and assuming uniform particle size, such that

$$S\ (\text{total}) = \frac{R\ (\text{total})}{15\, D}\, r_0^2 \quad .$$

At this point, it is necessary to estimate values for D because no data are available for hydrogen diffusivity (much less tritium) in $LiAlO_2$. We chose a value of D based on tritium diffusivity in Al_2O_3 where

$$D = 4 \times 10^{-10}\ \text{cm}^2/\text{s} \quad .$$

With this value, the total reactor inventory is 65 g. We note that the estimated value depends strongly on tritium diffusivity in the breeder, which can be altered many orders of magnitude by heat treatment, environmental exposure, and bombardment by ionizing radiation. We recommend that tritium diffusion in lithium-bearing compounds be further examined and analyzed.

Finally, the calculated inventory values for the MARS solid breeder scale as the particle radius is squared. For a 100-μm-diameter particle it is 65 g, and we have used this value as the baseline to scale to other particle uses. If the diffusion coefficient were an order of magnitude higher--4 x 10^{-9} cm^2/s--the tritium inventory would be about 6 g; or if it were an order of magnitude lower--4 x 10^{-11} cm^2/s--the tritium inventory would be 650 g. We have not considered T_2O solubility in the solid, which could add to the tritium inventory.

3.14.3 Tritium Oxide Formation Rate

A factor in the blanket design is the formation of T_2O by the oxygenated helium stream to reduce tritium loss by permeation. To determine the rate of T_2O formation, we examined the data available on hydrogen oxidation. A large amount of data is summarized in Fig. 3-33, where different rate-limiting regimes are identified.[33] The regime of interest is the

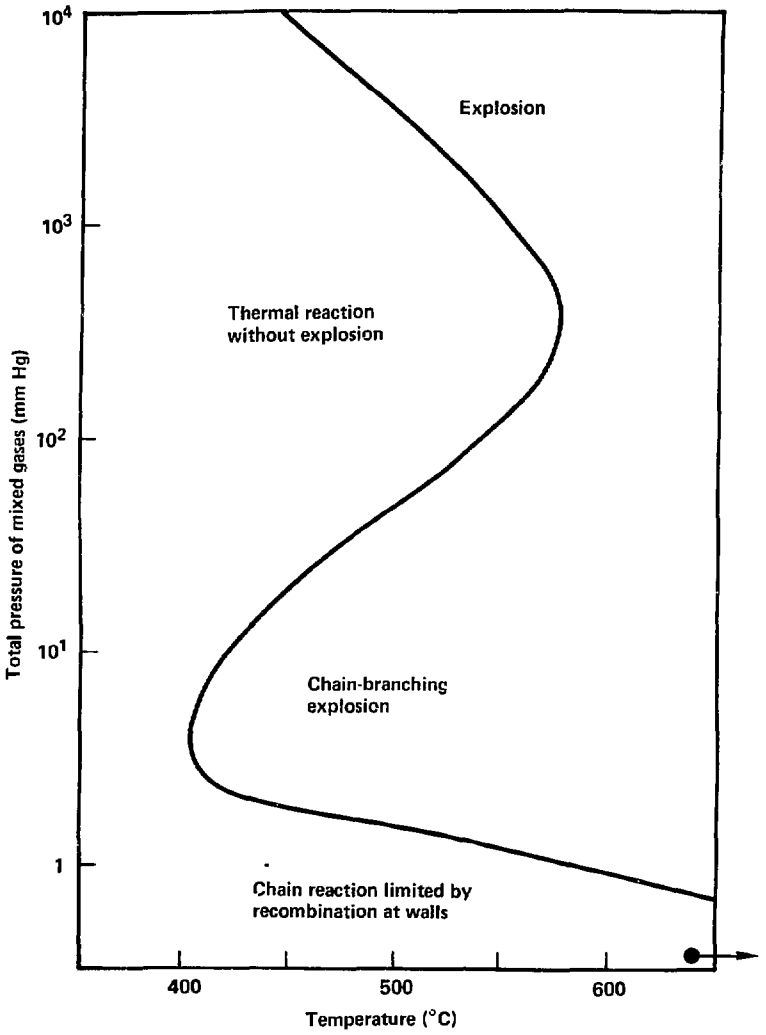

Fig. 3-33. Nature of reaction of stoichiometric mixtures of hydrogen and oxygen.

extreme lower right corner because the total pressure of H_2 and O_2 is 0.12 Torr at 1000°C. This is the regime where the oxidation of hydrogen is limited by recombination at a wall. (Note: The explosive regime does not exist in the presence of 50-atm He.) Thus, we turn to an analysis of heterogeneous reaction rates.

The rate of oxygen adsorption on a solid surface can be expressed as

$$r(ads) = \frac{3.51 \times 10^{22}}{(MT)^{1/2}} Pf \left(\frac{molecules}{cm^2\text{-}s}\right) ,$$

where

P = partial pressure of O_2 = (0.06 Torr),

M = molecular weight of O_2 (32),

T = absolute temperature (1273 K), and

f = fraction of the collisions that result in chemisorption.

The fraction of collisions f that result in chemisorption is

$$f = \exp(-\Delta E/RT) ,$$

where ΔE is the activation energy (for the chemisorption process). As a general rule, E is above 10 to 15 kcal/mole; we used these values because no data were available for the activation energy of O_2 on $LiAlO_2$.

Later results show that this sensitivity is not important. This is the rate of chemisorption of oxygen on any solid surface in the breeder module, including, of course, the surfaces of the solid breeder compounds. Using the above equation, we calculate the rate of oxygen chemisorption to be 6×10^{16} atoms/cm^2-s.

The next task is to determine the rate of arrival of tritium atoms from within the breeder compound. Tritium flux at the surface is found from the rate of tritium generation that is nearly constant throughout the particles. For a particle size of 100 μm the flux of tritium atoms at the surface is 1.7×10^{11} tritium atoms/cm^2-s.

This atomic tritium flux is much lower than the rate of chemisorption of oxygen (6×10^{16}), and indicates that the rate of tritium oxidation is limited by the rate of tritium diffusion through the solid breeder. The surface is effectively covered with oxygen and, based on Fig. 3-33, the oxidation rate at the surface is the same as the diffusion rate. As a rough estimate, the fraction of tritium desorbed as T_2 is proportional to the ratio of diffusion of T to adsorption of O_2. This is approximately 3×10^{-6} when the O_2 content of the helium is 1 ppm. Actually the O_2 content of the helium is expected to be a factor of 20 less than this (see Sec. 7 of this volume); however, this does not alter the conclusion about the large excess of chemisorbed O_2.

3.14.4 Tritium Extraction from Helium

Tritium is produced in the solid breeding blanket and diffuses into the helium loop as T_2O at the rate of 450 g/day. The function of the tritium extraction process is to recover the tritium produced in the blanket from the helium loop.

A slip-stream recovery process for steady-state tritium extraction is illustrated in Fig. 3-34. The input variables for the process design are the tritium production rate, the chemical form of the tritium, the slip-stream flow rate, and the main helium flow rate. The engineering variables to be specified or calculated are the selection of the thermodynamic sink for T_2O in the recovery process, the operating temperature for the T_2O recovery process, and the tritium concentrations in all the process streams. Figure 3-34 and the above independent/dependent variables apply to any tritium extraction process for the helium process loop, as shown.

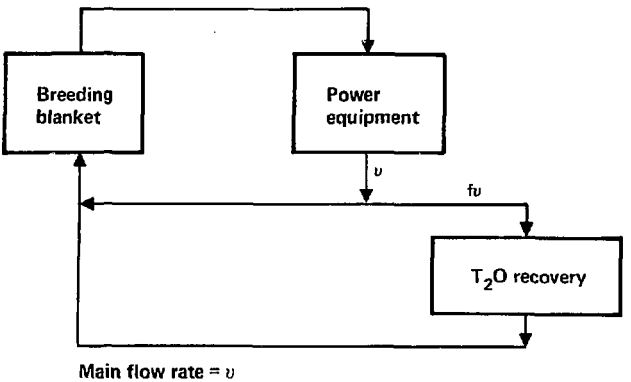

Fig. 3-34. Slip-stream tritium recovery process material balance diagram.

The tritium extraction process chosen for T_2O recovery is physical adsorption using a molecular sieve. The molecular sieve, designated 4A, provides the thermodynamic sink for T_2O and results in a T_2O partial pressure at the exit of the recovery unit on the order of 0.01 Torr at 60°C.[34] The 60°C temperature must be attained through recuperation in the slip stream. A higher or lower extraction temperature produces a correspondingly higher or lower T_2O exit partial pressure. Lowering this temperature to 40°C would result in a T_2O exit partial pressure of approximately 0.001 Torr.

The molecular sieve bed is regenerated to recover T_2O either by raising the bed temperature to 200 to 300°C and purging off the T_2O, or by vacuum pumping.[35] The T_2O is recovered in a cold trap and the liquid T_2O is delivered for final T_2 purification by electrolysis or cryogenic distillation.

Table 3-18 contains the results of calculations of the pertinent quantities of a steady-state T_2O material balance for slip-stream fractions of 1 and 5%. The recirculating inventory of radioactive tritium, i.e., that tritium as T_2O in helium, is calculated from $Ci = 8.4 \times 10^9 (y)(t_r)$, where t_r is the helium residence time (time to complete one loop of the coolant circuit) in seconds and y is the T_2O concentration in moles T_2O/mole He. For the case of a 1% slip stream where the T_2O concentration is approximately 7.4×10^{-7} moles T_2O/mole He, the recirculating activities in curies is 6.4×10^3 t_r; for a 5% slip stream the result is 2.4×10^3 t_r.

Table 3-18. Steady-state material balance for a T_2O slip-stream recovery.

Input variables	Value
Tritium production (g/day)	450
Helium flow at 50 atm (kg/s)	600
T_2O recovery exit pressure at 60°C (Torr)	0.01
Blanket exit temperature (°C)	1000
1% slip stream	
Slip-stream exit concentration T_2O (moles/mole)	1.645×10^{-7}
Return concentration (moles/mole)	7.374×10^{-7}
Blanket exit concentration (moles/mole)	7.432×10^{-7}
T_2O partial pressure entering blanket (Torr)	4.483×10^{-2}
T_2O partial pressure exiting blanket (Torr)	4.519×10^{-2}
Slip-stream flow (m^3/s)	0.819
5% slip stream	
Slip-stream exit concentration (moles/mole)	1.645×10^{-7}
Return concentration (moles/mole)	2.744×10^{-7}
Blanket exit concentration (moles/mole)	2.802×10^{-7}
T_2O partial pressure entering blanket (Torr)	1.669×10^{-2}
T_2O partial pressure exiting blanket (Torr)	1.704×10^{-2}
Slip-stream flow (m^3/s)	4.10

To design the hardware for T_2O recovery using a 4A molecular sieve, we had to specify the size of the vessels. Vessel sizing is based on 24-hour operation, a 1% slip stream, a tritium loading of 450 g (as T_2O, 1650 g), a loading of one pound of tritiated water per 100 lb of sieve, and a superficial velocity of 22.8 m/min. These specifications produce a process pressure drop of approximately 3.4 kPa (0.03 atm), a bed area of 1.33 m^2, a vessel diameter of 1.2 m, and a bed depth of 33 cm. The cost for a single stainless steel vessel rated at 10.3 MPa (102 atm) is $66,000.[36] Three vessels are required with one in operation, one in regeneration, and one in standby mode.

The tradeoffs for the process design of the tritium extraction system involve cost vs tritium in the process system. For the base case we selected a slip stream of 1% and a cycle time of 24 hours. This results in an inventory of approximately 470 g of tritium (4.5×10^6 Ci, 450 g on the bed and 20 g recirculating with a 30-s residence time). Clearly, cutting the cycle time in half would result in a 250-g tritium inventory reduction. However, at the present time it is not clear how fast a molecular sieve vessel can be heated, purged or vacuum pumped, and cooled for return to the process. The 24-hour cycle time is a subjective specification and appears reasonable from an engineering perspective. Thus, the apparent cycle time could be shortened by adding more vessels. Noting that the single stainless-steel vessel costs $66,000 and the installed cost is approximately 5.4 times this cost (including 25% contingency), increasing the number of vessels costs $356,000 per installed vessel. Further tradeoff studies must involve cost vs the tritium process inventory.

3.14.5 Tritium Extraction from Lithium-Lead

Tritium is bred in the $Li_{17}Pb_{83}$ eutectic at a rate of ~50 g/day and must be extracted at this rate. Tritium can be removed from the liquid Li-Pb mixture [2,30] by vacuum pumping, inert gas sparging, and molten salt extraction. For MARS we chose vacuum pumping as the primary Li-Pb tritium recovery scheme. The lead-rich Li-Pb mixtures are unique for use as liquid breeders because of their extremely low tritium solubility. The Sieverts' constant for tritium in $Li_{17}Pb_{83}$ in the temperature range from 400 to 600°C is 0.051 wppm $T/Torr^{1/2}$ (Ref. 31). Even at very low concentration levels (wppb), tritium will establish a reasonably high partial pressure above the alloy. Vacuum pumping at or below this partial pressure should provide an effective means of removing the tritium in a relatively simple and economical fashion. Although no experiments are presently being conducted on vacuum removal of gases from Li-Pb, considerable experience exists in the degassing of liquid steels to remove hydrogen and other volatile impurities.[32] We chose vacuum pumping without a helium purge gas in the base design to avoid possible large helium flow rates and helium/tritium separation problems at large $He:T_2$ ratios. This option may integrate well with the helium-tritium extraction system, but we have not investigated it here. Molten salt extraction of tritium from molten Li-Pb mixtures appears feasible and has been suggested in other designs.[2,30,33] Vacuum removal is a simpler alternative and it avoids the possible transport of molten salt residues through the coolant loop.

To determine the optimum steady-state concentration level in the breeding material, both the extraction and the containment systems must be considered. High concentrations place a burden on the containment systems, whereas low concentrations make extraction more difficult. The tradeoff between the partial pressure and the pumping requirements is illustrated in Fig. 3-35 (normalized to a tritium breeding rate of 10^{-3} moles/s, or 173 g/day). The major containment problem is in the transport of tritium through the heat exchanger. For a single-walled tube with an oxide coating giving a resistance factor of 100, the tritium partial pressure must be 2.4×10^{-9} Torr to keep losses through the heat exchanger to 10 Ci/day. A very high pumping rate of 2.3×10^{10} liter/s is needed at 500°C to achieve the required vacuum, which precludes tritium extraction at this low pressure.

We selected a tritium pressure of 10^{-4} Torr for the point design to ease the burden on the extraction system. At this pressure and 500°C, the pumping rate for recovery of 40 g/day of tritium is 5.3×10^{5} liter/s and the vacuum system cost is low, about $100,000. This pressure will require a confinement system that reduces the tritium permeation through the heat exchanger by a factor of $\sim 10^{5}$. Use of double-walled tubes in the heat exchanger are expected to be able to provide a barrier of this magnitude.

The parameters for the preliminary point design of the tritium recovery system (TRS)--using vacuum pumping at a tritium pressure of 10^{-4} Torr--are given in Table 3-19. With a Li-Pb flow rate about 1.4×10^{5} kg/s, the tritium flow rate is 7.1×10^{-5} kg/s. To extract tritium at the breeding rate of 6.8×10^{-6} kg/s, 9.6% of the tritium must be removed. The extractor is assumed to remove 44% of the tritium. Therefore, 22% of the Li-Pb must be continually diverted to the TRS.

At 500°C the vapor pressure above the eutectic corresponds to $P_{Pb} = 1.4 \times 10^{-5}$ Torr and $P_{Li} = 3.7 \times 10^{-7}$ Torr. In the vacuum system, both lithium and lead will be transported from the alloy in the ratio of their vapor-phase composition, at transport rates of 2.8×10^{-8} kg/s and 3.3×10^{-5} kg/s, respectively. Cooled surfaces will be used to trap the lithium and lead vapors before they can reach the cryopumps.

There are several possible ways of creating favorable transport conditions in the liquid metal to allow for tritium removal by vacuum: large-surface-area pools, pools with agitation or gas sparging, or a thin stream or droplet spray introduced into the vacuum vessel. We are currently comparing these methods for extraction capability, heat loss from the liquid metal, and simplicity of design. The following are some preliminary assessments and calculations for various extraction schemes.

3.14.5.1 Degassing from Liquid Metal Pools. The steps for transporting tritium gas from a liquid metal pool are:[32]

1. Transport from the interior to the interface of the metal. This occurs in liquids by convective transport processes in the interior to a zone near the surface and from there by diffusion to the interface.

2. Transition from the dissolved state to the adsorbed state at the surface.

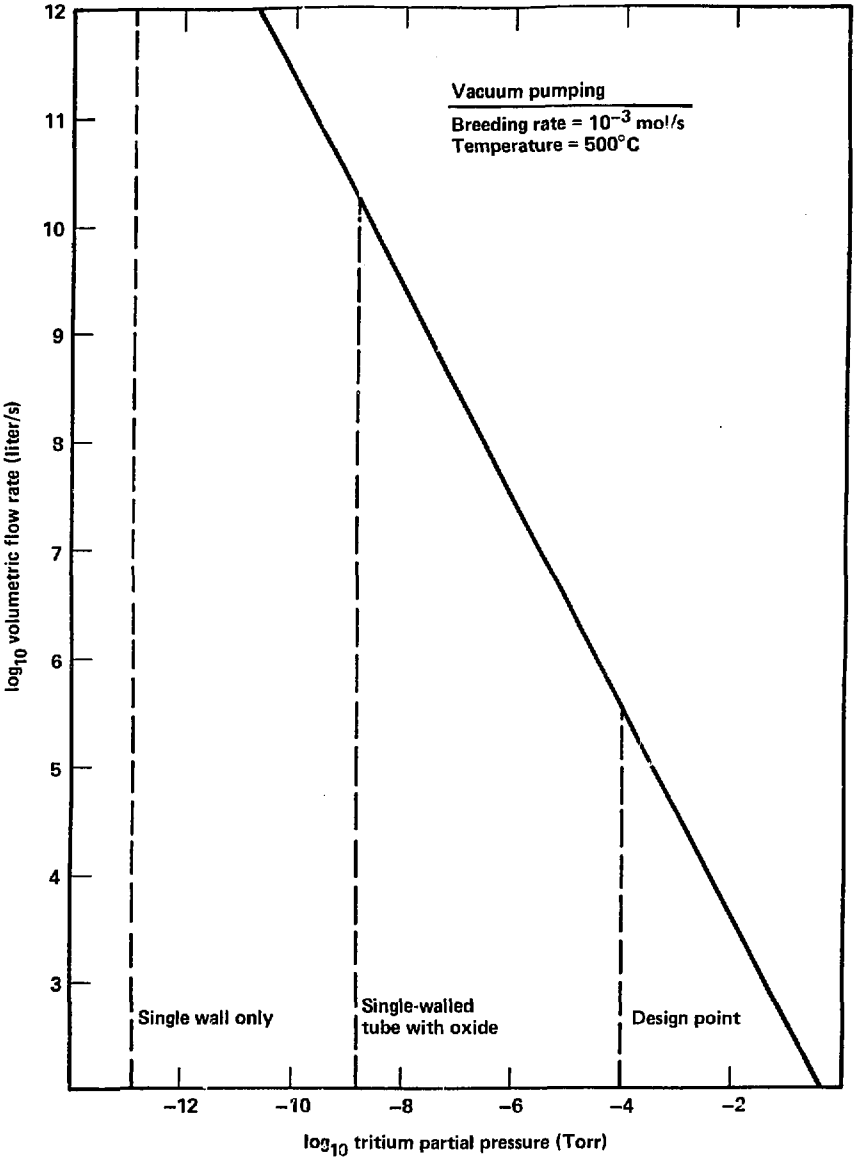

Fig. 3-35. Volumetric flow rate for tritium extraction by vacuum pumping at various tritium partial pressures.

Table 3-19. Point design parameters for tritium removal system by vacuum pumping.

Parameter	Value
Tritium removal rate (g/day)	40
Vacuum pumping speed at 10^{-4} Torr and 500°C (liter/s)	5.3×10^{5}
Tritium removed (%)	44
Li-Pb sent to extractor (%)	22
Li-Pb flow rate into extractor (kg/s)	3.1×10^{4}
Extraction temperature	500°C
Tritium inventory in pumps (g)[a]	49
Inlet tritium conditions	
Pressure (Torr)	1×10^{-4}
Concentration (wppm)	5.1×10^{-4}
Outlet tritium conditions	
Pressure (Torr)	3.0×10^{-5}
Concentration (wppm)	2.8×10^{-4}

[a]Two hours on-line.

3. Association of gas atoms in the adsorbed layer with each other to form molecules.

4. Desorption of molecules from the surface.

5. Diffusion of gas molecules into the gas space and removal by the pumping system.

Step 1, transport in the liquid phase, determines the rate of the entire process. Because mass transport in the liquid interior is by convection, then generating additional convection in the pool with a stirring coil or an inert gas purge improves performance. The key parameter is the mass transfer coefficient β, which is not known for hydrogen in $Li_{17}Pb_{83}$. Known values of 3.9×10^{-2} cm/s for hydrogen in liquid aluminum at 700°C and 1 cm/s for hydrogen in liquid steel at 1600°C give an idea of the order of magnitude.[30,34] The mass transfer coefficient can also be determined from the diffusion coefficient and boundary layer thickness, which are themselves unknown. An estimate gives $\beta = 1$. Experiments and further calculations are necessary to determine the value for the mass transfer coefficient.

Figure 3-36 shows the dependence of β on the extraction system parameters. For $\beta \lesssim 10^{-1}$, the extraction system requires high surface

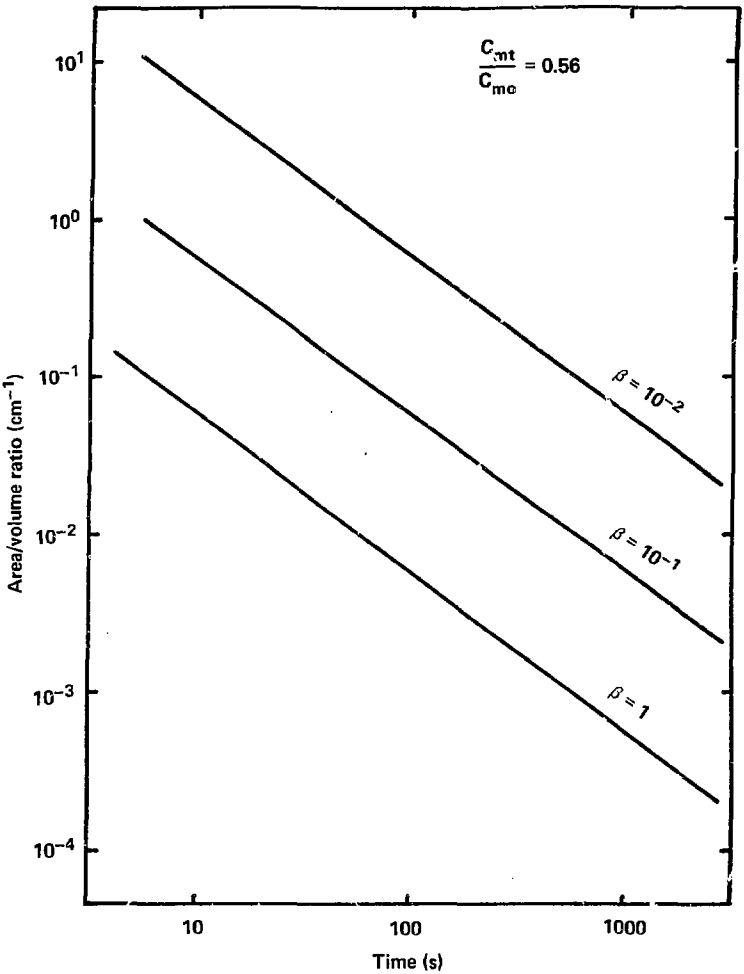

Fig. 3-36. Effect of the mass transfer coefficient β on area-to-volume ratio and the residence time for liquid metal degassing.

area-to-volume ratios for residence times of $\lesssim$100 s. An extraction system that creates a large surface area, such as a droplet spray, would be an alternative to creating large thin pools. If $\beta \approx 1$, then the ratio of area to volume is low enough to create a reasonably sized pool for residence times $\lesssim$100 s. Table 3-20 gives an example of the parameters for a pool degassing system with $\beta \approx 1$.

Table 3-20. Vacuum extraction from a liquid-metal-pool by vacuum pumping with stirring.

Parameter	Value
Mass transfer coefficient (cm/s)	1
Residence time (s)	100
Mass of Li-Pb in extractor (kg)	3.1×10^6
Tritium inventory in Li-Pb (g)	1.6
Pool dimensions	
Radius (m)	7.8
Height (m)	1.7
Surface area (m^2)	1.9×10^2
Volume (m^3)	3.3×10^2

3.14.5.2 Gas Sparging. The use of a scavenging gas has two important effects on mass transfer. First, it provides an increased surface area available for release; second, it causes agitation of the melt. Tritium is removed from the bulk of the liquid by diffusion into the gas bubbles and from the surface by the mechanism described in Sec. 3.14.5 of this volume. Surface losses may be increased because of the increased surface area caused by the boiling action of the bubbles.

We developed a simplified model to give a preliminary assessment of the purge gas requirements for tritium removal from the base design. The total tritium lost from the system is the tritium removed by transport into the gas bubbles and the tritium that diffuses from the surface. The tritium that enters the bubbles is calculated by assuming that the mass transfer into the bubbles is perfect and, therefore, that the bubble is always saturated at the equilibrium tritium pressure. This assumption should give the most optimistic result.

Table 3-21 shows the inert-gas flow rate required to remove various amounts of T_2. The amount of tritium removed from the bulk by the inner gas is small unless relatively large purge-gas flows are used; tritium losses from the surface dominate at low flow rates. Tritium can be separated from helium at a molar ratio of 10^{-4}; however, to avoid this separation process we did not use the helium purge in the baseline design.

Table 3-21. Removal of tritium from the bulk of the melt with an inert gas purge.[a]

% T_2 removed	Moles T_2/s removed	Volumetric flow rate (liter/s)[b]	Purge rate (g He/s)
100	1.1×10^{-3}	2.2×10^{8}	190
10	1.1×10^{-4}	2.2×10^{7}	19
1	1.1×10^{-5}	2.2×10^{6}	1.9
0.1	1.1×10^{-6}	2.2×10^{5}	0.19

[a]Does not include surface losses, which may be dominant.
[b]The volumetric flow rate of helium is calculated at 450°C and 10^{-2} Torr.

3.14.5.3 Stream Degassing. In stream degassing, the liquid metal is forced through a nozzle to form a stream of droplets that fall from a predetermined height into a pool. The height of fall and dwell time are minimized to reduce heat losses. We have studied the rate of diffusion from a spherical droplet in a vacuum and the time of fall.[36]

Table 3-22 shows the amount of gas liberated from falling drops with radii of 1 to 3 mm for fall times of 0.5 to 1 s. The desired value of 44% removal can be achieved for fall times slightly greater than 0.2 s with radii of 1 mm. Some degassing will also occur in the pool at the bottom of the chamber. This process can achieve a high degree of degasification in a short time period and, therefore, it appears to be the superior method. We are continuing to study the design of this system.

Table 3-22. Gas liberation from droplets during stream degassing.

	% gas liberated Time of fall (s)		
Drop radius (mm)	0.2	0.5	1.0
1	0.42	0.60	0.77
3	0.15	0.24	0.32

3.14.6 Tritium Isolation

The secondary and tertiary containment systems minimize personnel exposure to tritium and environmental effects of tritium by preventing tritium from escaping by permeation, leakage, or system malfunction. Containment systems have been developed for the Tritium Systems Test Facility at Los Alamos National Laboratory and other tritium facilities, and should be well-established on the time scale for a commercial fusion reactor.

We are particularly concerned about tritium losses from systems containing Li-Pb at high tritium partial pressures of 10^{-4} Torr. This problem is especially critical in the heat exchanger. In the central cell tritium that permeates through the blanket tubing is pumped by the reactor vacuum system along with the exhaust gases. The tritium extraction unit and liquid metal holding tanks will have thick, well-insulated walls to prevent heat loss and reduce tritium permeation. Large-diameter thick-walled well-insulated piping is used to transport the Li-Pb. In addition, aluminum sleeves can be used to provide a secondary containment barrier around the pipes. Additional jacketing or glove boxes can be used to enclose valves or other components where leakage may occur.

3.14.7 Tritium Control in the Reactor Hall

Tritium will enter the MARS reactor-hall atmosphere either as the oxide or as molecular tritium. It can enter the hall as a result of accidents, normal process leaks such as helium (T_2O) from piping, Li-Pb leaks containing molecular tritium (T_2), and permeation losses from molecular tritium inventories. In any event, the tritium-control process in the reactor hall must recover tritium that exists as T_2O, HTO, T_2, and HT.

The tritium recovery process that accepts T_2O and T_2 as feed is called catalytic oxidation/adsorption. It is shown in Fig. 3-37 with minor modifications.[37] In the process, the reactor-hall atmosphere is accepted and compressed to approximately 405 kPa (3 atm). The compressed gas is heated and passed through a catalytic recombiner where molecular tritium (or HT) is oxidized to T_2O (HTO). The gas exiting the catalytic recombiner is cooled and refrigerated to 275 K (2 °C) to condense water. The condensed water is drained from the process and this is essentially the only recovered-water exit from the process. The dried gas from the refrigerated dryer then passes through a molecular-sieve bed to remove more water. At the exit of this bed, steam is added to the process gas and the gas is passed through a final molecular sieve bed. The steam is added to allow a larger fraction of the tritiated water to be recovered. By increasing the dew point of the process stream before it reaches the final molecular sieve bed, a larger percentage of the water entering this bed can be recovered. Because the tritiated water and the added steam will be well-mixed, the same percentage of steam and water will be recovered. If the steam were not added, the potential for mass transfer of the water would be relatively low and thus its percentage of recovery would be low. The exiting gas from the last molecular sieve bed is vented to the stack or returned to the reactor hall. The molecular sieve beds are regenerated with hot process gas and the regeneration exhaust is recycled to the entrance of the process. The unit capital cost of this catalytic oxidation/adsorption process is estimated to be \$690,000 per 30 m^3/min.[37]

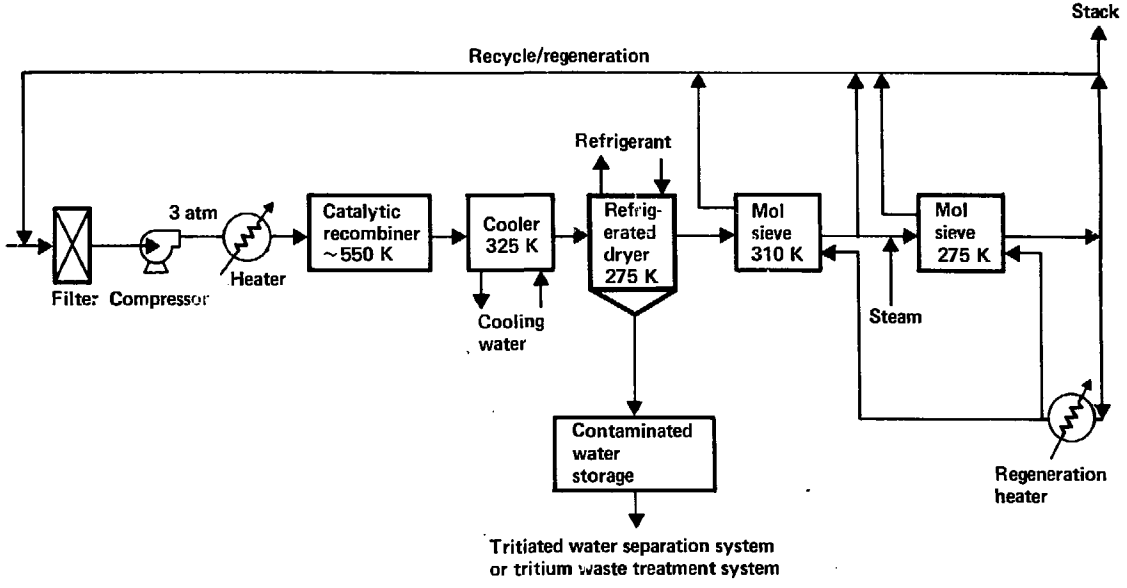

Fig. 3-37. MARS reactor-hall tritium recovery by catalytic oxidation/adsorption.[1]

To estimate the number of catalytic oxidation/adsorption units required to control the tritium concentration in the reactor hall, it is necessary to assume values for certain independent variables. The reactor-hall volume is assumed to be on the order of 1.2×10^6 m^3. An instantaneous tritium input of 6.46×10^4 Ci is assumed from the helium loop (approximately one-third of the recirculating inventory for the base case T_2O/helium loop because the total loss of pressure in the helium loop can be prevented by isolation valves). The system cleanup objective is assumed to be a reactor hall tritium concentration of 500×10^{-6} Ci/m^3 in 14 days (i.e., bubble suit protection). Assuming the reactor-hall atmosphere to be well mixed, the tritium concentration as a function of time will be $C/C_0 = \exp[-vt/V]$, where C_0 is the time = 0 concentration, V is the reactor hall volume, and v is the total feed rate capacity of the catalytic oxidation/adsorption process. Our assumption that the steam and water are well-mixed ignores tritium adsorption on the surfaces of the reactor hall. The required catalytic oxidation/adsorption flow rate for our assumptions is 280 m^3/min, or 10 units. Scaling directly at \$690,000 per unit yields a total cost of $\$6.9 \times 10^6$. We anticipate that the total cost for the capacity required will scale to some power less than unity. Therefore, because our assumptions are only preliminary and because of the lack of construction experience in this area, the stated cost should be regarded as an upper bound.

We still have to address the issue of the validity of the assumptions used in sizing the process equipment for the reactor hall. This equipment is well understood and in an advanced state of design and testing.[37] However, to determine equipment requirements, a range of material balance conditions must be provided. For this particular case, we must quantify tritium input to the reactor hall atmosphere by way of normal process leaks and potential accidents. We also need to specify the acceptable steady-state tritium concentration in the reactor hall atmosphere and the allowable time to attain a specified tritium concentration after accidental release.

3.15 CORROSION PRODUCT REMOVAL

Corrosion problems in liquid metal loops are usually most severe on the cold side, where corrosion products precipitate and can clog steam generators and valves. This problem can be dealt with in several ways. In the steam generator, heat transfer to the tube walls will occur faster than mass transfer, causing a super-saturated solution of the corrosion products in Li-Pb. The addition of particulates will cause most of the corrosion products to precipitate out in the flowing stream (rather than on the tube walls), allowing them to be removed by filtering, magnetic separations, and other methods. Alternatively, it may be possible to keep corrosion product concentrations to fairly low levels by removing them on chevrons at the cold side of the loop. The static test data (see Fig. 3-20) indicate that it will take about 1000 hours to reach saturation at 500°C. Because this is a long time compared to a single loop through the system, it may be possible to remove corrosion products in a slip stream, keeping concentrations in the Li-Pb to acceptable levels. Another method of controlling corrosion is to add a corrosion inhibitor to the Li-Pb.

Without improved measurements of the corrosion rates it is difficult to choose an appropriate control method or to determine if corrosion control is needed. We are currently working to quantify and further define some of the concepts mentioned above. At present it appears feasible to use Li-Pb with HT-9 at 500°C.

3.16 BLANKET MAINTENANCE

3.16.1 Maintenance Philosophy

The objective of the blanket module maintenance system on MARS is to minimize machine down-time for both normal and abnormal events while safely removing and replacing the blanket modules. Remote, manual, and automated handling methods will be used depending on radiation levels and the task. Because blanket replacement is a scheduled yearly maintenance operation, we are expending considerable effort to design the modules and module handling systems for rapid removal and replacement. The use of remote techniques increases the time required to perform any task. Although good component design for remote handling can lessen maintenance time, it cannot compare with normal manual servicing. Therefore, it is prudent to maximize the number of operations that can be performed "hands-on." Maintenance time can be reduced by increasing shielding in certain high-maintenance areas, but the cost of additional shielding must be compared with the cost of providing for remote maintenance procedures. The availability of the machine is maximized by moving a small number of large integral units on a fixed-rail or roller system. The number of operations, their complexity, and the cost of equipment are also reduced. This technique has been used successfully in ship building programs to decrease construction time. All central cell components are designed for rapid replacement. Failure of any component, including a central-cell superconducting magnet, will not result in excessive downtime.

In general, blanket module components weighing several hundred tons or less will be handled with an overhead (gantry) crane. Heavier items will be moved on a track or roller system specifically designed for and incorporated into the MARS facility. The use of several mobile transporters will eliminate the need to have a transport system built into each of the 24 modules, which produces a considerable cost savings and a less complex machine. In such a system, access to the modules must be provided. Consequently, services lines, main coolant piping, and bus systems must approach the machine from one side and from the top of the machine. Disconnection and reconnection of these connections could be done by hands-on maintenance.

A separate blanket maintenance cell must be provided in addition to the machine containment area for module repair work. This cell will be capable of handling enough modules simultaneously to allow six blankets to be repaired within the 1-year period between changeouts. This area will be sealed from the main reactor containment cell following module replacement to allow replacement work on the blanket structures to proceed during machine operation. Each of the hot bay areas will be equipped with overhead cranes for handling large components. Manipulator systems will be provided where required for disassembly operations, and specialized equipment and fixtures will be included.

Structural components removed from within the modules will be highly radioactive. These structures must be prepared for shipment off-site in shielded containers or for on-site storage. High level waste requiring off-site storage will probably be compacted to permit easier and more economical packaging. It may also be possible to dilute wastes for on-site low-level storage. To accomplish this, a waste preparation area has been included in the maintenance area. This area would be equipped to further disassemble and cut up the activated structures by totally remote means. A packaging and package decontamination area will also be provided.

3.16.2 Blanket Module Changeout Procedure

We have developed a preliminary removal and changeout procedure for the high temperture blanket. At this stage in the study, the purpose of outlining the procedure is to establish an overall approach and identify problem areas. Timelines are illustrated in Figs. 3-38 and 3-39.

Module removal will require remote shutdown and manual and remote disconnect operations. Initial remote shutdown operations include:

- Shut plasma off,
- Achieve magnet current rampdown,
- Remove afterheat removal and anneal structure,
- Return system to atmospheric pressure,
- Install temporary shielding.

The first wall and adjacent structures will be sufficiently radioactive to produce significant afterheat for the first day after shutdown. Modules not scheduled for replacement will require 60 hours of annealing at 450°C to lower the ductile-to-brittle transition temperature. Modules being replaced will also be annealed to ease handling, and slowly circulating Li-Pb will be used to remove the afterheat and anneal the structure. Coolant lines will be disconnected remotely because of the tritium hazard. The joint areas may be bagged to reduce tritium exposure, and temporary shielding may be required in certain areas to further reduce radiation exposure.

At least two days after shutdown, activation levels in the outer shield materials will have decayed enough to allow maintenance teams to enter the reactor central cell area. Six work teams will begin preparing the six modules to be removed. Hands-on operations performed during this time are:

- Drain and purge main coolant systems,
- Disconnect structural attachments,
- Position transhaulers,
- Disconnect main coolant lines,
- Disconnect magnet and other service lines.

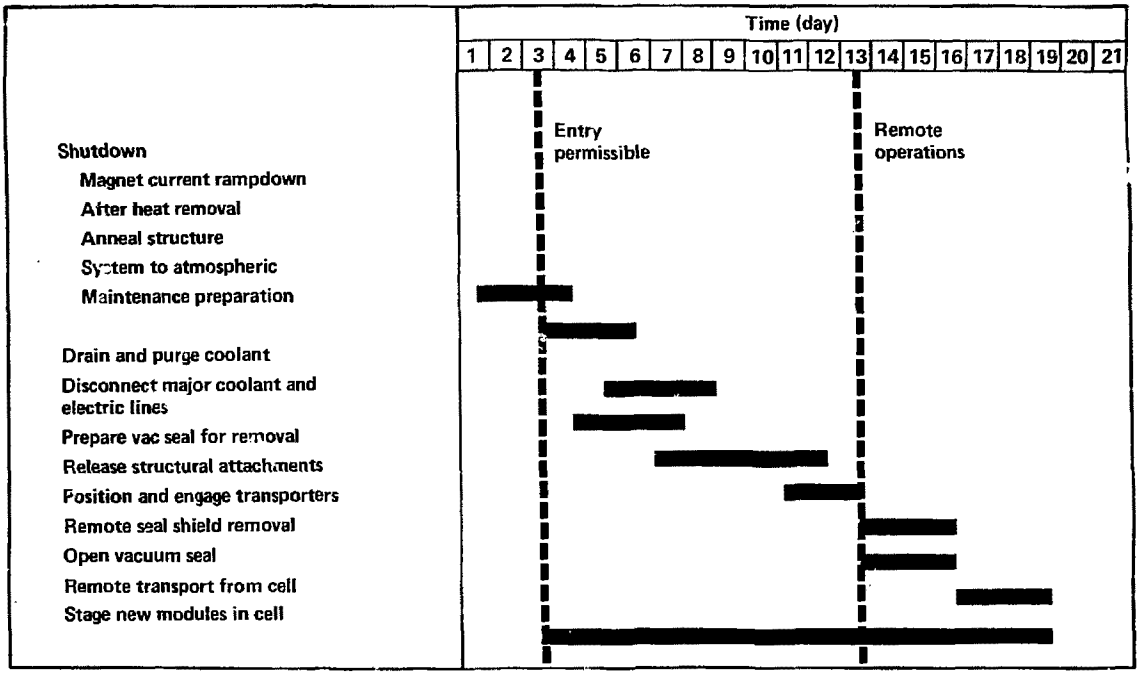

Fig. 3-38. Module removal time estimate.

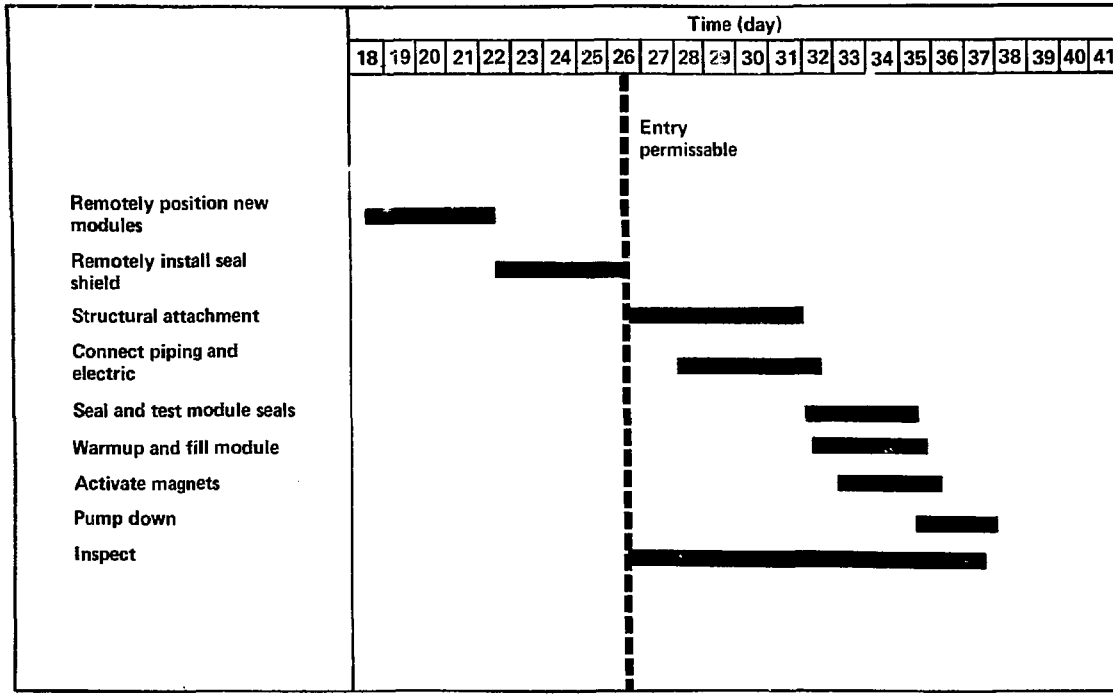

Fig. 3-39. Module replacement time estimate.

The area will then be cleared of personnel so the activated blanket modules can be moved. Remote operations performed before the modules are rolled out include:

- Open vacuum seals,
- Remove seal shields,
- Remove temporary shielding as necessary.

The modules will then be removed on six transhaulers each and replacement modules will be brought into place. Installation and startup tasks are essentially the reverse of shutdown and removal as follows:

- Remote operations--
  - Install seal shielding,
  - Install temporary shieldin .
- Manual Operations--
  - Prepare final positioning and clampdown,
  - Seal main coolant lines,
  - Connect services,
  - Close vacuum seals (remote inside shielding),
  - Complete testing of seals and diagnostics.
- Startup--
  - Ramp up magnet current,
  - Warm up and fill modules,
  - Pumpdown,
  - Inject plasma.

Interfacing central-cell maintenance operations with end-cell and balance-of-plant maintenance procedures has not been addressed. Systems will be needed for removing tritium from the helium and Li-Pb loops and for removing tritium-contaminated equipment. End-cell and balance-of-plant maintenance will be very similar to that of the MARS electric plant.

3.16.3 Equipment Requirements

The major equipment in the reactor compartment will be six manipulator/crane gantries for use on each of the modules to be removed. These will be sized for the seal shielding, which at present is the heaviest object to be handled.

Transporter units for the modules must have approximately a 1500-ton capacity. In addition, the transporters must be remotely controllable. They must also be capable of negotiating a 90-deg turn with the module aboard. This is required to minimize building size. Finally, to precisely align the module in its opening, the transporter must be capable of lateral load movement.

Maintenance hot bays will be equipped with 200-ton bridge cranes to disassemble the components from the modules. Manipulators will be located at appropriate intervals along the bay walls for remote disassembly.

3.16.4 Transhauler

The modules will be transported to hot cells for maintenance on the small-rail transhaulers shown in Fig. 3-40. These transhaulers, capable of 250 tons of lift, are currently used by General Dynamics Electric Boat Division to move submarine components, and by Kawasaki Heavy Industries in Japan to move ship components.

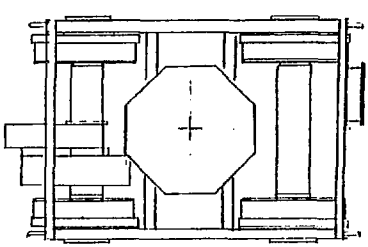

Current design

MFG	— Western gear
Capacity	— 250 tons
Drive	— Electric (2 ft/min)
Lift	— Hydraulic (¼ in./min)
Direction orientation	(90-deg rotation—manual)
Cost	— $75K (1980 dollars—60 units)

Modification required

Automate direction orientation

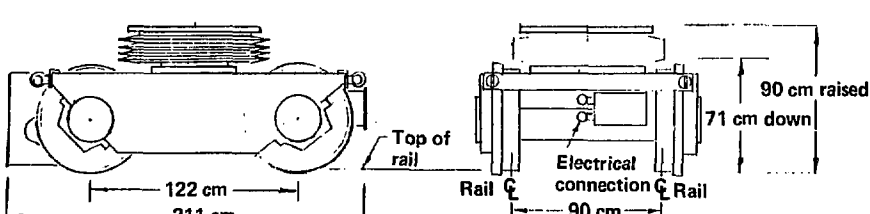

Fig. 3-40. Transhauler.

Manufactured by Western Gear at a 1980 cost of $75 K, the transhaulers are remotely controlled and are capable, along embedded rails, of speeds up to 2 ft/min and a 90-deg change in direction. When modified, the speed can increase to 20 ft/min; orientation of the transhauler to allow the 90-deg change in direction can be accomplished remotely. The six units required for each module can be simultaneously remotely operated in all movements.

3.17 BLANKET MODULE MANUFACTURING

Manufacturing engineering has been incorporated in the design of the high temperature blanket. This is vital to ensure that the design can be constructed without resorting to high cost or undeveloped techniques. Design details such as baffles to control MHD flow have not been included here but are not expected to have a significant impact on manufacturability. The following components make up the blanket module.

3.17.1 Primary Shield

The shield components can be fabricated with state-of-the-art manufacturing processes, as illustrated in Fig. 3-41. The inner and outer skins will be plasma arc-cut to near-net dimensions and the oxide surface that is generated by burning will be removed by hand-grinding during fitting for welding. The 2-in.-thick skins will then be rolled to their respective diameters and trimmed to size. Before the inner skin is rolled, the Li-Pb access ports will be machined into the inboard edge of the skin. The pod attach-rail details will be machined completely, including weld preparation.

3.17.2 Shield Subassembly

The manufacturing procedure for the shield subassembly is also shown in Fig. 3-41. The inner skin will be welded together to form a cylinder. On this skin the inner structural rings will be located and welded in place. The outer skin pieces will be attached and welded. The assembly will be complete when the pod rails have been welded in place. This operation will require a weld fixture to hold the rails in position during the tack and first pass weld. All other operations at this point will use shop and manufacturing aids for support during assembly.

A specialized subcontractor will construct the forged torus ring, which will be delivered complete with edge-weld preparation. Two rings that provide room for welding at assembly will be welded to the inner and outer rims of the forged torus. The torus ring will be ultrasonically inspected before welding, and x-ray and dye-penetrant inspection will be performed after welding. A flanged structural ring will be made up of segmented plates and a rolled ring. This welded subassembly forms one of the Li-Pb walls.

3.17.3 First Wall

Figure 3-42 illustrates the components and assembly of the first wall. The first wall subassembly will contain a bore, a Li-Pb flow diverter, and a skin. The bore will be rolled and welded to size and then the flow diverter

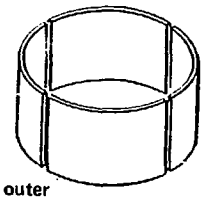

Shield outer skin

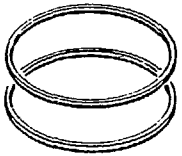

Shield structure rings

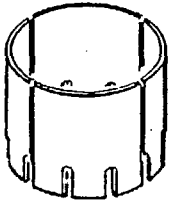

Shield inner skin

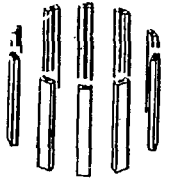

Pod attach rail receivers

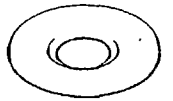

Torus ring

Inner weld adapter ring

Outer weld adapter ring

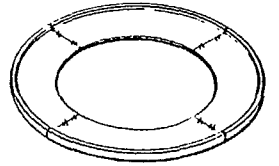

Flanged structural ring welded assembly

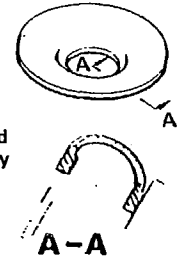

Torus ring welded assembly

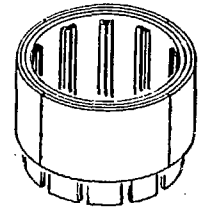

First weld assembly skins, rings and rail receivers

Fig. 3-41. Shield components.

will be resistance-welded to its outer diameter. The flow diverter will be made in segments and the channels will be die-formed. The inner skin will be made up in segments and resistance-welded to the flow diverter and then the longitudinal seams will be welded.

3.17.4 Shield Major Assemblies

Because of weight and size considerations, an optimum assembly site will be selected before the subassemblies are further married. Up to this point in the fabrication sequence the components and assemblies will have been built "in-plant." The weld assembly for the structural shield ring will receive the torus ring and flanged ring weld assemblies for welding (see Fig. 3-41). One shield half will have the first wall assembly positioned and welded in place, and it will then be ready to receive the pod assemblies (see Fig. 3-42).

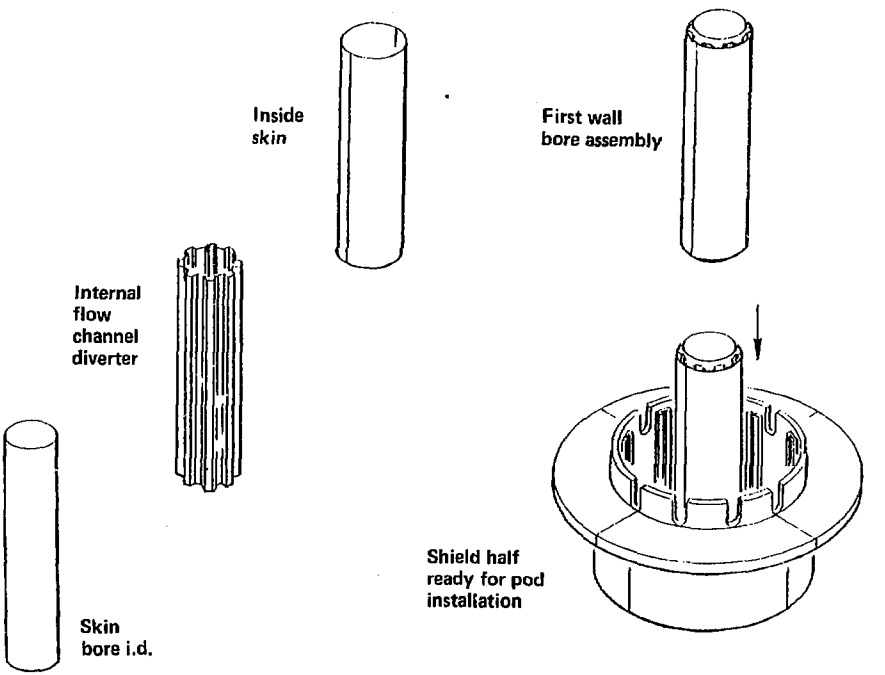

Fig. 3-42. First wall assembly.

3.17.5 Silicon Carbide Components

Cast SiC is as easy to work with as metal castings. Dimensions are accurate, detail is precise, and complex shapes can be achieved without difficulty. Generally, cast shapes are used as-produced. The material is far too hard to be conventionally machined. The sizes of the individual parts being produced today may range up to 1.2 m in length, 1 m in diameter, and from 6 to 10 mm in wall thicknesses. Some parts can be made with wall thicknesses of up to 76 mm, depending on the part configuration. Larger parts can be made by temporarily bonding separate pieces. These bonds must maintain integrity during assembly only and are not required to withstand high temperatures. These parameters fit the MARS components.

The SiC pod support panels will be bonded in place on the helium circulating tubes and this assembly will be bonded to the pod's SiC skin. After the ends are bonded in place, the pebbles will be placed in the cavity. Bonding the top in place will complete the SiC assembly (shown in Fig. 3-43).

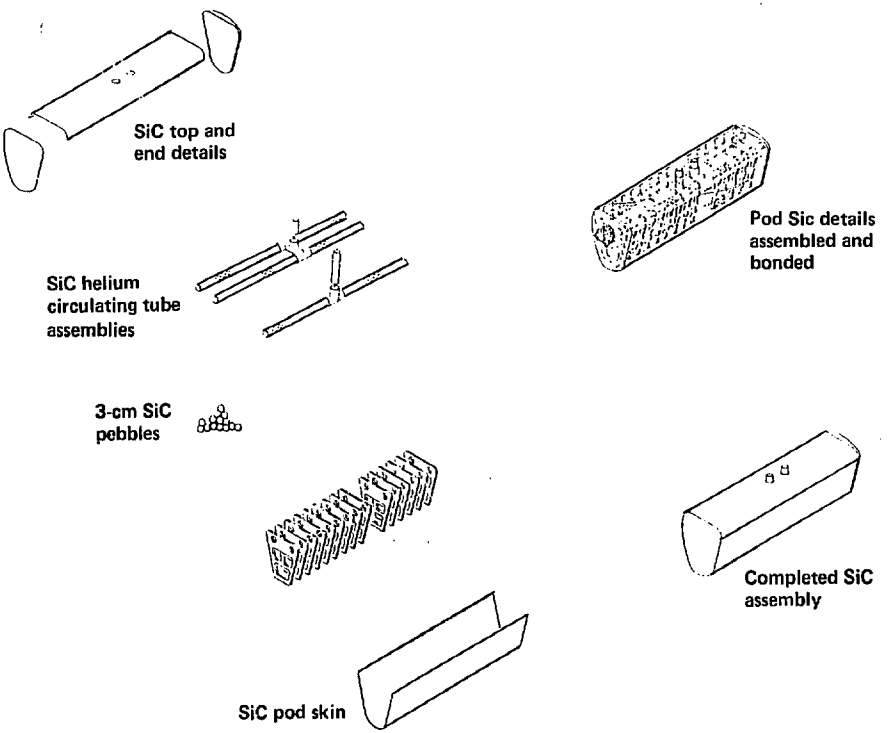

Fig. 3-43. Silicon carbide components.

3.17.6 HT-9 Pod Details and Assembly

The pod skin detail will be stretch-formed and the end pieces will be die-formed. The upper skin will also be die-formed, drilled, and machined to final size. The tubes and collars will be procured components. The pod interface panel will be a resistance-welded subassembly. The number of these parts required for MARS would qualify them for rate tooling.

The SiC assembly will have ceramic pedestals and ceramic felt bonded to its skin before it is assembled into the HT-9 pod. All the HT-9 details will be fitted to the pod and welded in place. After the tubes, collars, and doublers are welded in place, the completed assembly will be heat treated and tested (see Fig. 3-44).

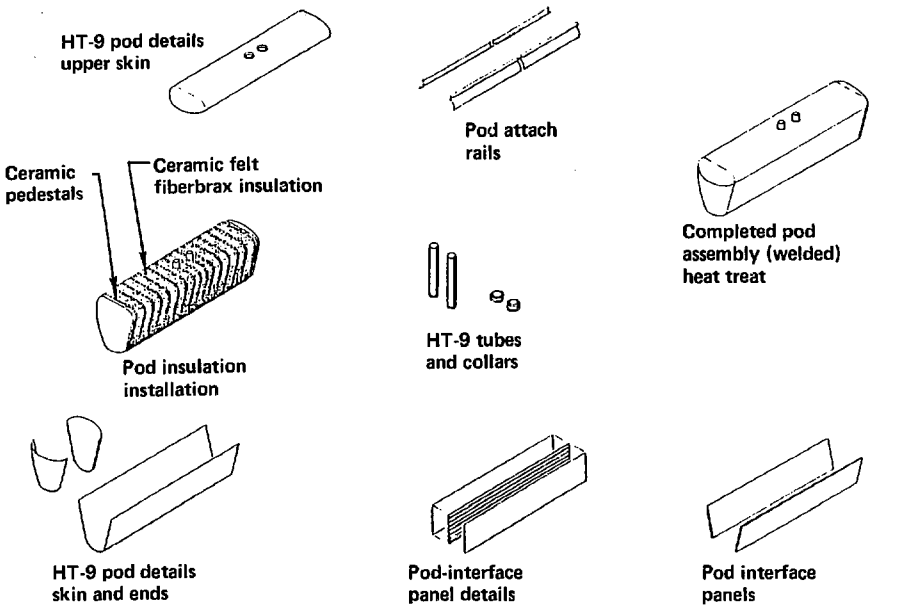

Fig. 3-44. Pod assembly.

3.17.7 Major Mating of the Blanket Assembly

Each pod assembly will be aligned and lowered in place in the shield rail guides. The pods will be locked in place by inserting Li-Pb separtion plates in the pod railkey slot. These plates will be tack-welded in place with each pod. Pod separation panels will be inserted between each pod and tack-welded in place (see Fig. 3-45). After all the pods are in place, the Li-Pb separation plates will be completely welded.

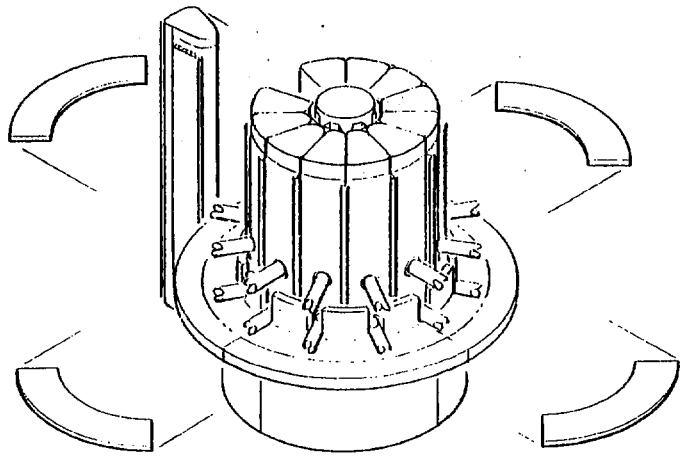

Fig. 3-45. Pod installation.

The second shield half will be brought to the assembled shield and lowered in place. To provide for "down-hand" welding, the mated assemblies will be rotated to horizontal and placed on a suitable weld positioner. The two halves will then be welded together at the Li-Pb separation plate (see Fig. 3-46). A close-out weld at the torus ring to first wall is also required.

The Li-Pb plenum chamber close-out plates, having been previously detailed, rolled, sized, and drilled, will be ready for installation over the helium tube roughouts. These plates will be welded to the Li-Pb separation plates and the wall of the flanged structure assembly. Weld collars will be placed over the helium tubes and welded to both the close-out plates and the tubes. This closes out the Li-Pb chamber. See Fig. 3-47 for an illustration of this process.

The helium manifold consists of tubes, flanged collar assemblies, and sleeves. A box assembly containing the helium disconnect is also a part of this assembly. The tubes will be rolled to shape, cut off to size, and ported with oversized holes. The collar assemblies will be made with large skirt doublers attached to a tube that is sized to slip-fit over the helium tubes. The collars will first be slipped over the tubes, which will be too long in a rough-out configuration. The detailed manifolds will be brought to the rough-out tubes and the assembly will be measured to determine the required length. The tubes will then be cut to length and welded in place both to the manifold and the tube. After all the ports of the manifolds have been welded, the sleeves will be located over the manifold joints and welded in place. The sleeves are used to provide for manifold alignment tolerances and size mismatch. Leak and pressure tests will be performed when the welding is

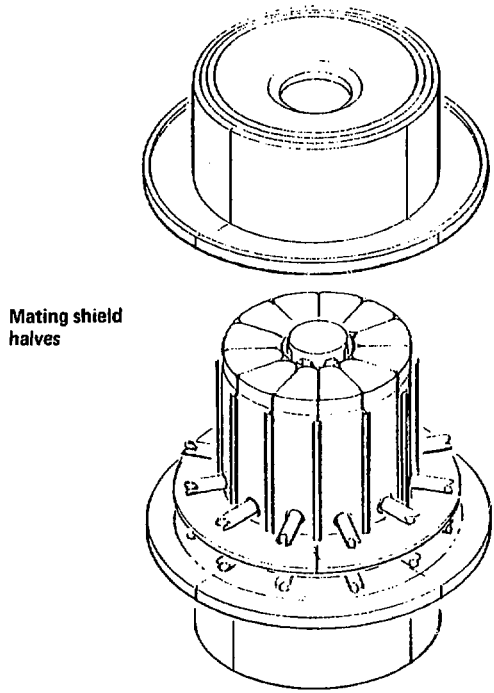

Fig. 3-46. Shield half assembly.

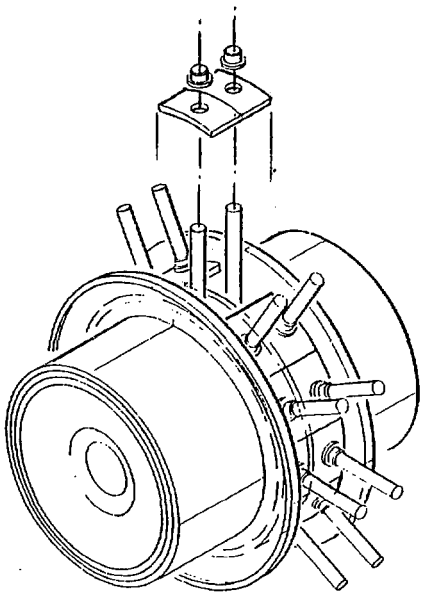

Fig. 3-47. Assembly rotated for downhand welding.

completed. Details and installation procedures are illustrated in Fig. 3-48. Two sump assemblies will be welded between the helium manifolds for the inlet and outlet of the Li-Pb.

The blanket and shield will be complete at this point and ready for installation on the module support structure.

3.18 ALTERNATE HIGH-TEMPERATURE BLANKET CONCEPT

This section outlines a preliminary feasibility study of a blanket concept that eliminates the MHD flow uncertainties. Research and experiments currently underway are expected to greatly increase our understanding of MHD pressure drops and velocity profiles in fusion blankets. If MHD flow turns out to present problems in the baseline blanket concept, additional flow baffling will be required, adding structure and increasing the pressure drop and the complexity of the design. The concept presented here is an attempt to maintain positive control with less design complexity and reduced structure.

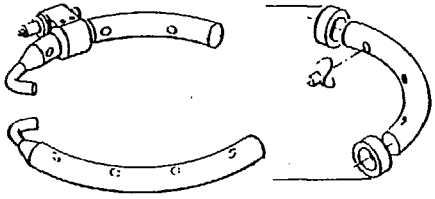

Helium manifold details

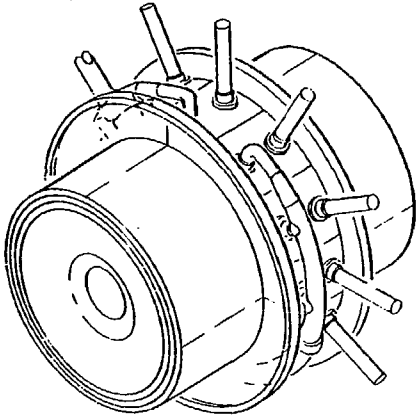

Helium manifold installation and test

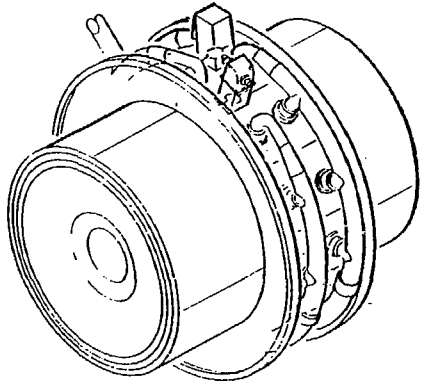

Li-Pb sump installation

Fig. 3-48. Helium manifold detailing.

The potential problems with the baseline design are: stagnation zones, flow control, and distribution caused by large differences in pressure gradients as the flow changes from perpendicular to parallel to the magnetic field, and uncertainty of the velocity profile behind the first wall. The alternate concept eliminates these problems by separately cooling the pods and first wall and by flowing the Li-Pb perpendicular to the magnetic field in high heat flux regions. This ensures relatively well-described Hartmann flow in critical areas and similar pressure gradients in different parts of the blanket. Another advantage arises from containing the Li-Pb in pods surrounding the helium pods and in tubes that make up the first wall. Pressure is reacted by tensile hoop stress in these containers, rather than by compressive stress, as in the baseline concept first wall. This increases flexibility because the design is less sensitive to increases in pressure. For example, we can more easily afford to overcool some portion of the blanket to ensure adequate cooling everywhere.

The disadvantages of the alternate blanket concept are greater void fraction and, if complicated flow baffling is not required in the baseline design, increased complexity. The alternate blanket concept has not received the level of attention given to the baseline blanket design, and other problems are expected to arise under closer scrutiny.

3.18.1 Configuration and Flow Distribution

The alternate blanket concept is basically a combination of the MARS high temperature blanket--helium cooled SiC and $LiAlO_2$ contained in pods--with a tube-bank (11.75-cm outside diameter) first wall similar to the MARS Li-Pd power production blanket (see Fig. 3-49). Lithium-lead enters the top of the module and is distributed to the first-wall tube inlet plenum and to the toroidal plenum that feeds the pods (see Fig. 3-50). The pod walls are cooled from the outside by Li-Pb flowing around the perimeter as shown in Figs. 3-50 and 3-51. Thermal insulation is required between the inlet and outlet toroidal plena and at the back of the pods to reduce thermal stress and recuperation losses. The first wall tubes and the pods both rely on the magnetic field to ensure adequate flow distribution. Very low pressure drops are encountered as the flow moves axially along the module (parallel to the magnetic field) at the back of the pods and in the first wall distribution and collection plena, and much higher pressure drops occur when the flow moves around the pods or through the tube bank perpendicular to the field (see Fig. 3-51). This tends to distribute the flow evenly throughout the first wall tube bank and around the front and sides of the pods. The flow is less predictable in the regions at the back of the pods and in the tube plena, where the flow changes from parallel to perpendicular to the field and vice versa, but heat fluxes are low in these areas and some stagnation is tolerable.

The toroidal entrance and exit plena are tapered to maintain constant flow velocity. This ensures equal flow to all pods and also allows operation at reduced power levels with the same fluid temperature rise by reducing the flow rate. Mixing the exit flow from the pods and first wall requires both temperature and pressure matching. First-cut calculations indicate very similar pressure drops (Table 3-23), implying that temperature and pressure could be matched with minor modification. Alternatively, the flow from the

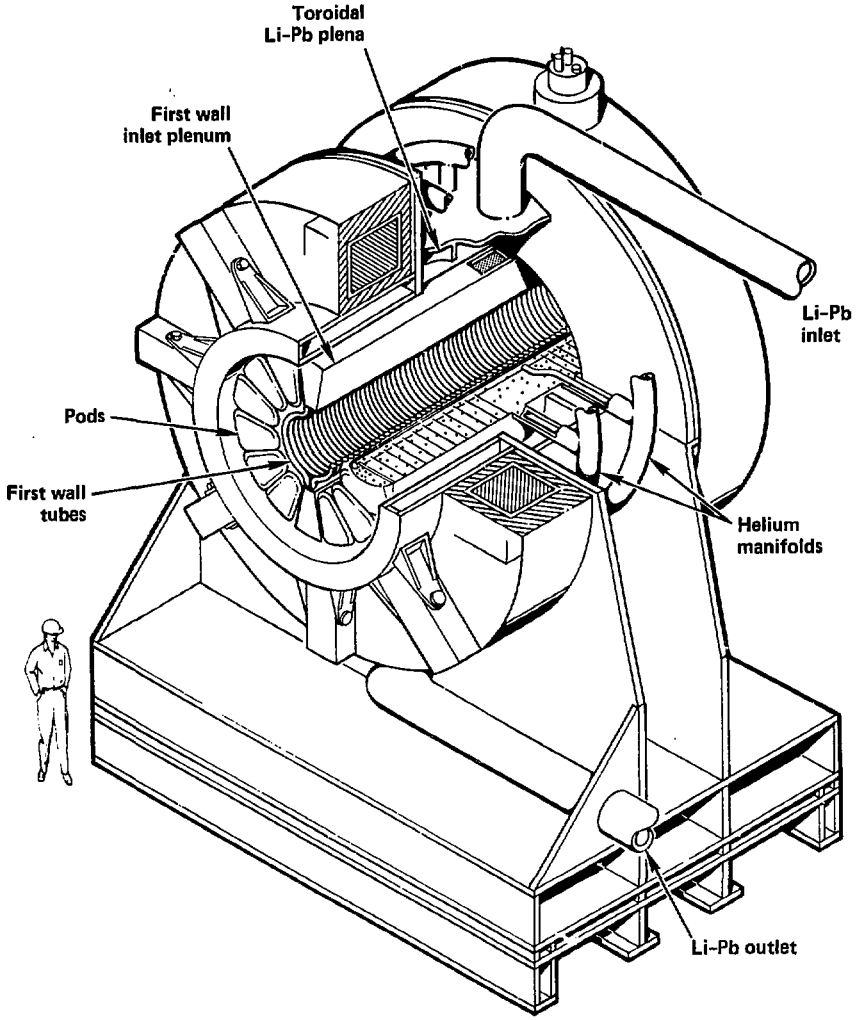

Fig. 3-49. Alternate blanket module.

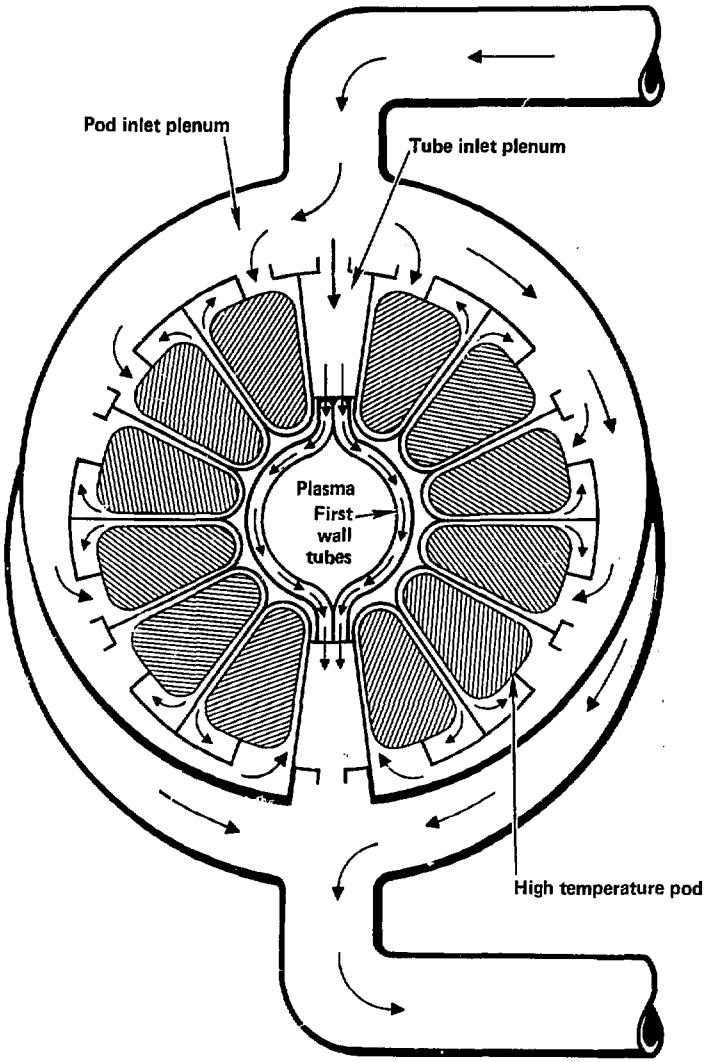

Fig. 3-50. Lithium-lead inlet flow paths.

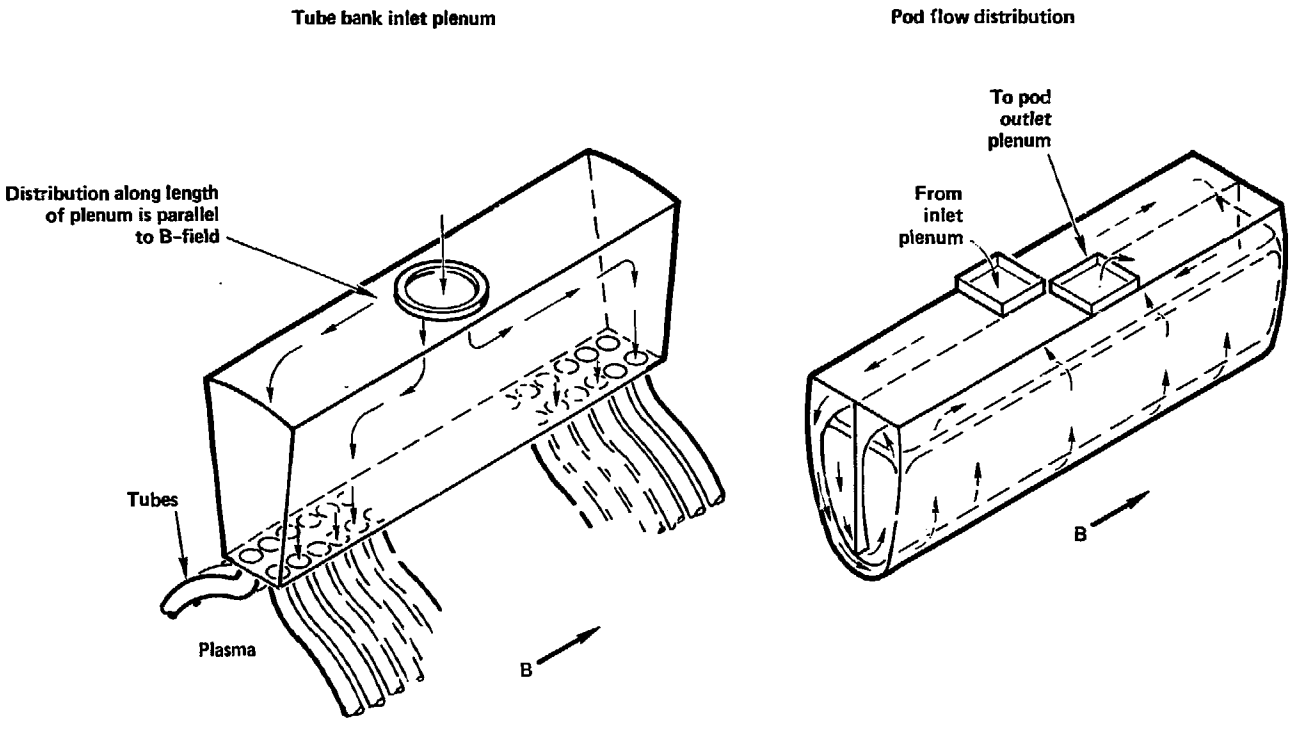

Fig. 3-51. Plenum flow distribution.

two zones could be kept entirely separate until it is outside the blanket, where flow matching could be controlled with throttle valves. The total pressure drop (2.1 MPa) and pumping power (15 MW_{th}) are very close to those of the baseline high temperature blanket.

Table 3-23. MHD summary. Pumping power is 7.29 M^3/s x 2.1 MPa = 15.3 MW.

	Velocity (cm/s)	Channel half (cm)	Wall thickness (mm)	Path (m)	B (T)	ΔP (MPa)
Tubes	23	5.88	3	2.39	4.7	1.1
Around pods	2.9	0.75	11	2.4	4.7	0.97
Inlet and outlet[a]						1.0
Total[b]						2.1

[a]Taken from MARS Li-Pb blanket.

[b]Tube and pod paths are in parallel.

3.18.2 Neutronic Considerations

No neutronic calculations were performed for the alternate blanket concept, but its performance is expected to be similar to that of the baseline blanket. Neutronic parameterizations with the baseline blanket showed that a certain amount of Li-Pb and steel in front of the solid breeder region improved performance (in terms of energy multiplication and TBR), largely because of reduced high energy capture in silicon and neutron multiplication in the lead. Thus, the tube size (11.75-cm outside diameter) was chosen to keep the same volume of Li-Pb and steel in front of the pods as in the baseline high temperature blanket, thereby roughly preserving the neutronic performance. The added void between tubes increases the blanket thickness by about 4 cm. The buckling force on the first wall has been eliminated, resulting in a slight decrease in structural fraction near the first wall: the baseline design has 14% structure from the first wall to the pod wall; the alternate design has 12%.

The materials used in the alternate blanket concept are identical to those used in the baseline blanket, and the material fractions are very similar. Material fractions can be varied by changing the first wall tube size, adding a second tube bank, changing the width of the flow channels surrounding the pods, and changing the amount of $LiAlO_2$ in the solid breeder zone. Performance predictions of the alternate blanket without neutronics calculations are uncertain, but there is enough design flexibility and similarity with the baseline design to ensure adequate tritium breeding and indicate an FHT in the 45 to 50% range.

3.18.3 Magnetohydrodynamic Calculations

Preliminary pressure drop and pumping power calculations were performed based on heating rates for the baseline high temperature blanket and pressure drop values calculated for the MARS Li-Pb power production blanket. Of the total heat deposited in the blanket, 54% was assumed to be removed in the Li-Pb. Of the heat deposited in the Li-Pb (73 MW per module), 89% goes to the first wall tube banks, 6.7% is deposited in the Li-Pb and steel surrounding the pods, and the remaining 4.3% is conducted from the high temperature helium zone to the Li-Pb surrounding the pods. This heating distribution is based on three-dimensional TARTNP neutronics calculations for the baseline blanket design. The calculated pressure drops--assuming 150°C ΔT and Hartmann flow--in the flow paths through the tubes and around the pods are given in Table 3-23. Inlet and outlet pressure drops were taken to be the same as the Li-Pb power blanket.[38] The values are approximate (as are all MHD pressure drop calculations in complex systems using current tools), but they establish the feasibility of this concept in regard to pressure drop. Because the Li-Pb is contained in tubes and pods that resist pressure by tensile hoop stress, much higher pressures can be tolerated. (Higher pressure drops could result from uncertainties in the calculations or from design considerations such as higher velocities for better heat transfer.) The major penalty of higher pressures is increased pumping power, currently 15 MW thermal.

Magnetic field ripple in the blanket region is greater than in the plasma and will significantly affect Li-Pb velocities. Directly under the magnets the field varies from approximately 5.3 T at the back of the blanket to 4.7 T at the first wall, whereas between magnets the field varies from 4.0 T at the back to 4.5 T at the first wall. Flow around the pods, in the first wall tubes, and in the tube inlet and exit plena is effected by ripple. If left unchecked, this ripple causes approximately 30% higher velocities in the regions between magnets. This would result in a 45°C lower temperature rise in the faster moving fluid. It may be possible to operate under these conditions by allowing temperatures to mix at the back of the pods and in the tube bank exit plenum because the change takes place gradually over about 160 cm. However, this will lower the exit temperature if the maximum allowable temperature is kept the same and temperature fluctuations induced in the structure by mixing are hard to predict. Flow rates can be balanced by narrowing the flow areas in the lower field regions around the pods and in the first-wall inlet and exit plena.

Heat transfer in the first wall area is assumed to be adequate because the velocity is slightly higher than in the MARS Li-Pb power blanket (23 vs 19 cm/s).[38] This indicates that the maximum temperature difference betwen the bulk fluid and structure is less than the 50°C reported for the Li-Pb blanket,[38] resulting in a 535°C maximum structure temperature and 520°C maximum structure/Li-Pb interface temperature. Although the velocity is very low (2.9 cm/s) around the pods, conduction in the Li-Pb will keep the film drop temperature well below 50°C unless energy deposition is higher than in the baseline blanket.

3.18.4 Mechanical Considerations

The alternate blanket concept has the advantage, as mentioned above, of supporting the pressures in tensile hoop stress rather than in compression, as in the baseline blanket first wall. However, the concept of combining tubes, pods, and tube distribution plena is complex. Major areas of concern are the pod interfaces with the tube distribution plena as well as the method of connecting the tubes to the plena. Some space (2 to 3 cm) is required between the tube bank and pods to allow for expansion. This would also indicate that a flexible joint at the tube/plenum connections would help relieve stress. These and other mechanical issues require further work, but the concept appears to be mechanically feasible.

3.18.5 Corrosion

Corrosion rates of HT-9 by Li-Pb in a nonisothermal loop are not well known. The results from current corrosion experiments may dictate a lower maximum operating temperature for Li-Pb/HT-9 systems, which would have an adverse effect on hydrogen conversion. Too low a temperature would make it very difficult to supply enough heat to the synfuels process unless the FHT were increased significantly. This remains an open issue for all Li-Pb-cooled designs.

3.18.6 Conclusion

The alternate blanket concept removes the MHD flow uncertainties of the baseline high temperature blanket without requiring complex flow baffling or electrical insulation in the high flux regions. Reacting pressure forces with tension in the structure eliminate buckling concerns. Neutronic performance is expected to be good, and there is considerable design flexibility to match process requirements for helium input/output temperatures and FHT below 50%. Several engineering issues remain to be worked out, but this preliminary study indicates that the basic concept is feasible.

REFERENCES

1. B. Badger et al., Witzmir-I, A University of Wisconsin Tandem Mirror Reactor Design, UWFOM-400 (1980).

2. C. C. Baker et al., STARFIRE - A Commercial Tokamak Fusion Power Plant Study, ANL/FPP-80-1 (September 1980).

3. ASME Boiler and Pressure Vessel Code, Section III, Division 1.

4. H. F. Allen, Analysis and Design of Structural Sandwich Panels (Pergamon Press, New York).

5. R. D. O'Dell, F. W. Brinkley, Jr., and D. R. Marr, User's Manual for ONEDANT, Los Alamos National Laboratory, Los Alamos, NM, LA-9184-M (1982).

6. E. F. Plechatt and J. R. Kimlinger, TARTNP: A Coupled Neutron-Photon Monte Carlo Transport Code, Lawrence Livermore National Laboratory, Livermore, CA, UCRL-50400, Vol. 14 (1976).

7. W. L. Thompson, MCNP - A General Monte Carlo Code for Neutron and Photon Transport, Los Alamos National Laboratory, Los Alamos, NM (1981).

8. C. C. Baker et al., Starfire - A Commercial Tokamak Fusion Power Plant Study, Argonne National Laboratory, ANL/FPP-80-1 (Sept. 1980).

9. E. B. Abrams, A Comparative Study of MCNP and TARTNP Using the TWR Blanket, Lawrence Livermore National Laboratory, Livermore, CA, Memorandum LLNL-MARS-83-017 (April 8, 1983).

10. C. O. Bennett and J. E. Myers, Momentum, Heat, and Mass Transfer, Second Edition (McGraw Hill, New York, 1962) pp. 208-211.

11. Heat Transfer and Fluid Flow Data Book (General Electric Company Corporate Research and Development, Schenectady, New York, 1980).

12. G. H. Miley, Fusion Energy Conversion (American Nuclear Society, 1976).

13. F. L. Horn et al., Thermal Conductivity Measurements of Insulators for Fusion Blankets, Brookhaven National Laboratory, Upton, NY, Report BNL-29779.

14. M. A. Hoffman, Magnetic Field Effects on the Heat Transfer of Potential Fusion Reactor Coolants, Lawrence Livermore National Laboratory, Livermore, CA, UCRL-73993 (1972).

15. J. C. R. Hunt and R. J. Holyroyd, Applications of Laboratory and Theoretical MHD Duct Flow Studies in Fusion Reactor Technology, Culham Laboratories, CLM-R169 (1977).

16. M. A. Hofman and G. A. Carlson, Calculation Techniques for Estimating the Pressure Losses for Conducting Fluid Flows in Magnetic Fields, Lawrence Livermore National Laboratory, Livermore, CA, UCRL-51010 (1971).

17. E. Y. Blum, Effect of Magnetic Field on Heat Transfer in the Turbulent Flow of Conducting Liquid, Institute of Physics and Power, Academy of Sciences of the Latv SSR, (Translation) (1967).

18. R. A. Gardner, P. S. Lykondis, "Magneto Fluid-Mechanic Pipe Flow in a Transverse Magnetic Field, Parts 1 and 2," Journal of Fluid Mechanics, 47 and 48 (1971).

19. S. Globe, "The Effect of Longitudinal Magnetic Field on Pipe Flow of Mercury," Journal of Heat Transfer (November 1961).

20. D. S. Kouner, E. Y. Krasil'nikov, I. G. Panerin, "Experimental Study of the Effect of a Longitudinal Magnetic Field on Convective Heat Transfer in a Turbulent Tube Flow of Conducting Liquid," Magnitnaya Gidrodinamika (Magnetohydrodynamics), 2, (4) (1966).

21. A. L. Lueffler, A. Maciulaitis, M. Huff, MHD Round Pipe Flow Experiments, Aerospace Research Laboratories, ARL 67-0236 (1967).

22. P. F. Tortonelli and J. H. Devan, "Corrosion of Austentitic and Ferritic Steels in Static Pb-17 at % Li," in Alloy Development for Irradiation Performance, DOE/ER-0045/8 (March 31, 1982).

23. G. J. Butterworth, Some Initial Considerations on the Suitability of Ferritic/Martensitic Stainless Steels as First Wall and Blanket Materials in Fusion Reactors, Euratom/UKAEA Fusion Association, CLM-R217 (1982).

24. N. M. Ghoniem and R. W. Conn, "Assessment of Ferritic Steels for Steady-State Fusion Reactors," in Proc. of Technical Committee Meeting and Workshop on Fusion Reactor Design and Technology, Tokyo, Japan (October 5-16, 1981).

25. J. F. Mancuso, J. A. Spitznagel, R. P. Shogan, and G. M. Jouris, "Irradiation and Annealing of Pressure Vessel Steels," ANS Trans. 38, p. 325 (1981).

26. N. M. Ghoniem and R. W. Conn, "High Temperature Evaluation of Ferritic Steels for Fusion Reactors," ANS Trans. (June 1982).

27. R. D. Watson, The Impact of Inelastic Deformation, Radiation Effects and Fatigue Damage on Fusion Reactor First Wall Lifetime, Ph.D. Thesis, University of Wisconsin (December 1981).

28. D. L. Smith et al., Fusion Reactor Blanket/Shield Design Study, ANL/FPP-79-1 (July 1979).

29. C. S. Caldwell et al., "A Survey of Lithium Compounds for Tritium Breeding Applications," in Proc. of Babcock & Wilcox, 4th Topical Meeting on the Technology of Controlled Nuclear Fusion (October 1980).

30. A. B. Johnson, Jr., T. J. Kakele, and W. E. Gurwell, BNWL-2097 (August 1976).

31. R. F. O'Neill et al., "Convair Thermal Analyzer Computer Program No. P4560D," 696-O-T-81-737 (June 1980).

32. R. H. Perry and C. H. Chilton, Chemical Engineering Handbook, Fifth Ed, (McGraw-Hill, New York, NY, 1973).

33. B. Lewis and G. von Gelbr, Combustion, Flames, and Explosions in Gases, (Academic Press, New York, 1953) p. 29.

34. Davison Molecular Sieves (4A), Technical Bulletin ADS-96-A-272, W. R. Grace and Co., Baltimore, MD.

35. E. F. Johnson, "The Use of Molecular Sieves for Tritium Control in Fusion Power Plants, in AICHE Symposium Series on Adsorption and Ion Exchange, 72 (152), p. 114-120 (1975).

36. R. S. Hall, J. Matley, and J. McNaughton, "Current Costs of Process Equipment," Chemical Engineering, 89 (7), p. 80-116 (April 5, 1982).

37. J. Bartlit, Tritium System Test Assembly (TSTA), Los Alamos Scientific Laboratory, Los Alamos, NM (July 1982).

38. B. G. Logan et al., MARS Interim Design Report, Lawrence Livermore National Laboratory, Livermore, CA, UCRL-53333 (1983).

4 Thermochemical Hydrogen Processes

4. Thermochemical Hydrogen Processes

In this section we describe the basic principles of thermochemical cycles for water splitting to produce hydrogen, including the criteria that determine cycle efficiencies and influence process design. We also briefly describe GA Technologies' sulfur-iodine cycle for hydrogen production, which we are coupling to the tandem mirror reactor (TMR) in our current design studies.

4.1 THERMOCHEMICAL CYCLES

4.1.1 Introduction

A thermochemical cycle for hydrogen production is a process that uses water as a feedstock along with a nonfossil high-temperature heat source to produce H_2 and O_2 as product gases. (Fossil fuels can be converted directly to hydrogen by chemical processing in a more energy-efficient and cost-effective manner than by using them as a heat source for thermochemical cycles.) The water splitting process is accomplished through a closed loop sequence of chemical reaction steps in which the chemical reagents are continuously recycled and reused in the process with essentially no loss of material. Practical thermochemical cycles, as currently envisioned, require input temperatures as high as ∿1200 K and operate at a thermal efficiency of 35 to 45%. We define thermal efficiency as the higher heating value of the H_2 produced--286 kJ/mol H_2 (combustion enthalpy of the H_2 to give liquid water at 298.15 K)--divided by the thermal heat per mole of H_2 delivered by the dedicated heat source.

Worldwide, about 30 thermochemical cycles are currently under investigation and development. Presently three possible energy sources are being considered to power these cycles: (1) high-temperature gas-cooled fission reactors; (2) solar central receivers; and (3) magnetic fusion reactors, our choice for this study.

Of the 30 cycles under study, only three have been developed to the stage where closed-loop table-top (or bench-scale) models have been built and tested in the laboratory. They are the sulfur-iodine cycle at GA Technologies,[1-3] the sulfur cycle at Westinghouse Electric Corporation,[4,5] and the sulfur-bromine cycle at the Joint Research Centre-Ispra Establishment.[6-9] These three cycles are illustrated in terms of their principal chemical steps and reaction temperatures in Fig. 4-1a,b,c. (Note that in each of the cycles the sum of the chemical reaction steps is $H_2O = H_2 + 1/2\ O_2$.) Our design choice is the sulfur-iodine cycle.

4.1.2 Basic Principles

The energetics of water decomposition are

$$H_2O(\ell) = H_2(g) + 1/2\ O_2(g) \quad , \qquad (1)$$

$$\Delta H^\circ_{298} = 285.8 \text{ kJ/mol} \quad ,$$

$$\Delta G^\circ_{298} = 237.2 \text{ kJ/mol} \quad .$$

(a) Sulfur-iodine cycle

$$2\ H_2O + SO_2 + x\ I_2 \xrightarrow{\text{aqueous}} H_2SO_4 + 2\ HI_x$$

$$2\ HI_x \xrightarrow{\sim 400\ K} x\ I_2 + H_2$$

$$H_2SO_4 \xrightarrow{\sim 1100\ K} H_2O + SO_2 + 1/2\ O_2$$

(b) Sulfur cycle (part electrochemical)

$$2\ H_2O + SO_2 \xrightarrow[\text{electrolysis}]{\text{aqueous}} H_2 + H_2SO_4$$

$$H_2SO_4 \xrightarrow{\sim 1100K} H_2O + SO_2 + 1/2\ O_2$$

(c) Sulfur-bromine cycle (part electrochemical)

$$2\ H_2O + SO_2 + Br_2 \xrightarrow{\text{aqueous}} H_2SO_4 + 2\ HBr$$

$$2\ HBr \xrightarrow[\text{electrolysis}]{\text{aqueous}} Br_2 + H_2$$

$$H_2SO_4 \xrightarrow{\sim 1100\ K} H_2O + SO_2 + 1/2\ O_2$$

Fig. 4-1. Thermochemical cycles whose chemistry and closed-loop operation have been verified in the laboratory.

Thus, the energy requirement for decomposing water into its elements is quite high. In addition, if water were decomposed in a single step, temperatures of about 2500 to 3000 K would be required to obtain significant yields. If we could attain these high temperatures, several other major problems would occur: a back-reaction recombination of H_2 and O_2 during cooldown, very serious materials problems, and the need for considerable recycling because of low decomposition yields.

These problems are avoided and several advantages result if water is decomposed in two or more chemical reaction steps. For example, the production of H_2 and O_2 can be in separate reaction steps, thus avoiding the back reaction problem. Also, the proper combination of reactions can lower the maximum reaction temperature, thus producing better reaction yields and increasing the availability of suitable materials. In actual practice, two-step cycles have shown only minimal lowering of the temperature compared to the single-step decomposition of water, unless one of the steps is electrochemical. A cycle that includes both thermal and electrochemical steps is called a "hybrid" cycle. With three or more steps, cycles based only on thermal input for the chemical reactions become possible at reasonable temperatures, and several will work efficiently at maximum temperatures of about 1200 K.

To illustrate some of the important considerations in developing and evaluating thermochemical cycles, we use the following generalized two-step cycle:

$$R + H_2O(\ell) \xrightarrow{T_1} RO + H_2(g), \quad \Delta G^\circ \leq 0, \quad \Delta H^\circ = \Delta H_1 \quad , \qquad (2)$$

and

$$RO \xrightarrow{T_D} R + 1/2\ O_2(g), \quad \Delta G^\circ \leq 0, \quad \Delta H^\circ = \Delta H_D \quad . \qquad (3)$$

In Reaction (2), a reducing agent R is used to reduce water to produce H_2 at temperature T_1, forming the oxide RO in the process. Reactions such as this are usually carried out near room temperature or at slightly elevated temperatures. To achieve a near-zero or negative ΔG° to make the reaction go, the enthalpy change is usually governing and ΔH_1 is negative (an exothermic reaction). Heat produced by Reaction (2) is usually of limited value for reuse in the cycle because of the low temperatures involved. Reaction (3) is carried out at a high temperature and is the decomposition step that regenerates the reducing agent R as well as O_2. Reaction (3) is also highly endothermic (ΔH_D is positive) and requires a large change in entropy (ΔS°) to produce a near-zero or negative ΔG°. This can be seen from the second law expression $\Delta G^\circ = \Delta H^\circ - T\Delta S^\circ$, where $T\Delta S^\circ$ becomes increasingly important as the temperature is raised. Hence, one of the requirements in selecting the oxide RO is that the ΔS° of decomposition be as large as possible to minimize the maximum temperature required in the thermochemical cycle. As an example, the gaseous molecule SO_3 (R = SO_2) meets the requirement for Reaction (3), but SO_2 falls short of the requirement for reducing water to produce H_2 in Reaction (2). The possible remedies are to assist Reaction (2) by forming a hydrogen compound of intermediate stability--such as HI or HBr--that can be

subsequently decomposed to obtain the desired H_2 product, or by using an electrolysis step at a voltage substantially less than required for direct water electrolysis. In the case of HBr decomposition, an electrolysis step would also be required because the yield is low for thermal decomposition of HBr.

Two types of cycle efficiencies are used to evaluate thermochemical cycles: (1) The work efficiency, i.e., the efficiency of converting heat into work, E(w), is given by

$$E(w) = \frac{237.2}{\Sigma\Delta H_D} \leq \frac{T_D - 298}{T_D} , \qquad (4)$$

where 237.2 (in kJ/mol) represents the maximum work ($\Delta G°$) available from the hydrogen produced [see expression (1)], and $\Sigma\Delta H_D$ represents the total external heat input for the cycle, i.e., the heat provided by our fusion heat source; and (2) the thermal efficiency, or the efficiency of heat utilization, E(H) is given by

$$E(H) = \frac{285.8}{\Sigma\Delta H_D} \leq 1.21 \frac{T_D - 298}{T_D} . \qquad (5)$$

For the electricity required in the cycle, the $\Sigma\Delta H_D$ term includes the equivalent heat required to produce that electricity. In the particular case of the tandem mirror reactor, some of the required electrical energy is available as output from the direct converter, and we add this directly to the $\Sigma\Delta H_D$ term, assuming it to be equivalent to thermal energy at 100% conversion.

We see that E(w) is limited by the Carnot expression for maximum efficiency. The thermal efficiency E(H) compares $\Sigma\Delta H_D$ with the combustion energy of the hydrogen produced to form liquid water at room temperature as the final product. The thermal efficiency can exceed the Carnot efficiency up to a maximum value given by the ratio of 285.8/237.2 = 1.21.

4.1.3 Some Important Criteria

A listing of the major reaction steps (like that in Fig. 4-1) gives only an indication of the complexity of a thermochemical cycle system. Choosing the best cycle and then refining it to be highly efficient and still economical is a challenging research goal. The criteria that must be considered include:

- Favorable thermodynamics.
- Fast reactions.
- High reaction yields.
- Simple separations.
- Process design factors (such as efficient use of heat, avoidance of scarce or hazardous reagents, and simplicity of construction).

Favorable thermodynamics imply both a negative and a very small free energy change (ΔG°) for each reaction step. If the free energy change is positive, the equilibrium constant of the reaction becomes unfavorable and much energy can be wasted in separating or concentrating the reaction products. If the free energy change is too negative, on the other hand, one or more of the reaction products becomes too stable and, therefore, difficult to regenerate into the original reactants.

Fast reactions are desirable, especially for reactions involving gaseous reactants, because they enable us to use smaller and less expensive reaction vessels. However, the requirement that the free energy change be nearly zero makes it difficult to achieve fast reactions because it allows very little driving force for the reactions. Reactions need to be selected in which the energy barriers are low enough to permit a very small free energy change to drive them rapidly. In many instances, the reaction rates can be enhanced by the use of catalysts.

High reaction yields are important to minimize recycling of unreacted reagents or diversion of material into undesirable by-products.

By using simple separations we avoid another area in which hidden costs can be substantial. Operations such as boiling, compression, and filtering can involve expensive process equipment and energy losses, and they need to be minimized.

Finally, careful process design can do much to provide the optimum tradeoff between the efficient use of heat energy and the economics of construction and operation. Process design contributions include new and innovative process equipment, plant layout, and siting.

4.2 SULFUR-IODINE CYCLE

4.2.1 Selecting the Cycle

We have selected GA Technologies' sulfur-iodine cycle for our current TMR/thermochemical cycle coupling studies because it is the closest of the most advanced cycles to a pure thermal cycle. This permits the economies of scale-up to apply for chemical process units in a large chemical plant of the type considered here. (Scale-up would not permit a similar reduction in costs for modular electrolysis units.) The sulfur-iodine cycle also involves the handling of only liquids and gases, which is advantageous from a chemical engineering standpoint.

4.2.2 Chemical Description

The current sulfur-iodine cycle can be described chemically as

$$2\ H_2O + SO_2 + x\ I_2 \rightarrow H_2SO_4 + 2\ HI_x \qquad (390\ K)\ , \qquad (6)$$

$$2\ HI_x \rightarrow H_2 + x\ I_2 \qquad (420\ K)\ , \qquad (7)$$

$$H_2SO_4 \rightarrow H_2O + SO_2 + 1/2\ O_2 \qquad (\sim 1000\ K \text{ to } 1250\ K)\ . \qquad (8)$$

All reactions in this system have been verified in the laboratory and total recycle has been illustrated in a small, closed-loop cycle experiment.[1] Major parts of the process are associated with separation and purification of the reaction products. A critical aspect for the successful operation of the process is the separation of the aqueous reaction products in Reaction (6) above. Workers at GA Technologies have solved this problem by using an excess of I_2 in Reaction (6), which leads to separation of the products into a lower density phase, containing H_2SO_4 and H_2O, and a higher density phase, containing HI, I_2, and H_2O. Reaction (7) shows the catalytic decomposition of HI, which is carried out under pressure ($\sim$80 atm) with HI and I_2 in liquid forms to enhance the decomposition yield. Laboratory decompositions are around 30% per pass and, therefore, use a recycle step. Unreacted HI is condensed out of the H_2 product and distilled away from the I_2 product. Pure H_2 is obtained by scrubbing out the remaining I_2 with H_2O.

The equilibrium for Reaction (8) lies to the right at temperatures above 1000 K, but up to temperatures of $\sim$1150 K catalysts are needed to attain sufficiently rapid decomposition rates. Several catalysts are available for this process, but cost vs effectiveness needs to be carefully considered.

Figure 4-2 is a simplified schematic flow diagram of the sulfur-iodine cycle showing product flows and recycle streams. For purposes of flowsheeting and process design, the cycle has been divided into the following process sections:

- Section I, H_2SO_4-HI production and separation.
- Section II, H_2SO_4 concentration and SO_3 decomposition.
- Section III, HI separation and purification.
- Section IV, HI decomposition and H_2 purification.
- Section V, energy distribution and the TMR-chemical plant interface.

Section II is the high temperature step of this chemical process and is perhaps the most difficult. In the following paragraphs we explain the thermodynamics data base of Section II. The remaining four process sections are discussed in Section 5 of this volume.

4.3 THERMODYNAMIC DATA BASE FOR SECTION II

A large proportion of the energy supplied by the TMR is required to operate Section II. The primary reactor heat into Section II is generally recovered and reused several times before it is discharged as waste heat. Because of the magnitude of heat handled in Section II, proper heat-matching and reuse of heat are critical to achieving a high efficiency process. Moreover, the accuracy of the thermodynamic data base is important if we are to achieve a realistic optimum or near-optimum in efficiency of heat use.

The current literature contains only a portion of the thermodynamic data needed to do heat-matching and mass and energy balances for Section II. However, we are able to fill in some portions of the missing data by deriving

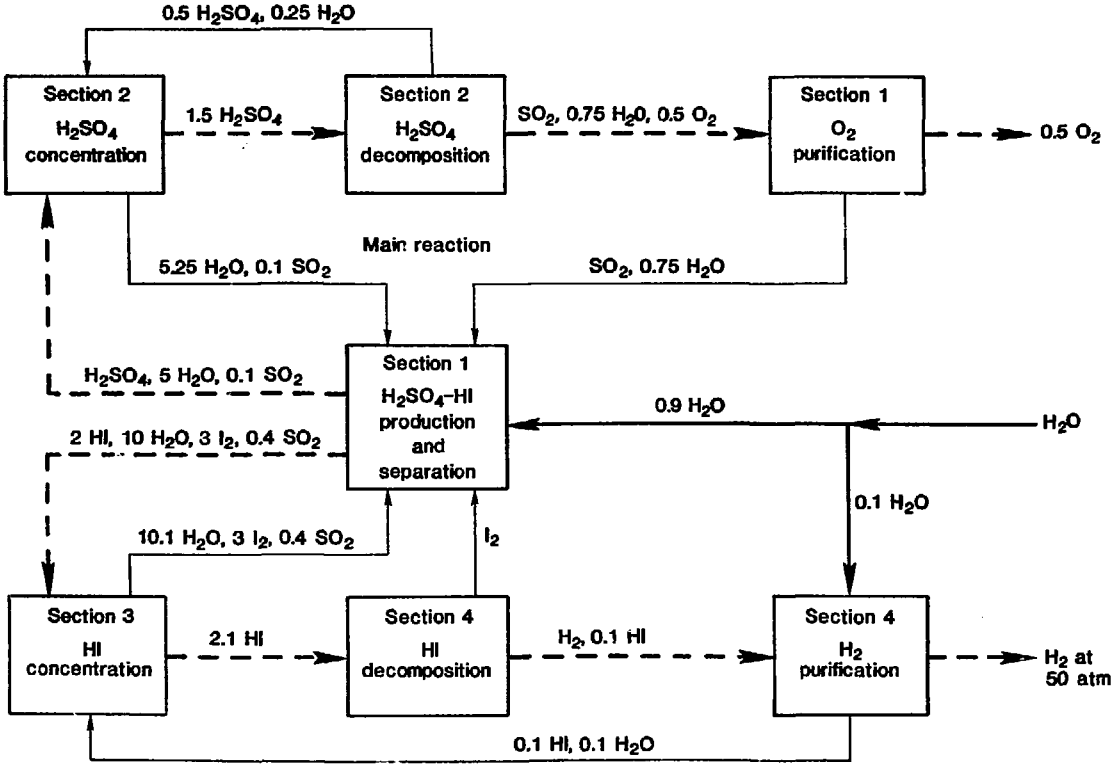

Fig. 4-2. Block diagram for GA Technologies' sulfur-iodine cycle.

approximate thermodynamic data based on recent unpublished measurements by Lennartz,[10] who gives pressure-composition-temperature (P,x,T) data for the H_2O-H_2SO_4 system. In addition, we have made some rough estimates needed to obtain a complete thermodynamic data base for use in Section II.

4.3.1 Sequence of Process Steps

The following are the process steps for Section II for which the thermodynamic database will be used (see Fig. 4-3).

4.3.1.1 Concentration of Sulfuric Acid. The feed material for this process step consists of two streams: (1) the 57 wt% (20 mole %) sulfuric acid product from Section I at ∿400 K, which supplies about 80% of the feed, and (2) a 50 wt% (15 mole %) sulfuric acid from the decomposer product stream at about 500 to 600 K, which makes up the balance of the feed. These acid streams are concentrated in H_2SO_4 by selectively vaporizing off water in a staged evaporator to produce the 98 wt% (90 mole %) H_2SO_4 azeotrope at ∿675 K. Pure water recovered from the evaporation is returned to Section I.

4.3.1.2 Boiling of Azeotrope. The 98 wt% H_2SO_4 azeotrope is boiled isothermally at about 5 atm and 670 K to obtain the gaseous feed for the decomposer. Gaseous species produced by the boiler are H_2SO_4, SO_3, and H_2O.

4.3.1.3 Preheating of Gas. The gas from the boiler is preheated from ∿670 K to about 1000 to 1100 K to prepare it as feed to the decomposer. Molecular H_2SO_4 decomposes endothermically to $SO_3 + H_2O$ during this preheat.

4.3.1.4 Decomposition of Sulfuric Trioxide. The gaseous feed from the preheater now contains about 50 mole % each of SO_3 and H_2O. About 64% of the SO_3 is decomposed at 5 atm and 1150 K to form SO_2 and O_2 as products.

4.3.1.5 Cooldown of Decomposition Products. The gaseous products from the decomposer are quenched to ∿1100 K to prevent back reaction of $SO_2 + O_2$. Quenching is accomplished by recycling some of the cooled decomposition product gases into the decomposer product stream. The product stream is then passed through a tube and shell recuperator to preheat the gas feed entering the decomposer. A portion of the cooled recuperator output gas (at ∿700 K) is used as quench gas (see above) and the balance is used to supply heat to the evaporator through a heat exchanger. Undecomposed SO_3 remaining in the product gas combines with H_2O and condenses out as aqueous H_2SO_4 at about 500 to 600 K. This aqueous H_2SO_4 is added to the evaporator stream for recycle, and gaseous SO_2 and O_2 are separated and sent to Section I.

4.3.2 Thermodynamic Data Requirements

The thermodynamic data requirements for each of the process steps described above will now be discussed in a general way. Details of the data derivation and methods for use of the thermodynamic data are covered in a later subsection.

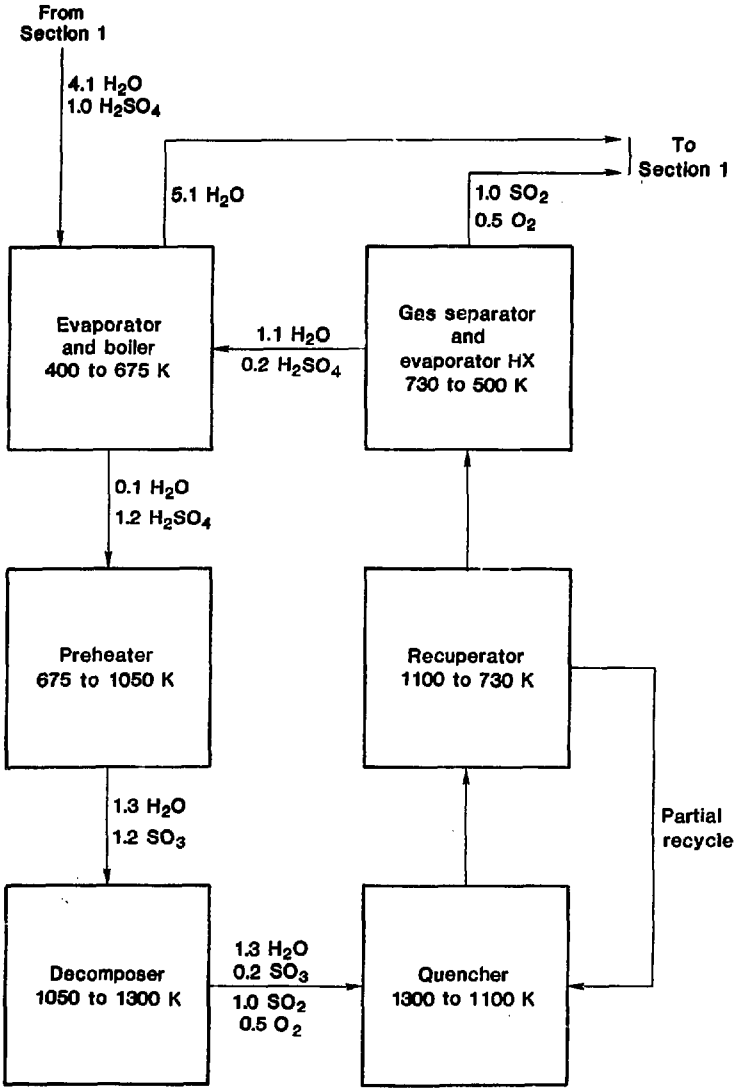

Fig. 4-3. Simplified flow diagram illustrating the process steps, temperatures, and approximate mass flows for which thermodynamic data need to be developed.

4.3.2.1 Thermodynamic Data for Concentration of Sulfuric Acid. Because the H_2SO_4 solutions are concentrated in a staged evaporator, we need to have the following information on several thermodynamic parameters for each stage: (1) the uptake of sensible heat as the solution is heated; (2) the vapor pressures of gaseous products and the resultant change in liquid phase composition; (3) the vaporization enthalpies to the gas phase, (4) the sensible heat, condensation temperature, and condensation enthalpy of the gas phase product; and (5) the sensible heat available in the condensate as it cools.

The chemical processes occurring in a single evaporation stage and the approximate enthalpy changes associated with the processes are illustrated in the following simplified example:

$$(H_2SO_4 + 4\ H_2O)_{400\ K,\ aq} \rightarrow (H_2SO_4 + 4\ H_2O)_{600\ K,\ aq};\ \Delta H_{9a} = 35.7\ kJ/mol \quad (9a)$$

$$(H_2SO_4 + 4\ H_2O)_{600\ K,\ aq} \rightarrow (H_2SO_4 + 3\ H_2O)_{600\ K,\ aq} + H_2O(\ell)_{600\ K,\ 1\ atm};\ \Delta H_{9b} = 8.1\ kJ/mol \quad (9b)$$

$$H_2O(\ell)_{600\ K,\ 1\ atm} \rightarrow H_2O(g)_{600\ K,\ 40\ atm};\ \Delta H_{9c} = -27.1\ kJ/mol \quad (9c)$$

$$H_2O(g)_{600\ K,\ 40\ atm} \rightarrow H_2O(g)_{525\ K,\ 40\ atm};\ \Delta H_{10} = -4.2\ kJ/mol \quad (10)$$

$$H_2O(g)_{525\ K,\ 40\ atm} \rightarrow H_2O(\ell)_{525\ K,\ 40\ atm};\ \Delta H_{11} = -29.5\ kJ/mol \quad (11)$$

$$H_2O(\ell)_{525\ K,\ 40\ atm} \rightarrow H_2O(\ell)_{430\ K,\ 5.6\ atm};\ \Delta H_{12} = -8.9\ kJ/mol \quad (12)$$

The first reaction above, corresponding to the uptake of enthalpy and boiling off of part of the water, is broken down into three parts for the convenience of thermodynamic calculations. Thus, (9a) represents the increase in sensible heat of the initial $(H_2SO_4 + 4\ H_2O)$ solution, (9b) represents the exsolution of water into a hypothetical 1-atm reference state, and (9c) is the boiling of the 1-atm reference state of water to the equilibrium partial pressure of steam above the final $(H_2SO_4 + 3\ H_2O)$ solution. The equilibrium steam pressure is estimated by extrapolating the data of Lennartz[10] to higher pressures.

Reactions (10), (11), and (12) represent the enthalpy available for reuse from the evaporated steam. This enthalpy is available as sensible heat in the steam, condensation energy of the steam, and sensible heat in the condensed water down to 430 K. Thus, with a total enthalpy input of 70.9 kJ/mol (35.7 + 8.1 + 27.1), 42.6 kJ/mol (4.2 + 29.5 + 8.9) or 60% is available for reuse above 430 K, with most of it actually available above ~500 K. The balance of the enthalpy remains primarily as sensible heat in the concentrated sulfuric acid.

In subsequent evaporation stages, as the H_2SO_4 is heated further and becomes more concentrated, the thermodynamics get complicated, as first $H_2SO_4(g)$ and then $SO_3(g)$ contribute in increasing amounts to the gas-phase composition. Upon reaching the azeotrope composition, the gas phase will consist of roughly 40% $H_2SO_4(g)$ and 30% each of $SO_3(g)$ and $H_2O(g)$. Also, the enthalpy for exsolution of $H_2O(\ell)$, Reaction (9b) above, will increase by nearly an order of magnitude. Thus, for the more concentrated H_2SO_4 solutions the condensate from the gas phase will contain a substantial amount of H_2SO_4, and several additional evaporation stages will be needed to obtain a separation of relatively pure water. Consequently, both the complexity of the H_2SO_4 concentration process and the energy requirements increase as the azeotrope is approached. Thus, it becomes especially important in this region to have accurate thermodynamic data and to do careful heat-matching.

4.3.2.2 Thermodynamic Data for Boiling the Azeotrope. The azeotrope represents the invariant boiling composition at which the gas-phase and liquid-phase compositions are identical at a given temperature. For the H_2O-H_2SO_4 system, the azeotrope occurs at ~90 mole% H_2SO_4, and is an experimentally determined parameter. At a given temperature, we can write down the following relationships for the gas phase above the boiling azeotrope:[11]

$$K_{eq} = (p_{SO_3})(p_{H_2O})/(p_{H_2SO_4}) \quad , \tag{13}$$

$$x_{H_2SO_4} = (p_{H_2SO_4} + p_{SO_3})/(p_{H_2SO_4} + p_{H_2O}) \quad , \tag{14}$$

$$P_{tot} = p_{H_2SO_4} + p_{SO_3} + p_{H_2O} \quad . \tag{15}$$

Reaction (13) represents the equilibrium degree of decomposition of $H_2SO_4(g)$, Reaction (14) gives the experimentally determined azeotropic composition expressed as mole fraction H_2SO_4, and Reaction (15) gives the experimentally determined total gas pressure for the particular azeotropic temperature. Using these relations, and assuming that decomposition of $SO_3(g)$ into $SO_2(g)$ and $O_2(g)$ is kinetically hindered under these conditions, we can calculate the partial pressures of $H_2SO_4(g)$, $SO_3(g)$, and $H_2O(g)$ for each azeotropic boiling point.

Having obtained the gas-phase compositions, we can now proceed to calculate the enthalpy of boiling, as illustrated by the following example for the 5-atm azeotrope, which boils at 671.5 K at a composition of $x_{H_2SO_4} = 0.9071$:[10]

$$H_2SO_4 \text{ (azeo. liq.)} + 0.102\ H_2O \text{ (azeo. liq.)} \rightarrow H_2SO_4(\ell) + 0.102\ H_2O(\ell);\ \Delta H_{16a} = 8.4 \text{ kJ/mol} \quad , \tag{16a}$$

$$H_2SO_4(\ell) \rightarrow H_2SO_4(g);\ \Delta H_{16b} = 56.5 \text{ kJ/mol} \quad , \tag{16b}$$

$$0.102\ H_2O(\ell) \rightarrow 0.102\ H_2O(g);\ \Delta H_{16c} = 2.2 \text{ kJ/mol} \quad , \tag{16c}$$

$$H_2SO_4(g) \rightarrow 0.620\ H_2SO_4(g) + 0.380\ SO_3(g) + 0.380\ H_2O(g);\ \Delta H_{16d} = 35.9 \text{ kJ/mol} \quad . \tag{16d}$$

Here again the reactions are broken down into intermediate steps for thermodynamic convenience, with $H_2SO_4(\ell)$ and $H_2O(\ell)$ representing 1-atm hypothetical reference states. The sum of the enthalpies for Reactions (16a) through (16d) gives 103.0 kJ/mole, which represents the boiling enthalpy per mole of H_2SO_4 for the 5-atm azeotrope.

4.3.2.3 Thermodynamic Data for Preheating the Gas. Molecular $H_2SO_4(g)$ gradually decomposes into $SO_3(g)$ and $H_2O(g)$ as the azeotropic gas mixture is preheated from the boiling point up to the point where it is introduced into the decomposer. It is assumed that the $H_2SO_4(g)$ decomposition equilibrium is rapid, and that the decomposition of $SO_3(g)$ into $SO_2(g)$ and $O_2(g)$ does not occur because it is kinetically hindered. The required thermodynamic data are the equilibrium constant for $H_2SO_4(g)$ decomposition; enthalpies for the sensible heats of gaseous H_2SO_4, SO_3, and H_2O; and the decomposition enthalpy of gaseous H_2SO_4. An illustration of the calculations involved is given in an earlier report.[11]

4.3.2.4 Thermodynamic Data for Decomposition of Sulfur Trioxide. The decomposition of $SO_3(g)$ is assumed to reach equilibrium at the exit temperature and pressure of the decomposer. The required thermodynamic data are the equilibrium constant and enthalpy for decomposition and the enthalpies for the sensible heat changes in the gaseous species between the inlet and outlet of the decomposer.

4.3.2.5 Thermodynamic Data for Decomposition Products. The thermodynamic data required for cooldown of the decomposition products involve enthalpies for sensible heats, recombination enthalpies, condensation enthalpies, and various equilibrium constants. Data for these processes are similar to data during heatup.

4.3.3 Summary of Thermodynamic Data

Major progress has been made in bringing the thermodynamic data base up to date and putting it into a form where it can be used to obtain reasonably accurate energy balances for Section II. Some work still remains to complete the data evaluations and summaries.

Table 4-1 provides a concise summary of the thermodynamic data requirements, the current data sources, and a listing of the tables and figures in this section that summarize the current data. In the discussions that follow, we describe the bases for these data.

4.3.3.1 Equilibrium Constant Data. Of the items designated in Table 4-1 under equilibrium constant data, the partial pressures of gaseous species above aqueous H_2SO_4 and the azeotrope parameters are the most difficult to obtain. The balance of the items are readily obtained from standard tabulations.[12,13]

Some years ago, Gmitro and Vermeulen[14] did an excellent theoretical job of calculating the equilibrium vapor compositions above H_2O-H_2SO_4 mixtures up to 673 K. The difficulty with their work was that they were limited to using the room temperature experimental data of Giauque and coworkers[15] for input data. As a consequence, their high temperature data do not agree with the recent experimental total pressure values and azeotrope compositions of Lennartz.[10]

Lennartz's total pressure data are summarized in Table 4-2 and Fig. 4-4. The pressures and temperatures in Fig. 4-4 have been extrapolated beyond the experimental range for convenience in doing pressure-staging calculations for the evaporator process step. An example of Gmitro and Vermeulen's data is given in Fig. 4-5. Note that the proportion of $H_2SO_4(g)$ in the vapor does not become important until ∿85 wt% (50 mole%) H_2SO_4 is reached; for $SO_3(g)$, ∿95 wt% (80 mole %) H_2SO_4 must be reached.

4.3.3.2 Enthalpy of Reaction Data. Most of the enthalpy of reaction data required here can be readily obtained from standard compilations such as the JANAF tables[12] and steam tables[13] (see Table 4-1). However, it is difficult to obtain data for the exsolution of aqueous H_2SO_4 into its pure components, as indicated in Reaction (18a), and an extrapolation needs to be made to higher temperatures to obtain data for vaporization of $H_2O(\ell)$ from its 1-atm reference state to $H_2O(g)$ [see Reaction (18c)].

To determine exsolution of aqueous H_2SO_4 into its components at room temperature, we used the excellent experimental data of Giauque et al.[15] The solution reactions are shown in Figs. 4-6 and 4-7 for the partial molal and integral enthalpies of solution at 298.15 K. (The enthalpies of exsolution are the negatives of these values.)

At higher temperatures, i.e., at ∿600 K, we have derived approximate values for the enthalpies of solution from the P,x,T data of Lennartz.[10] Thus, examining Lennartz's data in Table 4-2, we find that the product of the gas constant R times the parameter B is the total enthalpy of vaporization for all gaseous species at ∿600 K above the various aqueous H_2SO_4 solutions. Furthermore, based on the calculations of Gmitro and Vermeulen[14] (see Fig. 4-5), the vapor consists mainly of $H_2O(g)$ up to about $x_{H_2SO_4} = 0.6$. Hence, by subtracting out the vaporization enthalpy of $H_2O(\ell)$ in its 1-atm reference state from Lennartz's enthalpy of vaporization values, we obtain the partial molal enthalpy of exsolution of $H_2O(\ell)$ at 600 K up to $x_{H_2SO_4} = 0.6$. We can also obtain an additional value for the partial molal enthalpy of exsolution

Table 4-1. Summarized here are the thermodynamic data requirements for Section II. Included are references to the thermodynamic data sources currently in use, and a listing of the tables and figures where the data have been summarized.

Thermodynamic data required	Data source	Where summarized
Equilibrium constants for:		
Partial pressures of $H_2O(g)$, $H_2SO_4(g)$, and $SO_3(g)$ above aqueous H_2SO_4 as f(x,T)	Gmitro and Vermeulen,[14] Lennartz[10]	Table 4-2, Figs. 4-4 and 4-5
Azeotrope x and T for aqueous H_2SO_4 as f(P)	Derived from Lennartz[10]	Table 4-3
$H_2SO_4(g) = H_2O(g) + SO_3(g)$	JANAF[12]	
$SO_3(g) = SO_2(g) + 1/2\ O_2(g)$	JANAF[12]	
$H_2O(\ell) = H_2O(g)$, at saturation	Steam tables[13]	
Reaction enthalpies for:		
Exsolution of aqueous H_2SO_4 into pure $H_2O(\ell)$ and $H_2SO_4(\ell)$ in their 1-atm reference states	Derived from Giauque,[15] Lennartz,[10] and estimates	Figs. 4-6 and 4-7
$H_2O(\ell, 1\ atm) = H_2O(g)$	JANAF,[12] plus extrapolations	Fig. 4-8
$H_2SO_4(\ell, 1\ atm) = H_2SO_4(g)$	JANAF[12]	
$H_2SO_4(g) = H_2O(g) + SO_3(g)$	JANAF[12]	
$SO_3(g) = SO_2(g) + 1/2\ O_2(g)$	JANAF[12]	
$H_2O(\ell) = H_2O(g)$, at saturation	Steam tables[13]	Fig. 4-8
Sensible heats (enthalpies) for:		
Aqueous H_2SO_4 as f(x)	JANAF,[12] and data derived from Lennartz[10]	Figs. 4-9 and 4-10
$H_2O(\ell)$, 1-atm reference state	JANAF,[12] plus extrapolations	Fig. 4-11
$H_2SO_4(\ell)$, $H_2SO_4(g)$, $SO_3(g)$, $SO_2(g)$, and $O_2(g)$	JANAF[12]	Fig. 4-11
$H_2O(g)$ as f(P), and $H_2O(\ell)$ at saturation	Steam tables[13]	Fig. 4-11

Table 4-2. Parameters are summarized for the expression $\ln P = A - B/T$, which gives the total equilibrium pressure, P (in atm), above various H_2O-H_2SO_4 mixtures as a function of T (in K). The experimental data and A and B parameters are from Lennartz.[10]

Temperature range (K)	$x_{H_2SO_4}$	A	B
433-532	0.2144	12.2538	4968.27
443-538	0.2460	12.1593	5041.11
453-566	0.3173	12.5265	5507.69
463-576	0.3407	12.3389	5485.73
473-588	0.3832	12.5012	5718.92
464-598	0.3998	12.6682	5891.34
475-610	0.4187	12.4767	5875.56
479-622	0.4536	12.3088	5887.03
521-652	0.5512	12.6858	6471.72
534-682	0.6388	12.6410	6746.30
502-719	0.7181	13.0419	7287.66
589-718	0.7522	13.2453	7519.31
568-741	0.8189	13.4854	7840.62
503.744	0.8386	13.8296	8123.06
507-741	0.8840	14.5261	8659.33
621-693	0.8921	14.6010	8740.04
535-744	0.9050	14.6863	8792.67
583-603	0.9195	15.1161	9071.12
503-743	0.9296	15.1626	9101.92
503-744	0.9349	15.2487	9143.64
504-737	0.9806	15.3841	9076.25

Table 4-3. Temperature, pressure, and composition conditions for the H_2O-H_2SO_4 azeotrope based on the experimental data of Lennartz[10] and JANAF[12] for the vapor species.

T (K)	P (atm)	x_{H_2O} [a]	$x_{H_2SO_4}$ [a]	P_{H_2O} (atm)	$P_{H_2SO_4}$ (atm)	P_{SO_3} (atm)
522.6	0.1	0.0602	0.9398	0.02363	0.05763	0.01874
566.4	0.4	0.0682	0.9318	0.10576	0.21001	0.08423
600.3	1	0.0752	0.9248	0.28591	0.48625	0.22784
628.7	2	0.0818	0.9182	0.60345	0.91751	0.47904
646.9	3	0.0863	0.9137	0.93582	1.32331	0.74086
660.5	4	0.0899	0.9101	1.27763	1.71365	1.00872
671.5	5	0.0929	0.9071	1.62702	2.09141	1.28158
680.6	6	0.0954	0.9046	1.97991	2.46415	1.55595
688.8	7	0.0978	0.9022	2.34168	2.82162	1.83671
695.9	8	0.0998	0.9002	2.70528	3.17644	2.11828
702.3	9	0.1017	0.8983	3.07585	3.51899	2.40516
708.2	10	0.1035	0.8965	3.44943	3.85740	2.69317
749.7	20	0.1165	0.8835	7.29778	7.07937	5.62285

[a]Mole fraction in the liquid phase.

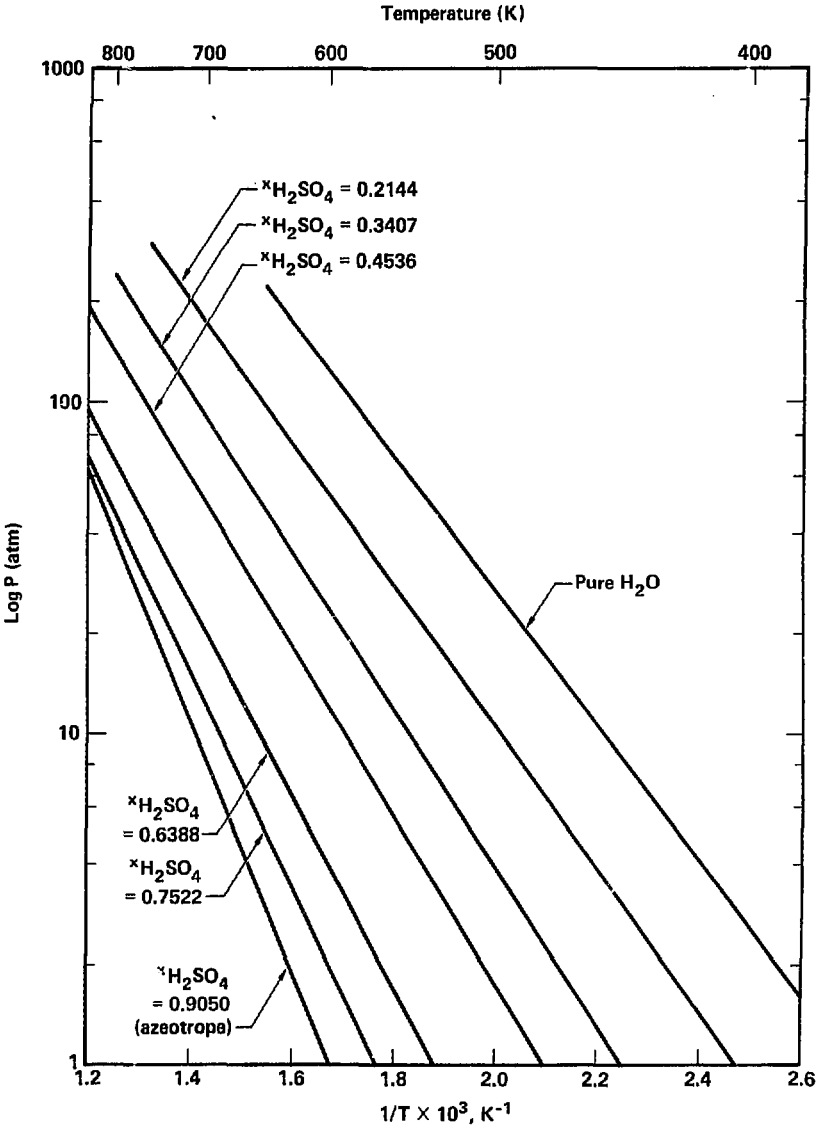

Fig. 4-4. Variation of total pressure above H_2O-H_2SO_4 mixtures as a function of composition and temperature. The curves include an extrapolation of Lennartz's data[10] to higher temperatures and pressures than the experimental determinations.

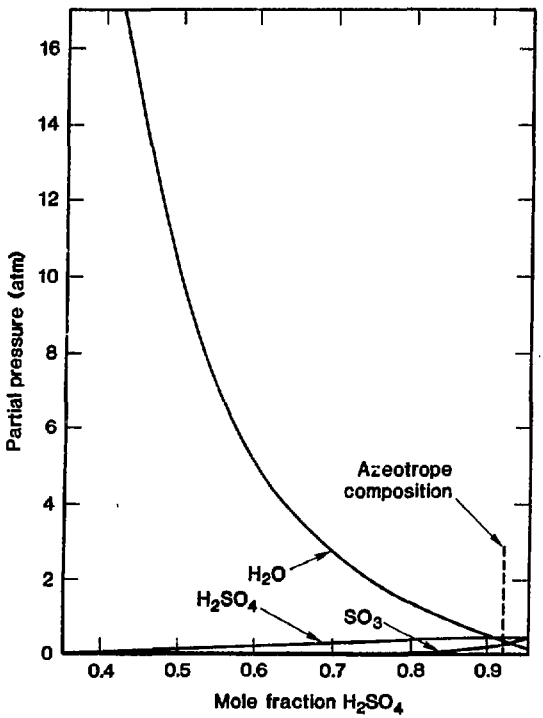

Fig. 4-5. Partial pressures of gaseous H_2O, H_2SO_4, and SO_3 above H_2O-H_2SO_4 mixtures at 600 K, based on the calculated values of Gmitro and Vermeulen.[14]

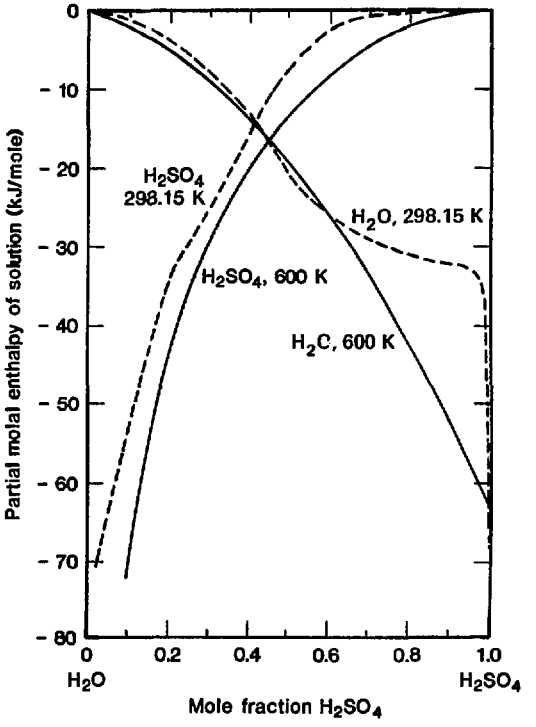

Fig. 4-6. Partial molal enthalpies of solution for H_2O and H_2SO_4 are shown for H_2O-H_2SO_4 mixtures at two temperatures. The curves at 298.15 K are from Giauque et al.,[15] and the curves at 600 K have been derived here based on the data of Lennartz.[10]

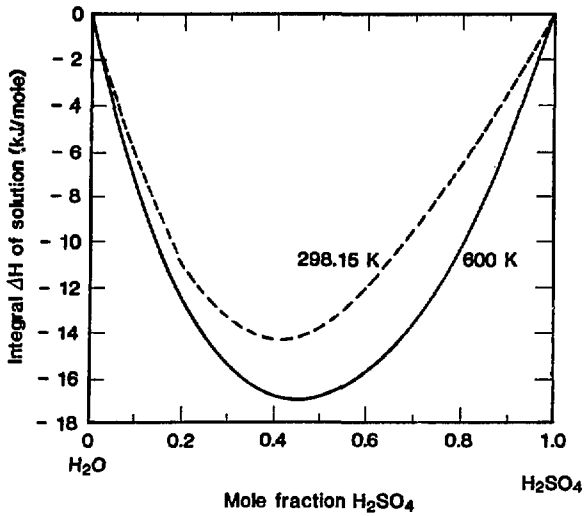

Fig. 4-7. Integral enthalpy of solution for H_2O-H_2SO_4 mixtures is shown for two temperatures. The curve at 298.15 K is from Giauque et al.,[15] and the one at 600 K has been derived here based on the data of Lennartz.[10] The data are presented for one total mole of solution.

of $H_2O(\ell)$ at the azeotropic composition by using the azeotropic relationships given by Reactions (13), (14), and (15) to derive the partial pressure of $H_2O(g)$ as a function of temperature based on Lennartz's data. A $\ln(p_{H_2O})$ vs $1/T$ plot then gives the enthalpy of vaporization of $H_2O(g)$ from enthalpy of vaporization of $H_2O(g)$ from the azeotropic composition, and subtracting out the enthalpy of vaporization from the reference state $H_2O(\ell)$ gives the enthalpy of exsolution (as before). These data, extending over the range of $x_{H_2SO_4} = 0.2$ to 0.9, allow us to construct the partial molal enthalpy of solution curve for H_2O at ~600 K, as shown in Fig. 4-6. The curve for H_2SO_4 at 600 K is then derived from the H_2O curve by using a Gibbs-Duhem integration procedure.

The integral enthalpies of solution (given in Fig. 4-7) are obtained by summing the partial molal enthalpies of solution as

$$\Delta H_I = x_{H_2O}\,\overline{\Delta H}_{H_2O} + x_{H_2SO_4}\,\overline{\Delta H}_{H_2SO_4} \quad . \tag{17}$$

Thus, the integral enthalpy of solution ΔH_I represents the solution enthalpy for one total mole of solution and must be multiplied by the sum of the moles of $H_2O + H_2SO_4$ involved when making calculations. It is more convenient for

our purposes to use integral rather than the partial molal enthalpies of solution for calculations. Interpolations and extrapolations can be made as needed in Fig. 4-7 to obtain data at intermediate and higher temperatures.

We obtained the values for the enthalpy of water vaporization from the hypothetical 1-atm reference state (see Fig. 4-8) as follows: We took data up to 500 K directly from the JANAF Tables,[12] whereas at higher temperatures we extrapolated down to 1 atm from higher pressure JANAF data. As is apparent in Fig. 4-8, there is a significant difference between the enthalpy of water vaporization in its 1-atm reference state and at saturation.

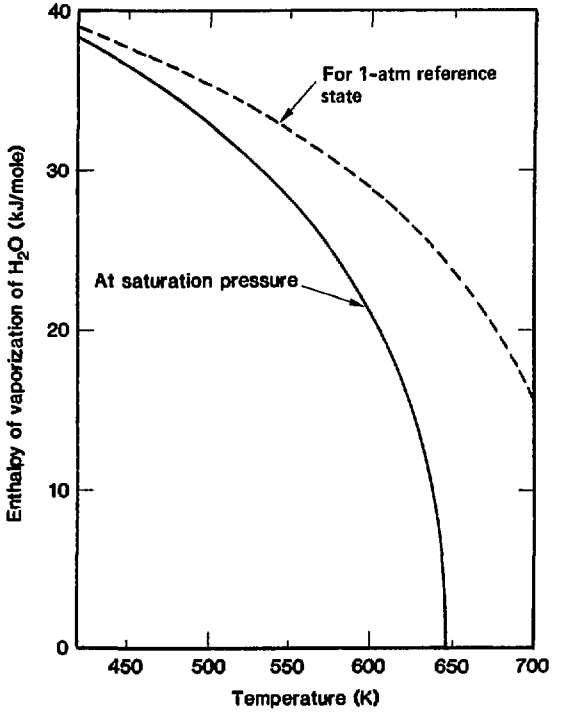

Fig. 4-8. Enthalpy of water vaporization is shown for both the hypothetical 1-atm reference state and at the equilibrium saturation pressure.

4.3.3.3 Data on Sensible Heats (Enthalpies). The area of greatest need for sensible heat (enthalpy increment) data is for aqueous H_2SO_4 as a function of composition (see Table 4-1). Data for the pure liquids and gases are either generally available in standard tabulations or can be obtained by extrapolations.

We can draw on two sources of data to estimate the enthalpy increments for aqueous H_2SO_4 : (1) values for $H_{600}-H_{298}$ derived from Lennartz's data,[10] and (2) the JANAF Tables,[12] which summarize enthalpy increments for several compositions ranging from $H_2SO_4 \cdot H_2O$ to $H_2SO_4 \cdot 6.5\ H_2SO_4$.

To illustrate the derivation of $H_{600}-H_{298}$ values from Lennartz's data, consider the solution reaction

$$0.5\ H_2O(\ell) + 0.5\ H_2SO_4(\ell) = 0.5\ H_2SO_4 \cdot H_2O(\ell) \quad . \tag{18}$$

Here, the pure liquids H_2O and H_2SO_4 in their 1-atm reference states are combined to produce a 50:50 mole ratio solution. The $\Delta H_{600}-\Delta H_{298}$ for the overall reaction is obtained from Fig. 4-7 and is found to be $-16.87 - (-13.92) = -2.95$ kJ/mol. This can be equat d to the difference in individual $H_{600}-H_{298}$ values between tne product $0.5\ H_2S \cdot H_2O(\ell)$ and the reactants. Thus, $X - 0.5(25.648) - 0.5(50.639) = -2.95$, and $X = 70.388$ kJ/mol for the $H_{600}-H_{298}$ value of $0.5\ H_2SO_4 \cdot H_2O$. Figure 4-9 summarizes the $H_{600}-H_{298}$ values thus derived as a function of composition across the $H_2O - H_2SO_4$ diagram.

We can now compare the $H_{600}-H_{298}$ values derived from Lennartz with the JANAF data (see Fig. 4-10). We find that agreement is good for the two compositions $H_2SO_4 \cdot H_2O$ and $H_2SO_4 \cdot 2\ H_2O$, but that a major discrepancy occurs in the more dilute H_2SO_4 concentrations. A comparision cannot be made at higher H_2SO_4 concentrations since JANAF data are not available. Moreover, we believe that the values derived from Lennartz's data are the more reliable. Further work is needed to develop the data base over the full range of temperatures required for the process studies.

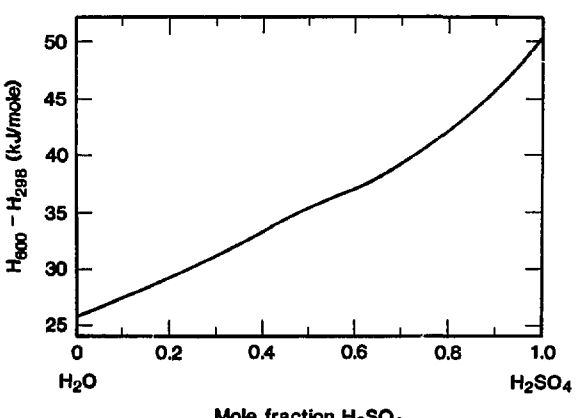

Fig. 4-9. Enthalpy increment $H_{600}-H_{298}$ shown as a function of composition for one total mole of H_2O-H_2SO_4 solution. The curve is based on the $H_{600}-H_{298}$ values for pure H_2O and H_2SO_4 in their 1-atm reference states plus the integral ΔH°s of solution given in Fig. 4-7.

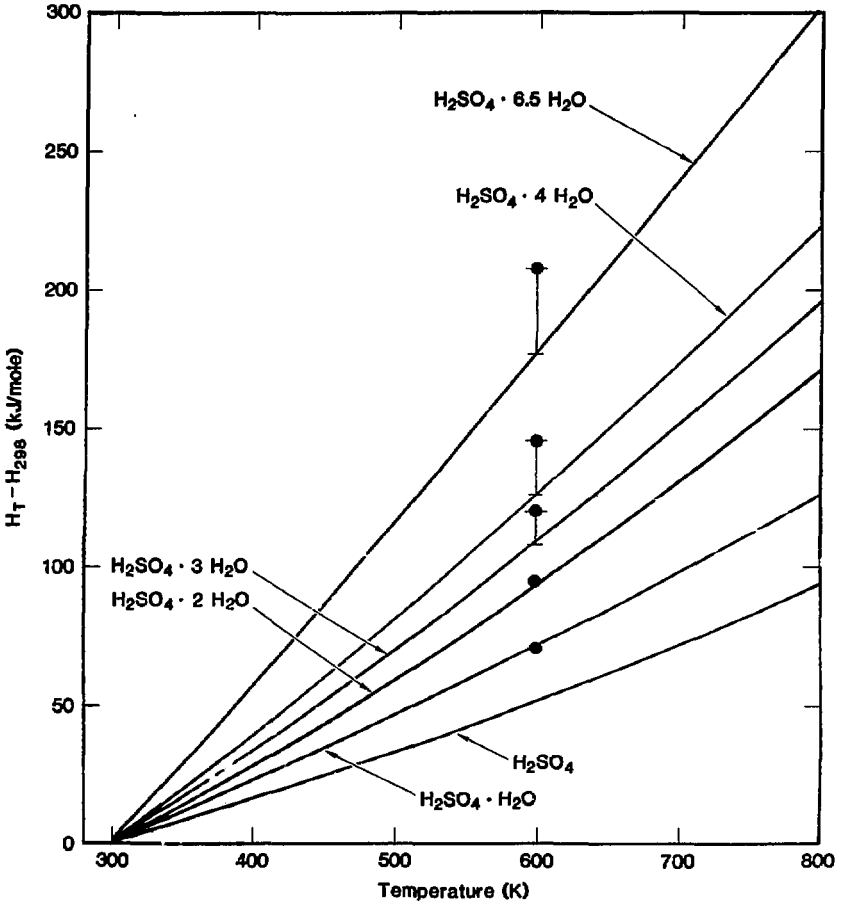

Fig. 4-10. Enthalpy increments $H_{600}-H_{298}$ calculated from Lennartz's data[10] (circles) compared with the JANAF data[12] (solid curves) for various H_2O-H_2SO_4 mixtures. It is apparent that large differences occur in the presence of higher water content. No JANAF data are available for comparison in the region between 50 mole % H_2SO_4 and the 90 mole % azeotrope.

Enthalpy increments for the other chemical substances in Section II are summarized in Fig. 4-11. Note the difference in enthalpy increments for saturated liquid H_2O and the 1-atm liquid H_2O at reference state. Note also the differences in enthalpy increments for steam taken at different pressures.

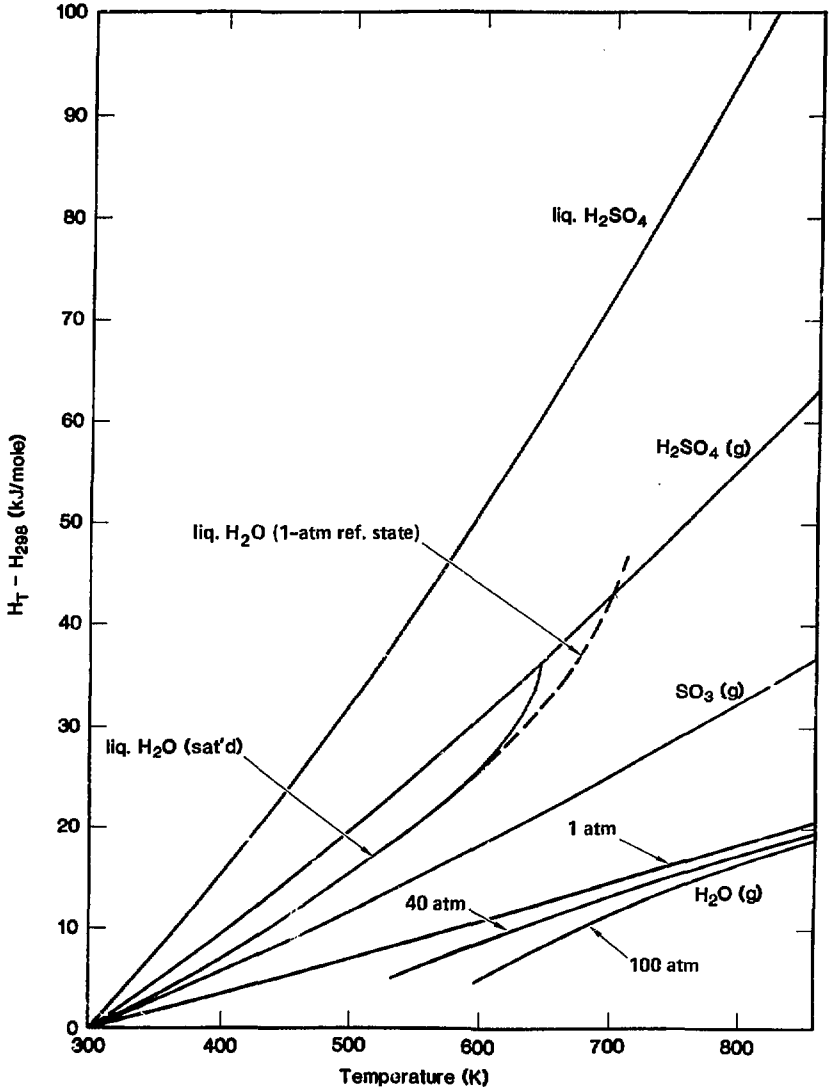

Fig. 4-11. Enthalpy increments above 298.15 K are summarized for various liquid and gaseous species.

REFERENCES

1. R. W. Werner, F. Ribe, and O. Krikorian, Synfuels From Fusion-Producing Hydrogen With the Tandem Mirror Reactor and Thermochemical Cycles, Lawrence Livermore National Laboratory, Livermore, CA, UCID-18909, Vols. I and II (1981).

2. G. E. Besenbruch, K. H. McCorkle, J. H. Norman, D. R. O'Keefe, J. R. Schuster, and M. Yoshimoto, "Hydrogen Production by the GA Sulfur-Iodine Process. A Progress Report," in Hydrogen Energy Progress, Proceedings of the 3rd World Hydrogen Energy Conference, Tokyo, Japan, 23-26 June 1980, Vol.1, edited by T. N. Veziroglu, K. Fueki, and T. Ohta (Pergamaon Press, Oxford, 1980), p. 243.

3. J. H. Norman, K. Mysels, R. Sharp, and G. G. Williamson, "Studies of the Sulfur-Iodine Thermochemical Water-Splitting Cycle," in Hydrogen Energy Progress, Proceedings of the 3rd World Hydrogen Energy Conference, Tokyo, Japan, 23-26 June 1980, Vol.1, edited by T. N. Veziroglu, K. Fueki, and T. Ohta (Pergamaon Press, Oxford, 1980), p. 257.

4. D. R. O'Keefe, and J. H. Norman, "The Liquid Hydrogen Iodide Decomposition Process Step for Water Splitting Applications," in Hydrogen Energy Progress, Proceedings of the 3rd World Hydrogen Energy Conference, Tokyo, Japan, 23-26 June 1980, Vol.1, edited by T. N. Veziroglu, K. Fueki, and T. Ohta (Pergamaon Press, Oxford, 1980), p. 277.

5. P. W. T. Lu and R. L. Ammon, "Development Status of Electrolysis Technology for the Sulfur Cycle Hydrogen Production Process," in Hydrogen Energy Progress, Proceedings of the 3rd World Hydrogen Energy Conference, Tokyo, Japan, 23-26 June 1980, Vol.1, edited by T. N. Veziroglu, K. Fueki, and T. Ohta (Pergamon Press, Oxford, 1980), p. 439.

6. H. A. Irwin and R. L. Ammon, "Status of Materials Evaluation for Sulfuric Acid Vaporization and Decomposition Applications," in Hydrogen Energy Progress, Proceedings of the 3rd World Hydrogen Energy Conference, Tokyo, Japan, 23-26 June 1980, Vol.4, edited by T. N. Veziroglu, K. Fueki, and T. Ohta (Pergamaon Press, Oxford, 1981), p. 1977.

7. D. van Velzen and H. Langenkamp, "Status Report on the Operation of the Bench-Scale Plant for Hydrogen Production by the Mark-13 Process," in Hydrogen Energy Progress, Proceedings of the 3rd World Hydrogen Energy Conference, Tokyo, Japan, 23-26 June 1980, Vol.1, edited by T. N. Veziroglu, K. Fueki, and T. Ohta (Pergamaon Press, Oxford, 1980), p. 423.

8. A. Broggi, K. Joels, G. Mertel, M. Morbello, and B. Spelta, "CHRISTINA--A Process for the Decomposition of Sulfuric Acid," in Hydrogen Energy Progress, Proceedings of the 3rd World Hydrogen Energy Conference, Tokyo, Japan, 23-26 June 1980, Vol.4, edited by T. N. Veziroglu, K. Fueki, and T. Ohta (Pergamon Press, Oxford, 1981), p. 1929.

CONTENTS

9. P. J. Fiebelmann and G. H. Schuetz, "Technological Aspects in HBr Electrolysis Development," in Hydrogen Energy Progress, Proceedings of the 3rd World Hydrogen Energy Conference, Tokyo, Japan, 23-26 June 1980, Vol.4, edited by T. N. Veziroglu, K. Fueki, and T. Ohta (Pergamaon Press, Oxford, 1981), p. 1949.

10. H. Lennartz, Experimental Investigation of the Vapor-Liquid Phase Equilibrium of the System H_2O-H_2SO_4, doctoral thesis submission at RWTH Aachen (University of Aachen), March 31, 1980. We acknowledge the advance availability of this data to us by Professors H. Hartmann and K. F. Knoche of the University of Aachen prior to publication.

11. O. H. Krikorian, Hydrogen production Based on Magnetic Fusion, Lawrence Livermore National Laboratory, Livermore, CA, UCRL-86600 (1981).

12. D. R. Stull and H. Prophet, JANAF Thermodynamic Tables, Second Edition, U.S. National Bureau of Standards, Washington, D.C. (1971), with supplements through December 31, 1979, from M. B. Chase, Project Director, The Dow Chemical Company, Midland, MI.

13. Steam and Air Tables in SI Units, edited by T. F. Irvine, Jr., and J. P. Hartnett (Hemisphere Publishing Corp., Washington, D.C., 1976).

14. J. I. Gmitro and T. Vermeulen, Vapor-Liquid Equilibria for Aqueous Sulfuric Acid, Lawrence Berkeley National Laboratory, Berkeley, CA, UCRL-10886 (1963).

15. W. F. Giauque, E. W. Hornung, J. E. Kunzler, and T. R. Rubin, J. Am. Chem. Soc. 82, 62 (1960).

5 Interfacing the Sulfur–Iodine Cycle

CONTENTS

5. Interfacing the Sulfur-Iodine Cycle

A viable fusion-powered thermochemical synfuels economy will only become a reality when the thermal output of fusion reactors is closely matched to the load demands of the thermochemical process. Likewise, thermal energy sources within the chemical process must be matched to the heat demands of the same chemical process as well as to the heat requirements of the power production systems or power bottoming cycles.

Since we developed the TMR-driven synfuels plant two years ago (shown in Fig. 5-1) we have gained an even deeper understanding of the factors governing the economic match of the fusion reactor to the synfuels plant.[1] Last year[2] we made major modifications to the H_2SO_4 processing sections and applied energy conservation techniques to the HI purification section. We have since further improved the H_2SO_4 section to the advanced stage described for this improved design. We discuss details of the preliminary design of each process unit in the chemical plant, including heat and mass flow, equipment sizes, and safety. Our findings are based on chemical processes that have been demonstrated by laboratory experiments.

5.1 BASE CHEMICAL PROCESS

GA Technologies' water-splitting cycle[3,4] is described in the following four reactions:

$$2\ H_2O + SO_2 + X\ I_2 \rightarrow H_2SO_4 + 2\ HI_x \quad , \tag{5-1}$$

$$H_2SO_4 \rightarrow H_2O + SO_2 + 1/2\ O_2 \quad , \tag{5-2}$$

$$2\ HI_x \rightarrow 2\ HI + (x-1)\ I_2 \quad , \tag{5-3}$$

$$2\ HI \rightarrow H_2 + I_2 \quad . \tag{5-4}$$

These equations represent three chemical reactions and one separation process. The species HI_x represents an aqueous complex of HI and I_2 formed by Reaction 1. The H_2SO_4 product of Reaction 1 is obtained as a moderately concentrated aqueous solution that is immiscible with HI_x.

We have divided the overall process into five sections for design purposes. Sections I through IV roughly correspond to the four reactions and Section V represents the heat and energy transmission equipment required to match the fusion heat source to the chemical process.

Since 1974 GA Technologies has developed the sulfur-iodine cycle along three parallel and mutually supportive lines:

- Chemical investigations,
- Engineering flowsheet development,
- Process demonstration.

Chemical investigations are the basis for developing the engineering flowsheets and demonstrating the process, and they in turn give impetus and direction to further chemical investigations. Likewise, each of these tasks raises new questions in its own area.

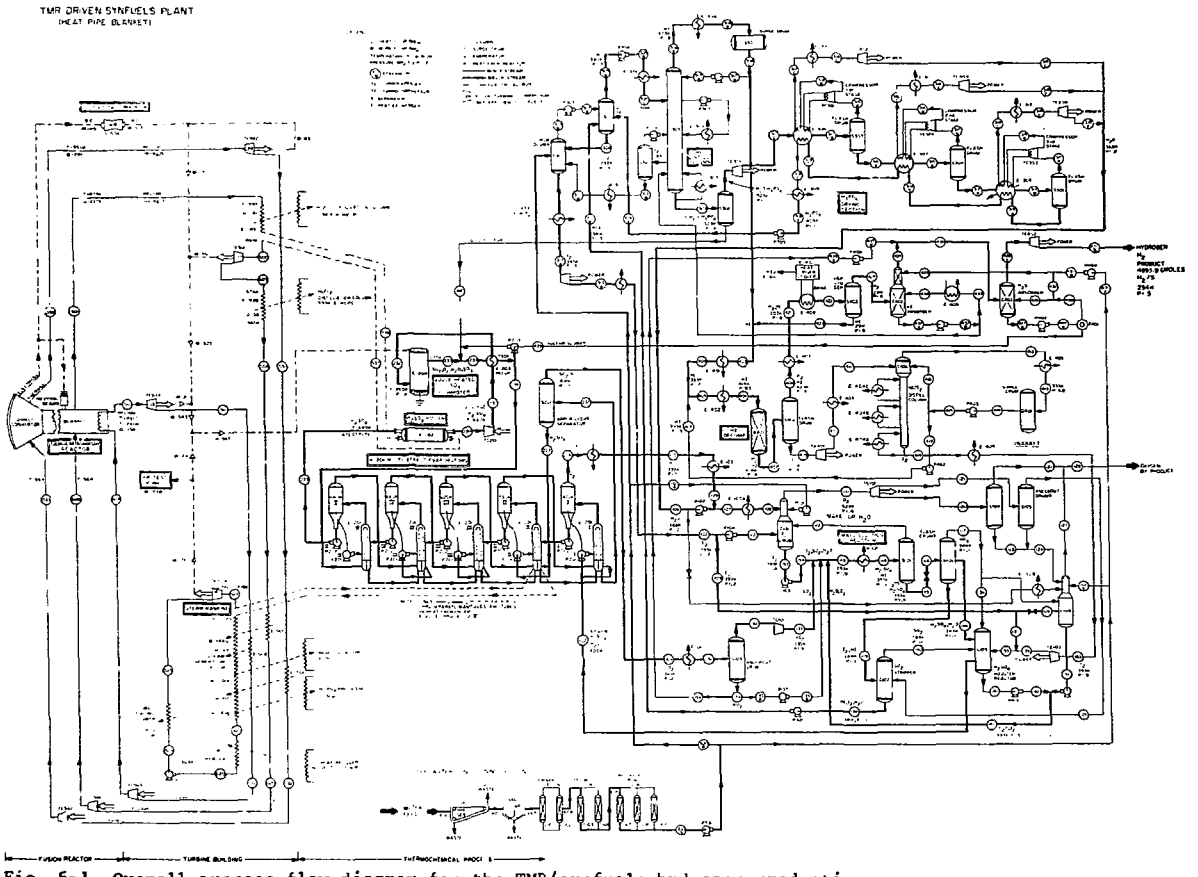

Fig. 5-1. Overall process flow diagram for the TMR/synfuels hydrogen production plant (1981 version).

5.2 RECENT DEVELOPMENTS IN PROCESS CHEMISTRY

GA Technologies water splitting process is continually being upgraded. The following are two recent innovations to the process: (1) HI decomposition by homogeneous catalysis,[3] which will eventually be incorporated into the fusion synfuels design; and (2) the H_2SO_4 chemical energy storage system,[5] which has the potential for long-term energy storage. Long-term storage could permit a fusion synfuels plant to keep operating while the TMR is not operating because of scheduled or unscheduled maintenance. This system could also provide on-site power for cold startup of the TMR.

5.2.1 Hydrogen Iodide Decomposition by Homogeneous Catalysis

The present version of the sulfur-iodine water-splitting process uses HI decomposition in the liquid phase. Calculations indicate that high conversion levels are possible using such a scheme, and indeed high conversions have been verified experimentally.[6] In addition, extrapolation of the rate data to high process temperatures yields rates high enough to produce a viable HI decomposition process. GA Technologies obtained these rate data by extrapolating measured rate data from lower temperatures and pressures in batch studies performed on supported platinum and ruthenium catalysts.

Recently, GA Technologies obtained some data for a supported platinum catalyst at closer to actual engineering temperatures and pressures in a new, flowing-liquid HI bench-scale system. The rate value obtained supports the use of the extrapolated lower temperature data and thus verifies the present flowsheet and equipment sizing calculations.

Further in-depth studies, however, revealed that at least platinum, whether supported or not, does dissolve in the liquid HI to a non-negligible degree. This requires the use of some kind of catalyst recovery and remanufacture scheme, which is commonplace in the chemical industry but adds to the complexity and operational and capital costs of the overall process. Because of this additional requirement, homogeneous catalysis began to be considered as a means of decomposing HI, along with several separation schemes inherent in the practical application of homogeneous catalysis.

In one homogeneous catalyst concept[3] the catalyst is innately separated from the HI liquid, thereby allowing the catalyst to be totally recycled to the reactor. The concept is based on some unique findings concerning the phase behavior of $HI-I_2H_2O$ mixtures. For certain compositions of these three chemicals, two liquid phases in equilibrium can exist. One phase is a very dry phase of HI and I_2; the other is an aqueous phase containing both I_2 and HI. It has been found that in this latter phase certain homogeneous catalyst compounds tend to concentrate. This means that the aqueous phase essentially acts as the catalyst carrier and can be recycled to the HI decomposition reactor without having to recover the catalyst.

The potential advantages over a process that uses heterogeneous catalysts with the need to recover and remanufacture 100% of the catalyst are clear. We have developed a flowsheet of the proposed homogeneous process (but at too late a date for inclusion in this overall process design), and have also identified the major areas to be investigated. We still need to identify the solubility and distribution of the catalyst in the process train fluids at engineering

conditions, discover the best area of the HI-I_2-H_2O phase diagram in which to work, and determine the best schemes for catalyst recycle. The results of this work have supported this concept as a viable engineering process.

5.3 PLANT DESIGN STATUS

The present chemical plant design coupled to the MARS reactor is based on the most recent integrated flowsheets. The flowsheets for the main reaction (Section I), HI purification (Section III), and HI decomposition (Sec. IV) are the same as for previous reports.[2] We have revised the H_2SO_4 processing section (Section II) to match the thermal energy available from the MARS blanket. We have increased thermal energy recovery of the H_2SO_4 concentration step while still maintaining a good thermal match to the blanket heat source. Also, at this level of preliminary design, the process equipment size was estimated to determine approximate equipment costs. The design calculations use standard chemical engineering correlations for the sizing calculations. When the required physical and transport properties were unavailable we approximated them.

5.4 SECTION I: MAIN SOLUTION REACTION STEP

5.4.1 Design Considerations

The main solution reaction step includes all equipment associated with the chemical reaction

$$2H_2O(L_1) + SO_2(g) + I_2(L_2 \leftarrow H_2SO_4(L_1) + 2HI(L_2), \qquad (5\text{-}6)$$

where gaseous SO_2 reacts with an excess of molten iodine and water to produce two immiscible liquid phases. The designation L_1 indicates that water is the major component in the H_2SO_4 product phase and L_2 indicates that iodine is the major component in the HI product phase. The H_2SO_4 phase, which is the lighter (lower density) phase, also contains a trace of iodine. The heavy phase, referred to as HI_x because it contains excess iodine, also contains water. The main solution reaction is exothermic, and Section I requires no heat input from the fusion reactor but exports a significant quantity of low-grade heat to a power bottoming cycle. The Section I process is shown schematically in Fig. 5-2.

Even though Section I requires no heat input from the fusion reactor, the design of the main solution reaction step has a major influence on the overall process efficiency and thus on the reactor size and the hydrogen production cost. Although variations in heat and power recovery within Section I affect efficiency, the composition and temperature of the light phase flowing to process Section II (the H_2SO_4 processing step) and of the heavy phase flowing to Section III (the HI concentration step) strongly influence the overall efficiency of the process. In the interest of efficiency, both streams should leave Section I at the highest possible temperature and acid concentration. Because the equilibrium of an exothermic reaction shifts toward the reactants as the temperature is raised, a compromise must be made between high temperature and high acid concentration

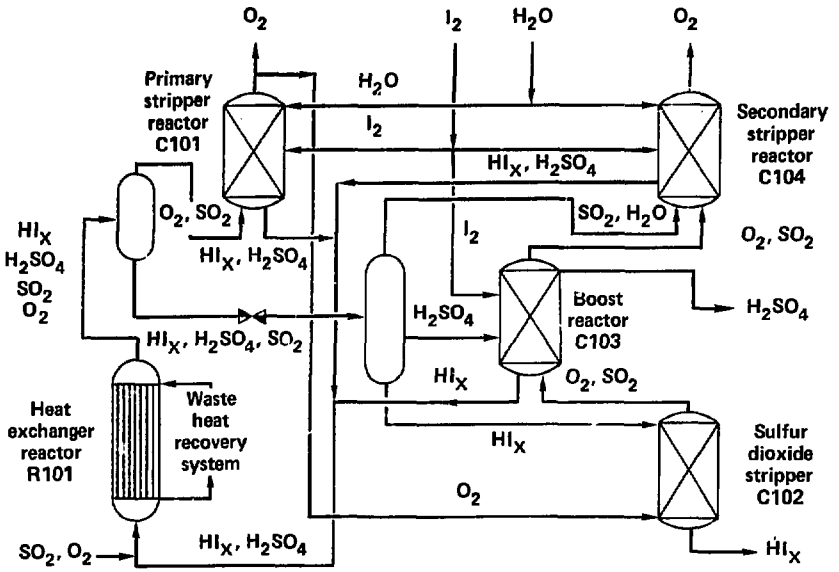

Fig. 5-2. Schematic of Section I, reaction of SO_2 with iodine and water to give H_2SO_4 and HI_x as immiscible liquid products.

in the products. In deciding the operating conditions for Section I we made some economic trade-off calculations, but a full-scale process optimization was not in the scope of this work. The basis for the resulting decisions as well as for the rest of this study may best be termed "engineering judgment." When trade-off calculations were not definitive, the decision was usually made on the side of high efficiency, not low capital cost.

Two main factors influenced the design of Section I: (1) the large quantity of heat produced by the main solution reaction must be removed; and (2) the combination of hydrogen iodide and iodine in the heavy aqueous phase is extremely corrosive to materials normally used for heat transfer surfaces. The only metals known to resist HI_x are refractory metals such as niobium, tantalum, and molybdenum. The present design uses niobium for heat transfer surfaces that come in contact with HI_x.

Niobium is relatively expensive. Therefore, to reduce the capital cost of Section I we used a number of design techniques to improve heat transfer and decrease the amount of niobium required. Some of these are:

1. Cool feed streams to Section I. Before carrying out the main solution reaction, we transfer the heat from the Section I feed streams to the power bottoming cycle. This involves less expensive heat transfer materials than niobium and reduces the amount of heat transferred from the reaction products of the main solution reaction.

2. Operate adiabatically. Instead of cooling the reaction products from 393 to 368 K (to shift the equilibrium toward the products) and then reheating the separated products, we operate adiabatically and maintain the desired production rate of the main solution reaction by increasing the iodine concentration to provide the needed shift in the equilibrium.

3. Use direct-contact heat exchange. Where possible, we employ direct contact heat exchange between immiscible liquid phases or gas and liquid phases.

4. Apply enhanced heat transfer techniques. Using two-phase gas-liquid flow through the heat exchanger gives higher than normal convective heat transfer coefficients. Spiral-fluted tubing provides enhanced heat transfer and, as a result of the wall stiffening due to the fluting, thinner tube walls are possible.

5.4.2 Heat Exchanger Reactor

Almost 52% of the chemical reaction that forms HI and H_2SO_4 takes place in the heat exchanger reactor (R-101 in the flow diagram of Fig. 5-2) and in the piping immediately preceding the reactor. The reactor selected is a shell and tube heat exchanger with fixed tube sheets. The vessel, tube sheets, and heads are fabricated from mild steel. The heads are lined with fluorocarbon and the spiral-fluted niobium tubes are welded to a niobium tube sheet liner. The process fluid is on the tube side of the heat exchanger and the shell side is part of the power bottoming cycle.

Upstream of the heat exchanger, the SO_2/O_2 from Section II (H_2SO_4 processing) is mixed with the predominantly iodine stream from the boost reactor (C-103) and aqueous streams from the scrubbing reactors (C-101 and C-104). The combined streams react exothermically as they flow through a fluorocarbon-lined pipe and into the heat exchanging reactor. The pressure drop through the heat exchanger reduces the system pressure from an initial 0.50 to 0.44 MPa, at which point the temperature reaches 393 K. At the exit of the heat exchanger the O_2 is removed from the stream in the first of two separators (S-101). In the second separator (S-102), operating at 0.11 MPa, three phases separate: the heavy liquid phase (HI_x), the light liquid phase (H_2O/H_2SO_4), and a gas phase (SO_2 and steam). The vaporization of water and SO_2 causes the temperature to decrease from 393 to 385 K.

5.4.3 Lower Phase Sulfur Dioxide Stripper

The lower phase solution (HI_x) is saturated with SO_2, which, when allowed to remain, forms sulfur and H_2S by way of tramp reactions. An oxygen recycle stream strips most of the SO_2 in a packed bed stripper (C-102), thus minimizing the tramp reactions. A minimum amount of oxygen is used for this operation because the evaporation of water into the oxygen cools the HI_x, requiring more heat input in Section III (HI purification). With a 10% O_2 recycle, the HI_x is cooled from 385 to 381 K.

The stripper, sized for operation at 70% of flooding, is a standard packed-column design. The fluorocarbon-lined mild steel vessel is packed with

50-mm ceramic Raschig rings. Because the operating pressure is near atmospheric, a glass-lined steel vessel is a possible option but would require fluorocarbon packing to prevent liner damage.

5.4.4 Boost Reactor

In the boost reaction, the H_2SO_4 concentration of the light phase is increased from 50 to 57% by contact with molten iodine in the presence of SO_2. The increased H_2SO_4 concentration is realized through the action of the main solution reaction. Water is used up by reaction with SO_2 and I_2 to form H_2SO_4 and HI. More than 7% of the total chemical reaction in Section I occurs in the boost reactor. Because the contact is performed in a counter-current manner, the reactor also acts as a direct-contact heat exchanger, raising the temperature of the H_2SO_4 stream from 383 to 393 K.

Although the mechanical design of the boost reactor is straightforward, i.e., a fluorocarbon-lined mild steel vessel packed with 50-mm ceramic Raschig rings, the sizing calculations are not. Standard counter-current-packed columns operate with either a gas rising through a descending liquid phase or a light liquid phase rising through a descending heavy liquid phase. The boost reactor has both a gas phase (SO_2 in O_2) and a light liquid phase (H_2SO_4 and water) rising through the descending heavy liquid phase (I_2). The present design is based on adding the cross-sectional areas required if the gas and light liquid separately come in contact with the heavy liquid. This is a very conservative approach. We believe that a design based on information gained in a pilot plant would result in a smaller boost reactor vessel.

5.4.5 Scrubbing Reactors

The oxygen is purified before it is discharged to the atmosphere in the scrubbing reactors. The packed column reactors operate in a titration mode in which enough iodine is added to the scrub water in the lower part of the column to react stoichiometrically with the SO_2 present in the oxygen. In the upper part of the column the oxygen is washed with pure water. The primary scrubbing reactor (C-101) operates at 0.44 MPa to purify the gaseous product of the heat exchanger reactor (R-101). More than 19% of the Section I reaction takes place in the primary scrubbing reactor. Almost 22% of the total reaction takes place in the secondary scrubbing reactor at 0.10 MPa. The secondary scrubber cleans up the oxygen stream exiting the boost reactor as well as the steam/SO_2 stream produced during depressurization of the liquid reaction product coming from the heat exchanger reactor.

Both scrubbing reactors perform a second function as direct contact heat exchangers. Oxygen leaving the process is cooled to near ambient conditions while it preheats the water entering the process. The scrubber vessels are composed of fluorocarbon-lined mild steel and the packing is 50-mm ceramic Raschig rings. Pilot plant tests may demonstrate reduced vessel costs. The upper portions of the scrubber contain only water and oxygen so that no lining should be required in this area. Depending on the temperatures reached in the lower portions of the scrubber, less expensive linings may be possible.

5.4.6 Heat and Power Recovery

The total heat transferred to the power bottoming cycle from Section I is 802 MW_t. The majority of this is transferred by means of the heat exchanger reactor, but significant quantities of heat are also transferred from the hot water products of Sections II and III and from the SO_2/O_2 product of Section I. Because the heat transfer materials used for water and SO_2 are much less expensive than the niobium used in the heat exchanger reactor, there is the potential for further cost reduction by performing more of the cooling on water and SO_2 streams. Ultimately, economics will determine the optimum split in heat transfer duties on the basis of minimum hydrogen production cost.

A total of 5.5 MW is recovered in Section I using turbines for pressure reduction. Preliminary indications are that the turbines are economic, but a final determination must await an analysis based on the hydrogen production cost resulting from this study.

5.5 SECTION II: SULFURIC ACID PROCESSING

5.5.1 Design Considerations

The H_2SO_4 processing step takes H_2SO_4 from Section I, decomposes it, and returns the resulting SO_2, O_2, and H_2O back to Section I. The process flow diagram is given in Fig. 5-3.

The three major unit operations in Section II are H_2SO_4 concentration, vaporization, and decomposition. Equipment layout and designs are based on previous work, but we have made completely new flowsheets for the section to match the MARS blanket. Newly available thermodynamic data were used to make the flowsheets.

5.5.2 Acid Concentration

Early versions of the sulfur-iodine water-splitting process relied on vapor recompression to achieve high thermodynamic efficiency, though at high capital cost. We tried several techniques to recover the heat of vaporization of the water removed from the H_2SO_4 without resorting to vapor recompression. These included the use of multi-effect evaporators, pressure-staged flash evaporators (adiabatic and nonadiabatic), and column evaporators. However, it became evident that no single technique could achieve the desired goal, so we used a combination of four different concentration techniques in the final flowsheet.

We used staged isobaric boiling at 7.5 MPa to remove water at useful steam temperatures. Low pressure distillation concentrates the acid to its final azeotropic composition. Two adiabatic flash stages at 2.0 and 0.5 MPa match the isobaric staged boiling to the low pressure distillation column. Finally, staged partial condensation removes H_2SO_4 from the decomposer product along with a minimum of water.

The isobaric staged boiling takes place in what can be best described as a horizontal distillation column. The design is patterned after the H_2SO_4 vaporizer described in previous work and shown in Fig. 5-4. The horizontal

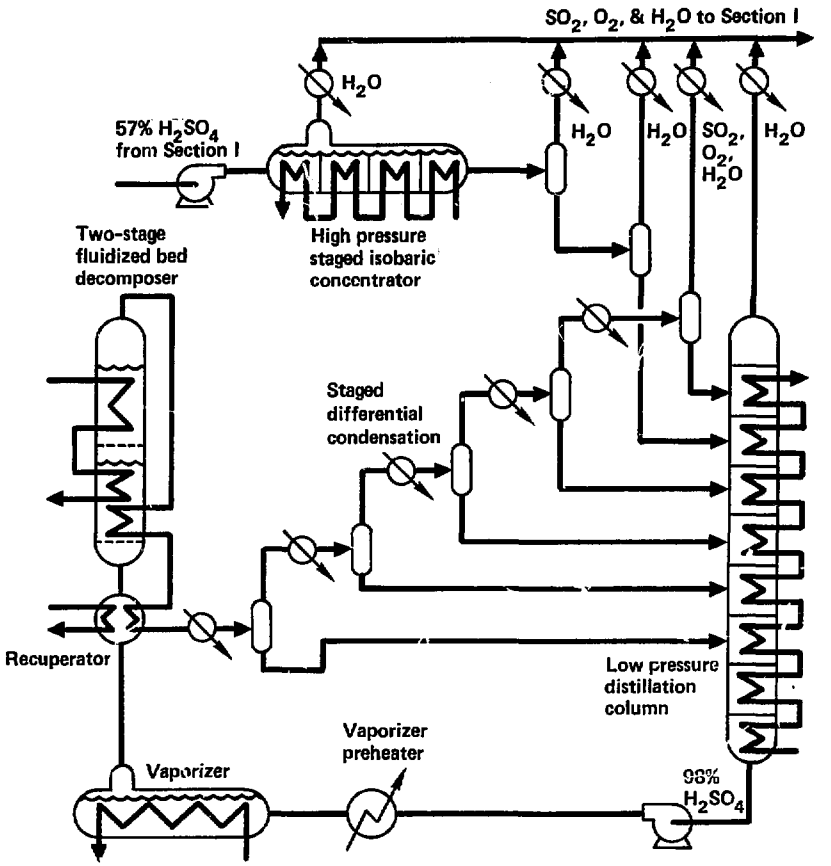

Fig. 5-3. Schematic of Section II, concentration and decomposition of H_2SO_4.

vessel is lined with fluorocarbon to protect the mild steel from the H_2SO_4 and then lined with brick to protect the fluorocarbon from heat. Heat is supplied through siliconized SiC tubes to vaporize the water. The vessel is partitioned into multiple stages by weirs made from acid brick. Above the weirs the vapor space is interconnected with the vapor outlet at the low-acid-concentration end of the unit. Mixing the vapors from many stages produces a vapor composition typical of the mass average temperature. The vapors are cooled

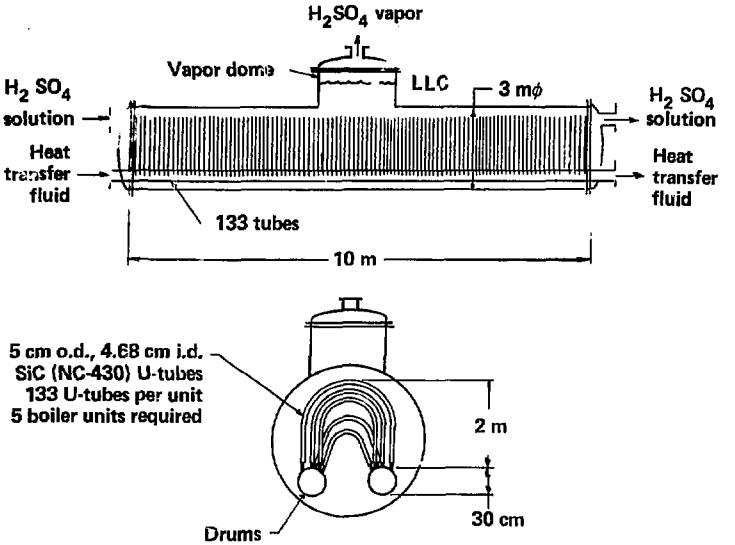

Fig. 5-4. Design for the H_2SO_4 azeotrope vaporizer.

slightly to condense the trace of acid present, and the separated acid is added to the acid product of the concentrator. After the acid is removed, the steam passes through a total condenser, transferring the heat of condensation to the evaporators in Section III.

The acid, concentrated to 79% at 7.5 MPa, is flashed first to 2.0 MPa, then to 0.5 MPa, and again to 0.02 MPa. The vapors from the first two flashes are treated by partial condensation to remove H_2SO_4 and are then recycled to Section I. The combined liquid/vapor stream from the third flash is fed to the low pressure distillation column.

An eight-stage distillation column completes the concentration of the acid up to 98%. Because the column must accommodate a large variation in liquid rates over its length, a tray-type column is preferred over a packed column. Ceramic internals are used in the form of trough-type trays. The bottom reboiler and the intermediate reboilers are again constructed with siliconized SiC U-tubes. Each tray, except for the top, has its own intermediate reboiler.

The product gases from the decomposer are subjected to five stages of partial condensation to remove the undecomposed acid along with a minimum of water. The liquid products from the partial condensation stages are returned to the atmospheric distillation column, with the liquid from the final stage providing column reflux.

5.5.3 Sulfuric Acid Vaporizer

The H_2SO_4 vaporizer is a particularly challenging design problem because either ceramic materials or high-silicon metallic alloys need to be used to simultaneously withstand both the corrosion from H_2SO_4 and the 3.0-MPa pressure from the helium heat transfer fluid.

Our best choice is to use siliconized SiC U-tubes for the heat exchangers in the H_2SO_4 vaporizer. The Norton Company[7] has used this approach in conjunction with AiResearch, Inc., for high pressure (5-MPa) helium "heat exchanger applications." We developed a special geometric configuration that established a rough optimization between the heat transfer and pumping losses in the helium and the boiling instabilities that could occur in the liquid H_2SO_4. This configuration is shown in Fig. 5-4.

5.5.4 Sulfur Trioxide Decomposer

The decomposer consists of multi-staged catalytic fluidized bed reactors operating at 1100 K in the last stage. Each unit contains internal heat exchanger tubes to provide the heat required to drive the highly endothermic SO_3 decomposition reaction. Final conversion of 64% is achieved using platinum on Zr_2O_3. The less expensive Fe_2O_3 catalyst can be used at 1100 K, but it loses its catalytic activity at significantly lower temperatures as a result of sulfation.[8] Noble metal catalysts on nonsulfating supports may be used over the whole temperature range. Details of a four-stage fluidized bed decomposer are given in Sec. 8 of this volume.

5.5.5 Decomposer Recuperator

The decomposer recuperator is a heat exchanger unit that preheats the feed to the decomposer using heat from the hot SO_2, O_2, H_2O, and SO_3 that leave the decomposer. This unit is important because without it the blanket would have to supply a larger quantity of sensible heat in the temperature range of 680 to 1000 K. In addition to the sensible heat requirement, additional heat is, of course, required to supply the endothermic heat for decomposing SO_3 into SO_2 and O_2. Recuperation cannot provide the total sensible heat required to treat the H_2SO_4 vapors from the boiling point to the decomposer inlet temperature because the heat needed to decompose H_2SO_4 to H_2O and SO_3 must be provided over this temperature range. The recuperator thus includes a "boost" loop of TMR-supplied heat. This concept is difficult to design because it is a gas-to-gas heat exchanger and these types of units characteristically have very low heat transfer coefficients. The design we evolved is a techno-economic compromise. We used Incoloy-800H in a standard shell and tube configuration, as shown in Fig. 5-5.

5.5.6 Decomposer Coolers

The decomposer cooler continues cooling the decomposer product after recuperation is no longer possible. Heat removed in the decomposer coolers is supplied to the low pressure still and the multistage isobaric flash preheater. Sulfuric acid condenses out as the decomposer products are cooled. This H_2SO_4

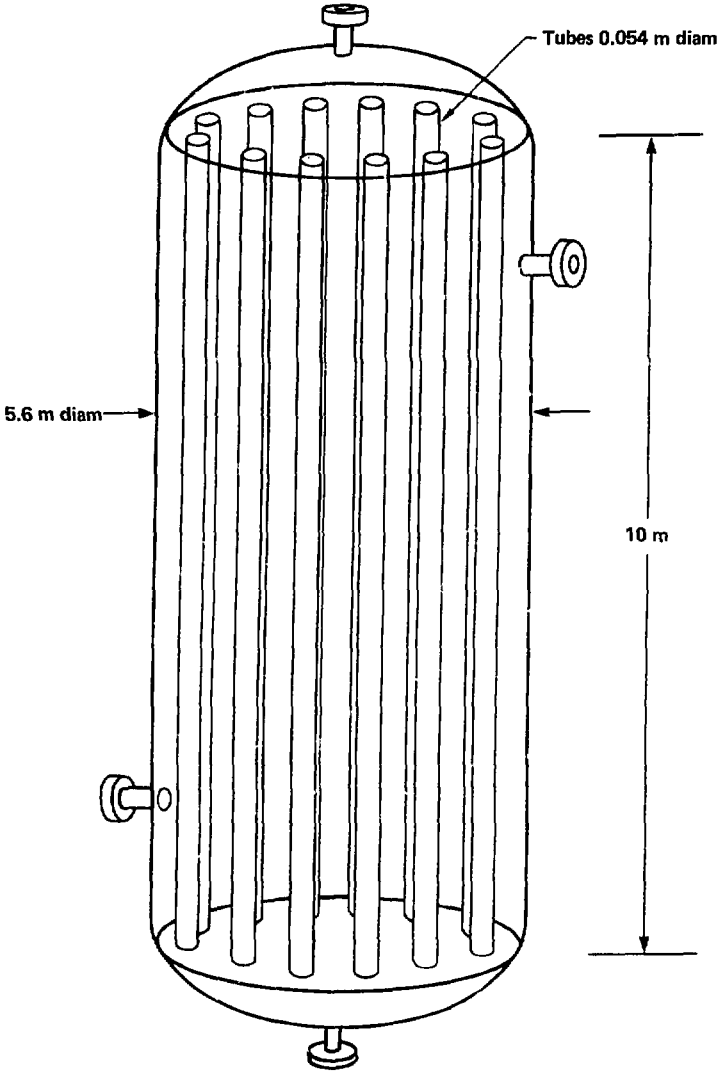

Fig. 5-5. Design for the SO_3 decomposer recuperator.

is removed in several stages. The liquid phase from the final cooler is predominantly water; therefore, it is returned to Section I along with the gases.

Silicon carbide is required where H_2SO_4 is condensing. At high temperatures, before the onset of condensation, Incoloy 800H would suffice except that SiC is required for boiling H_2SO_4 on the cold side of the tubes. After the majority of the H_2SO_4 has been condensed and decanted, more conventional construction materials can be used. In the low temperature region the requirement to heat 57% H_2SO_4 dominates the material selection.

5.6 SECTION III: HYDROGEN IODIDE CONCENTRATION STEP

5.6.1 Design Considerations

The HI concentration step entails separating a mixture of HI, I_2, and H_2O (HI_x) into its component parts. A simplified flow diagram of Section III is presented in Fig. 5-6. The iodine and water are separately returned to Section I, the main solution reaction step, and the HI is decomposed in Section IV of the process. The use of H_3PO_4 as an extractive distillation agent, first proposed in 1975,[9] is still the reference process for HI purification. The alternative process, liquid HBr extraction, although attractive from a theoretical standpoint, is not yet able to compete with the H_3PO_4 process in terms of efficiency.

The system HI-H_2O forms a maximum boiling azeotrope at a composition of 57% HI, which is approximately the composition on HI_x of an iodine-free basis. Iodine is held in the HI-H_2O solution through the formation of polyiodides such as HI_3, HI_5, HI_7, HI_9, etc., which are formed only in the presence of water. Adding H_3PO_4 lowers the activity of water, which performs two functions: first, it destabilizes the polyiodide complexes, thus permitting iodine to form as a separate liquid phase; second, it breaks the azeotrope, which allows the HI to be distilled from the mixture. The HI is distilled under pressure so that liquid HI is available for decomposition in Section IV. Water is removed from the H_3PO_4 by evaporation, and the H_3PO_4 is recycled back into the process.

5.6.2 Iodine Separation

Liquid iodine is separated from the HI_x in two steps. Both operational steps are performed in fluorocarbon-lined mild steel vessels packed with 20-mm ceramic saddles. In the iodine knock-out column (C-302), the HI_x is contacted counter-currently with 96% H_3PO_4. The HI and H_2O are extracted into the H_3PO_4, leaving molten iodine saturated with H_3PO_4. This H_3PO_4 is washed away from the iodine with water in the iodine wash column (C-301). The wash column is operated at 0.3 MPa and 393 K to maintain both iodine and water in the liquid state.

5.6.3 Hydrogen Iodide Distillation Column

Hydrogen iodide is distilled from the H_3PO_4 solution in a plate column operating at 0.9 MPa. Operation at this pressure requires a higher temperature

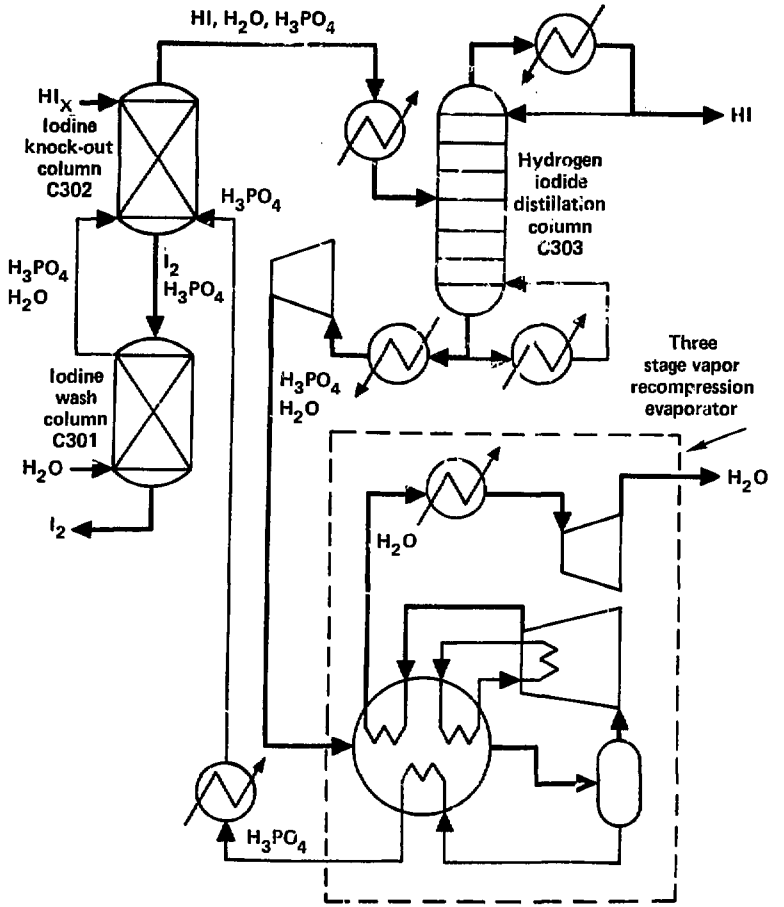

Fig. 5-6. Schematic flow diagram of Section III, seperation of HI_x into HI, I_2, and H_2O.

in the bottoms than would be required at low pressure, but eliminates an expensive HI liquefaction step. Efficient use of the thermal energy, required to operate the HI distillation column, is made possible by producing the HI as a liquid and thus eliminating the thermodynamic inefficiency associated with a liquefaction compressor and with the production of power to operate the compressor. In addition, an intermediate condenser allows parts of the condensing heat to be withdrawn from the column at a useful temperature. Although a majority of the heat required to preheat the feed and operate the column is obtained by using heat recovered in Section III, 355 MW is required from Section II at 523 K.

To design the HI distillation column we had to make a trade-off between capital and operating costs. The use of an intermediate condenser and operation at a relatively low reflux ratio reduce thermal energy requirements, but require more trays in the column for adequate chemical separation. The final design includes 50 Hastelloy-C trays in a Hastelloy-C clad mi' steel tower. We chose trough-type trays because they are a reasonable compromise between the more efficient, more expensive bubble cap trays and the less efficient, less expensive sieve trays.

An additional small design complication arises because the feed to the HI distillation column is saturated with iodine. Liquid iodine must be continuously removed from the middle of the column to avoid buildup. A stream containing two liquid phases made up of H_3PO_4 and liquid iodine is withdrawn from the iodine buildup region. The H_3PO_4 returns to the column from the top of a liquid-liquid separator and the bottom iodine phase passes to the iodine wash column for H_3PO_4 removal before returning to Section I.

The small quantitites of H_2SO_4 and SO_2 that remain in the lower phase product from Section I react chemically with HI in the feed preheater of the HI distillation column. The products of the reactions are H_2O, I_2, H_2S, and S. The quantities involved are so small that we have not determined the relative amounts of S and H_2S. For flowsheeting and cost estimating purposes, we have assumed that half the sulfur in H_2SO_4 and SO_2 ends up as H_2S and half becomes S. The H_2S leaves the column in the overhead product and the S is assumed to exit the column with the H_3PO_4. The liquid S is separated from the H_3PO_4 and oxidized back to SO_2 in Section II.

5.6.4 Phosphoric Acid Concentration

Vapor-recompression-driven flash evaporation removes water from the H_3PO_4 in three stages. We have modified the operating condition of each stage to reduce the capital cost for heat exchange. Each stage now operates at a different pressure, with the pressure decreasing as the acid concentration increases. Our major cost savings was incurred by eliminating the heat exchanger that conditioned the evaporator feed. Only the first and last stages require any heat input from the fusion reactor, but all three stages require significant quantities of power for vapor recompression. A total of 641 MW of shaft power is required to operate the compressors, whereas only an additional 104 MW of thermal power at 484 K is required from Section V to heat the high temperature evaporator. Heat is recovered within each evaporation stage from interstage cooling of the six-stage compressor, from the condensation of the compressed steam, and from the concentrated H_3PO_4 product.

The H_3PO_4 concentration step is simple in concept but the capital costs of the turbine compressors and heat exchangers are significant factors contributing to the overall hydrogen production cost. Even though we have considerably reduced the cost of concentrating H_3PO_4, we are continuing to study alternative chemical systems with the goal of eliminating H_3PO_4 from the process.

5.7 SECTION IV: HYDROGEN IODIDE DECOMPOSITION STEP

5.7.1 Design Considerations

The HI decomposition step includes the following operations:

- Decompose HI(l) to H_2(g) and I_2(l),
- Separate HI from the I_2 and recycle to the decomposer,
- Separate HI from the H_2 and recycle to the decomposer,
- Scrub the H_2 product in preparation for distribution.

A simplified schematic flow diagram of Section IV is presented in Fig. 5-7.

Three process variables dominate the design of Section IV and have a direct impact on the fusion reactor interface. The temperature and pressure of the HI decomposition reactor govern the size of the equipment and the amount of recycling through the reactor, whereas the pressure of the HI-I_2 distillation column determines the maximum process temperatu e required from the fusion reactor. Variables governing the cleanup of the hydrogen product have a smaller, but still significant, impact on the cost of producing hydrogen.

5.7.2 Hydrogen Iodide Decomposition

Hydrogen iodide is decomposed in the HI decomposition reactor (R-401). The extent of the decomposition reaction is limited by thermodynamic equilibrium. Therefore, to limit the amount of HI that is recycled back through the reactor, the process conditions must provide a high conversion per pass through the reactor. Previous studies at GA Technologies[5] have demonstrated that when decomposition is carried out under high enough pressures so that HI and I_2 are present as liquids, a much higher decomposition yield is obtained than with the analogous gas phase decomposition. Selecting the temperature and pressure involves a number of tradeoffs. The critical temperature of HI places an upper limit on the initial reaction temperature of an adiabatic flow reactor, whereas the required hydrogen delivery pressure places a lower limit upon the system pressure.

For this system design we still rely on an adiabatic flow reactor using an activated charcoal catalyst. The recently developed homogeneous catalysis concept[3] became available after we had already chosen this year's design base.

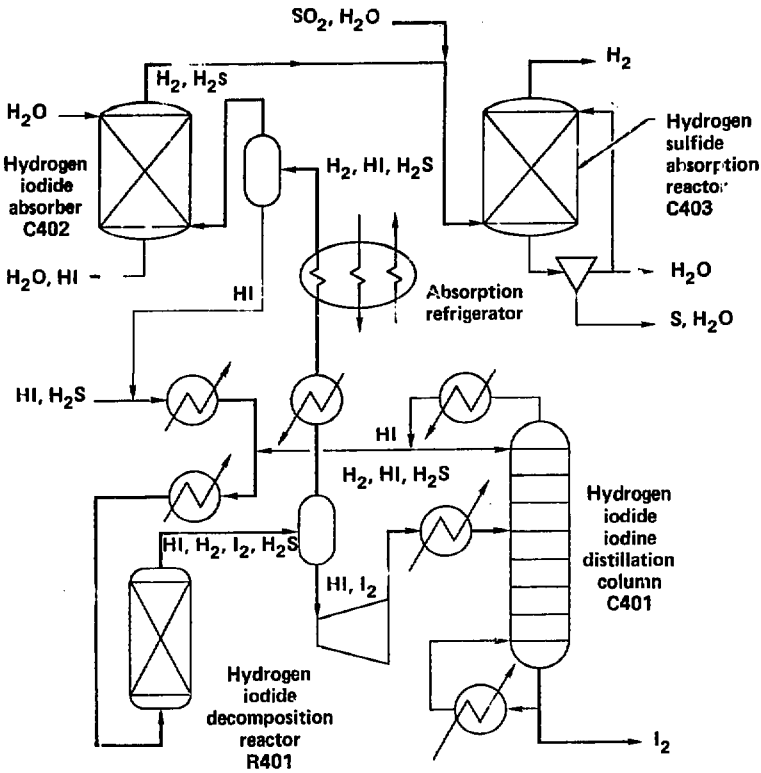

Fig. 5-7. Schematic flow diagram of Section IV, the HI decomposition step.

The reactor is sized for a 4-min residence time. The mild steel vessel is lined with fluorocarbon to protect it from the HI and iodine. The reactor operates at 8.3 MPa. The reaction temperature increases from 415 K at the inlet to 424 K at the outlet because the reaction is slightly exothermic under these conditions. The majority of the energy required to bring the HI to reaction temperature is supplied by recycled heat within Section IV. Only 6% of the energy (10.9 MW_t) must be supplied from the fusion reactor.

A design based on a continuously stirred tank reactor deserves future consideration. It would require a considerably longer residence time than the adiabatic flow reactor, but the system pressure could be lowered to 5 MPa, which may lead to reduced capital costs.

5.7.3 Hydrogen Iodide-Iodine Distillation

The liquid product from the HI decomposition reactor passes through a pressure-reducing turbine to the HI-I_2 distillation column (C-401). The pressure of the still (5.1 MPa) sets the temperature of the still bottom at 713 K. The pressure and temperature in the still may be decreased further, thus decreasing the high temperature heat load on the fusion reactor but at the expense of increased low-temperature heat requirements to reheat the overhead product from the still for recycle to the HI cracker. In addition, the heat now supplied from the overhead condenser to the evaporative refrigerator and from the bottom product to the liquid HI heat exchangers would instead have to be supplied from other sources.

In addition to the 41 MW required from the fusion reactor helium stream, 36 MW is required at 522 K. This additional heat may be used at a lower temperature because the distillation column is designed with intermediate reboilers. The use of intermediate reboilers increases the capital cost because of the cost of both the boilers and additional trays in the column, but the overall thermal efficiency is improved significantly.

The distillation column, constructed from Hastelloy-B clad mild steel, is 2.7 m in diameter for the bottom 12 m and expands to 4.7 m in diameter for the upper 3 m. There are 25 Hastelloy-B trough-type trays in the bottom section and six in the top. The expanded top section is required because of both the higher flow rates and lower density encountered in this section of the column.

5.7.4 Hydrogen Cleanup

The hydrogen from the decomposer is cleaned in three operations. First, the bulk of the HI is removed by condensation. Second, the remaining HI is removed with a water wash. Finally, the trace of H_2S is removed by a combination of chemical reaction and water wash.

The gaseous product of the HI decomposition reactor is cooled in three stages. A heat exchanger removes the high temperature portion of the heat to the power bottoming cycle and dumps the low temperature heat to cooling water. The stream is further cooled from 303 to 291 K by an absorption refrigeration system. The LiBr-based refrigeration[8] is driven by waste heat from the condenser of the HI-I_2 distillation column. After condensate separation, only a small quantity of HI and possibly H_2S remain in the hydrogen.

The remaining HI is easily removed using a water wash (C-402). Only a minimum amount of water is used because any water added at this point must be removed by distillation in Section III. Without iodine, HI is not corrosive to nonmetallics; therefore, hydrocarbon-lined mild steel is sufficient for this application. Because traces of iodine could enter the HI scrub column as a result of process upsets in the HI condensation system, the lower portions of the column are lined with fluorocarbon. The column is packed with 25-mm ceramic Raschig rings.

The high acidity in the lower portions of the column prevents H_2S absorption. Thus, H_2S builds up slightly in the upper section of the column until it reaches steady state, at which point it passes on to the H_2S removal

column (C-403) at the same rate at which it enters the HI scrub column. Because H_2S has a relatively low solubility in water, a simple water scrub would require that an excessive amount of water be processed through Section II to reconvert the H_2S to SO_2. The problem is solved by adding a small amount of SO_2 to the H_2S absorber; H_2S reacts with SO_2 in the presence of water to produce a sulfur slurry. The slurry is concentrated by a filter with back-flush, so only a small amount of water accompanies the sulfur back to Section II where it is converted to SO_2 by reaction with SO_3. The mild steel column, packed with 25-mm ceramic Rashig rings, is lined with a hydrocarbon-based material to prevent corrosion.

The H_2 pressure is dropped to the distribution pressure of 5.1 MPa using a power recovery turbine and thus exits the process.

5.8 SELECTION OF MATERIALS FOR THE THERMOCHEMICAL PLANT

Because of the corrosive nature of the chemicals involved in the sulfur-iodine cycle, an extensive materials testing program was necessary. Because H_2SO_4 is common to other thermochemical cycles and is industrially significant, several materials have been extensively investigated for use in the H_2SO_4-H_2O system.

5.8.1 Section I

The extensive material testing program for the sulfur-iodine cycle has produced a great deal of data on corrosion in iodine systems.[10] Table 5-1 presents a summary of the test results. Early results indicated that niobium is impervious to attack by the HI-I_2-H_2O solutions typical of the main solution reactor, but the most recent work regarding the effect of the H_2SO_4 upon the system questions the use of niobium in this portion of the process. Tantalum can be substituted for the niobium at higher cost, but we have not used it in the present equipment design.

Although glass-lined steel is an ideal material for use with the HI-I_2-H_2O system, it is unavailable in the equipment sizes required for the TMR-powered plant. Fluorocarbon-lined steel performs the same function and is available in the required sizes.

5.8.2 Section II

Materials must be selected for the following process units in Section II:

- Isobaric concentrator,
- Low pressure distillation column,
- H_2SO_4 boiler,
- Fluidized bed decomposer,
- Decomposer recuperator,
- Decomposer cooler.

Table 5-2 presents a summary of the material investigations by GA Technologies[11] for the H_2SO_4 sections of the process.

Table 5-1. Possible materials for use with process fluids containing HI_x and I_2.

Principal operation	Fluids	Temperature range (K)	Material candidates for: heat exchangers, vessels, pumps, and hardware
Main solution reaction	$SO_2 + I_2 + H_2O \rightarrow HI_x + H_2SO_4$ (55 wt% acid)	398	Glass-lined steel; fluorocarbon plastics and elastomers; ceramics - SiC, Al_2O_3, carbon impervious graphite; tantalum
I_2 and H_2O separation	$HI_x + H_3PO_4$	393-431	Glass-lined steel; tantalum-lined steel; Hastelloy B-2; fluorocarbon plastics
I_2 recycle	I_2	393	Hastelloys B-2, G, C-276, glass
Decomposition	HI_x (low H_2O); I_2; H_2	393	Hastelloy B-2; fluorocarbon plastics; glass-lined steel

Table 5-2. Candidate materials for use with H_2SO_4.

Principal operation	Fluids	Approximate fluid temperatures (K)	Material candidates for heat exchangers, vessels, pumps, and other hardware
Main solution reaction	$SO_2 + I_2 + H_2O + HI_x + H_2SO_4$ (55 wt%)	398	Glass-lined steel; fluorocarbon plastics and elastomers; ceramics-SiC, Al_2O_3, carbon; impervious to graphite tantalum
Concentration	H_2SO_4 55 to 65 wt%	368-423	Hastelloys B-2 or C-276. impervious graphite; glass or brick-lined steel
Concentration	H_2SO_4 65 to 75 wt%	423-453	Hastelloys B-2 or C-276, impervious graphite; glass or brick-lined steel
Concentration	H_2SO_4 75 to 98 wt%	453-693	Brick-lined steel; cast Fe-14 wt% Si
Vapor formation and decomposition	$H_2SO_4 + H_2O + SO_3$	603-873	Brick-lined steel; cast Fe-14 wt% Si, silicide coatings on steel; Hastelloy G
Vapor decomposition	$SO_3 + H_2O \rightarrow H_2O + SO_2$ 1/2 O_2	873-1123	Incoloy 800H with aluminide coating

5.8.2.1 Sulfuric Acid Boiler. The isoboric concentrator, low pressure distillation column, and H_2SO_4 boiler all have similar materials problems. The main problem is to provide a heat exchanger that tolerates hot concentrated H_2SO_4. All known metallic heat exchanger materials (except for expensive noble metals such as gold and platinum) are severely corroded by these H_2SO_4 solutions above temperatures of 500 K. A number of ceramic and intermetallic materials have been tested in hot concentrated H_2SO_4 at 633 to 693 K in recent years at LLNL[11,12] and at Westinghouse.[13] The top candidate materials from both corrosion resistance and heat exchanger design standpoints are siliconized SiC, "$CrSi_2$" coated Incoloy-800, and Durichlor-51 (Fe-14%, Si-4%, Cr). All of these materials depend on the development of a corrosion-resistant SiO_2 scale on the surface to provide protection against corrosion by H_2SO_4. Similarly, it is well known that pure SiO_2, as in the form of silica brick, is inert to corrosion by H_2SO_4.

The SiC is currently the best prospect as a heat exchanger material. Siliconized SiC (a two-phase composition consisting of a mixture of SiC and Si) is produced at the Norton[14] and Carborundum[15] companies and is especially suited for this application. This type of material, which contains about a 10 to 15% excess of silicon metal, is impervious to gases, has a high thermal conductivity, high strength, good thermal shock resistance, and can be fabricated in complex shapes and bonded together to form heat exchanger assemblies.[16] Corrosion testing of SiC for 1121 hours and Si for 592 hours in 97% H_2SO_4 at 673 K at LLNL showed no evidence of corrosion,[11] thus confirming the corrosion resistance of both SiC and Si for this application.

Specimens of Incoloy-800 coated with chromium disilicide were tested at LLNL[14] for corrosion for 240 hours at 673 K in 97% H_2SO_4.[12] The tests showed a very low rate of corrosion (extrapolated weight loss rate of 15 mg/cm^2-year). The coatings were about 120 μ thick, uniform in thickness, well-bonded to the substrate, and without evidence of fractures. The coatings were prepared by Dr. Charles M. Packer of Lockheed Missiles and Space Company of Palo Alto, California, using a slurry coat and rapid melt technique. Although the above results are preliminary, they are encouraging because they indicate that a conventional heat exchanger material such as Incoloy-800 can be protected against corrosion by a coating process.

Durichlor-51 is a commercial high silicon cast iron material that is yet another candidate as a heat exchanger or container material. It is basically an intermetallic compound with a composition of approximately Fe_3Si and, as such, presents the disadvantages common to most intermetallics of poor ductility, low tensile strength, and poor machining and fabrication characteristics. Also, being a cast material, the control of internal porosities and nonuniformities presents production problems. Nonetheless, with proper quality control and using good engineering design and practices, these problems can be controlled. From a corrosion standpoint, tests of up to 524 hours on Durichlor-51[12] have shown only a moderate amount of attack (5-μ surface penetration). However, very importantly, corrosion appears to proceed very uniformly over the surface of this material. It therefore seems reasonable to extrapolate to a lifetime on the order of 5 years for this application. In contrast to Durichlor-51, Duriron is another high-silicon cast iron alloy that shows a rather irregular corrosion behavior with grain pullouts, corrosion pits, and spallation in similar H_2SO_4 corrosion tests at 673 K.[11]

Low temperature cycles are often discussed in terms of alternate working fluids. The motivation for fluids other than steam is to reduce the size and capital cost of the low pressure components. A study at United Technology Laboratories[2] evaluated the relative merit of having several fluids in the bottoming cycles. The study considered steam, ammonia, thiophene, and several Freons. Although the use of fluids other than steam could reduce the size of equipment, that advantage is somewhat offset because the alternate fluids provide lower specific work and require higher volumetric flow rates. The alternate fluids also have some undesirable properties. Ammonia is toxic and flammable; thiophene is flammable; they are all expensive fluids compared to steam.[2,3]

For purposes of the MARS synfuel application, we feel that a conventional low pressure steam cycle is the most suitable.

The particular cycle that we have chosen is a conventional low pressure steam cycle with superheat, as shown on the T-S diagram in Fig. 6-7. The boiler temperature is 373 K at a pressure of 0.1 MPa (1 atm). The steam is superheated to 403 K and then expanded through the turbine with an isentropic efficiency of 0.85 to 311 K at a pressure of 0.0066 MPa (0.06 atm). The exit steam contains 7.5% moisture. The condenser operating at 311 K corresponds to cooling tower operation on an average day. The condensate is returned to the boiler through the feedwater pump and heaters.

The enthalpy at various points in the cycle is shown in Fig. 6-7. The net workout is 346 kJ/kg, and the total energy input is 2579 kJ/kg, giving an overall thermal efficiency of 0.13. If the condenser operates at a lower temperature of 300 K the efficiency increases to 0.16.

It could be argued that the bottoming power plant is too costly and that it would be more economic to remove it and dump all process reject energy to the cooling tower. Bottoming plant removal has an important impact on the overall interface power balance because the electric power loss must be picked up by the steam power plant. The effect of removing the bottoming plant is summarized in Table 6-6. The overall cycle efficiency drops from 0.37 to 0.32. This corresponds to a 12% reduction in hydrogen production from 5223 and 4587 mole/s. The fractional use of blanket power also changes where more of the high temperature blanket power is needed for the low temperature process and more low temperature blanket power is required for the stream power plant. The economic impact of removing the bottoming plant is discussed in Sec. 9 of this volume.

6.7 CONCLUSIONS

The analysis presented here produces an overall plant efficiency of 37%. To obtain that efficiency requires the use of a bottoming steam-electric power plant to recover waste heat from the TCP. Without the bottoming plant, the overall efficiency drops to 0.32. Steam provides the simplest working fluid and technology for the bottoming plant.

Because the TCP has a sizable electrical power demand to drive the compressors, electrical power production is an important part of the interface. Standard steam Rankine technology can satisfy that electrical requirement in the main and bottoming power plants.

5.8.3 Sections III and IV

Sections III and IV have constraints similar to those in Sections I and II. The information in Table 5-1 also applies to the iodine-HI regions of Sections III and IV. Phosphoric acid adds no new complexity except that in the high temperature portions of the process, acid brick is necessary as a thermal protection for teflon liners. In addition, Hastelloy C has been recommended[17] for use with boiling concentrated H_3PO_4.

5.9 SAFETY CONSIDERATIONS

The main safety issues involve the control, handling, and containment of tritium, liquid Li-Pb, and H_2SO_4. The safety issues for tritium and liquid Li-Pb were reviewed and discussed in a study in 1980,[18] which concluded that adequate controls were designed into the system to maintain proper safety. We have applied similar considerations in the current designs, paying particular attention to both residual and accidental leakages of tritium into the environment or product, tritium inventories in the system, and potential problems of liquid lithium fires. We feel that the safety issues have been well met, and many of the details have been covered in this report. We refer the reader to our previous report[2] for further details.

Because H_2SO_4 is a serious health hazard if introduced into the environment, it is important that conservative designs be maintained on the vessels and piping containing hot liquid and gaseous H_2SO_4 and its decomposition products. We feel that we have taken adequate measures in our design studies we further recognize that the H_2SO_4 industry is large and well-established, and available for consultation for future design information as needed to ensure a safe plant.

REFERENCES

1. R. W. Werner et al., Conceptual Design Study FY 1981, Synfuels from Fusion Using the Tandem Mirror Reactor and a Thermochemical Cycle to Produce Hydrogen, Lawrence Livermore National Laboratory, Livermore, CA, UCID-19311 (1982).

2. R. W. Werner, T. H. Zerguini, and F. L. Ribe, Synfuels from Fusion Using the Tandem Mirror Reactor and a Thermochemical Cycle to Produce Hydrogen," Lawrence Livermore National Laboratory, Livermore, CA, UCID-19609 (1982).

3. J. H. Norman, G. E. Besenbruch, L. C. Brown, D. R. O'Keefe, and C. L. Allen, Thermochemical Water-Splitting Cycle, Bench-Scale Investigations and Process Engineering, Final Report for the Period Ending February 1977 through December 31, 1981, Department of Energy, Washinngton, D.C., DOE/ET/26225-1, also published by General Atomic Company, San Diego, CA, Report GA-A16713 (1982).

4. G. E. Besenbruch, K. H. McCorkle, J. H. Norman, D. R. O'Keefe, J. R. Schuster, and M. Yoshimoto, "Hydrogen Production by the GA Sulfur-Iodine Process, A Progress Report," Hydrogen Energy Progress, Proceedings of the 3rd World Hydrogen Energy Conference, Tokyo, Japan, 23-26 June 1980, Vol. 1 edited by T. N. Veziroglu, K. Fueki, and T. Ohta (Pergamon Press, Oxford, 1980) p. 243.

5. J. H. Norman, G. E. Besenbruch, and L. C. Brown, "Solar Production of Hydrogen Using the Sulfur-Iodine Thermochemical Water Splitting Cycle, Final Report," General Atomic Company, San Diego, CA, GA-C-16493.

6. D. R. O'Keefe and J. H. Norman, "The Liquid Hydrogen Iodide Decomposition Process Step for Water-Splitting Applications," Hydrogen Energy Progress, Proceedings of the 3rd World Hydrogen Energy Conference, Tokyo, Japan, 23-26 June 1980, Vol. 1, edited by T. N. Veziroglu, K. Fueki, and T. Ohta (Pergamon Press, Oxford, 1980) p. 277.

7. M. Coombs et al., High-Temperature Ceramic Heat Exchanger, Final Report, July 1979, AiResearch Manufacturing Company of California, Torrance, CA, FP-1127, Research Project 545-1; report prepared for Electric Power Research Institute, Palo Alto, CA, R. H. Richman, EPRI Project Mgr. (1979).

8. F. J. Evans, Jr., Equipment Design Handbook for Refinery and Chemical Plants, 2nd Ed., Vol. 1 (Gulf Publishing Co., Houston, TX, 1979) pp. 184-191.

9. HTGR Thermochemical Water-Splitting for Hydrogen Production, Annual Report for the Period January 1, 1975 through December 31, 1975, General Atomic Company, San Diego, CA, GA-A13800 (1976).

10. P. W. Trester and H. G. Staley, Assessment and Investigation of Containment Materials for the Sulfur-Iodine Thermochemical Water-Splitting Process for Hydrogen Production, Final Report (July 1979-December 1980), Gas Research Institute, GRI-80/0081 (1981).

11. O. H. Krikorian, Material Corrosion Studies for a Sulfuric Acid Vaporized, Lawrence Livermore National Laboratory, Livermore, CA, UCRL-81856 (1978).

12. O. H. Krikorian, Corrosion Testing of Materials in Hot Concentrated Sulfuric Acid, Lawrence Livermore National Laboratory, Livermore, CA, UCRL-83411 (1979).

13. R. L. Ammon, G. Yatsko, A. Irwin, and G. H. Furbman, "Materials Consideration for the Westinghouse Sulfur Cycle Hydrogen Production Process," in Proc. Second World Hydrogen Energy Conference, Zurich, Switzerland, 21-24 August 1978.

14. M. L. Torti, J. W. Lucek, and G. Q. Weaver, "Densified Silicon Carbide - An Interesting Material for Diesel Applications," Technical paper Series 780071, Society of Automotive Engineers Congress and Exposition, Detroit, MI, February 27 through March 3, 1978. See also brochures of the Norton Company, Worchester, MA on "Noralide Advanced Ceramics," and "Ceramics for Energy."

15. E. Craft, Carborundum Co., Niagara Falls, NY, private communication regarding bending of KT-Silicon carbide to form U-tubes (October 1979).

16. T. N. Tiegs, Materials Testing for Solar Thermal Chemical Process Heat, Oak Ridge National Laboratory, Oak Ridge, TN, ORNL/TM-7833 (1981).

17. J. H. Perry, editor, Chemical Engineers' Handbook, 3rd Ed. (McGraw Hill, NY, 1950) p. 1507.

18. R. W. Werner, F. L. Ribe, R. Busch, et al., Synfuels from Fusion - Producing Hydrogen with the Tandem Mirror Reactor and Thermochemical Cycles, Lawrence Livermore National Laboratory, Livermore, CA, UCID-18909, Vols. I and II (1981).

6 Interfacing the Reactor with the Thermochemical Process

CONTENTS

6. Interfacing the Reactor with the Thermochemical Process

The thermochemical process (TCP) has three important energy requirements:

1. High temperature energy (1100 K) for the SO_3 decomposer;

2. Low temperature (760 K) energy for the balance of the TCP and steam power plant;

3. Shaft work (electrical) for the TCP compressors and pumps.[1]

To satisfy those requirements the TMR blanket has been designed to provide both high and low temperature energy. High temperature energy is supplied by a helium heat transport stream from the high temperature blanket. Low temperature energy is supplied by a Li-Pb heat transport stream from the low temperature blanket. Additional low temperature energy is supplied by thermal discharge from the direct converter through a water loop.

Electrical energy for shaft work is obtained from the direct converter and from Rankine cycle systems that use low temperature blanket energy and heat recovery from the thermochemical process.

To match the TMR and TCP, the type and arrangement of the process equipment and its acceptable operating range must be carefully chosen. The SO_3 decomposer is especially important in this regard. It operates at high temperature (1100 K) and at low pressure (7 atm). The high temperature helium from the blanket is at 50 atm so it is necessary to support this pressure difference at some point in the heat transport system.

We have made several assumptions about the development of a suitable interface:

1. The blanket heat transport loop is directly coupled to the SO_3 decomposer without the use of an intermediate heat exchanger. This requires that the decomposer heat exchanger, operating at 7 atm, be able to support the 50-atm helium pressure from the blanket heat transport loop. The decomposer heat exchanger must also serve as a partial means of keeping tritium out of the TCP hydrogen product. Section 7 of this volume discusses tritium isolation. Section 8 of this volume details a staged SO_3 decomposer design that supports the 50-atm pressure.

2. The SO_3 decomposer is taken to have an energy demand that can be approximated as linear for purposes of heat exchanger supply and demand. This requires staged fluidized beds or a continuous reaction with temperature along the flow path through the decomposer. The design in Sec. 8 of this volume can satisfy this assumption.

3. The Li-Pb heat transport stream from the low temperature blanket is directly coupled to the TCP heat exchangers without use of an intermediate loop. High reliability is provided by using duplex heat exchanger tubing.

4. The upper limit on supply temperature for the high temperature blanket is 1273 K.

5. The upper limit on supply temperature for the low temperature blanket is 773 K. This limit is the corrosion attack by Li-Pb, on the tube material in which it is contained.

6.1 SUMMARY OF INTERFACE RESULTS

The TMR and TCP are coupled by the arrangement shown in Fig. 6-1; and specific operating conditions are presented in Tables 6-1 and 6-2.

The 3500-MW_f TMR provides thermal power by three heat transport loops: (1) high temperature blanket; (2) low temperature blanket; and, (3) direct converter thermal cooling. Electrical power is supplied to the TCP from the direct converter, steam power plant, and bottoming waste heat power plant. The overall thermal efficiency of the plant is 0.37 where the efficiency is defined by the ratio of the hydrogen chemical power output divided by the total thermal power available from the TMR.

Thermal power from the high temperature blanket drives the SO_3 decomposer. It is also used in parallel with the decomposer recuperator to drive the decomposer preheater and part of the sulfuric acid boiler. Of the blanket power at high temperature, 0.46, of the total blanket power, the high temperature decomposer uses 0.26 and the low temperature process uses 0.20.

Thermal power from the low temperature blanket drives both the low temperature process and the steam power plant. Of the low temperature blanket power fraction, 0.54, the low temperature process uses 0.29 and the steam power plant uses 0.25. Thermal discharge from the direct converter and the fusion halo provides only low temperature power to the TCP.

Electrical power from the direct converter is first used to satisfy the power requirements to drive the TMR--injectors, coils, and pumps. Of the 449 MW_e produced, 173 MW_e is excess from the TMR driver. The direct converter provides 0.21 of the total TCP electrical requirement.

The steam power plant uses the same technology that MARS uses for electrical production. The steam generator has duplex tubing to provide highly reliable separation between the Li-Pb and steam. It uses conventional steam cycle technology with a turbine efficiency of 0.85% and an overall plant efficiency of 0.37%. It provides 0.54% of the total TCP electrical requirement.

The bottoming power plant uses waste heat at about 400 K to produce electricity. The plant uses low pressure steam and has an overall thermal efficiency of 0.13%. Organic fluids (butane, Freon, etc.) could be used with about the same efficiency and at some reduction in capital cost as an alternative to steam; however, such fluids are costly and some are toxic or flammable. The bottoming plant provides 0.25% of the total TCP electric requirement.

Temperature matching of the TMR and TCP was found to meet the limits placed on the TMR blanket. The temperature range of the high temperature blanket's helium transport loop is 730 to 1220 K at a pressure of 50 atm. The temperature range of the low temperature blanket's Li-Pb heat transport loop is 605 to 755 K. The temperature range of the direct converter's water

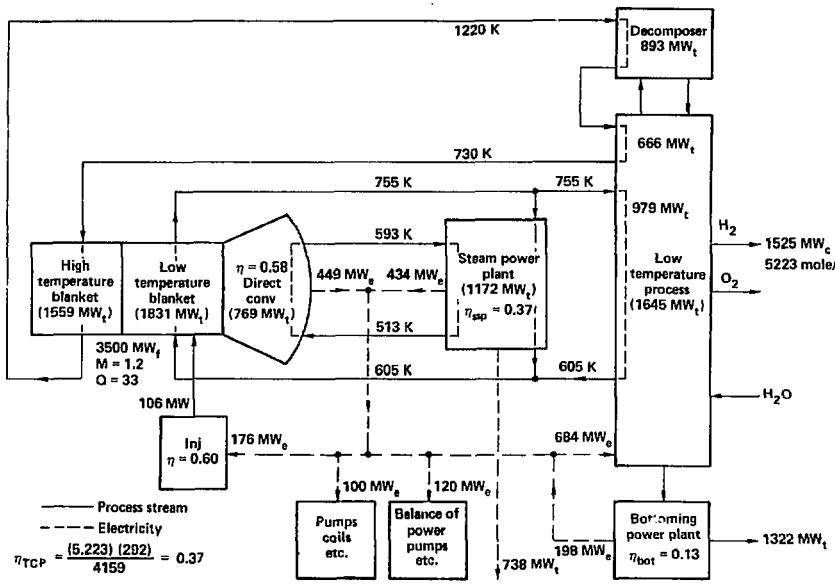

Fig. 6-1. Power interface for MARS/synfuel option.

Table 6-1. Interface power balance results for the MARS/synfuel option.

Fusion driver	
Fusion power (MW)	3500
Fusion Q	33.0
Blanket multiplication	1.20
Blanket thermal power (MW)	3390.0
Total power to DC (MW)	769.0
Total thermal power (MW)	4159.0
Electric power from DC (MW)	449.0
Net DC elect. to TCP (MW)	173.0
TCP operating results	
Hydrogen flow rate (mole/s)	5223
Overall efficieny	0.37
Blanket energy fractions	
High temperature total	0.46
Decomposer	0.26
Low temperature process	0.20
Low temperature total	0.54
Low temperature process	0.29
Steam power plant	0.25
Component efficiencies	
Steam power plant	0.37
Fusion injectors	0.60
Bottoming power plant	0.13
Direct conversion to electricity	0.58

Table 6-2. Parameters for electricity use for the MARS/synfuel option.

	Energy and power distributions				
	Power (MW)	Energy (kJ/mole)	T-in (K)	T-out (K)	Flow (kg/s)
Thermal energy supplied by TMR					
High temperature blanket	1559.3	298.6	730	1220	612
Low temperature blanket	1830.6	350.5	605	755	78736
Direct converter thermal	320.0	61.3	513	593	784
Electrical energy supplied					
Steam power plant	433.6	83.0			
Bottoming power plant	197.6	37.8			
Direct converter (net)	173.0	33.1			
Thermal energy used by thermochemical process					
High temperature process					
High temperature blanket	893.1	171.0			
Low temperature process					
High temperature blanket	666.3	127.6			
Low temperature blanket	978.8	187.4			
Steam power plant					
Low temperature blanket	851.8	163.1			
Direct converter thermal	320.0	61.3			
Electrical energy used by thermochemical process					
Thermochemical process	684.2	131.0			
Balance of plant	120.0	23.0			
Thermal energy rejected to cooling					
Steam power plant	738.3	141.4			
Bottoming power plant	1322.2	253.2			
Net hydrogen chemical energy	1525.0	292.0			

cooling loop is 513 to 593 K. These temperature ranges provide reasonable temperature differences for the interface heat exchangers, as shown in Fig. 6-2. In the figure, the arrows pointing to the right represent the process stream energy requirement; the arrows pointing to the left indicate the energy supply from the TMR heat transport loops.

The following discussion presents additional details of the interface.

6.2 REACTOR POWER PRODUCTION

We assume that the TMR has the operating parameters shown in Fig. 6-1. The fusion power is 3500 MW_f with an injection power requirement of 106 MW and Q of 33.

The power available to the direct converter (alphas, halo) is 769 MW. The direct converter electrical output is 449 MW_e, which provides 176 MW_e to the injectors, 100 MW_e to TMR coils and pumps, and a net 66 MW_e to the TCP. The remaining TCP electrical demand is supplied by Rankine power plants. The 320-MW_t thermal discharge from the direct converter is used for feedwater heating in the steam power plant.

Eighty percent of the fusion power (2800 MW) is available as high energy neutrons to the blanket. For a blanket multiplication of 1.2, plus 30 MW from Bremsstrahlung, the thermal power available in the blanket is 3390 MW_t. The blanket thermal power plus the 769 MW to the direct converter gives a total of 4159 MW of thermal power. This is the power used in the denominator of the plant efficiency calculation.

Additional details of the fusion driver are presented in Sec. 3 of this volume.

6.3 THERMOCHEMICAL PROCESS POWER REQUIREMENTS

Table 6-3 presents a summary of the thermal and electrical energy requirements for the TCP together with their respective temperature ranges. Additional details of the energy requirements of Section II are presented in Fig. 6-3, and the method used to calculate those energies is presented in Appendix 6-A. All energy units are presented as kJ/mole of hydrogen produced.

The evaporator has two energy inputs, as shown in Fig. 6-3. One is 29 kJ/mole from low temperature thermal energy and the other is 195 kJ/mole from energy recovered from the decomposer cooler. We calculated the evaporator energy requirement by assuming that pressure staging can condense 55% of the water. Condensation of the remaining vapor permits a further energy recovery of 103 kJ/mole at 430 K. The other recoverable energies are listed in Table 6-4. Section 5 of this volume contains an additional discussion of the TCP.

6.4 COUPLING THE REACTOR AND THERMOCHEMICAL PROCESS

The actual coupling of the TMR and TCP requires two steps. The first is to satisfy the overall power requirements of each system. Once that has been accomplished, the second step is to match the temperatures of the interface heat exchangers and power systems.

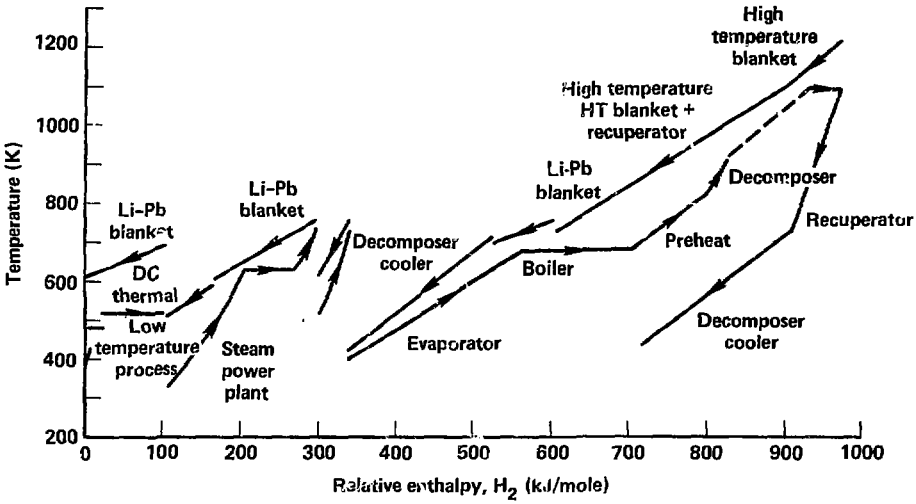

Fig. 6-2. Temperature vs enthalpy for interface heat exchangers for MARS/synfuel option.

Table 6-3. Thermal and electrical demands for the thermochemical process.

Component	Electrical demand (kJ/mole)	Thermal demand (kJ/mole)	Temperature range (K)
Section II (high temperature)[a]			
Decomposer (four-stage)	--	98	875 to 1100
Preheater	--	73	825 to 1100
Total	--	171	
Section II (low temperature)[a]			
Preheater	--	34	680 to 722
Boiler	-	140	680
Evaporator (Net)	--	29	400 to 680
Section III[b]			
HX E303	--	72.4	523
HX E308D	--	21.2	484
TC 301, 302, 303	131	--	--
Section IV[b]			
HX E404A	--	6.7	713
HX E404B2	--	1.7	616
HX E404C2	--	7.4	522
HX E402C	--	2.2	393 to 415
Total	131	315	

[a]Calculated by the method in Appendix 6-A.
[b]Provided by GA Technologies (see Sec. 5 of this volume).

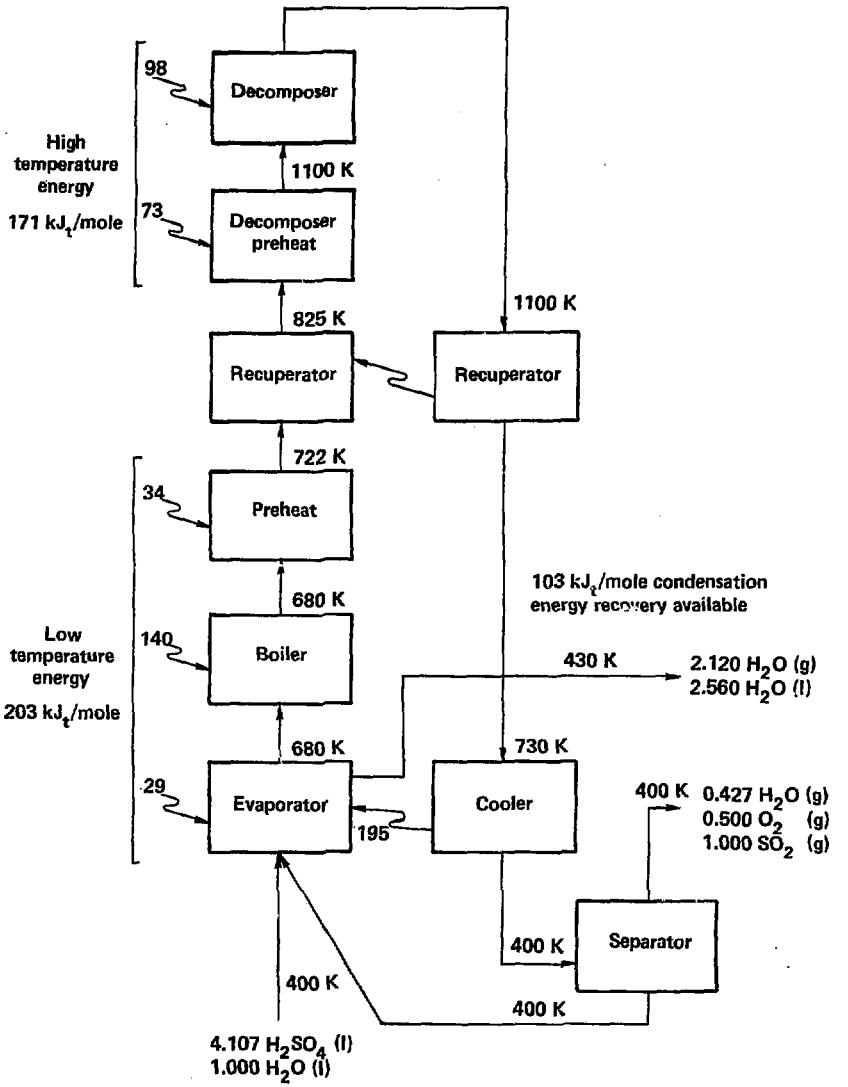

Fig. 6-3. Thermal energy requirements for H_2SO_4 process stream (Section II).

Table 6-4. Recoverable waste heat from the thermochemical process.

Source	Amount (kJ/mole)	Temperature (K)
Section I	111	393
	21	425
Section II	103	430
Section III	56	368 to 417
Total	291	

6.4.1 Overall Power Balance

To satisfy the interface arrangement in Fig. 6-1, it is necessary to simultaneously satisfy the low- and high-temperature power requirements and electrical requirements on each side of the interface. This can be accomplished by writing interface power balances.

The electrical requirements for the TCP are supplied from the net electrical power from the TMR, the steam power plant, and the bottoming power plant. The algebraic expression is

$$NE_e = P_{DC_{net}} + (f_{l_2} P_b + P_{DC_{th}}) n_{SPP} + E_w \dot{N} n_{BOT} - P_{BOP} \quad . \tag{6-1}$$

The low temperature requirement for the TCP is satisfied from both low- and high-temperature blanket power such that

$$\dot{N}E_l = (f_h - f_{h_l}) P_b + (f_l - f_{l_2}) P_b \quad . \tag{6-2}$$

The high temperature requirement for the TCP is satisfied from a fraction of the high-temperature blanket power. The algebraic expression is

$$\dot{N}E_h = f_{h_l} P_b \quad . \tag{6-3}$$

The above three equations contain three unknowns: (1) the hydrogen production rate (N); (2) the fraction of blanket power supplied to the steam power plant (f_{l2}); and (3) the fraction of blanket power used in the high temperature TCP (f_{hl}). All other parameters are known or can be assumed. These equations can be combined and solved for $\dot{N}$ and then f_{l2} and f_{hl}. The results are

$$\dot{N} = \frac{P_{DC_{net}} + (P_b + P_{DC_{th}}) n_{SPP} - P_{BOP}}{E_e + (E_l + E_h) n_{SPP} - E_w n_{BOT}} \quad , \tag{6-4}$$

$$f_{l_2} = 1 - \frac{(E_l + E_n)\,\dot{N}}{P_b} \quad , \tag{6-5}$$

$$f_{h_l} = \frac{\dot{N}E_h}{P_b} \quad , \text{ and} \tag{6-6}$$

$$n_{TCP} = \frac{\dot{N}E_{H_2}}{P_b + P_{DC_{net}} + P_{DC_{th}}} \quad . \tag{6-7}$$

Note that temperature is not explicitly contained in the previous equations. Temperature enters, but only to the extent that it affects the power plant efficiencies. Temperature considerations become more important regarding temperature matching for heat exchanger supply and demand.

To perform the calculation for the hydrogen production rate and plant efficiency it is necessary to define the TMR and TCP parameters contained in Eqs. (6-4) through (6-7). The parameters used for the calculations are as follows:

M	=	1.2	P_f	=	3500 MW_f
P_b	=	3390 MW_t	P_{DCth}	=	320 MW_t
P_{DCnet}	=	173 MW_e	P_{BOP}	=	120 MW_e
E_l	=	315 kJ/mole	E_h	=	171 kJ/mole
E_e	=	131 kJ/mole	E_w	=	291 kJ/mole
f_l	=	0.54	f_n	=	0.46
n_{SPP}	=	0.37	n_{BOT}	=	0.13 .
E_{H2}	=	292 kJ/mole			

The efficiencies for the steam and bottoming power plants are discussed in Secs. 6.5 and 6.6 of this volume. We assume that the interface between the TMR and TCP and other balance of plant requirements is 120 MW_e.

The result of the calculation gives an overall plant efficiency of 0.37 with a hydrogen production rate of 5223 mole/s. The fraction of blanket power supplied to the steam plant is 0.25 and the fraction supplied to the sulfur trioxide decomposer is 0.26.

6.4.2 Temperature Matching the Interface

Now that the power requirements for the interface are known, details of the temperature match can be completed. This can be done by first constructing the thermal demand curve for the process. Table 6-5 contains the incremental thermal energy requirements of the process (including the steam power plant) and temperature ranges. The table also includes the summation (integral) of the energy requirements; it is also plotted in Fig. 6-2 as temperature vs enthalpy.

Table 6-5. Incremental and integral thermal energy demands.

Component	Temperature (K)	Energy required (kJ/mole)	Integral energy (kJ/mole)
E402C	393 to 415	2.2	2.2
E308D	484	21.2	23.4
E404C2	522	7.4	30.8
E303	523	72.4	103.2
E404B2	616	1.7	104.9
Steam power	313 to 733	224	328.91
E404A	713	6.7	335.6
Evaporator	400 to 680	224	559.6
Boiler	680	140	699.6
Preheater	680 to 722	34	733.6
Recuperator (in)	722 to 825	67	800.6
Decomposer	825 to 1100	73	873.6
Decomposer	1100	98	971.6
Recuperator (out)	1100 to 730	-67	904.6
Decomposer cooler	730 to 430	-195	709.6

In the figure the process requirements are indicated by the arrows pointing to the right. The blanket energy supply needed to satisfy the demand is shown by the arrows pointing to the left. It is at this point where the temperature range of the TMR heat transport streams is defined. It is necessary to select large enough temperature differences to allow heat to be

exchanged between the pair of counter flow streams. The slope of the supply must also provide a proper match to avoid "pinch points," or excessive temperature differences. The slope of the supply curve is inversely proportional to the flow in the TMR heat transport loops.

The temperature matching shown in Fig. 6-2 provides a reasonable coupling of the TMR and TCP systems. The fluidized bed decomposer is heated by a combination of energy from the high temperature blanket and the recuperator. There is also sufficient energy to provide a substantial amount of energy to the boiler. The remainder of the thermal energy is supplied from the low temperature blanket. The evaporator is primarily driven by energy recovered from the gases cooling in the decomposer.

The Li-Pb transport loop is directly coupled to the TCP without intermediate heat exchangers. The Li-Pb is isolated from the TCP streams by using duplex tubing in the heat exchangers. We did not use intermediate heat exchangers because they would have required larger temperature differences that would have caused excessive Li-Pb temperatures.

6.5 STEAM POWER PLANT

As we stated in Sec. 6.1 of this volume, the steam power plant uses the same technology that MARS uses for electrical production. The overall power plant arrangement is shown in Fig. 6-4. The steam generator, superheat, reheat, and part of the feedwater heat exchangers use a duplex tube design with Li-Pb on the tube side. Additional feedwater heating is provided by the thermal discharge from the direct converters. Some waste heat from the TCP could be used for feedwater heating; however, we feel it is better to separate the two systems so that the steam power plant can operate independently of the TCP.

The heat input and turbine expansions are shown in the temperature-entropy diagram in Fig. 6-5. The high pressure turbine expansion remains in the superheated region. The low pressure turbine is expanded into the "wet" region at about 10% moisture. The steam turbines uses conventional technology and is assumed to have an efficiency of 0.85 based on an isentropic expansion. Steam extraction for feedwater heating is not required because of thermal energy from the direct converter.

The overall efficiency of the steam plant is 0.37.

6.6 BOTTOMING POWER PLANT

The large amount of unused energy leaving the TCP at about 400 K can be used to produce electricity. This is done by using a conventional steam power cycle, as shown in Fig. 6-6. The steam cycle selected gives an electrical power output of 198 MW_e, or 0.25 of the total TCP requirement. The bottoming plant efficiency is 0.13.

A low temperature Rankine cycle has a low thermal efficiency compared to a conventional high temperature power cycle. This is because of the low temperature range of the cycle's thermodynamics rather than the inefficiency of the components.

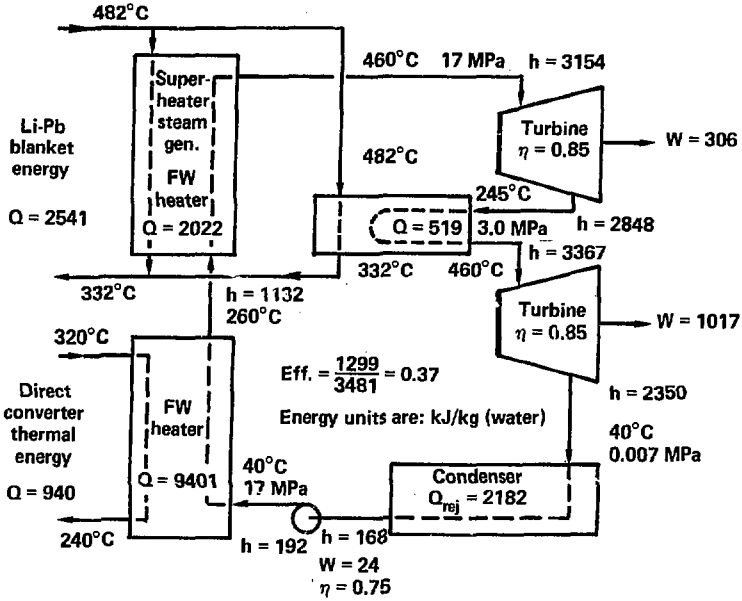

Fig. 6-4. Schematic arrangement for the steam power plant.

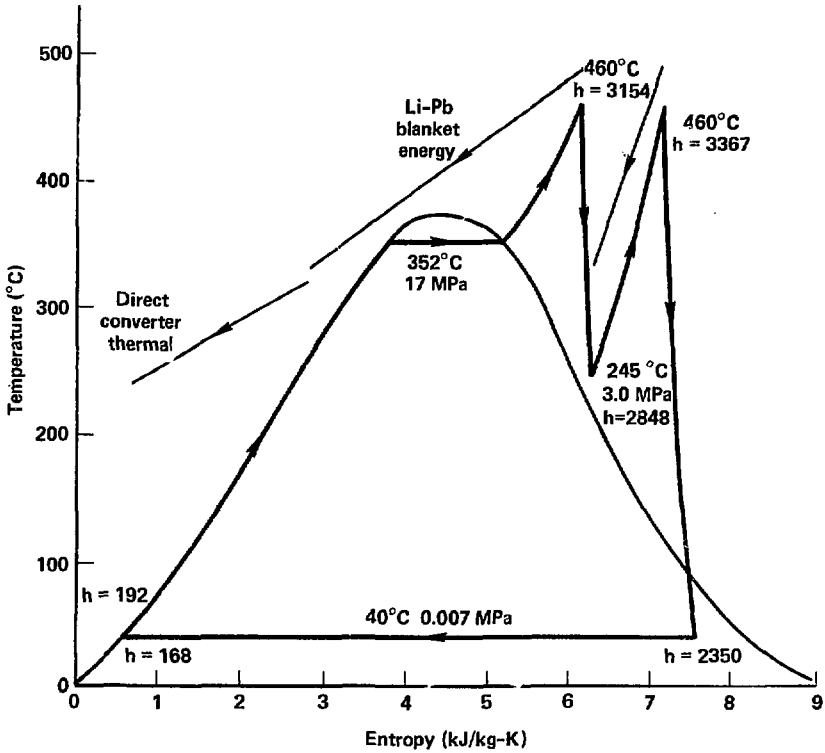

Fig. 6-5. *Temperature-entropy plot for the steam power plant.*

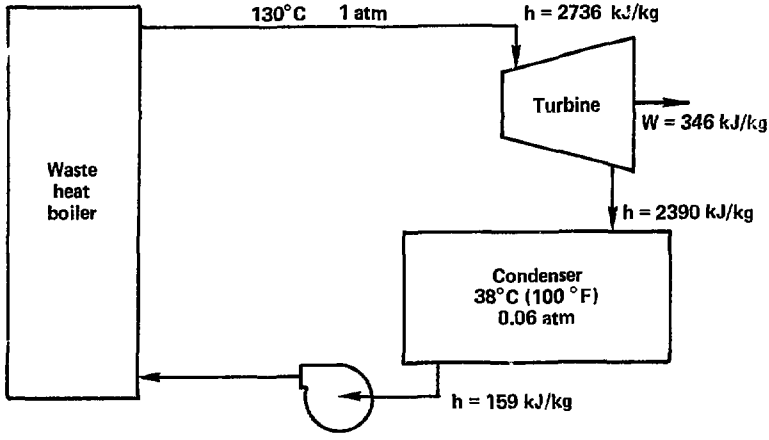

Fig. 6-6. Schematic arrangement for bottoming power plant.

Low temperature cycles are often discussed in terms of alternate working fluids. The motivation for fluids other than steam is to reduce the size and capital cost of the low pressure components. A study at United Technology Laboratories[2] evaluated the relative merit of having several fluids in the bottoming cycles. The study considered steam, ammonia, thiophene, and several Freons. Although the use of fluids other than steam could reduce the size of equipment, that advantage is somewhat offset because the alternate fluids provide lower specific work and require higher volumetric flow rates. The alternate fluids also have some undesirable properties. Ammonia is toxic and flammable; thiophene is flammable; they are all expensive fluids compared to steam.[2,3]

For purposes of the MARS synfuel application, we feel that a conventional low pressure steam cycle is the most suitable.

The particular cycle that we have chosen is a conventional low pressure steam cycle with superheat, as shown on the T-S diagram in Fig. 6-7. The boiler temperature is 373 K at a pressure of 0.1 MPa (1 atm). The steam is superheated to 403 K and then expanded through the turbine with an isentropic efficiency of 0.85 to 311 K at a pressure of 0.0066 MPa (0.06 atm). The exit steam contains 7.5% moisture. The condenser operating at 311 K corresponds to cooling tower operation on an average day. The condensate is returned to the boiler through the feedwater pump and heaters.

The enthalpy at various points in the cycle is shown in Fig. 6-7. The net workout is 346 kJ/kg, and the total energy input is 2579 kJ/kg, giving an overall thermal efficiency of 0.13. If the condenser operates at a lower temperature of 300 K the efficiency increases to 0.16.

It could be argued that the bottoming power plant is too costly and that it would be more economic to remove it and dump all process reject energy to the cooling tower. Bottoming plant removal has an important impact on the overall interface power balance because the electric power loss must be picked up by the steam power plant. The effect of removing the bottoming plant is summarized in Table 6-6. The overall cycle efficiency drops from 0.37 to 0.32. This corresponds to a 12% reduction in hydrogen production from 5223 and 4587 mole/s. The fractional use of blanket power also changes where more of the high temperature blanket power is needed for the low temperature process and more low temperature blanket power is required for the stream power plant. The economic impact of removing the bottoming plant is discussed in Sec. 9 of this volume.

6.7 CONCLUSIONS

The analysis presented here produces an overall plant efficiency of 37%. To obtain that efficiency requires the use of a bottoming steam-electric power plant to recover waste heat from the TCP. Without the bottoming plant, the overall efficiency drops to 0.32. Steam provides the simplest working fluid and technology for the bottoming plant.

Because the TCP has a sizable electrical power demand to drive the compressors, electrical power production is an important part of the interface. Standard steam Rankine technology can satisfy that electrical requirement in the main and bottoming power plants.

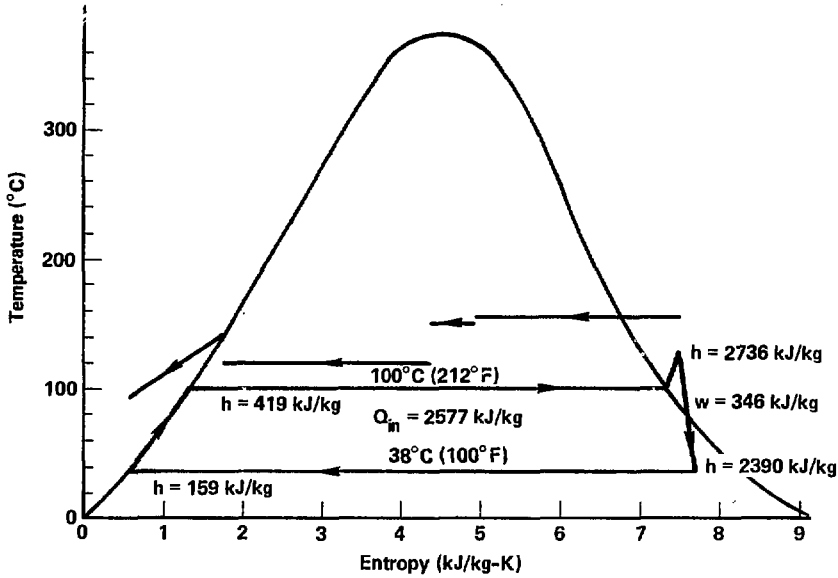

Fig. 6-7. Temperature vs enthalpy for the bottoming power plant.

The selected temperature matching can satisfy the TCP requirements and the TMR design constraints with reasonable temperature differences. To make this we possible, we used duplex tube heat exchangers rather than separate intermediate heat exchangers.

Table 6-6. Interfacing summary results with and without the bottoming power plant.

	With bottoming	Without bottoming
TCP efficiency	0.37	0.32
Hydrogen production (mole/s)	5223	4587
Blanket energy fractions		
Decomposer (f_{n_1})	0.26	0.23
Low temperature process (f_{n_2})	0.20	0.23
Low temperature process (f_{l_1})	0.29	0.20
Steam plant (f_{l_2})	0.25	0.34
Thermal energy required (kJ/mole)		
Decomposer	171	171
Low temperature process	315	315
Steam plant	224	323
Thermal energy supplied (kJ/mole)		
High temperature blanket	299	340
Low temperature blanket	351	399
Direct converter thermal	61	70

APPENDIX 6-A
THERMOCHEMICAL CALCULATIONS FOR THE SULFURIC ACID PROCESS STREAM--SECTION II

D. S. Rowe

As part of the University of Washington's support to LLNL, we completed an independent calculation to define the energy requirements for the H_2SO_4 process stream. The discussion presented here grew out of work done by Mark Abhold as part of a student design project and computations performed by Oscar Krikorian at LLNL.

The calculations considered the H_2SO_4 process stream represented in Fig. 6-A-1. The objective of the calculation was to calculate the energy requirement for each component based on the enthalpy of the inlet and outlet streams. Each numbered stream could have up to seven chemical species and the molar flow rates were defined based on the chemical processes taking place in each of the components.

The total mass flow rate for each stream (j) was calculated from

$$\dot{m}_j = \dot{N} \sum_i n_{i,j} M_i \ ,$$

where

$\dot{m}_j$ = mass flow in stream j (g/s);

$n_{i,j}$ = mole fraction of species i in stream j normalized to production of 1 mole of hydrogen ($mole_i/mole_{H2}$);

M_i = molecular weight of species i (g/mole);

$\dot{N}$ = molar production rate of hydrogen ($mole_{H2}/s$).

The mass balance for each component was calculated from

$$\sum_j (\dot{m}_j)_{out} - \sum_j (\dot{m}_j)_{in} = 0 \ .$$

The stream enthalpy was calculated from

$$h_j = \sum_i [n_{i,j}(h_i^o - h_{298}^o) + n_{i,j} \Delta h_f^o] \ ,$$

where h_j = mixture enthalpy of stream j ($kJ/mole_{H2}$) ,

$h_i^o - h_{298}^o$ = enthalpy of species i above 298 K ($kJ/mole_i$) ,

Δh_f^o = enthalpy of formation for species i ($kJ/mole_i$) .

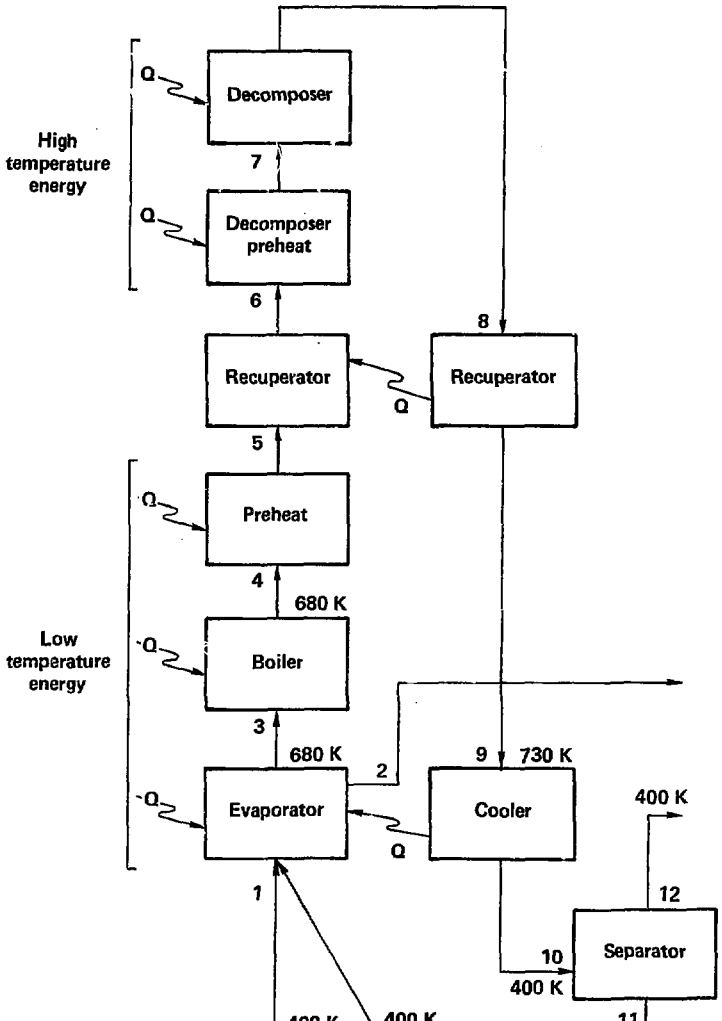

Fig. 6-A-1. H_2SO_4 component and process stream identification.

The thermal energy requirement for each component was calculated from

$$q = \dot{N}\left[\sum_j (h_j)_{out} - \sum_j (h_j)_{in}\right],$$

where

q = net thermal power (kJ_t/s).

The enthalpy data for each species were taken from the JANAF tables.* The enthalpy of mixtures of liquid H_2O and H_2SO_4 was interpolated from the tables containing the various hydrates of H_2SO_4 and thus includes the enthalpy of mixing.

The molar flow rates for each species were taken from Krikorian's† composition and where the following assumptions were made for each stream:

- Stream 1--Input mixture of liquid H_2SO_4 and H_2O at 400 K.
- Stream 2--Partially condensed vapor (55%) as output from evaporator available for energy recovery at 430 K.
- Stream 3--Azeotrope mixture of liquid H_2O and H_2SO_4 at 680 K.
- Stream 4--Equilibrium molar composition of vapors (H_2O, SO_3...). based on calculations of Krikorian.
- Stream 5--Same as Stream 4.
- Stream 6--Same as Stream 4.
- Stream 7--Same as Stream 4.
- Stream 8--SO_3 decomposition at 0.64 conversion ratio.
- Stream 9 --Sensible cooling of decomposer products to 730 K only-- no recombination of SO_2 and O_2.
- Stream 10--Cooling of products to 400 K without recombination of SO_2 and O_2 but with recombination of SO_3 and H_2O to yield H_2SO_4.
- Stream 11--Liquid H_2O and H_2SO_4 recycle at 400 K.
- Stream 12--Product stream gases at 400 K.

We automated the calculations for a microcomputer and performed them iteratively to obtain stream temperatures that would allow energy matching of the recuperator. Stream temperatures, molar flow rates, and enthalpy results are presented in Table 6-A-1. The energy requirement results are presented in Table 6-A-2.

*JANAF Thermochemical Data, Dow Chemical Co., Medland, MI (data through 1979).
†O. H. Krikorian, Hydrogen Production Based on Magnetic Fusion, Lawrence Livermore National Laboratory, Livermore, CA, UCRL-86600 (1981).

Table 6-A-1. H_2SO_4 process stream thermochemical calculations for fluidized bed decomposer.

H2S04 Process stream thermochemical calculations

Fluidized bed
Conversion ratio 0.64
Hydrogen production 5223 (mole/s)

	Thermochemical calculations based on 1 mole/s of hydrogen					
	Molar flow (mole/s)	H-H298 (kcal/mole)	Deltah (kcal/mole)	H (kcal/mole)	Flow*H (kcal/s)	Mass flow (G/s)
Stream 1 (400 K)						
H2S04(L)	1.000	9.877	-488.074	-478.197	-478.197	98.000
H20(L)	4.107	0.000	0.000	0.000	0.000	73.926
Stream 2 (430 K)						
H20(G)	2.120	1.074	- 57.798	- 56.724	-120.256	38.160
H20(L)	2.560	0.000	- 68.315	- 68.315	-174.886	46.080
Stream 3 (680 K)						
H2S04(L)	1.551	16.737	-202.957	-186.220	-288.827	151.998
H20(L)	0.174	0.000	0.000	0.000	0.000	3.132
Stream 4 (680 K)						
H2S04(G)	1.032	9.633	-175.700	-166.067	-171.381	101.136
H20(G)	0.693	3.214	-57.798	-54.584	-37.827	12.474
S03(G)	0.519	5.646	-94.590	-88.944	-46.162	41.520
Stream 5 (722 K)						
H2S04(G)	0.755	10.851	-175.700	-164.849	-124.535	74.034
H20(G)	0.970	3.590	-57.798	-54.208	-52.571	17.456
S03(G)	0.796	6.352	-94.590	-88.238	-70.198	63.644
Stream 6 (825 K)						
H2S04(G)	0.240	13.921	-175.700	-161.779	-38.903	23.566
H20(G)	1.485	4.535	-57.798	-53.263	-79.083	26.726
S03(G)	1.311	8.127	-94.590	-86.463	-113.312	104.843
Stream 7 (1100 K)						
H2S04(G)	0.011	22.552	-175.700	-153.148	-1.622	1.038
H20(G)	1.715	7.210	-57.798	-50.588	-86.742	30.864
S03(G)	1.540	13.077	-94.590	-81.513	-125.563	123.233

Table 6-A-1. (continued).

H2S04 Process stream thermochemical calculations

Fluidized bed
Conversion ratio 0.64
Hydrogen production 5223 (mole/s)

Thermochemical calculations based on 1 mole/s of hydrogen

	Molar flow (mole/s)	H-H298 (kcal/mole)	Deltah (kcal/mole)	H (kcal/mole)	Flow*H (kcal/s)	Mass flow (G/s)
Stream 8 (1100 K)						
H2S04(G)	0.002	22.552	-175.700	-153.148	-0.306	0.196
H20(G)	1.723	7.210	-57.798	-50.588	-87.163	31.014
S03(G)	0.549	13.077	-94.590	-81.513	-44.751	43.920
02(G)	0.500	6.265	0.000	6.265	3.133	16.000
S02(G)	1.000	9.540	-70.947	-61.407	-61.407	64.000
Stream 9 (730 K)						
H2S04(G)	0.002	11.087	-175.700	-164.613	-0.329	0.196
H20(G)	1.723	3.663	-57.798	-54.135	-93.275	31.014
S03(G)	0.549	6.489	-94.590	-88.101	-48.368	43.920
02(G)	0.500	3.226	0.000	3.226	1.613	16.000
S02(G)	1.000	4.804	-70.947	-66.143	-66.143	64.000
Stream 10 (400 K)						
H2S04(L)	0.551	5.880	-294.969	-289.089	-159.288	53.998
H20(G)	0.427	0.825	-57.798	-56.973	-24.327	7.686
02(G)	0.500	0.723	0.000	0.723	0.362	16.000
S02(G)	1.000	1.016	-70.947	-69.931	-69.931	64.000
H20(L)	0.747	0.000	0.000	0.000	0.000	13.446
Stream 11 (400 K)						
H2S04(L)	0.551	5.880	-294.969	-289.089	-159.288	53.998
H20(L)	0.747	0.000	0.000	0.000	0.000	13.446
Stream 12 (400 K)						
H20(G)	0.427	0.825	-57.798	-56.973	-24.327	7.686
02(G)	0.500	0.723	0.000	0.723	0.362	16.000
S02(G)	1.000	1.016	-70.947	-69.931	-69.931	64.000

Table 6-A-2. H_2SO_4 process stream thermochemical summary results for fluidized bed decomposer system.

Process Stream Summary

No.	Temperature (K)	Enthalpy, H2 (kJ/mole)	Mass flow (kg/s)	Energy flow (MW)
1	400.00	-2000.78	897.97	-10450.10
2	430.00	-1234.87	439.99	-6449.75
3	680.00	-1208.45	810.24	-6311.75
4	680.00	-1068.47	810.24	-5580.62
5	722.00	-1034.72	810.27	-5404.34
6	825.00	-967.75	810.27	-5054.57
7	1100.00	-895.07	810.27	-4674.97
8	1100.00	-797.03	810.24	-4162.88
9	730.00	-864.00	810.24	-4512.68
10	400.00	-1059.33	810.24	-5532.86
11	400.00	-666.46	352.26	-3480.93
12	400.00	-392.86	457.98	-2051.93

Total mass balance error 1.52588E-05

Component Summary

Component	Enthalpy change, H2 (kJ/mole)	Net power (MW)
Evaporator	223.91	1169.48
Boiler	139.98	731.13
Preheater	33.75	176.27
Recup (in)	66.97	349.77
Recup (out)	-66.97	-349.80
Recup (net)	-0.00	-0.03
Decomp (preht)	72.68	379.60
Decomp (react)	98.04	512.08
Cooler	-195.32	-1020.18
Total	373.04	1948.38
System total	373.04	1948.38

REFERENCES

1. R. W. Werner, Fribe et al., Synfuel From Fusion--Using the Tandem Mirror Reactor and a Thermochemical Cycle to Produce Hydrogen, Lawrence Livermore National Laboratory, Livermore, CA, UCID-19609 (1982).

2. S. L. Robson, et al., Technological and Economic Feasibility of Advanced Power Cycles and Methods of Producing Nonpolluting Fuels for Utility Power Stations, UARL Report J-970855-13, (1970).

3. Evaluation of Phase 2 Conceptual Designs from the Energy Conversion Alternatives Study (ECAS), NASA-TM-X-73515 (April 1977).

7 Tritium Control in the Blanket System

CONTENTS

7. Tritium Control in the Blanket System

7.1 INTRODUCTION

7.1.1 An Overview of Tritium Issues in MFE

Tritium is a beta emitter with a half life of 12.3 years. It is a particular biological hazard because it can enter the life cycle by substituting for hydrogen in water or organic compounds. Containment and control of tritium in the reactor system present some special problems because tritium can permeate through metallic materials and form volatile species, such as HT and HTO, that can enter the environment. The following are some of the important problems concerning tritium containment and control:

- Permeation rates of tritium through metallic containment materials.
- Processes for recovering tritium fuel from the breeder materials and coolant streams in the blanket.
- The amount of tritium retained in the blanket and coolant system materials (such as in the form of dissolved tritium).
- Rates and processes for isotopic exchange of tritium with hydrogen, both in the reactor system and in the environment.
- Behavior and disposition of tritium in the event of a reactor accident.
- Management and disposal of tritium-contaminated blanket materials.

Although we have only a preliminary understanding of how to resolve these problems, we do know several things about the behavior of tritium. The tritium (hydrogen) permeation rate through metallic materials varies by many orders of magnitude among different metals and alloys. Furthermore, the results of different experiments show large variations for a given metal or alloy because of differences in measurement techniques and factors such as surface conditions, impurities, and radiation damage effects.

For example, ferritic alloys (such as HT-9, which is used as a first-wall material in many reactor designs) when free of surface oxide have a relatively high rate of tritium diffusion for the entire temperature range from room temperature to more than 1100 K (i.e., $D = 10^{-4}$ to 10^{-3} cm^2/s). Stainless steel alloys, such as 316 SS, have a much larger variation in diffusion rates with temperature than ferritic alloys, with values ranging from $\sim 10^{-11}$ cm^2/s at room temperature to $\sim 10^{-4}$ cm^2/s at 1000 K. Tritium permeation rates generally follow the diffusion rates in the above examples because the permeation rate is the product of the diffusion rate and solubility, and the solubility of tritium is about the same in all the iron-based alloys.

It is significant to note that even though the tritium diffusion rate is inherently high in ferritic alloys, an oxide surface scale on a ferritic alloy provides a surface barrier that can readily reduce the observed tritium diffusion rate from $\sim 10^{-7}$ to $\sim 10^{-9}$ cm^2/s. Similarly, the presence of an oxide scale reduces the tritium permeation rates for a number of metal alloys. The phenomenon is not true for all alloys, however, because the oxide scale must be coherent (free of cracks) and composed of a material that has an inherently low tritium diffusivity (e.g., Cr_2O_3 or Al_2O_3).

A tritium inventory can build up in both metallic and ceramic blanket materials because of surface adsorption, solid solution formation, occlusion in bubbles or radiation-induced traps, and other processes. For a given reactor design, the tritium inventory can range from a few grams to tens of grams in metallic blanket materials, and can be on the order of hundreds of grams to kilograms for ceramic blanket materials. We need much more information in this area because even a few grams of tritium inventory in the blanket may pose safety problems in the event of an accident, depending on the chemical form of the tritium and the nature of the accident. In contrast, many kilograms of tritium may be safe if properly contained in a chemically inert form.

Several problems must be addressed when developing methods for disposing of reactor blanket wastes contaminated with tritium. For example, if we were to store a blanket module in a pond of water for several years to allow short half-life nuclides to decay, we would ask the following questions:

- Will tritium permeate out of metals and ceramics rapidly and be released to the pond?
- Does radiation damage in metals and ceramics provide additional mechanisms for tritium permeation losses at room temperature?
- Will surface oxides on metals provide a tritium diffusion barrier? If so, will these oxides be corroded by the pond water and lose their effectiveness as a barrier?
- Will the pond water cause stress corrosion cracking and enhanced tritium release in the metal alloys?
- Will the isotopic exchange of tritium with protium play a role in the release of tritium to the environment?

Here again we have an area where we have no data, and speculation is difficult. It is therefore important to maintain as low a tritium inventory in the blanket as we can prudently design until definitive information becomes available on tritium waste disposal issues. One approach that we expect to take is to bake out the blanket waste materials to outgas off a large fraction of the tritium before storing the waste materials in the pond.

7.1.2 Water Removal and Tritium Exchange during Reactor Startup

During the initial startup of the reactor, we will have a large amount of ordinary protiated water in the high temperature zone of the blanket and in the helium piping regions. This water comes from several sources: as a common constituent of metal and ceramic construction materials, as an impurity in the starting helium, and as a consequence of exposing the system to air. Furthermore, the amount of this initial water can vary substantially depending on the procedures used to build and assemble the blanket and piping systems. We estimate this initial water inventory to be on the order of 500 moles of H_2O, which can be compared with a tritium production rate of 74 moles/day of T_2O and T_2.

Hence, during reactor startup we expect that the helium coolant will sweep out substantially more protiated water than tritiated water. Eventually this water will all reach the molecular sieve bed set up for tritium recovery. We expect that most of the protiated water will be removed from the blanket system during the first 2 to 4 weeks of reactor operation, and that relatively little protiated water will be reintroduced into the system if adequate care is exercised in future blanket maintenance operations.

As protiated water continues to diminish by being swept out and tritium continues to be produced at a nearly constant rate in the blanket, the tritiated water that is recovered will shift from an initial mixture of H_2O and HTO to mostly T_2O as steady state is approached.

The equilibrium amount of water (i.e., the saturation concentration of water) that can be dissolved and adsorbed on blanket and piping materials at any given time will be a function of the vapor pressure of the total residual water (H_2O, HTO, and T_2O) in the helium flow stream. Tritium exchange with this dissolved or adsorbed water should be a relatively rapid process at blanket operating temperatures. It should be comparable to the rate of water evolution into the helium sweep stream. We can therefore anticipate that after a few weeks of reactor operation the inventory of dissolved and adsorbed water in the blanket system (except in the SiC components) will drop to the equilibrium condition for the blanket temperatures involved, and that isotopically the dissolved and adsorbed water will be essentially all T_2O.

In addition to tritium in the form of dissolved or adsorbed water, a substantial amount of tritium will also be dissolved and retained as elemental hydrogen (HT or T_2) in metals and ceramics in the blanket system. The isotopic composition and amount of this dissolved elemental hydrogen will be a function of time as tritium gradually replaces protium. Even though most of the tritium may initially be generated as HTO or T_2O, these species can be readily reduced to elemental HT and T_2 by metals and carbon-containing materials in the system, followed by dissolution of the HT and T_2 in the metal and ceramic components.

To determine the tritium inventory in the blanket system, several factors must be considered, including the time-dependent changes in the amount and isotopic composition of water compared to the initial water inventory, the retention of tritiated water and elemental HT and T_2 by adsorption, solubility, and occlusion in blanket materials under operating conditions. Before we quantitatively estimate these inventory values, we will discuss current knowledge of tritium migration mechanisms in metallic and ceramic materials, especially in relation to the MARS/synfuel design.

7.1.3 Tritium Migration Mechanisms in Metallic and Ceramic Blanket Materials

Tritium follows a rather complex path from the moment it is generated in the MARS blanket until it is recovered for use as a fuel. The efficient tritium recovery, maintenance of a low inventory in the reactor, plus safe containment of tritium from the environment and the synfuel product all pose difficult design problems. A good understanding of the mechanisms by which tritium undergoes chemical reactions and permeates through metallic and ceramic materials is therefore essential for a proper design.

In general, the tritium migration mechanisms and permeation rates through metals are fairly well known, including the three metallic alloys of the most interest to the MARS/synfuel blanket and to the blanket/process interface: HT-9, Waspaloy, and Incoloy-800H. Compositions in weight percent of these alloys are nominally: 85.1 Fe, 11.5 Cr, 1.0 Mo, 0.6 Mn, 0.5 W, 0.5 Ni, 0.4 Si, 0.2 V, and 0.2 C for HT-9; 58.2 Ni, 19.5 Cr, 13.5 Co, 4.3 Mo, 3.0 Ti, 1.3 Al, 0.08 C, 0.06 Zr, and 0.006 B for Waspaloy; and 44 Fe, 32.5 Ni, 21 Cr, 0.8 Mn, 0.5 Si, 0.4 Al, 0.4 Ti, 0.3 Cu, and 0.08 C for Incoloy-800H. However, the information on ceramics is grossly inadequate and does not permit us to obtain a clear-cut interpretation of tritium migration mechanisms.

The ceramic materials of particular interest to the MARS/synfuel design are as follows:

- $LiAlO_2$,
- SiC,
- $MgAl_2O_4$,
- Fiberfrax,
- Cr_2O_3,
- Al_2O_3.

We have chosen $LiAlO_2$ as the solid breeder. The SiC, manufactured as 3-cm-diam balls of 80% theoretical density, is used to contain the $LiAlO_2$, which occurs as 100-μm particles within the open porosity of the balls. It is also the main neutron moderator for generation of process heat, is used as plates and other specially formed parts to provide some of the structure within the blanket, and is also used to make piping manifolds for the helium stream. The $MgAl_2O_4$ is an alternate material to SiC for use in the blanket. Fiberfrax is a fibrous, glassy, wool-like material used to provide thermal insulation between the SiC structure and the HT-9 pressure shell. The alloy HT-9 is also used for the first wall and as a containment material for the Li-Pb coolant in the low temperature zone. Waspaloy is the most likely choice as a heat exchanger material between the helium coolant stream and the SO_3 decomposer in the hydrogen production thermochemical plant. Both the helium stream and SO_3 decomposer sides of the Waspaloy are aluminided to provide additional protection against corrosion. Under oxidizing conditions, the aluminide forms an Al_2O_3 scale, which serves as a permeation barrier for

tritium. On the helium side, the aluminided surface is intentionally preoxidized before use to obtain the Al_2O_3 scale, whereas on the SO_3 side the aluminized surface is converted to Al_2O_3 in situ under the oxidizing conditions of the SO_3 decomposer. The AL_2O_3 scale also provides corrosion resistance for the Waspaloy against attack by the reactive gases in the SO_3 decomposer. Incoloy-800H is a lower cost alternative to Waspaloy, but it is not as strong at higher temperatures and would therefore be used in the lower temperature regions of the decomposer. Aluminide coatings would also be applied to both sides of the Incoloy-800H and preoxidized on the helium side to form a protective Al_2O_3 scale as a permeation barrier.

7.1.3.1 The Chemistry of Tritium Generation. We do not know of any direct information about the chemistry of tritium generation in ceramics. Nonetheless, from our own chemical perception, we believe that the tritium generation reactions from ^6Li and ^7Li in $LiAlO_2$ can be written as

$$n + {}^6LiAlO_2 \rightarrow AlO_2^- + \square + T^+ + He^{++} + 2\,e^- + \text{energy, and} \qquad (1)$$

$$n + {}^7LiAlO_2 + \text{energy} \rightarrow AlO_2^- + \square + T^+ + He^{++} + 2\,e^- + n' \,. \qquad (2)$$

Reaction (1) is exothermic and Reaction (2) is endothermic from a nuclear reaction standpoint. However, from a chemical standpoint the product nuclei are produced in both cases at high enough energies so that they are completely ionized to their core nuclei, i.e., T^+ and He^{++}. As T^+, He^{++}, and the excess electrons recoil from the original Li lattice position, we are left with a lattice vacancy that we designate as $\square$. Furthermore, if we assume an ionic structure for $LiAlO_2$, the Li undergoing nuclear reaction is originally present as Li^+ and an excess negative charge (electron) is present on the surrounding oxygens. After nuclear reaction, an excess electron is left with an oxygen that is adjacent to the vacancy. This structural arrangement is chemically designated as AlO_2^-. The core ions (T^+ and He^{++}) are extremely small compared with normal atoms, and with their excess kinetic energy they will migrate rapidly through the lattice until they expend most of their energy and find an active site with which to react. From a chemical and thermodynamic standpoint these core ions are extremely reactive. The He^{++} should eventually find and react with the two excess electrons in the lattice and form a neutral atom located in either an interstitial or lattice position.

We expect T^+ to end up in the $LiAlO_2$ lattice in one of several possible chemical forms:

- As the OT^- group bonded to Li or Al [i.e., as LiOT or AlO(OT) dissolved in solid solution in the $LiAlO_2$ lattice];
- As the T^- group bonded to Li or Al (i.e., as TLiO or $TAlO_2$, where T is bonded directly to Li or Al rather than to O, and dissolved in the $LiAlO_2$ lattice);
- T_2 or HT (dissolved in the $LiAlO_2$ lattice);
- T (free neutral atom in an interstitial position).

The evidence in the case of silicate glasses (when careful spectroscopic studies have been carried out) indicates that the first three types of reactions do occur with SiO_2,[1] i.e., both SiOT and SiT bonds form as well as molecular T_2 (actually the H and D analogs were studied but are chemically similar to T). There is no evidence however for interstitial T. We would surmise that the T atoms can indeed form as an intermediate product in $LiAlO_2$, but like T^+, these atoms would be extremely reactive with the lattice and would convert at first opportunity to one of the first three forms above. Possible migration mechanisms for these species will be examined later in this discussion.

7.1.3.2 Tritium Migration in Metals. Tritium migrates through most metals as a neutral atom, most likely through interstitial positions. The permeation rate of tritium through the metallic lattice depends both on the solubility and diffusion rate of tritium, as given by the expression

$$K = C \cdot D, \tag{3}$$

where K is the permeability, C is the concentration (solubility) of dissolved tritium, and D is the diffusivity of tritium. The diffusivity follows an Arrhenius type of temperature dependence as long as there is no change of diffusion mechanism, i.e.,

$$D = A \exp(-E/RT). \tag{4}$$

Permeation also follows an Arrhenius type relation. However, tritium solubility usually decreases with temperature for metals so that the activation energy for permeation is usually less than that for diffusion.

The diffusing species in metals is surmised by exposing the metal to a series of hydrogen pressures at a fixed temperature and noting the power dependence of hydrogen pressure on the diffusion rate. A first power dependence indicates that H_2 is the migrating species, whereas a square root of pressure dependence indicates that H is the migrating species. This can be seen from the equilibrium expression for dissociation of H_2 to H atoms, such that

$$H_2 = 2\,H,\ K = \frac{(p_H)^2}{(p_{H_2})}, \tag{5}$$

where (p_H) is seen to be proportional to the square root of the imposed H_2 pressure, and p_H provides the chemical potential for diffusion when H is the migrating species.

It is not clear that H is always the migrating species in metals. For example, in the case of vanadium, H_2 appears to be the migrating species at low pressures.[2]

Many times the permeation of hydrogen through metals is hindered by a surface scale of oxide on the metal. This is believed to be the case for metals such as niobium and vanadium at low to moderate temperatures and for aluminum and beryllium at all temperatures of use. All four of these metals

readily form protective oxide scales even at room temperature in air. Metal alloys, such as the stainless steels or the nickel-based superalloys may also form surface oxide scales if they are intentionally preoxidized at high temperatures in air or oxidizing atmospheres. Some of these scales (e.g., Cr_2O_3- and Al_2O_3-rich scales) may also be effective barriers against tritium permeation.

7.2.3.3 Tritium Migration in Glasses. A significant amount of quantitative information has been generated on silicate glasses that could give us some insight into tritium behavior in ceramics. Most of this work on glasses has been conducted in recent years at the Sandia Livermore National Laboratory.[1,3-6] These studies have shown that at temperatures below ∿600 K, hydrogen diffuses through silica and silicate glasses as molecular H_2 with essentially no chemical interaction with the silicate network that makes up the lattice. At temperatures above ∿600 K, hydrogen that diffuses into silica and silicate glasses reacts to varying degrees depending on the characteristics of the glass. The reaction rate is enhanced by lattice defects in the glass, such as defects resulting from impurities or irradiation.

For pure SiO_2 glass containing very low levels (<5 ppm) of dissolved water as hydroxyl (OH^-), reaction of hydrogen with the silica matrix begins at ∿800 K and results primarily in the formation of hydroxyl groups. This reaction is believed to occur mainly at peroxide defect sites in the SiO_2 lattice, i.e.,

$$Si\text{-}O\text{-}O\text{-}Si + H_2 \rightarrow 2\ Si\text{-}O\text{-}H. \qquad (6)$$

For SiO_2 glass that contains normal amounts of impurities (including 0.01 to 0.1% of dissolved water as hydroxyl) but where the glass is not radiation damaged, hydrogen will interact with the silicate lattice above ∿600 K to produce both hydride and hydroxyl groups until a saturation point is attained. Hydrogen then permeates through the glass as molecular H_2. This reaction of hydrogen with the silicate lattice can be represented by

$$Si\text{-}O\text{-}Si + H_2 \rightarrow Si\text{-}OH + Si\text{-}H\ . \qquad (7)$$

In irradiated SiO_2 glass, the reaction rate of hydrogen with the silicate matrix to form hydroxyl and hydride groups is greatly accelerated. Relatively rapid rates have been observed at as low as 300 K. Clearly, radiation-induced lattice defects greatly accelerate these reaction rates. The reaction of hydrogen with the glass to form Si-OH and Si-H must reach saturation before significant amounts of hydrogen will permeate through the glass under these irradiated conditions.

In unirradiated silicate glass and SiO_2 glass that contains hydroxyl groups (dissolved water), isotope exchange begins above ∿600 K, if a hydrogen isotope other than the dissolved form permeates through as molecular hydrogen. There is a gradual increase in the isotopic content of the permeated hydrogen until the exchange is completed. For irradiated silica the behavior is similar but the rates are accelerated and hence isotope exchange begins at lower temperatures.

Thus, from these studies on silicate glasses and SiO_2 glass, we see that tritium diffusion and permeation through the glasses begins at relatively low temperatures. We further find that radiation-induced defects and impurities such as dissolved water significantly affect the reactivity and migration rates of tritium in the glasses.

7.1.3.4 Tritium Migration in Ceramics. Kudo and Okuno[7,8] have studied tritium release rates from Li_2O, LiOH, and Li_2C_2; Elleman and coworkers[9-11] have studied hydrogen solubilities (including deuterium and tritium isotopes) and diffusion and permeation rates in Al_2O_3 and SiC; and Boothe and Ache[12-14] have studied tritium release rates from graphite, SiC, and B_4C. Some limited information also exists on tritium release rates from Li_3N, Li_7Pb_2, LiAl, Li(1 wt%)-Al, Li_2CO_3, $LiAlO_2$, Li_2SiO_3, Li_2TiO_3, and Li_2ZrO_3.[15] More recent unreported information may also be available on other lithium compounds. Nearly all the above work represents tritium release rates from tritium bred in lithium compounds by neutron irradiation or from tritium-implanted materials. As such, the information is not very useful for deducing the tritium migration mechanisms. An exception to this is the work of Elleman and coworkers,[9-11] who studied actual hydrogen solubilities as well as diffusion and permeation rates.

In studying the power dependence of the hydrogen diffusion rate with pressure, Elleman and coworkers found a power dependence for hydrogen pressure of 0.43 for Al_2O_3 at 1600 K and 0.61 for SiC at 1500 K. In the case of SiC, we could interpret the above result to mean that the diffusing species is a mixture of H atoms and H_2 moleclues; or, if we ascribe a sufficiently large error of measurement, that the power dependence is actually 0.5 and the species are H atoms.

The interpretation for Al_2O_3 is not so straightforward, however. If the power dependence of 0.43 could be assumed within the uncertainty of measurement to actually be 0.5, this suggests that the migrating species could be either H atoms or OH^- (i.e., the hydroxyl ion). Elleman and coworkers believed the migrating species to be H atoms. We believe that OH^- is the more probable species. If Al_2O_3 behaves similarly to SiO_2, the reaction of hydrogen with the Al_2O_3 lattice could be illustrated by

$$H_2 + Al_2O_3 \rightarrow HAlO + AlO(OH). \qquad (8)$$

Under more oxidizing conditions, HAlO should not form. For example, if water is present the reaction should be

$$H_2O + Al_2O_3 \rightarrow 2\ AlO(OH). \qquad (9)$$

In the case of $LiAlO_2$, we believe that the principal mode of hydrogen transport, as was the case with Al_2O_3, is by migration of the hydroxyl group. Referring back to Reactions (1) and (2), we see that a negative charge is created in the lattice each time a T^+ is generated from lithium. This negative charge would reside on an oxygen atom and have a vacancy associated with it. This combination is represented in Equations (1) and (2) by the designation $AlO_2^- + \square$; when lithium is present, we also get $LiO^- + \square$. Thus, the rapidly

migrating species T^+ should eventually combine with an oxygen to form AlO(OT) and LiOT groups in the lattice, i.e.,

$$AlO_2^- + \square + T^+ \rightarrow AlO(OT), \quad (10)$$

$$LiO^- + \square + T^+ \rightarrow LiOT. \quad (11)$$

Subsequent migration of tritium is expected to occur by diffusing OT^- through the lattice. At the surface of the solid, the OT^- should react with an OH^- impurity to form HTO and generate Al_2O_3, $LiAlO_2$, or Li_2O according to the relations

$$AlO(OT) + AlO(OH) \rightarrow Al_2O_3 + HTO, \quad (12)$$

$$AlO(OT) + LiOH \rightarrow LiAlO_2 + HTO, \quad (13)$$

$$LiOT + LiOH \rightarrow Li_2O + HTO. \quad (14)$$

As a result of the high concentration of defects and impurities compared with the concentration of tritium in a real $LiAlO_2$ material, a number of side reactions can occur with tritium in addition to what we believe is the major process above. Thus, only about 87% of the tritium is recovered as HTO in tritium release experiments on $LiAlO_2$.[15] In addition, some 8% is recovered as HT, 1% is recovered as CH_3T, and the balance is recovered mostly as higher carbon-containing hydrocarbons. Furthermore, as protium and/or carbon-containing species are continuously removed from the system, we expect in time that the tritium-containing analogs will dominate. Hence, we expect at steady state that about 90% of the tritium will be released as T_2O and 10% as T_2.

We must re-emphasize that this discussion is only an initial and incomplete attempt to summarize our present thoughts as to the mechanism of tritium migration in the materials of interest to MARS/synfuels. Further experimental work is clearly needed in this area to define the actual tritium migration behavior. In the absence of such data, we have resorted to these rough assessments.

7.1.4 Tritium Solubility in Blanket System Materials

We need to know the tritium solubility in blanket materials to determine the amount of tritium retained in the blanket. The required background information is generally lacking, and we have had to review the available literature and make some assessments.

Materials that are likely to dissolve tritium in the high temperature zone of the MARS/synfuel blanket and in the helium piping include the following:

- SiC,
- $MgAl_2O_4$,

- Fiberfrax insulation,
- SiO_2 glass insulation,
- $LiAlO_2$,
- HT-9.

We will discuss the tritium solubility of each of these materials in turn.

7.1.4.1 Tritium Solubility in SiC. Silicon carbide is available in two allotropic forms: α-SiC, which has a hexagonal structure and is the stable form up to about 2373 K, and β-SiC, which has a cubic structure and is the stable form above 2373 K. The α-β transformation is sluggish at 2373 K, but becomes more rapid at higher temperatures, so α-SiC needs to be sintered at temperatures lower than 2373 K. However, sintering rates are generally slow below 2373 K, which presents a production problem. Until recently, an economical process was not available for producing high-density high-strength bodies of pure SiC in either the α or β form.

Commercially, the conventional high strength SiC that has been produced for more than 20 years is made by a reaction bonding process where free carbon and silicon powders are mixed with α-SiC powder. The body is pressed or extruded to shape and fired. Free carbon then reacts in situ with silicon (which is in excess compared to the amount of free carbon needed for stoichiometric SiC) to form a mixture of SiC plus Si, which serves as a sintered bond between the SiC particles. This type of material (e.g., KT-SiC) contains about an 8 wt% excess of Si, attains 97% of theoretical density, is relatively impermeable to gases, and has good strength properties up to 1600 K.

Recently, the industry has developed a simple furnace process for mass-producing submicrometer-sized powders of α-SiC that can be sintered at temperatures below 2373 K. Fabricated bodies of pure α-SiC are now being produced in a variety of sizes and shapes in densities greater than 95% of theoretical using conventional ceramic fabrication methods. Densities both higher and lower than this can also be attained by controlling the sintering conditions.

Fine β-SiC powders can also be produced, but complex processes such as gas pyrolysis or plasma synthesis methods need to be used to produce β-SiC making the β-SiC starting material considerably more expensive than α-SiC. It is also difficult to maintain pure β-SiC during sintering because of partial transformation into α-SiC. Hence, β-SiC is presently fabricated primarily using a pyrolytic vapor deposition process. This product is limited to thicknesses of about 1 cm, and usually contains small amounts of free carbon.

Causey et al.[9] have measured D_2 solubility in pure α-SiC powder and in a vapor-deposited β-SiC specimen; Verghese et al.[11] measured the solubility of H_2 containing trace amounts of HT in a fabricated tube of KT-SiC (α-SiC + 8 wt% Si). Causey et al. have also measured the D_2 solubility in vapor-deposited β-SiC as a function of D_2 pressure ranging from 0.02 to 1.0 atm at a temperature of 1473 K. They find that D_2 solubility varies by a 0.61 ± 0.06 power dependence with pressure. As we said earlier, a 0.5 power dependence would imply hydrogen

atom diffusion through SiC, whereas a 1.0 power dependence would imply molecular hydrogen diffusion. Both Causey et al. and Verghese et al. have accepted a 0.5 power dependence as the best interpretation of the data. They also reported their solubilities at 1 atm hydrogen pressure by normalizing the measured values using the 0.5 power dependence. The actual D_2 pressures used by Causey et al. are not given, although we surmise that they were probably a few tenths of an atmosphere. Verghese et al. used 0.05 to 0.18 atm of H_2 pressure in permeation experiments carried out in the same study as the hydrogen solubility work, and we guess that the hydrogen pressure was about the same for the solubility measurements.

Results of the various reported hydrogen solubilities have all been normalized to 1 atm H_2 pressure (assuming D_2 is equivalent to H_2) and are summarized in terms of g-atoms H/cm^{3}SiC in Fig. 7-1. A cubic meter of SiC is assumed to be at full theoretical density. In the case of KT-SiC, the free Si is assumed to be equivalent to SiC for purposes of summarizing hydrogen solubility in the material and the densities of α-SiC and Si have been combined to obtain an overall material density. Densities are taken as 3.215 g/cm^3 for α-SiC, 3.120 g/cm^3 for KT-SiC, and 3.214 g/cm^3 for β-SiC. We see from Fig. 7-1 that hydrogen solubility is much lower in α-SiC than in β-SiC; hence, α-SiC is the preferred material to use to minimize tritium inventories.

Using Fig. 7.1 and assuming a 0.5 power dependence on H_2 pressure, we obtain the following expression for H_2 solubility in α-SiC,

$$C_H = 5.00 \times 10^{-11} \left(p_{H_2}\right)^{1/2} \exp(19260/T), \qquad (15)$$

where p_{H_2} is in atm and C_H is the hydrogen solubility in g-atoms H/cm^3 SiC. We assume tritium solubility to be identical to protium solubility in α-SiC.

Although Eq. (15) is based on the solubility of the H_2 species in SiC, we believe that the H_2O species present in the surrounding gas will diffuse rapidly through the thin surface layer of SiO_2 glass that is normally present on SiC (see the discussion on tritium migration in glasses in Sec. 7.1.3), and that it will react rapidly enough[16] with the SiC substrate to produce additional SiO_2 and leave H atoms in solution in the SiC. In practice, we use the sum of p_{H_2O} or the equivalent tritium species to calculate the solubility of hydrogen in the SiC. The expression for tritium solubility in α-SiC therefore becomes

$$C_T = 5.00 \times 10^{-11} \left(p_{T_2} + p_{T_2O}\right)^{1/2} \exp(19{,}260/T) \qquad (16)$$

in g-atoms T/cm^3 SiC.

7.1.4.2 Tritium Solubility in $MgAl_2O_4$. Because tritium solubility in α-SiC increases markedly with decreasing temperature, unacceptably high inventories of tritium will be held up in regions where the SiC parts are operated at low temperatures (i.e., at 800 to 1000 K). Hence, the SiC in these low temperature regions (such as in the helium inlet and distributive piping regions that operate at ∿850 K) will need to be replaced with a material that has a low tritium solubility. This substitute material must be tolerant of

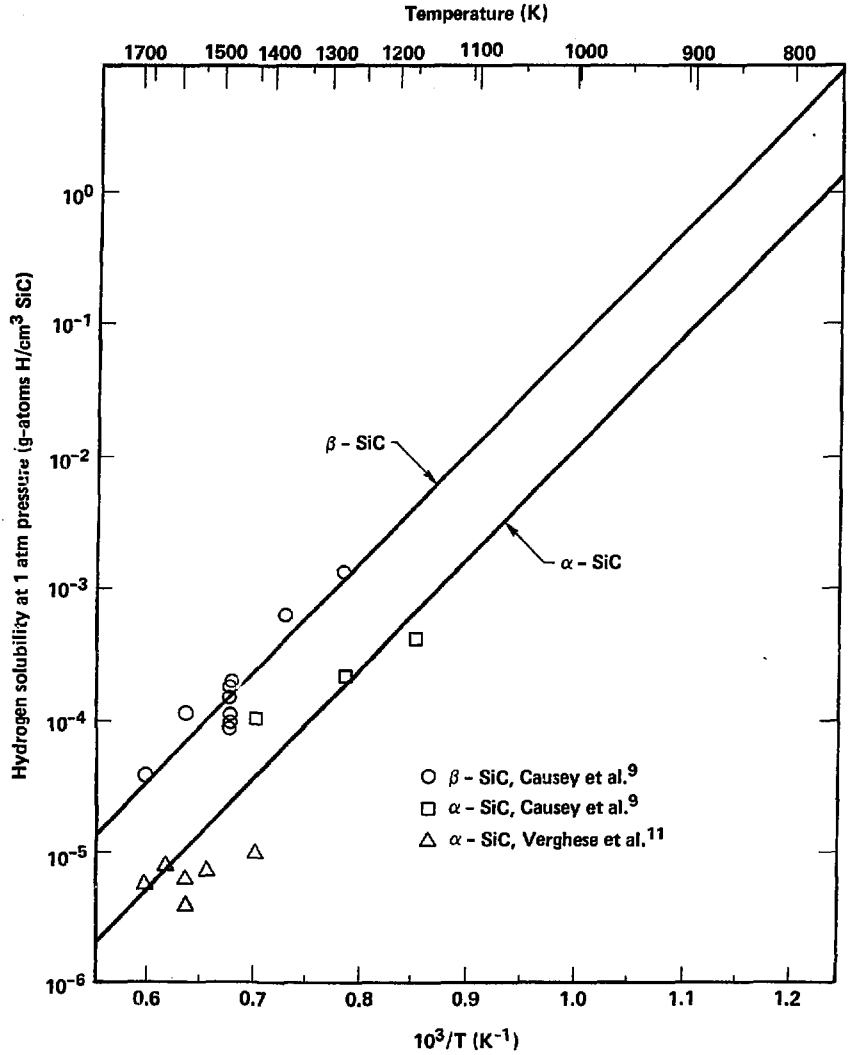

Fig. 7-1. Solubilities of hydrogen in α- and β-SiC as a function of temperature. Solubilities have been normalized to 1 atm hydrogen pressure.

radiation damage effects, must be a low activation material, and must be capable of maintaining good mechanical property characteristics for a temperature rise to about 1300 K during the transients that occur during an unplanned reactor shutdown that involves a stoppage of coolant flow.

The ceramic $MgAl_2O_4$ (spinel) is a good choice as such an alternate material because it is known to have good resistance to radiation damage[17] low activation, and good characteristics as a high temperature ceramic material. Tritium solubility in $MgAl_2O_4$ is not known, however, and we will need to estimate it.

The only crystalline oxide for which we have solubility data for $H_2O(g)$ is Li_2O.[18] Based on the data for Li_2O at an $H_2O(g)$ pressure of 2.88×10^{-5}atm, we derive the approximate relation

$$S(H_2O) = 5.00 \times 10^{-4}\exp(-2582/T), \qquad (17)$$

where $S(H_2O)$ is the $H_2O(g)$ solubility in $Li_2O(s)$ in moles H_2O/mole Li_2O at temperatures from 800 to 1300 K. To estimate the $H_2O(g)$ solubility in $MgAl_2O_4$, we assume that the solubility of $H_2O(g)$ is controlled primarily by the molar content of MgO in the compound, and that the affinity of MgO for $H_2O(g)$ is comparable to the affinity of Li_2O for $H_2O(g)$ (because Mg and Li are both strong hydroxide formers and Al is a relatively weak hydroxide former). Also, because Mg is divalent, one mole of MgO should be equivalent to one mole of Li_2O. On the basis of these assumptions, and taking the solubility of $T_2O(g)$ to be the same as that of $H_2O(g)$ and the density of $MgAl_2O_4$ to be 3.58 g/cm^3, we obtain

$$S(T_2O) = 1.258 \times 10^{-5}\exp(-2582/T), \qquad (18)$$

where $S(T_2O)$ is the solubility of $T_2O(g)$ in $MgAl_2O_4(s)$ in moles T_2O/cm^3 $MgAl_2O_4$ at a T_2O pressure of 2.88×10^{-5}atm and temperatures from 800 to 1300 K.

In making the above estimate for solubility of T_2O in $MgAl_2O_4$, we have ignored the presence of T_2 and its solubility in $MgAl_2O_4$. Considering the uncertainties in our estimate, this is probably not a significant omission. We do not know of any data on H_2 solubility in $MgAl_2O_4$. However, data are available on H_2 solubility in Al_2O_3, indicating that the solubility in that case is exceedingly low.[11]

7.1.4.3 Tritium Solubility in Fiberfrax and SiO_2. Fiberfrax ($3\ Al_2O_3 \times 2\ SiO_2$) is used as a low-density fibrous insulator surrounding the SiC shroud (basket) structure in the high temperature zone, and SiO_2 is used as an insulator lining on the inside of the helium piping walls. We are discussing the tritium solubility of Fiberfrax and SiO_2 together because both are in a glassy state in these applications.

Bedford,[19] in reviewing water vapor solubility in molten silicates, found the water vapor solubility to be nearly independent of temperature in the range from 873 to 1773 K, and to be proportional to the square root of the water vapor pressure within these temperatures. Furthermore, he found that there is not much variation in water vapor solubility among a wide variety of melts of natural rocks.

The dependence of water solubility on the square root of water vapor pressure suggests that in the solubility process only one-half mole of water is required to produce an OH^- group within the silicate structure, i.e.,

$$1/2\ \text{Si-O-Si} + 1/2\ H_2O(g) \rightarrow \text{Si-OH}. \qquad (19)$$

The concentration of OH^- is thus proportional to the square root of the water vapor pressure. Hence, the concentration of water dissolved in the molten silicate (or glass) over the temperature range from 873 to 1773 K can be expressed by the relation

$$C_w = K_w (p_{H_2O})^{1/2}, \qquad (20)$$

where C_w is the moles of dissolved H_2O per mole of SiO_2 in the silicate, and K_w is the solubility constant in units of moles H_2O/mole SiO_2-atm$^{1/2}$. We assume that only the SiO_2 content of the silicate controls H_2O solubility. We believe that this is a reasonable approximation for naturally occurring silicates, and from the data in Bedford's[19] review, we calculate an average value of K_w = 6.1 x 10^{-3} moles H_2O/mole SiO_2-atm$^{1/2}$.

Bedford also conducted an experiment on the solubility of steam in pure SiO_2 glass, where he found a solubility of 0.86 wt% water in SiO_2 at a steam pressure of 30 atm at 1668 K. This gives a value of K_w = 5.2 x 10^{-3} moles H_2O/mole SiO_2-atm$^{1/2}$, thus essentially confirming the value of K_w derived above from molten silicates. We therefore select the above value of K_w = 6.1 x 10^{-3} moles H_2O/mole SiO_2-atm$^{1/2}$ for use in our calculations and take K_w to be independent of temperature.

7.1.4.4 Tritium Solubility in $LiAlO_2$. We are not aware of any measurements of water solubility in $LiAlO_2$. However, recent work at GA Technologies[18] gives data on the water solubility in Li_2O as a function of water vapor pressure and temperature. We use their data as a guide to estimate the values for $LiAlO_2$.

Similar to molten and glassy silicates, GA Technologies' data on water solubility in Li_2O show a square root dependence on water vapor pressure; but unlike the silicates where water solubility is independent of temperature, the water solubilities in Li_2O increase rapidly with increasing temperature. Using an average temperature of 1265 K for the solid breeder in the MARS/synfuel blanket and a water vapor pressure of 2.88 x 10^{-5} atm, we obtain a solubility of 6.5 x 10^{-5} moles H_2O/mole Li_2O from the GA Technologies' data. In the case $LiAlO_2$, we believe that lattice positions in the vicinity of Li will be more reactive with H_2O than lattice positions in the vicinity of Al because the Li-OH bond is stronger relative to the Li-O bond than is the Al-OH bond relative to the Al-O bond. If we assume that the H_2O solubility in $LiAlO_2$ is determined only by the molar content of Li in $LiAlO_2$, we might expect the water solubility in $LiAlO_2$ to be one-half that in Li_2O (i.e., 0.5 x 6.5 x 10^{-5} = 3.25 x 10^{-5} moles H_2O/mole $LiAlO_2$) because $LiAlO_2$ contains one-half as many atoms of Li per mole as does Li_2O. We believe this to be the best guess that we can make, and therefore take 3.25 x 10^{-5} moles T_2O/mole $LiAlO_2$ as our estimate of tritium solubility in $LiAlO_2$ at a temperature of 1265 K and a T_2O vapor pressure of 2.88 x 10^{-5} atm.

It is useful to compare the above solubility estimate for T_2O in $LiAlO_2$ with the T_2O solubility in molten silicates. Using a solubility constant of $K_W = 6.1 \times 10^{-3}$ moles T_2O/mole SiO_2-atm$^{1/2}$, as given in the previous section, and a T_2O pressure of 2.88×10^{-5} atm, we calculate a solubility of 3.3×10^{-5} moles T_2O/mole of SiO_2. The good numerical agreement between this value and our estimated T_2O solubility in $LiAlO_2$ is strictly coincidental, but the solubility value for T_2O in SiO_2 does suggest that we are roughly in the right regime of solubility for H_2O dissolved in oxides.

7.1.4.5 Tritium Solubility in HT-9. The iron-rich ferritic alloy, HT-9, has been selected for the first wall of the MARS/synfuel blanket. It is further used to contain the Li-Pb coolant and as the pressure shell for the helium coolant. The nominal composition (in wt%) of a typical HT-9 alloy is: 85.1 Fe, 11.5 Cr, 1.0 Mo, 0.6 Mn, 0.5 W, 0.5 Ni, 0.4 Si, 0.2 V, and 0.2 C.

We believe that when T_2O is in contact with iron-based alloys over long periods of time it establishes a steady state condition in which the T_2O diffuses through the surface oxide film and reacts with the iron alloy beneath to produce additional oxide and to release the tritium to dissolve and permeate through the alloy. As a consequence of this reaction, the T_2 produced will have a pressure equivalent to the pressure of T_2O in the environmental gas above the iron alloy.

There are no direct data on the T_2 solubility in HT-9, but for pure Fe at an average temperature of ~773 K and an H_2 pressure of 3.20×10^{-5} atm, we calculate an H_2 solubility of 1.6×10^{-8} moles H_2/cm^3 of Fe based on data given in the review by Galaktionova.[20] Taking into account the effects of alloying additives on H_2 solubility in HT-9,[19] give a net positive effect as a result of the presence of V, and we calculate an H_2 solubility of 2.5×10^{-8} moles H_2/cm^3 of HT-9. We assume the solubility of T_2 in HT-9 to be identical to this value at a temperature of 773 K and a T_2 pressure of 3.20×10^{-5} atm.

7.2 TRITIUM INVENTORY AND RECOVERY

7.2.1 Slip-Stream Tritium Processor

After allowing a sufficient period of time after reactor startup (i.e., several weeks) for the concentration of protiated water to drop to a negligible level in the helium stream, tritium, mainly in the form of T_2O, will establish a steady-state concentration level in the helium. It is important to determine the value of this tritium concentration as the first step in a tritium inventory analysis because the inventory of tritium retained in blanket materials is functionally dependent on the tritium concentration in the helium stream.

The steady-state T_2O concentration in the helium can be calculated if we know the following:

- The rate at which tritium is being produced in the blanket;
- The fraction of the helium flow stream that is sent through a slip stream for tritium recovery;
- The concentration of unrecovered tritium returned to the main helium stream from the slip stream.

The rate of tritium production in the high temperature zone of the blanket is fixed at about 500 g/day, which is equivalent to 9.59×10^{-4} moles/s as T_2O (atomic mass of T = 3.01697). The other two items above depend on the design of the slip-stream system for tritium removal, which is illustrated for a 1% slip-stream in Fig. 7-2, and which we will discuss below.

7.2.1.1 Tritium Oxidizer. To be able to use a molecular sieve to remove the tritium from the helium stream, all of the tritium needs to be in the form of T_2O. Even though most of the tritium is generated as T_2O from the $LiAlO_2$ breeder at steady state, still-significant amounts of T_2 and tritiated hydrocarbons are either also produced by $LiAlO_2$ or will form by reactions of the tritium with materials in the blanket environment. Therefore, to convert all of the tritium-containing species to T_2O, we need to set up an oxidizer bed at the front end of the slip-stream train, which we assume to be set up as a 1% slip stream (see Fig. 7-2). Following conventional analytical chemistry practice, we use an oxidizer bed that consists of a reaction chamber containing a fibrous copper matri. where the surface of the copper fibers have been oxidized to cuprous oxide (Cu_2O). The bed operates at ∿1100 K, at which point the Cu_2O is continuously reduced by T_2 and tritiated hydrocarbons to produce copper metal and $T_2O(g)$. The following reactions illustrate the oxidation process for T_2 and CT_4:

$$T_2(g) + Cu_2O(s) \xrightarrow{1100\ K} T_2O(g) + 2\ Cu(s), \text{ and} \qquad (21)$$

$$CT_4(g) + 3\ Cu_2O(s) \xrightarrow{1100\ K} 2\ T_2O(g) + 6\ Cu(s) + CO(g)\ . \qquad (22)$$

Thus, Cu_2O is used both to provide a surface for the catalytic oxidation of T_2 and tritiated hydrocarbons and to provide just the right amount of oxygen required for the oxidation process without contaminating the helium stream with oxygen. The decomposition pressure of O_2 above Cu_2O is actually calculated to be 2.3×10^{-6} atm, which corresponds to 46 molar ppb in the 50-atm pressure helium coolant. The oxidizer bed is regenerated by periodically removing it from the helium stream and exposing it to a limited amount of oxygen in a carrier gas at 1100 K to reoxidize the surface of the copper to Cu_2O, taking care not to carry the oxidation too far because formation of the higher oxide CuO would release much larger quantities of O_2 into the helium stream than Cu_2O.

Because helium coming from the blanket enters the slip-stream at 1273 K, a regenerative heat exchanger needs to be placed upstream of the oxidizer bed to drop the helium temperature at the entrance of the oxidizer bed to 1100 K. The recovered heat is used to provide part of the energy for reheating the processed helium before it is returned to the blanket.

7.2.1.2 Molecular Sieve Bed. After the tritium has been converted to $T_2O(g)$ in the oxidizer bed, the slip-stream is cooled from 1100 to 333 K by again using a regenerative heat exchanger that preheats the processed helium stream that is subsequently returned to the blanket. The slip-stream then passes through a molecular sieve bed at 333 K (see Fig. 7-2).

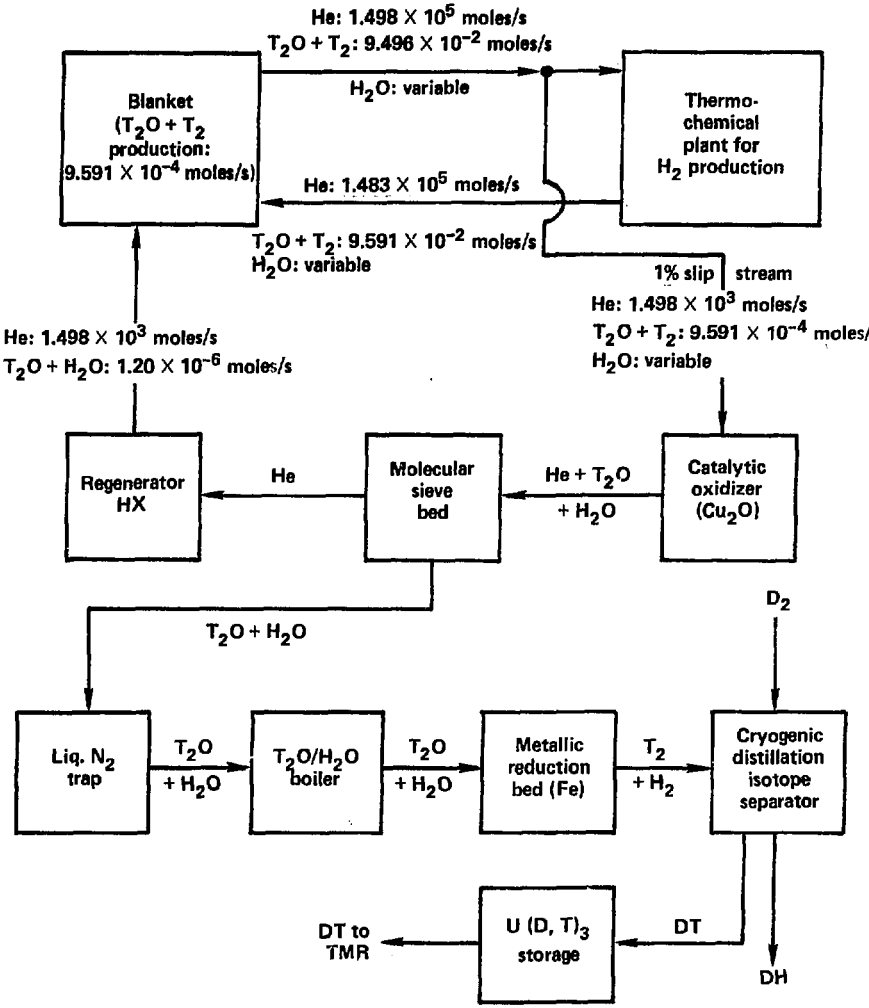

Fig. 7-2. Scheme for processing and storing the tritium after it is absorbed on the molecular sieve bed.

For the molecular sieve bed, we use a Linde 5A molecular sieve with a bulk density of 0.752 g/cm^3 (see Ref. 21). The bed is run batch-style with 10 process units on line in a parallel arrangement while 10 process units are in a regeneration mode. The process is run on a 24-hour cycle for regeneration of the beds.

We are now in a position to develop a conceptual design for a molecular sieve bed and to calculate the concentrations of tritium in the helium entering and leaving the molecular sieve bed.

The important design criteria that we have selected for a molecular sieve bed are as follows: We assume that the sieve is regenerated by baking it out under vacuum at 600 K to a final equilibrium partial pressure of 1 x 10^{-5} atm of T_2O. From the Linde data, the residual water content of the sieve under these conditions is 0.05 lb H_2O/100 lb of sieve (or in our case, the equivalent amount of T_2O). After bakeout, the sieve is cooled to an operating temperature of 333 K and the T_2O equilibrium pressure above the sieve drops to 4 x 10^{-8} atm, which then represents the residual partial pressure of T_2O in the helium stream exiting the molecular sieve bed.

In using the sieve in the adsorption mode at 333 K, the T_2O capacity of the sieve will be determined by the partial pressure of water vapor in the helium slip stream (i.e., by the sum of the T_2O, HTO, and H_2O partial pressures). Under steady-state conditions, that is, after protiated water has been depleted from the blanket system, we can assume that the T_2O partial pressure is fixed by the production rate of tritium in the blanket, and that the amount of protiated species becomes negligible. Thus, we calculate that the partial pressure of T_2O in the helium stream entering the molecular sieve bed at steady state is

$$P_{T_2O} = \frac{9.59 \times 10^{-4} \text{ moles/s } T_2O}{1.4982 \times 10^{3} \text{ moles/s He}} \times 50 \text{ atm He} = 3.20 \times 10^{-5} \text{ atm } T_2O \quad . \quad (23)$$

From the Linde data, the sieve capacity at 333 K and 3.20 x 10^{-5} atm H_2O pressure is 4.35 lb H_2O/100 lb of sieve. Subtracting out the initial water loading on the sieve after regeneration (see above), we obtain a capacity of 4.35 - 0.05 = 4.30 lb H_2O/100 lb of sieve, which translates to 2.39 moles T_2O/kg of sieve by substituting T_2O for H_2O on a molar basis.

To size the sieve beds, we note that 500 g/day of tritium production is equivalent to 82.86 moles T_2O/day, which for a 24-hour regeneration cycle and the sieve capacity given above, requires a minimum of 82.86/2.39 = 34.7 kg of sieve. We take twice this amount, or 69.4 kg, as a conservative estimate of the amount of sieve required to give a breakthrough time[22] of 24 hours (breakthrough time is the time at which the partial pressure of water in the exit stream from the bed begins to exceed the background pressure of water set by the sieve regeneration process). Using a bulk density of 0.752 g/cm^3 for the sieve, we calculate a volume of 69.4 x 10^3g /0.752 g-cm^{-3} = 9.22 x 10^4 cm^3 of molecular sieve needed for recovery of the tritium. To allow enough bed capacity to take up the protiated water as well, especially during initial reactor startup, we further increase the sieve bed volume by a factor of 3, i.e., total sieve volume = 2.77 x 10^5 cm^3. Assuming a bed thickness of 20 cm, as based on current design guidelines,[22] we find that the total cross-

sectional area required for the 10 sieve beds in the train is 2.77 x 10^5 cm^3/20 cm = 1.38 x 10^4 cm^2, which corresponds to a diameter of 42 cm per bed.

Another guideline for current sieve bed designs[22] is that the apparent linear velocity of helium through the bed (apparent linear velocity is the calculated average velocity of flow in the bed, ignoring the volume of the molecular sieve) should be within the range of 50 to 100 cm/s. For the helium slip stream used here, the helium flow rate is 1.498 x 10^3 moles/s. From this and the total cross-sectional area of A = 1.38 x 10^4 cm^2 for 10 beds, we calculate the apparent helium linear velocity as

$$\frac{1}{A} \cdot \frac{V}{s} = \frac{1}{A} \cdot \frac{n}{s} \cdot \frac{RT}{P} = \frac{(1.498 \times 10^3)(82.06)(333)}{(1.38 \times 10^4)(50)} = 59 \text{ cm/s} \quad , \qquad (24)$$

which is well within the desired velocity range.

7.2.1.3 Tritium Processing and Storage. We have worked out a first-cut process scheme here (see Fig. 7-2) on how to process and store the tritium after it has been adsorbed on the molecular sieve bed. As with the molecular sieve bed, we assume that 10 parallel process trains are carried through all of the process units to avoid large tritium inventories in any one unit.

The T_2O (and H_2O) is driven off the molecular sieve during the regeneration step by baking out the bed under vacuum and trapping out the T_2O on a high-surface-area liquid nitrogen trap. After collecting all the T_2O, the trap is warmed up and the tritium is transferred as liquid T_2O to a boiler where it is boiled at a controlled rate to produce T_2O gas at somewhat below atmospheric pressure. The T_2O gas is then sent through a powdered iron reduction bed at 950 K, where 72% of the T_2O is converted to T_2 for each pass through the bed. The T_2O gas remaining in the product is condensed to liquid T_2O near the ice point temperature and returned to the boiler for recycle, while the T_2 product is sent on to a cryogenic distillation column for isotopic separation of tritium and protium. A large excess of D_2 is also added to the cryogenic distillation unit to scavenge out the protium and produce DT and DH as the main products plus some T_2.[23] Isotopically impure D_2 is recycled back into the cryogenic distillation unit. The DT and T_2 products from the isotopic separator plus sufficient D_2 to give the proper D/T ratio are reacted with U powder at 523 K and stored as solid $U(D,T)_3$ until ready for use as fuel for the TMR.[24] The DT is released as needed by heating $U(D,T)_3$ to 630 K or higher.[24] The DH product from the separator is reacted with metallic Ti at >573 K to produce a solid solution of hydrogen in α-Ti, and is stored in this form as a stable, low-level radioactive waste because of its tritium content.

This first cut process scheme is not necessarily the best way in which to process the tritium product. It does however present some advantages in terms of simple equipment, processing speed, relatively low inventories of tritium in the process units, and low volumes of safe chemical forms for disposal of tritium-contaminated byproducts. We will give some additional details on the process scheme to clarify these advantages.

We believe that use of a vacuum instead of a carrier gas to recover T_2O from the molecular sieve gives a more rapid and more complete recovery of tritium from the sieve. The T_2O boiler allows us to conveniently control the

flow of T_2O gas through the metallic reduction bed. The use of a metal reducing agent, such as iron, allows us to reduce the tritium inventory in the process unit for T_2O reduction, because tritium is maintained in a gaseous form instead of a liquid form. Also, the equipment is quite simple and highly reliable as compared, for example, with an electrolyzer. The chemical reaction that takes place is

$$0.94\ Fe(s) + T_2O(g) \rightarrow Fe_{0.94}O(s) + T_2(g), \qquad (25)$$

which is known to be kinetically rapid at 950 K.[25] This approach further contrasts with an electrolyzer approach in that the tritium undergoes rapid isotopic exchange with the aqueous electrolytes and plastic components used in an electrolyzer, leading to a considerable buildup of tritium in the electrolyzer equipment (hundreds of grams) and radiation damage in the plastic components. However, it is possible that future electrolyzer cell designs that are specifically aimed toward use with tritium can be developed to bypass these problems (e.g., high-temperature steam electrolyzers that use solid state ceramic electrolytes). Other chemical reducing agents, such as carbon or zinc, could also be used to reduce T_2O, but iron is currently advantageous in that its chemical reducing behavior for steam is fairly well known, and also because the iron oxide product can be readily regenerated into iron powder.

Reduction of $Fe_{0.94}O$ to regenerate Fe is carried out rapidly at 1000 K using CO as the reducing agent, i.e.,

$$Fe_{0.94}O(s) + CO(g) \rightarrow 0.94\ Fe(s) + CO_2(g). \qquad (26)$$

The CO_2 produced in this reaction is disposed of by reacting it at 900 K with CaO to produce ~400 kg/year of a $CaCO_3$ (synthetic limestone) product which is sufficiently inert in the environment so that it can be stored as a low level tritium-contaminated radioactive waste. As mentioned above, DH that is contaminated with tritium is stored as a safe low level waste in the form of hydrogen dissolved in α-Ti.

Cryogenic distillation is currently accepted as the best method for separating hydrogen isotopes and gives very clean separations.[26]

Tritium storage in the form of $U(D,T)_3$ is convenient because $U(D,T)_3$ has a high capacity for storing tritium, and the hydriding rate of uranium metal powder is rapid at the relatively low temperature of 523 K. Tritium is released rapidly from $U(D,T)_3$ by heating the hydride to temperatures of 630 K or higher, depending on the desired pressure (e.g., p_{DT} ranges from 130 Torr at 630 K to 760 Torr at 710 K). When DT is released from $U(D,T)_3$ uranium metal is left behind as a finely divided powder that can be rapidly rehydrided for subsequent tritium storage.

7.2.2 Tritium Inventory in the Blanket High Temperature Zone

In summarizing the tritium inventories in this and the following sections, we will assume that a steady-state condition has been attained in which the initial protium present in the blanket has been swept out (see Sec. 7.1.2) and tritium solubilities have reached saturation levels in the blanket materials. We will also assume that the tritium content of the helium

flow stream is 6.40×10^{-7} moles for the sum of T_2O plus T_2 for each mole of helium [see Eq. (23)]. About 90% of the tritium is assumed to be in the form of T_2O and 10% as T_2 for a total tritium species pressure of 3.20×10^{-5} atm. On a partial pressure basis, the T_2O pressure is 2.88×10^{-5} atm and the T_2 pressure is 3.20×10^{-6} atm.

The types and amounts of materials present in the high temperatue zone of the MARS/synfuel blanket design have been described in the MARS interim report,[27] and the design is illustrated in Figs. 7-3 and 7-4. Based on this design, we obtain the amounts of materials summarized in Table 7-1. Although the material for the helium piping and for the shroud (basket) and support panels in the high temperature zone (see Table 7-1) was specified as SiC in the interim report, we are using the more general term ceramic materials in Table 7-1, with α-SiC or $MgAl_2O_4$ as alternative materials for these components. As we will see shortly, the use of SiC at temperatures as low as 800 to 1000 K leads to an unacceptably high inventory of tritium, thus necessitating the use of some other ceramic in its place. At temperatures above 1000 K, α-SiC becomes acceptable but β-SiC still has unacceptably high inventories of tritium. $MgAl_2O_4$ is our tentative choice for the unspecified ceramic components at the present time, although it may not be the optimum material.

In addition to the amounts of materials in the high temperature zone, we need to know the temperature distribution in the materials to properly assess tritium solubilities. We have derived the temperature profiles for the helium flow stream and for the surface of the SiC fuel balls based on data given in Ref. 27 (see Fig. 7-5). The data for 1.0-, 1.9-, and 2.4-cm-radius SiC balls were interpolated to obtain the value for the selected 1.5-cm radius. The data were then extrapolated to higher temperatures by adding a constant 103 K to the helium and SiC temperatures to bring them up to the values selected for this year's design. The center point temperatures for the SiC balls were also calculated to see if they were significantly different from the surface temperatures (see Fig. 7-5) because tritium solubility in SiC is a sensitive function of temperature. Except for the first 10 to 15 cm near the nose (helium distributive piping region), the difference in temperature was found to be small.

For temperature distributions in the rest of the high temperature zone, we assumed the helium inlet and distributive piping to be at 850 K and the exit piping 1273 K with ~ 3 m^3 of net pipe material volume in each of these two regions. The ceramic shroud (basket) was taken to have the same temperature distribution as the helium flowing next to it. Similarly, the ceramic support panels were assumed to conform to the temperature of the adjacent helium. The $LiAlO_2$ fuel was assumed to have the same temperature as the SiC balls. The Fiberfrax was at 800 to 1300 K, the $MgAl_2O_4$ standoffs at $\sim$1000 K, and the HT-9 pressure shell at $\sim$773 K.

The calculated tritium inventories in the high temperature zone are summarized in Table 7-2. The calculations were made as follows.

7.2.2.1 Tritium Inventory in the Helium. The moles of helium in the blanket at any given time, assuming an average helium temperature of 1100 K, are given by $n_{He} = PV/RT = (50)(444 \times 10^6)/(82.06)(1100) = 2.46 \times 10^5$ moles. The combined partial pressures of T_2O plus T_2 are 3.20×10^{-5} atm, which gives a

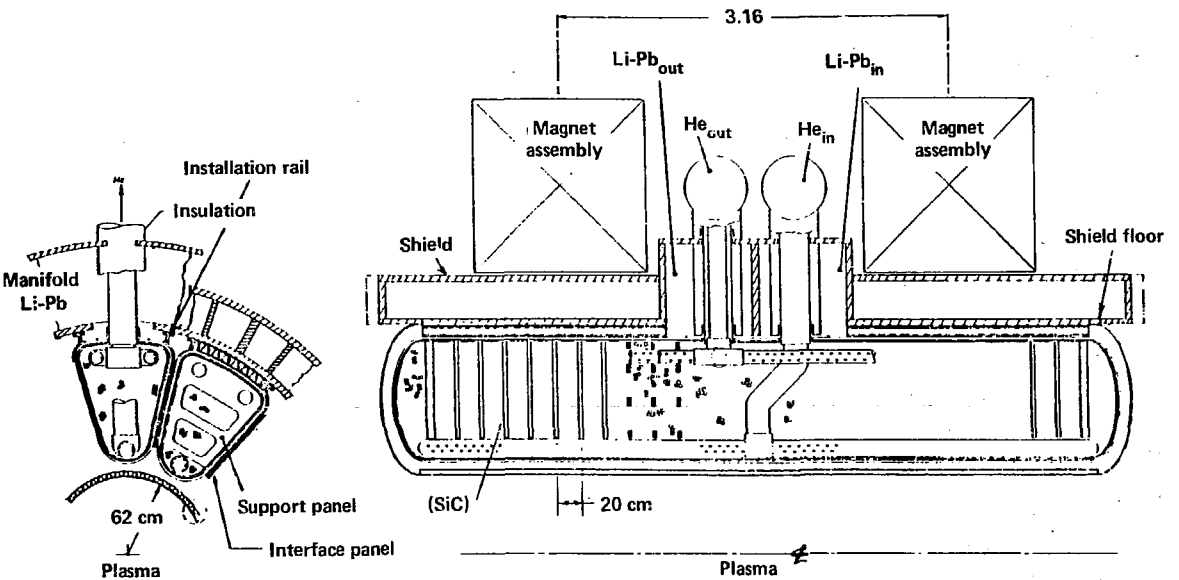

Fig. 7-3. High-temperature blanket design.

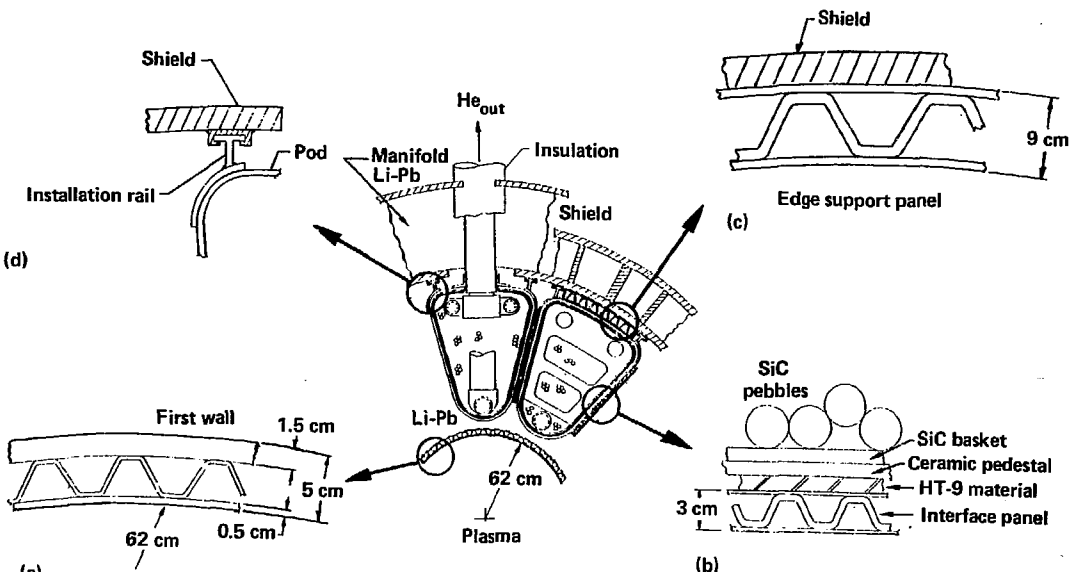

Fig. 7-4. Blanket first wall and interface structure.

Table 7-1. Summary of materials and their corresponding volumes that make up the high temperature zone of the 288 pods in the MARS/synfuel blanket.

Blanket material	Gross material volume, (m^3)	Volume of open porosity, (m^3)	Net material volume, (m^3)
Helium coolant	-	-	444[b]
Ceramic piping[b]	8	2	6
Ceramic shroud (basket)[b]	54	11	43
Ceramic support panels[b]	67	13	54
α-SiC fuel balls	487	89	398
$LiAlO_2$ fuel	10	0	10
Fiberfrax insulation	55	50	5
Standoff insulators, $MgAl_2O_4$	1	0	1
HT-9 pressure shell	67	0	67
Total blanket volume			1028

[a]The volume of helium within the main flow stream of the blanket at any time is 279 m^3, which, when combined with a volume of 165 m^3 of stagnant helium within the pores of the blanket materials (see column 3 above), gives a total volume of 444 m^3 of helium within the blanket.

[b]From a structural standpoint, either α-SiC or $MgAl_2O_4$ can be used for these ceramic components. $MgAl_2O_4$ is the preferred material from the standpoint of maintaining a low tritium inventory.

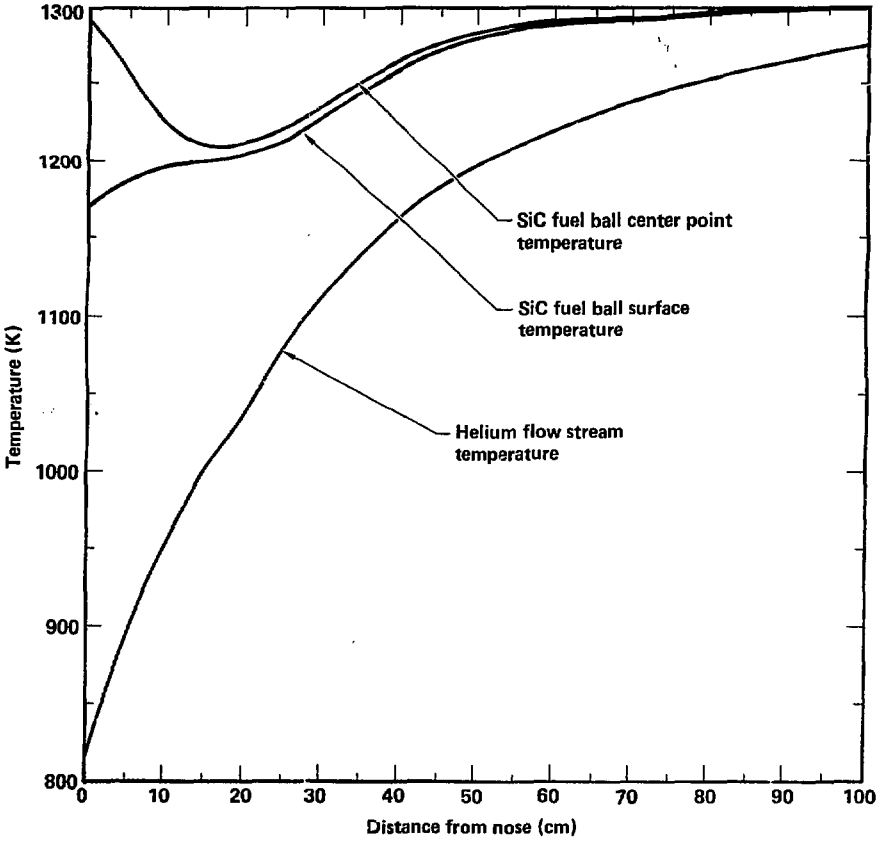

Fig. 7-5. Temperature profiles for the helium flow stream and for the surface of SiC fuel balls based on data from Ref. 27.

Table 7-2. Summary of tritium inventories in the high temperature zone. For purposes of comparison, tritium inventories are given for both α-SiC and $MgAl_2O_4$ as alternate materials for the ceramic structure and piping in the blanket. Although data have not been included for using β-SiC in place of α-SiC, the tritium inventories are expected to be about five times higher, i.e., about 844 kg when using β-SiC as compared with 169 kg for α-SiC.

Blanket material	Tritium inventory (g)	
	α-SiC ceramic	$MgAl_2O_4$ ceramic
Helium coolant	1	1
Ceramic piping	17,745	41
Ceramic shroud (basket)	142,948[a]	247
Ceramic support panels	6,19	464
α-SiC fuel balls	1,475	1,400
$LiAlO_2$ fuel	74	74
Fiberfrax insulation	15	15
Standoff insulators, $MgAl_2O_4$	6	6
HT-9 pressure shell	10	10
Total T inventory	168,893[a]	2,258

[a]The tritium inventory cannot exceed the total amount of tritium produced in the high temperature zone of the blanket in one year, which, assuming 73% operational availability, is (500)(0.73)(365) = 133,225 g of tritium. Therefore, the inventory limit here cannot exceed 133,225 g/year.

molar ratio of $3.20 \times 10^{-5}/50 = 6.40 \times 10^{-7}$ for the sum of T_2O plus T_2 compared to helium. Multiplying this ratio times the moles of helium gives $(6.40 \times 10^{-7})(2.46 \times 10^{5}) = 0.157$ moles of T_2O plus T_2, which is equivalent to $(0.157)(3.01697 \times 2) = 0.95$ g of tritium in the helium.

7.2.2.2 Tritium Inventory in the Ceramic Piping. For 3 m^3 of the inlet and distributive helium piping for α-SiC as the material at 850 K, we find from Eq. (16) that $C_T = (5.00 \times 10^{-11})(3.20 \times 10^{-5})^{1/2} \exp(19{,}260/850) = 1.960 \times 10^{-3}$ g-atoms T/cm^3, which is equivalent to 17,736 g of T for 3 m^3. Similarly, for 3 m^3 of helium recovery and outlet piping of α-SiC at 1270 K, we obtain a tritium solubility of 9 g, which gives a total tritium solubility of 17,736 + 9 = 17,745 g in the α-SiC piping.

Using $MgAl_2O_4$ in place of α-SiC for the piping and assuming identical volumes and temperatures, we find from Eq. (18) a solubility of 11 g of tritium for the inlet and distributive piping, and 30 g of tritium in the recovery and outlet piping for a total solubility of 41 g of tritium in the $MgAl_2O_4$ piping.

7.2.2.3 Tritium Inventory in the Ceramic Shroud (Basket). Assuming that the ceramic shroud (basket) has the same temperature distribution as the helium flow stream, and using Eq. (16) to do a stepwise integration, we find that tritium solubility for an α-SiC shroud (basket) is 142,948 g. Of this, 136,800 g of tritium are dissolved at temperatures below 900 K, and 142,724 g are dissolved at temperatures below 1000 K. This suggests a lower temperature limit of ∿1000 K for use of α-SiC in blanket structures to prevent excessively high tritium inventories. Actually, the inventory of 142,948 g of tritium exceeds the total amount of tritium produced in the high temperature zone in one year of blanket operation, which based on a 73% plant availability, is $(500)(0.73)(365) = 133{,}225$ g of tritium. Hence, the total tritium inventory in the high temperature zone is limited to a maximum of 133,225 g/year.

Using $MgAl_2O_4$ in place of α-SiC for the shroud (basket) and using identical volumes and temperatures gives 247 g of dissolved tritium in $MgAl_2O_4$ based on Eq. (18).

7.2.2.4 Tritium Inventory in the Ceramic Support Panels. Using α-SiC to make the support panels for the shroud (blanket) and assuming that the temperature of the support panels follows the helium temperature profile, we follow the same procedures described above and find a tritium solubility of 6619 g. When $MgAl_2O_4$ is used in place of α-SiC for the support panels, tritium solubility is calculated to be 46 g.

7.2.2.5 Tritium Inventory in the SiC Fuels Balls. Using a T_2O plus T_2 pressure of 3.20×10^{-5} atm with Eq. (16) and the surface temperatures in Fig. 7-5 as the α-SiC fuel ball temperatures and applying a stepwise integration, we obtain a tritium inventory of 1506 g for the α-SiC fuel balls. This value should be an upper limit. If, instead, we use the center-point temperatures for the fuel balls, the inventory becomes 1366 g of tritium, which should be a lower limit. Actually, the assumption of 3.20×10^{-5} atm for the pressure of T_2O plus T_2 somewhat underestimates the tritium species pressures in the pores of the SiC where tritium is being generated. Hence, the above limits of tritium solubility should be raised somewhat. Therefore,

1475 g of tritium is our best estimate of the inventory of tritium in the α-SiC fuel balls. This value does not include the tritium dissolved in the $LiAlO_2$ fuel.

7.2.2.6 Tritium Inventory in the $LiAlO_2$ Fuel. Assuming a T_2O partial pressure of 2.88×10^{-5} atm, an $LiAlO_2$ fuel temperature of 1265 K, and and $LiAlO_2$ density of 2.55 g/cm^3, we use the solubility constant estimated in Sec. 7.1.4.4 to calculate a solubility of 74 g tritium in the $LiAlO_2$.

7.2.2.7 Tritium Inventory in the Fiberfrax Insulation. Using a density of 3.156 g/cm^3 and a net material volume of 5 m^3 for the 3 Al_2O_3· 2 SiO_2 glass (Fiberfrax) in the blanket, we calculate that 74,075 moles of SiO_2 are present in the Fiberfrax. Taking the T_2O partial pressure to be 2.88×10^{-5} atm and the solubility constant of 6.1×10^{-3} moles H_2O/mole SiO_2-atm$^{1/2}$ estimated in Sec. 7.1.4.3, we obtain an inventory of 15 g of tritium dissolved in the Fiberfrax insulation.

7.2.2.8 Tritium Inventory in the $MgAl_2O_4$ Standoff Insulators. Assuming an average temperature of 1000 K and using the solubility constant estimated for $T_2O(g)$ in $MgAl_2O_4$ [Eq. (18)], we calculate an inventory of 6 g of tritium in the $MgAl_2O_4$ standoff insulators.

7.2.2.9 Tritium Inventory in the HT-9 Pressure Shell. Assuming that the T_2O and T_2 in the helium generate an equivalent T_2 partial pressure of 3.20×10^{-5} atm in the HT-9, and using the solubility constant estimated in Sec. 7.1.4.5 for an HT-9 temperature of 773 K, we calculate a tritium inventory of 10 g for the HT-9 pressure shell.

7.2.3 Tritium Inventory in the Helium Transport Piping

To estimate the tritium inventory in the helium piping outside of the MARS/synfuel blanket, we have made some rough estimates of piping sizes and calculated the volume occupied by the helium and the pipe wall areas. These are summarized in Table 7-3. We used the following estimates as input: (1) the module ring manifolds are 690 cm in average ring diameter and 46 cm in pipe diameter with two pipes per module, 24 pipes each 30 cm in diameter and 100 cm long joining the ring modules to the pods, and 350 cm of 46-cm-diameter piping joining the ring modules to the helium supply and return manifolds; (2) the helium supply and return manifolds to the ring modules consist of 294 m of 2-m-diameter piping; (3) the piping to and from the process plant has 300 m of 3-m-diameter piping; (4) the heat exchanger has 33,000 heat exchanger tubes, each 2 cm in diameter and 10 m long; and (5) the helium ballast tank is a round-ended cylinder, 3 m in diameter and 50 m long.

We have selected HT-9 as the material for the helium piping between the blanket and the process plant, whereas Waspaloy is used for the piping in the heat exchanger that interfaces the helium loop with the process plant. The inside of the HT-9 piping is lined with ceramic insulation to both reduce heat loss from the helium and to lower the temperature of the pressure wall to ∿500 K, thus reducing the requirements that the materials must withstand. Assuming that the principal stress on the HT-9 wall is a hoop stress, and

Table 7-3. Summary of the helium volume and the pipe wall area in the piping outside of the MARS/synfuel blanket region.

	Helium volume in piping (m^3)	Piping wall area (m^2)
Module ring manifolds	190	2,170
Module supply and return	925	1,850
Piping to process plant	2,120	2,830
Heat exchanger piping	105	20,700
Helium ballast tank	350	480
Totals	3,690	28,030

taking a design strength of 25,000 psi for HT-9 gives us a wall thickness of 0.0294 R (where R = HT-9 wall radius). This further leads to a total material volume of 214 m^3 for the HT-9 piping in this region. For the Waspaloy wall material in the heat exchanger, assuming a 2.5-mm-thick wall for 20,700 m^2 of wall area gives us a volume of 5 m^3 of Waspaloy.

We considered two materials for the ceramic thermal insulator that lines the HT-9 wall, namely silica brick and Fiberfrax board. Fiberfrax has a much lower mass for a given insulating quality and therefore will dissolve much less tritium. For this reason we selected Fiberfrax.

Table 7-4 summarizes the tritium inventories retained by the various materials in the helium piping region. We used the following methods to obtain these inventories.

7.2.3.1 Helium. To calculate the moles of helium in the piping at any given time, we assume that half of the ~3690 m^3 of helium (see Table 7-3) is at 823 K and half is at 1273 K. Then, $n_{He} = \Sigma\, PV/RT = (50)(1845 \times 10^6)/(82.06)(823) + (50)(1845 \times 10^6)/82.06)(1273) = 2.25 \times 10^6$ moles of helium. Using the ratio of 6.40×10^{-7} for the sum of T_2O plus T_2 compared with helium, as derived in Sec. 7.2.2, we find that the helium contains $2.25 \times 10^6 \times 6.40 \times 10^{-7} = 1.44$ moles of T_2O plus T_2 in the helium, which is equivalent to 9 g of tritium.

7.2.3.2 HT-9. Galaktionowa[20] shows that H_2 solubility in Fe drops by about a factor of 8 as the temperature is reduced from 773 to 500 K. Therefore, by reducing the solubility constant that we derived in Sec. 7.1.4.5 for T_2 in HT-9 by a factor of 8, we obtain 3.1×10^{-9} moles T_2/cm^3 of HT-9 at 500 K. For

Table 7-4. Summary of tritium inventories in the helium transport piping region.

	Tritium inventory (g)
Helium coolant	9
HT-9 pipe material	4
Waspaloy heat exchanger	6
Fiberfrax insulator[a]	128
Total	147

[a]If silica brick with approximately the same insulating characteristics is substituted for Fiberfrax, the tritium inventory becomes 4,385 g.

214 m^3 of HT-9 at an equivalent T_2 pressure of 3.20×10^{-5} atm, this gives us a tritium inventory of 4 g.

7.2.3.3 Waspaloy. Waspaloy is a nickel-based alloy with a nominal wt% composition of 58.2 Ni, 19.5 Cr, 13.5 Co, 4.3 Mo, 3.0 Ti, 1.3 Al, 0.08 C, 0.06 Zr and 0.006 B. Based on Galaktionowa's[20] data for H_2 solubility in nickel, we conclude that T_2 solubility is about eight times higher in Waspaloy at temperatures from 950 to 1250 K than the T_2 solubility we derived for HT-9 at 773 K (see Sec. 7.1.4.5). We therefore take the solubility constant for T_2 in Waspaloy from 950 to 1250 K to be $\sim 2.0 \times 10^{-7}$ moles T_2/cm^3 of Waspaloy at an equivalent T_2 pressure of 3.20×10^{-5} atm. For 5 m^3 of Waspaloy, this gives a tritium inventory of 6 g.

7.2.3.4 Silica Brick and Fiberfrax Board. To determine the tritium inventory in the silica brick, we first calculate a gross volume for the brick by using a thickness of 11.4 cm, which, based on the area of HT-9 from Table 7-3, gives $0.114 \times 7330 = 836$ m^3. Using a density value of 1.68 g/cm^3 for commercial silica brick gives a total SiO_2 mass of 1.40×10^9 g, which is equivalent to 2.34×10^7 moles. From the solubility constant of 6.1×10^{-3} moles T_2O/mole SiO_2-$atm^{1/2}$, as given in Sec. 7.1.4.3, and taking the T_2O partial pressure to be 2.88×10^{-5} atm, we calculate a T_2O solubility of 766 moles, which is equivalent to a tritium inventory of 4,622 g.

For the case of Fiberfrax board, we find that the material density is 0.19 g/cm^3 (6% of theoretical density), which is considerably lower than the material density of for SiO_2. Moreover, Fiberfrax board at 1/10 the weight of silica brick provides equivalent thermal insulation under atmospheric conditions. Therefore, for calculational purposes, we take the amount of

Fiberfrax to be 1/10 the weight of the silica brick, or 1.40×10^8 g. This is equivalent to a liner thickness of 10 cm. It is also equivalent to 3.24×10^5 moles of $3\ Al_2O_3 \cdot 2\ SiO_2$, or 6.48×10^5 moles of SiO_2. From the solubility constant given in Sec. 7.1.4.3 and again taking the T_2O partial pressure as 2.88×10^{-5} atm, we obtain a tritium inventory of 128 g.

7.2.4 Tritium Inventory in the Slip-Stream Processor

The main flow of the 1% slip stream in the tritium recovery processor is the flow of the helium stream through the catalytic oxidizer, the molecular sieve bed, and the regenerative heat exchanger (see Fig. 7-2). The largest part of the equipment in the tritium recovery unit is contained within this helium flow loop. Even so, the amount of metal directly exposed to the tritium is relatively small. We estimate the piping for the helium flowstream to be 0.5 m in diameter and 20 m long, and for the T_2O stream, 0.02 m in diameter and 20 m long. After estimating vessel and heat exchanger sizes, we obtain a total gas volume of 18 m^3, a wall area of 250 m^2, and a metal volume for the wall of 18 m^3.

Assuming that the piping and vessel material is 316 stainless steel and that the heat exchanger is Incoloy-800H, we estimate that the tritium solubility in the wall material of the helium flow processor is less than 0.2 g. The amount of tritium inventory in the helium slip-stream is negligible compared with that in the metal. The size of the equipment used to process the T_2O recovered from the molecular sieve is less by about a factor of 30 compared to the size of the equipment in the main slip-stream flow. In addition, the temperatures involved are much lower. Therefore, in this part of the process equipment we estimate the amount of tritium dissolved in the wall material to be less than 0.005 g. In addition to dissolved tritium, there will be some surface-adsorbed tritium, mainly in the form of T_2O, on the metal surfaces. We estimate this surface-adsorbed tritium to have an inventory of $\sim$0.5 g. The total inventory of tritium dissolved or adsorbed in the helium stream and the metal parts of the T_2O stream processor will therefore be about 0.7 g. We expect that the amount of tritium holdup in the catalytic oxidizer and in the metallic reduction bed will be very low because these are gas-phase processors and the bed sizes are small.

The main tritium inventories in the slip-stream processor will be in the molecular sieve bed, the liquid nitrogen trap, the T_2O boiler, the cryogenic distillation unit, and in the $U(D,T)_3$ storage unit. We will discuss each of these in turn.

Taking the tritium production rate from the high temperature zone of the blanket as 500 g/day and from the low temperature zone as 40 g/day, we need to process some 540 g/day of tritium from the reactor blanket. The tritium is recovered directly as T_2 from the Li-Pb in the low temperature zone, but is sent to the cryogenic distillation unit to remove any trace protium and to convert it to DT. Therefore, the 500 g/day from the high temperature zone is the maximum amount of the daily tritium production that will be held up in the molecular sieve bed. After recovering the tritium from the bed, some 6 g of residual tritium will still remain on the molecular sieve. Hence, the total maximum tritium inventory in the molecular sieve bed is 512 g (500 g of daily production plus 6 g each on the bed in operation and on the bed being

regenerated), and the minimum inventory is about 90 g (assuming about 4 hours needed to regenerate a bed). The maximum inventory occurs just before regeneration of a fully loaded bed and the minimum inventory occurs about 3 hours after beginning a 4-hour regeneration cycle.

The maximum amount of tritium in the T_2O stream processor--in the liquid nitrogen trap, the T_2O boiler, and the cryogenic distillation unit--will consist of 500 g tritium transferred from the molecular sieve regenerator, plus the tritium holdup in the cryogenic distillation unit. The 40 g/day of tritium transferred from the low temperature zone would be processed continuously and not contribute significantly to the steady-state tritium inventory here. Based on the cryogenic distillation design of Bartlit et al.,[23] who found a tritium holdup of 100 for a tritium production rate of 1086 g/day (as DT plus T_2), we estimate a proportionate amount of 50 g of tritium holdup for our production rate of 540 g/day of tritium. For the combined molecular sieve bed-T_2 processor system, we obtain a maximum tritium inventory of 687 g (125 + 12 = 137 g in the molecular sieve bed and 500 + 50 = 550 g in the T_2O processor) occurring about 6 hours after regeneration of the molecular sieve bed, and a minimum tritium inventory of 562 g (0 + 12 + 500 + 50 = 562 g) occurring at the initiation of regeneration.

For the $U(D,T)_3$ tritium storage unit, we assume that we need a maximum storage capacity of 4000 g to compensate for lithium burnup near the end of fuel life, and the minimum tritium inventory would be for one day's operation, or 540 g of tritium.

Results of these tritium inventories in the slip-stream processor are summarized in Table 7-5.

Table 7-5. Summary of maximum and minimum tritium inventories in the helium slip-stream processor, including the input of tritium recovered from the Li-Pb coolant.

	Maximum inventory of T (g)	Minimum inventory of T (g)
Metal parts of helium processor	1	1
Molecular sieve bed and T_2O stream processor	687	562
$U(D,T)_3$ storage unit	4,000	540
Total tritium	4,688	1,103

7.2.5 Tritium Inventory in the Blanket Low Temperature Zone

To estimate tritium inventories we have made some rough estimates of the volume of Li-Pb coolant and HT-9 structure both in the low temperature zone of the blanket and in the equipment that handles Li-Pb outside the blanket (see the summary in Table 7-6).

Table 7-6. Summary of material volumes and tritium inventories in the blanket low temperature zone and in the Li-Pb handling system external to the blanket.

	Material volume (m^3)	Tritium inventory (g)
Li-Pb coolant in blanket	218	1.1
Li-Pb coolant outside of blanket	129	0.7
HT-9 structure in blanket	79	0.8
HT-9 structure outside blanket	47	0.5
Cyropumps	∿0	20.0[a]
Total tritium		23.1

[a]This value is based on the maximum inventory in the cryopumps. The minimum inventory would be 3.3 g in the cryopumps and 6.4 g in the total system (see text).

We first estimate the volume of the HT-9 structure within the low temperature zone. The includes the HT-9 in the first wall, the support structure between the pods, the support structure between the pods and the shield, and the hangers supporting the pods (see Fig. 7-4). We calculate a total volume of 79 m^3 for the HT-9 structure. We next calculate the total blanket volume within the pod structure as $\pi(182^2 - 62^2)(600)(24) = 1.325 \times 10^9$ cm^3 or 1325 m^3. Now, subtracting out the volume of the high temperature zone (see Table 7-1) gives 1325 - 1028 = 297 m^3 for the volume of the low temperature zone; further subtracting out the volume of the HT-9 structure gives 297 - 79 = 218 m^3 for the volume of Li-Pb in the low temperature zone.

To estimate the volumes of Li-Pb and HT-9 outside the blanket, we assume 400 m of 50-cm-diameter piping with a 5-mm-thick wall and a cylindrical ballast tank 2 m in diameter and 10 m long with a 5-mm-thick wall and with hemispherical ends on the tank. We take the heat exchanger to be 20% as large as the helium coolant heat exchanger (see Sec. 7.2.3) with 20% as much volume and surface area and a 3.8-mm-thick wall.

The tritium concentration in the Li-Pb is given as 5.1×10^{-4} wppm at a tritium partial pressure of 1.32×10^{-7} atm.[27] Assuming a Li-Pb density of 10 g/cm^3, we calculate a weight of 2,180 Mg of of Li-Pb in the blanket, or $(2,180)(5.1 \times 10^{-4}) = 1.1$ g of tritium. Similarly, the tritium content of the Li-Pb outside of the blanket is estimated to be 0.7 g.

The solubility constant for tritium in HT-9 was given in Sec. 7.1 4 as 2.5×10^{-8} moles T_2/cm^3 of HT-9 for a T_2 overpressure of 3.20×10^{-5} atm at 773 K. Correcting the solubility constant to a tritium overpressure of 1.32×10^{-7} atm at 773 K (using the 0.5 power law for making the T_2 pressure correction) gives $2.5 \times 10^{-8}(1.32 \times 10^{-7}/3.20 \times 10^{-5})^{1/2} = 1.61 \times 10^{-9}$ moles T_2/cm^3 of HT-9. Using the HT-9 volumes listed in Table 7-6, we obtain $(1.61 \times 10^{-9})(79 \times 10^6) = 0.127$ moles of T_2, which is equivalent to 0.8 g of tritium in the HT-9 structure within the blanket region. Similarly, the tritium content of the HT-9 outside the blanket is calculated to be 0.5 g.

A vacuum system is required to pump the tritium out of the Li-Pb. We believe that cryopumping backed by diaphragm pumps is the best method of avoiding tritium contamination of oils used in conventional pumps. Two different cryopumping temperature regimes would be needed. One cryopump would trap the residual gaseous Li and Pb and any other condensible gases present as impurities. A liquid nitrogen cryopump could easily perform this function. A lower temperature cryopump operating with liquid helium would remove the tritium. These two pumping systems would be used with a switchover every 12 hours to recover the material held up on the cryopumps inbetween pumping modes. Hence, the maximum inventory of tritium expected in the cryopumps, assuming a maximum tritium production rate of 40 g/day, is $(1/2)(40) = 20$ g; and the minimum inventory, assuming 2 hours to recover tritium from the cryopumps, is $(2/12)(20) = 3.3$ g.

The various tritium inventories in the low temperature zone of the blanket and for the Li-Pb handling system outside the blanket are summarized in Table 7-6. We see that except for the cryopumping region, the tritium inventories in this part of the reactor system are quite low.

7.2.6 Tritium Inventory in the Shield Region

The shield is a 40-cm-thick composite wall that forms a cylindrical shell surrounding the pod structure. The inner side of the shield wall is separated from the pod by a corrugated structure (see Fig. 7-4). The shield wall structure is as follows. Going radially outward from the inner wall, the following layers of material are: 5 cm of steel (HT-9) for the inner wall, a 5-cm-wide passage for high-pressure water coolant, 2 cm of steel (HT-9), 15 cm of lead, 5.5 cm of polyethylene, 2.5 cm of 2% borated polyethylene, and finally 5 cm of steel (HT-9) for the outer wall.

Materials in the shield region have been selected to produce essentially negligible amounts of tritium by neutron reactions. However, this is an area that needs to be looked at more carefully, especially in regard to nuclear reactions involving trace elements and minor alloy constituents.

We assume that tritium enters the shield region only through the Li-Pb that is in contact with the shield inner wall, and that it saturates the full 5 cm of the inner wall based on an average wall temperature of ~600 K.[27] The wall temperature actually drops from 773 K when it is in contact with the Li-Pb to 438 K in contact with the water coolant. Calculating the amount of material in this inner wall, we obtain an HT-9 volume of $\pi(187^2 - 182^2)(151.6 \times 10^2) = 8.79 \times 10^7$ cm^3 or 88 m^3. From Galaktionowa[20] we find that tritium solubility at 600 K is 30% of the value that we had assumed for the Li-Pb region (see Sec. 7.2.5) because of the lower temperature here. The tritium solubility in the inner shield wall is thus $(0.3)(1.61 \times 10^{-9})(8.79 \times 10^7) = 0.042$ moles of T_2, or 0.3 g of tritium. We therefore take the total inventory of tritium in the shield region to be about 0.3 g.

7.2.7 Summary of Tritium Inventories

We are now in a position to give a summary of the tritium inventories that we have estimated for the various parts of the MARS/synfuel blanket system. We have obtained these tritium inventories assuming a steady state operation in which the initial protium in the system has been swept out, and the tritium has reached its saturation solubility in all the components of the system. Tritium inventories within the blanket and shield region of the central cell are summarized in Table 7-7; tritium inventories for the helium and Li-Pb coolant systems outside the blanket are summarized in Table 7-8. An overall tritium summary, including the $U(D,T)_3$ storage unit, is given in Table 7-9. Some 3 kg of tritium are present in the blanket and the associated coolant systems during reactor operation, and an additional 0.5 to 4 kg of tritium are stored as DT reactor fuel in the $U(D,T)_3$ storage unit.

To maintain the tritium inventories in the blanket at acceptable levels, we used $MgAl_2O_4$ to replace the SiC that had been chosen for the piping, shroud (basket), and support panels in the MARS interim high temperature blanket design.[27] This was necessary because we calculated an extremely high tritium inventory in SiC in these components under saturation conditions, i.e., $\sim$169 kg in α-SiC and 844 kg in β-SiC (assuming saturation can be reached). These high inventories occur mainly below $\sim$1100 K.

We selected $MgAl_2O_4$ because neutron irradiation damage studies have shown very few adverse effects on its physical properties.[16] However, fracturing of the $MgAl_2O_4$ resulting from thermal stresses may be a problem in the manufacture of the large parts required for the piping, shroud (basket) and support panels, or design changes may be necessary to overcome this problem. Other better choices may exist, but for now $MgAl_2O_4$ is our choice. We further anticipate that replacing SiC with $MgAl_2O_4$ will have a negligible effect on the original neutronic calculations for the MARS/high temperature blanket design.

Because permeation rates of tritium into α- and β-SiC are known to be slow, calculation of a high saturation inventory is not by itself a sufficient reason for rejecting these materials. We therefore estimate the amounts of tritium that permeate into α- and β-SiC in one year by using the following expression for the integrated permeation of tritium based on a semi-infinite media approximation:

$$M_t = 2\, C_o\, (Dt/\pi)^{1/2} \quad , \tag{27}$$

where M_t is the integrated permeation of T in g-atoms/cm^2 of surface area, C_{o_3} is the surface concentration (saturation solubility) of tritium in g-atoms/cm^3, D is the diffusivity of tritium in cm^2/s, and t is the time in seconds. By

Table 7-7. Summary of tritium inventories in the MARS/synfuel blanket under steady state operating conditions. We have selected $MgAl_2O_4$ as a ceramic structural material in place of SiC to minimize tritium inventories.

	Tritium inventory (g)	Tritium inventory (g)
Blanket high temperature zone		
Helium coolant	1	
$MgAl_2O_4$ piping	41	
$MgAl_2O_4$ shroud (basket)	247	
$MgAl_2O_4$ support panels	464	
α-SiC fuel balls	1,400	
$LiAlO_2$ fuel	74	
Fiberfrax insulation	15	
$MgAl_2O_4$ standoff insulators		
HT-9 pressure shell	10	
Subtotal	2,258	2,258
Blanket low temperature zone		
Li-Pb coolant	1	
HT-9 structure	1	
Subtotal	2	2
Magnet shielding/blanket region	~0	~0
Total		2,260

Table 7-8. Summary of tritium inventories in the helium and Li-Pb coolant handling systems. Fiberfrax board has been selected as the thermal insulator here for lining the inside walls of the helium piping to minimize the tritium inventory. If silica brick were used in place of Fiberfrax, the tritium inventory would increase by more than 4 kg.

	Tritium inventory (g)	Tritium inventory (g)
Helium coolant system		
Helium coolant	9	
HT-9 pipe material	4	
Waspaloy heat exchanger	6	
Fiberfrax insulator	128	
Subtotal	147	147
Slip-stream tritium processor		
Piping and heat exchanger materials	1	
Molecular sieve bed and T_2O stream processor	687[a]	
Subtotal	688	688
Li-Pb coolant system		
Li-Pb coolant	1	
HT-9 piping and HX	1	
Cyropump system	20[b]	
Subtotal	22	22
Total		857

[a]The tritium inventory in the combined molecular sieve bed and T_2O stream processor will vary from a maximum of 687 g to a minimum of 562 g.

[b]The tritium inventory in the cryopumps will vary from a maximum of 20 g to a minimum of 3 g.

Table 7-9. Summary of maximum and minimum tritium inventories in the MARS/synfuel blanket, in the associated coolant handling systems, and in the $U(D,T)_3$ storage unit.

	Tritium inventory (g)	
	Maximum	Minimum
MARS/synfuel b anket	2,260	2,260
Coolant handling systems	857	715
$U(D,T)_3$ storage unit	4,000	540
Totals	7,117	3,515

extrapolating the C_o and D data of Causey et al.[9] to lower temperatures, we obtain the values for tritium permeation in one year (shown in Table 7-10). These tritium permeation values depend on our assumptions on the porosity and grain sizes that make up the SiC structure. We have assumed a characteristic grain size of 10 μm with an open porosity of 20% and a pore surface area equivalent to that of 2-μm-diameter spherical pores. This gives a total open porosity surface area of about 3×10^{11} cm^2 for the low temperature portions (40 m^3 volume) of the ceramic piping, shroud (basket), and support panels.

The tritium inventories indicated in Table 7-10 for one year are still unacceptably high, although they are significantly lower than the saturation values given in Table 7-2.

We can expect to further reduce tritium inventories in SiC by decreasing the exposed surface area. This must be done with care, however, because commercially used sintering aids such as B and Al additives in SiC increase the hydrogen diffusion and permeation rates by several orders of magnitude.[9] The same problem occurs when SiC is densified using reaction bonding with a mixture of Si and C containing excess Si (as in KT-SiC).[11] Methods such as hot pressing--although it is expensive--and sintering of fine powders of α-SiC show promise for fabricating high density α-SiC, but these methods are currently limited to relatively small sizes compared with the sizes needed for the piping, shrouds (baskets), and support panels. Vapor deposition methods for β-SiC are also limited to small sizes and layers up to 1 cm thick. We believe future developments for producing acceptable grades of SiC for use in fusion reactor blankets certainly cannot be ruled out because, based on current information, $MgAl_2O_4$ provides a more conservative alternative.

Table 7-10. Summary of the amount of tritium that permeates into α- and β-SiC after one year based on extrapolated data from Causey et al.[9] for diffusivities (D) of hydrogen into single-crystal α-SiC and powder α-SiC, and for single-crystal vapor-deposited β-SiC and saturation concentrations (C_o) of hydrogen in powder α-SiC and vapor-deposited β-SiC. The calculations are based on Eq. (27) for permeation into semi-infinite media using a total SiC surface area of 3×10^{11} cm^2. This area is split into three increments of 1×10^{11} cm^2 each, assumed to be at average temperatures of 900, 1000, and 1100 K, and representing the low temperature parts of the ceramic piping, shroud (basket), and support panels.

T(K)	D (cm^2/s)	C_o, g-atoms T per cm^3 SiC	M_t, g-atom T/cm^2 in 1 year	Total dissolved in 1 year (g)
α-SiC (single crystal data base)				
900	5.0×10^{-16}	5.3×10^{-4}	7.5×10^{-8}	7,500
1000	1.0×10^{-14}	6.2×10^{-5}	3.9×10^{-8}	3,900
1100	1.1×10^{-13}	1.1×10^{-5}	2.3×10^{-8}	2,300
			Total dissolved tritium	13,700
β-SiC (single crystal data base)[a]				
900	4.5×10^{-15}	3.4×10^{-3}	1.45×10^{-6}	145,000
1000	1.5×10^{-13}	4.0×10^{-4}	9.8×10^{-7}	98,000
1100	2.7×10^{-12}	6.9×10^{-5}	7.2×10^{-7}	72,000
			Total dissolved tritium	315,000[b]
Vapor-deposited β-SiC				
900	2.1×10^{-18}	3.4×10^{-3}	3.1×10^{-8}	3,100
1000	1.6×10^{-16}	4.0×10^{-4}	3.2×10^{-8}	3,200
1100	3.6×10^{-15}	6.9×10^{-5}	2.6×10^{-8}	2,600
			Total dissolved tritium	8,900

[a]Tritium solubility in single-crystal β-SiC has not been measured. We assume it to be the same as in vapor deposited β-SiC for the purposes of these calculations.

[b]This value of 315,000 g of tritium exceeds the total amount of tritium produced in the high temperature zone of the blanket in one year, which as discussed in Section 7.2.2.3 is limited to a maximum of 133,225 g. Hence, the tritium saturation conditions at the surface are not met.

Other changes from last year's high temperature blanket design are to replace the MgO standoff insulators with $MgAl_2O_4$ for better radiation damage resistance, and to use Fiberfrax board as the thermal insulation for lining the inside of the helium transport piping. The liner material was not specified in the interim MARS high temperature blanket design.[27] If silica brick were used in place of the Fiberfrax, it would increase the tritium inventory by more than 4 kg.

We have assumed that the tritium levels are at saturation in the Li-Pb region of the blanket system. This is only a good assumption if all of the Li-Pb in the blanket flows continuously (without stagnant pockets) and a high surface area of the Li-Pb is exposed (such as in a droplet spray stream) so that the tritium can be removed by vacuum pumping. Plute, et al.,[28] have addressed this problem calculationally, but experimental work is needed to ensure that the tritium can be fully recovered. Hence, we note that it is possible that a much larger inventory of tritium than we have estimated could accumulate in the Li-Pb region if proper flow and processing conditions are not met.

We have made very rough assessments of piping and equipment sizes and indicated the types of equipment designs that could be used in order to arrive at approximate numbers of tritium inventories. This is an area that deserves more detailed attention.

Finally, we also need to give more attention to the shielding region. The direct production of tritium should be considered in this region, especially tritium that is produced by the reactions of neutrons with trace elements or impurities in the shielding materials, and the level of tritium in the water coolant (although believed to be low) needs to be quantitatively established.

7.3 TRITIUM SAFETY AND CONTROL

7.3.1 Permeation Barriers

Permeation barriers are used as the primary means for containing tritium within the reactor blanket and the associated coolant handling system. As such these permeation barriers need to be well-designed and be highly reliable to maintain proper safety and control of tritium in the plant and surroundings. The design of these permeation barriers is complicated by the high temperatures and high pressures required for the coolants, by the large surface areas exposed by the piping and heat exchangers, and by the general scientific uncertainties in the reliability of permeation barriers. Because of the limited information in this area, we will describe here an approach for using permeation barriers without necessarily selecting the optimum materials or establishing their reliability. The best candidate materials that we know of for tritium permeation barriers are Al_2O_3 and SiC. We speculate that Cr_2O_3 is also a good tritium permeation barrier because of its similarity to Al_2O_3. Further scientific studies are clearly needed to better define this area.

The region of greatest concern for tritium containment is the region of the heat exchangers, especially for the helium-to-process heat exchanger, because this is where we encounter the most extreme conditions of full

temperature and pressure. At the same time, we have high surface areas with relatively thin walls, as required for efficient heat transfer, and we are at the interface with the chemical plant where we need to avoid tritium contamination. The second most important region is the transport piping region. Here, the pipe wall temperatures are considerably lower than in the helium-to-process heat exchanger, yet we still have a relatively large surface area of piping spread out over a large area of the plant. Another area of concern for tritium containment is within the blanket itself, where the primary containment boundary is a 5-cm-thick steel shell located between the blanket pod region and the magnet shields. Any tritium permeating through this steel shell will end up in the pressurized cooling water passing adjacent to it (see Sec. 7.2.6).

Tritium permeation barriers can be built using three approaches: (1) by allowing a metallic containment member (either bare or coated) to develop a surface oxide scale in-situ by reacting with water or oxygen or some other oxidant in its environment; (2) by intentionally preoxidizing a metal or a coating on its surface before putting it into use; and (3) by surrounding the member with a secondary containment shroud that has good permeation resistance.

We have used the first approach on the SO_3 decomposer side of the helium-to-process heat exchanger, where an aluminide coating is applied to the metal alloy surface and allowed to oxidize in situ to form an Al_2O_3 surface scale during use in the decomposer. We have used the second approach on the helium side of the helium-to-process heat exchanger, where an aluminide coating is applied and then preoxidized before it is used in the process. Either the first or second approach can provide a permeation barrier along the water coolant passage in the magnet shields. The third approach, which uses a shroud for a permeation barrier, appears best suited for the piping and its associated valves, circulating pumps, the slip-stream processor, and so on.

Several metals are known to develop natural oxide scales in moderately oxidizing environments, and these oxide scales reduce the permeation rate of hydrogen by orders of magnitude compared with metals having clean surfaces. Pure iron and ferritic alloys are a prime example of this behavior, where mild exposure to oxidizing conditions reduces the apparent hydrogen diffusion coefficient by about an order of magnitude at 700 K, and by about 3 to 4 orders of magnitude at room temperature.[20,29] Other metals, such as niobium, beryllium, and aluminum, also show a major reduction in hydrogen permeation rates resulting from surface oxide films. Aluminum is especially promising as a shroud material for piping when temperatures are not very high because aluminum with even a very thin natural oxide film gives us an extremely effective permeation barrier.[30]

When a surface oxide such as Al_2O_3 or Cr_2O_3 is used on a metallic alloy as a permeation barrier for tritium, the oxide either must remain dense and crack-free throughout its useful lifetime or, if it fractures or spalls off, the substrate must be able to rapidly regenerate a new scale in-situ to prevent a tritium leak. This type of self-healing process can only occur in an oxidizing environment in the case of surface oxide scales. The long-term stable behavior observed for aluminide coatings in SO_3/H_2O environments[31] suggests that such a self-healing process occurs in this instance. In developing coatings that are not self-healing, care must be taken to ensure that the coatings are thin, dense, and adhere tightly to the substrate metal.

There is a poor thermal expansion match between coating materials such as Al_2O_3, Cr_2O_3, and SiC with substrate alloys based on iron or nickel. Hence, we need to maintain relatively thin coatings (e.g., typically less than about 10 μm) to provide the coating material with enough flexibility coupled with strong adherence to avoid cracking.

7.3.2 Tritium in the Hydrogen Product

The two areas where tritium permeates into the hydrogen plant are: (1) at the helium-to-process heat exchanger, which supplies heat to the SO_3 decomposer, and (2) at the Li-Pb-to-process heat exchanger, which supplies heat that boils the sulfuric acid. Tritium permeation through the LI-Pb-to-process heat exchanger presents a relatively minor problem because of the low temperatures involved as compared with the heat exchanger for the SO_3 decomposer. A natural oxide barrier on the H_2SO_4 boiler side of the Li-Pb heat exchanger should suffice to prevent tritium permeation. We will therefore be concerned here primarily with the helium-to-process heat exchanger.

We assume, as we did in Sec. 7.2.3, that the helium-to-process heat exchanger has a wall area of 20,700 m^2 exposed to the helium stream. We also assume that the heat exchanger is broken down into three heat exchangers run in series with wall temperatures ranging from 950 to 1050 K, 1050 to 1150 K, and 1150 to 1250 K for each of the stages (see Table 7-11), and we take the average wall temperatures for calculational purposes to be 1000, 1100, and 1200 K in these three stages. Helium is on the tube side at 50 atm and SO_3/H_2O is on the shell side at 7 atm. The wall areas for each stage are 6,900 m^2. We assume that the walls are constructed of duplex tubing with a helium purge stream at 20 atm flowing through the gap region, which has an average gap width of 0.1 mm. The gap is actually 10 μm wide over most of the area, but wider channels are located periodically around the periphery of the gap to carry the main helium purge flow. We further assume that both the tube and shell sides are protected with an Al_2O_3 permeation barrier whose thickness varies from 5 μm at 1000 K to 15 μm at 1100 K and 30 μm at 1200 K. Finally, we assume that the permeation rates through the metal in the walls are sufficiently more rapid than the permeation rates through Al_2O_3, so that permeation through Al_2O_3 becomes the rate determining step.

7.3.2.1 Critical Review of T_2 Permeability into Al_2O_3. To calculate the permeation rates of tritium through the duplex tubing walls, we need data on the permeability of tritium through the Al_2O_3 barriers. Because both T_2 and T_2O are present in the helium stream, we need data on permeabilities of both of these gaseous species through the first Al_2O_3 barrier. In subsequently passing through the duplex tubing metal walls, the tritium is reduced to elemental tritium (migrating as T atoms) and recombines to form T_2 at the second Al_2O_3 barrier, which is the interface layer at the SO_3 decomposer. Hence, at the second Al_2O_3 barrier we need data on permeability of T_2 through Al_2O_3. Because of the limited amount of information on the required permeabilities, we will review the literature and do a critical assessment of the available information. We will assume for our purposes that the behavior of the isotopic forms of hydrogen are all equivalent.

Table 7-11. Tritium permeation rates shown from the main helium stream through the walls of the duplex-tube heat exchanger into the SO_3 decomposition unit in the chemical plant. The duplex-tube heat exchanger is split into three temperature zones. A helium purge stream at 20 atm pressure flows through a narrow gap between an inner and outer tube in the duplex-tubing. The main helium stream, at 50 atm, flows on the tube side, and the SO_3 decomposer, at 7 atm, flows on the shell side of the heat exchanger.

Heat exchanger stage/ wall area (m^2)	Average temperature (K)	Permeation rate into gap (moles/s)		Helium purge rate (moles/s)	Permeation rate into SO_3 decomposer (moles/s)	
		T_2	H_2		H_2	HT
1/6900	1000	2.09×10^{-7}	6.74×10^{-5}	1	2.62×10^{-11}	1.63×10^{-13}
2/6900	1100	4.13×10^{-7}	1.34×10^{-4}	2	1.27×10^{-9}	7.89×10^{-12}
3/6900	1200	9.13×10^{-7}	2.95×10^{-4}	5	3.79×10^{-8}	2.35×10^{-10}
	Totals	1.53×10^{-6}				2.43×10^{-10}

The only direct measurement of permeability is the work at North Carolina State University[10,11] on H_2 permeability through Al_2O_3 at temperatures of 1500 to 1700 K. However, a number of measurements have been made on the diffusivity of H_2 in Al_2O_3, and some data are also available on solubilities of H_2 and D_2 in Al_2O_3. The systems studied were not entirely free of H_2O, therefore, we will be able to use the data to also make some rough assessments of the diffusivity and solubility of water in Al_2O_3. Thus, using the data on diffusivities and solubilities of H_2 and H_2O in Al_2O_3, we will be able to calculate additional values of permeabilities through the relation $K = S \cdot D$.

The diffusivity data for hydrogen in Al_2O_3 are summarized in Fig. 7-6. The data at 1600 to 1800 K were obtained on sintered Al_2O_3 in conjunction with permeability measurements,[10,11] whereas the balance of the data is on a variety of forms of high purity Al_2O_3 and on Al_2O_3 doped with MgO. The data are obtained by using a technique in which tritium is injected into the specimens by recoil, and the time rate of release of tritium is measured during post-irradiation heating.[32] The tritium release results were found to be consistent with the classical solutions for the diffusion equations. Also, injection of 30 times smaller amounts of tritium into several of their specimens was found to give diffusivity results consistent with the higher tritium injection levels, thus indicating that radiation damage effects were not an important contributor to the diffusion process.

Tritium was recovered from the specimens during heating using a mixture of H_2 and He as the sweep gas. It was found that a large fraction of the tritium was recovered in the form of tritiated water. Some 70 to 95% of the tritium in the powdered Al_2O_3 specimens was recovered as tritiated water and the balance was recovered as tritiated hydrogen. In sintered and single-crystal Al_2O_3, the fraction of tritium in the form of water ranged from 0 to 25% with the balance being tritiated hydrogen. Using only helium for the sweep gas or annealing the specimens at high temperature before tritium injection had little effect on the percent of tritium recovered as water. However, passing the sweep gas through a liquid nitrogen cold trap (to remove traces of H_2O) before sweeping out the tritium, did reduce the observed tritium diffusivity values in the case of powdered Al_2O_3 specimens (see Fig. 7-6). This latter effect suggests to us that if we can estimate the water content of the untrapped sweep gas we can estimate the diffusivity dependence of tritium on water vapor pressure. Looking back to Sec. 7.1.3.4, we see that this effect of water on the diffusivity of tritium indicates that Eq. (9) (reaction of H_2O with Al_2O_3) is much more favorable than Eq. (8) (reaction of H_2 with Al_2O_3). From a bond energy standpoint, this is reasonable because Al-H bonds are much weaker than Al-O bonds, therefore, H_2O should interact more strongly with the Al_2O_3 lattice than does H_2, and in so doing should create a large number of defects that are conducive to OT^- transport.

On the basis of these arguments, in Fig. 7-6 we fit a straight line to what we believe are the driest conditions. This curve passes through the 1600 to 1800 K sintered Al_2O_3 data and the 900 to 1300 K single-crystal Al_2O_3 data, and envelops the lowest diffusivity values for tritium in sintered Al_2O_3 at 900 to 1200 K and in powdered Al_2O_3 at 500 to 900 K. The diffusivity of T_2 in Al_2O_3 under these dry conditions can be described by the relation

$$D = 43.9 \exp(-3.169 \times 10^4/T) \text{ cm}^2/\text{s}. \quad (28)$$

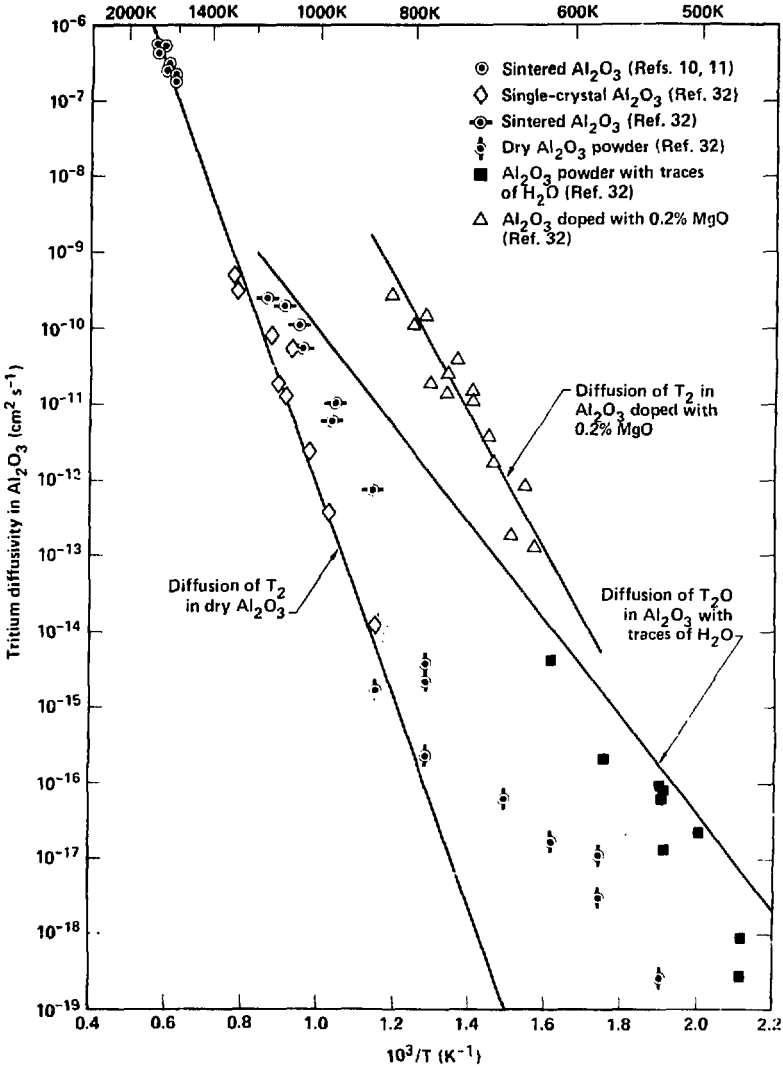

Fig. 7-6. Experimental diffusivities are summarized for hydrogen isocopes in Al_2O_3, and solid lines are used to indicate our selected values for diffusivities assumed to apply for the T_2 and T_2O species. Data are also shown for the enhanced T_2 diffusivity in Al_2O_3 that results when 0.2% MgO is added to Al_2O_3 as a dopant.

For diffusivity of T_2O in Al_2O_3, under conditions where traces of moisture are present, we draw a straight line that envelops the powdered Al_2O_3 data (70 to 95% of the tritium was recovered as HTO) and also appears above the sintered Al_2O_3 data (~20% of the tritium was recovered as HTO). The diffusivity of T_2O in Al_2O_3 under these conditions with trace amounts of water can be described very approximately by the relation

$$D = 2.36 \times 10^{-4} \exp(-1.479 \times 10^{4}/T) \text{ cm}^2/\text{s}. \quad (29)$$

The H_2O vapor pressure in the atmosphere surrounding the Al_2O_3 is believed to be roughly on the order of 10^{-5} atm.

As a further check on Eq. (29), we compare it with the approximate tritium diffusivity obtained by Alire et al.[30], which is 6×10^{-26} cm^2/s at 22°C for tritium diffusing into an Al_2O_3 surface oxide film on Al metal. Under these conditions, H_2O was known to be present as an adsorbed film on the surface of the Al_2O_3. Equation (20) gives a value of $4.0\ 10^{-26}$cm^2/s, which is in good agreement with Alire et al., considering the temperature extrapolation involved.

Before leaving the topic of T_2 diffusivity, note the importance of maintaining a low impurity level in the Al_2O_3 to attain the low T_2 diffusivities described above. This is best illustrated by the case where MgO added as a dopant at 0.2 wt% to Al_2O_3 enhances the diffusivity of T_2 by more than five orders of magnitude compared to that in high purity Al_2O_3 under dry conditions (see Fig. 7-6). Therefore, considerable care is needed when using Al_2O_3 coatings as tritium permeation barriers to ensure that the Al_2O_3 is either present in a highly pure form, or that any impurities present will not degrade the resistance of Al_2O_3 to tritium permeation.

The available solubility data on H_2 and D_2 in Al_2O_3 [10,11,33-35] are summarized in Fig. 7-7. Except for the lowest temperature set of data,[35] which is for the solubility of D_2 in Al_2O_3 powder at 1000 to 1200 K, the agreement is good. Therefore, with the exception of the 1000 to 1200 K data, we can express the solubility of T_2 in Al_2O_3 by the relation

$$S = 7.49 \exp(-2.312 \times 10^{4}/T) \text{ moles/cm}^3\text{-atm}^{1/2}, \quad (30)$$

where a 0.5 power dependence is assumed for the dependence of solubility on T_2 pressure.

We believe that the deviation of the 1000 to 1200 K data occurs because of moisture in the system. It is difficult to completely remove moisture from ceramic powders at these temperatures because of the high surface areas, porosities, and chemical affinities involved. We therefore believe that the high apparent solubility of D_2 in the Al_2O_3 is actually due to the solubility of deuterated water. Assuming the partial pressure of deuterated water in the system to be $\sim 5 \times 10^{-5}$ atm and converting to 1 atm water pressure by using a 0.5 power dependence of solubility on water pressure, we obtain the estimated solubilities for water (given as T_2O) in Al_2O_3 shown in Fig. 7-7.

The solubility value for T_2O of $\sim 4 \times 10^{-5}$ moles T_2O/cm^3 Al_2O_3 at 1000 to 1200 K for 1 atm T_2O pressure (see Fig. 7-7) can be compared with $\sim 5 \times 10^{-4}$ moles T_2O/cm^3 Li_2O and $\sim 2 \times 10^{-4}$ moles T_2O/cm^3 SiO_2 under the same conditions (see Sec. 7.1.4.3). The indicated solubility of T_2O in Al_2O_3 is thus about an order of magnitude lower than the solubility of T_2O in either Li_2O or SiO_2.

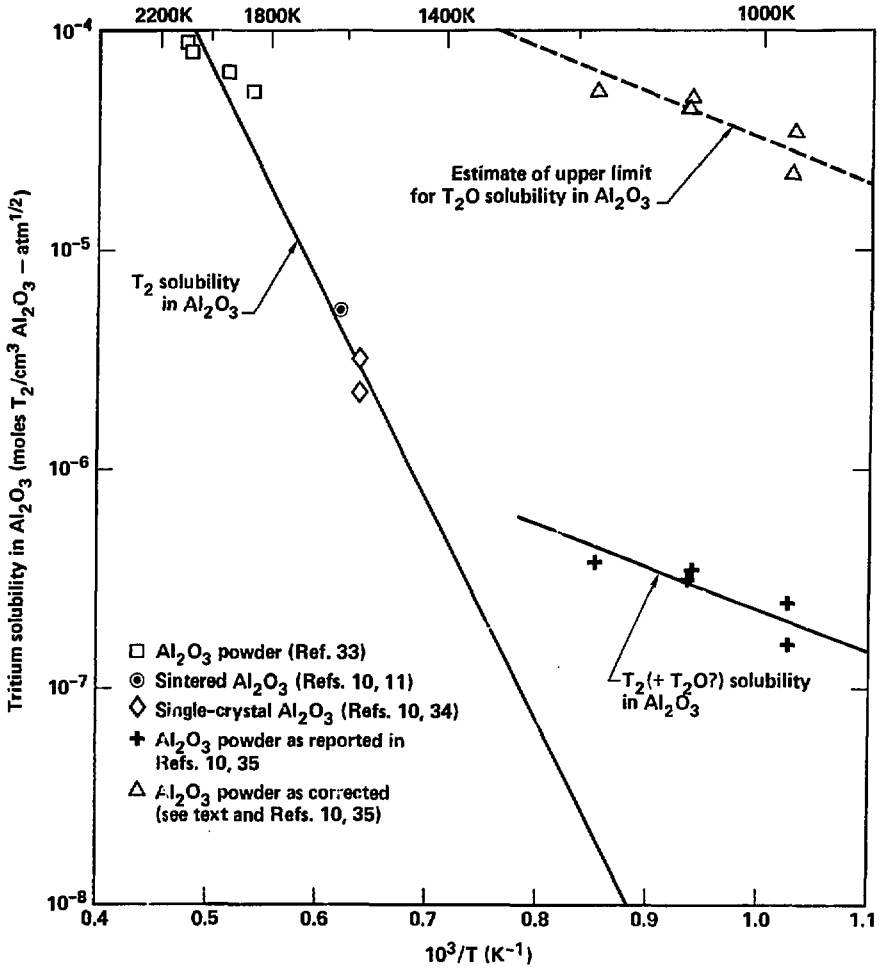

Fig. 7-7. Solubility data are given for hydrogen isotopes in Al_2O_3 and are assumed to apply to T_2 and T_2O in Al_2O_3. Our selected values for T_2 solubility in Al_2O_3 are represented by the solid curve through the highest temperature points. The solid curve through the lowest temperature curves suggests to us the presence of T_2O as well as T_2. The dashed curve gives our estimate of the upper limit for T_2O solubility in Al_2O_3 at a T_2O pressure of $\sim$1 x 10^{-5} atm.

This is certainly in the proper direction, but probably still on the high side by about an order of magnitude because of the presence of surface-adsorbed water. We therefore take the solubility of T_2O in Al_2O_3 to be one-tenth of the values estimated in Fig. 7-7 with plus or minus an order of magnitude uncertainty. The selected expression for the estimated solubility of T_2 in Al_2O_3 is

$$S = 3.89 \times 10^{-4} \exp(-4.804 \times 10^3/T) \text{ moles/cm}^3\text{-atm}^{1/2}. \quad (31)$$

Only one study has been conducted on the permeability of hydrogen in Al_2O_3;[10,11] and the data are summarized in Fig. 7-8. However, we are in a position now to calculate the permeabilities of both T_2 and T_2O in Al_2O_3 based on our derived diffusivity and solubility data and using the relation $K = S \cdot D$. We thus calculate the permeabilities of T_2 and T_2O in Al_2O_3 to be:

$$K(T_2) = 3.29 \times 10^2 \exp(-5.481 \times 10^4/T) \text{ moles/cm-s-atm}^{1/2}, \quad (32)$$

$$K(T_2O) = 9.17 \times 10^{-8} \exp(-1.960 \times 10^4/T) \text{ moles/cm-s-atm}^{1/2}. \quad (33)$$

These relations are illustrated by the solid lines in Fig. 7-8. We can see that the agreement with the experimental measurements is excellent for the permeability of T_2 in Al_2O_3, thus lending support to our interpretation of the corresponding diffusivity and solubility data. If instead of Eq. (32), we were to use the slope of the experimental data points in Fig. 7-8 to extrapolate to lower temperatures, we would obtain substantially higher values for K at lower temperatures. We have selected Eq. (32) for our calculations because we believe that it is more representative of the actual situation. There is no direct check on the permeability of T_2O in Al_2O_3, and we have therefore used dashed lines in Fig. 7-8 to indicate an order of magnitude uncertainty in our predicted permeability.

7.3.2.2 Tritium Permeation Rate into the SO_3 Decomposer. Now we can calculate the tritium permeation rate through the walls of the helium-to-process heat exchanger and into the SO_3 decomposer. From the amount of tritium in the SO_3, we can estimate the amount of tritium in the hydrogen product for synfuels applications on the basis that each mole of SO_3 leads to the production of one mole of H_2.

The mechanism of tritium permeation through the duplex tube walls is postulated as follows. Tritium present mainly as T_2O in the helium stream permeates through the protective Al_2O_3 scale on the first wall, migrating as OT^-. It then converts to atomic T at the Al_2O_3 to metal (Waspaloy) interface and leaves behind some metal oxide (probably Cr_2O_3). It then migrates rapidly through the metal tube wall and enters the gap region where it converts to HT by reacting with H_2 present in excess in the gap region both on wall surfaces and in the helium flow stream. A portion of the HT is now swept out by the helium flow and a portion converts to T atoms at the second tube wall and permeates up to the Al_2O_3 barrier interface at the SO_3 decomposer. It now undergoes isotopic exchange with H atoms at the interface to form HT and permeates through the Al_2O_3 barrier into the SO_3 decomposer. At the same time

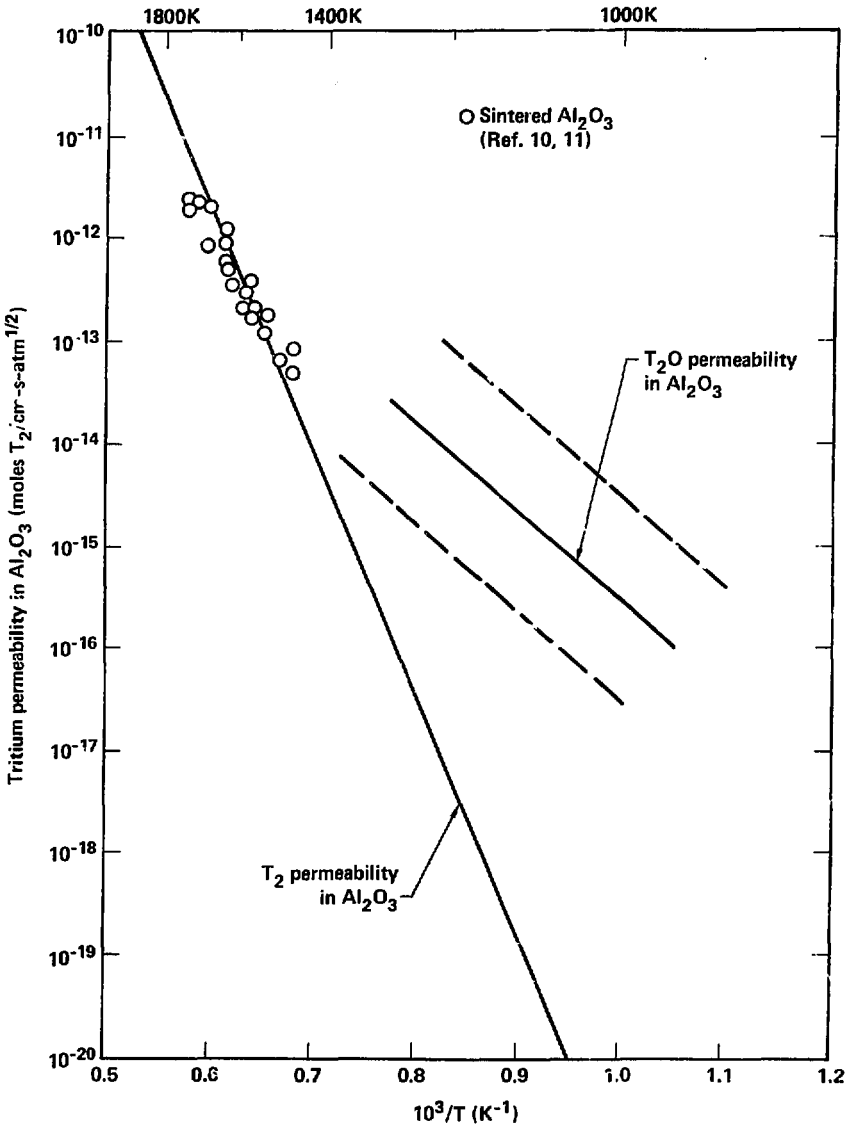

Fig. 7-8. The experimental data for permeability of hydrogen in Al_2O_3 are summarized and solid lines are used to represent our selected values for T_2 and T_2O permeabilities in Al_2O_3. The dashed lines show our estimated uncertainty in the T_2O permeability values.

that tritium is migrating toward the SO_3 decomposer region, H_2O that is present at a pressure of about 3 atm in the SO_3 decomposer gases is permeating inward as OH^- through the Al_2O_3 barrier and converting to H atoms as it forms metal oxide (probably Cr_2O_3) at the metal to Al_2O_3 interface. The H atoms then migrate into the gap where they react to form H_2 and some HT, which is swept out by the helium sweep stream. We expect the H_2/T_2 ratio (assuming no isotope exchange) in the gap--based on the source pressures of H_2O and T_2O across equivalent Al_2O_3 barriers--to be about (3 atm/2.88 x 10^{-5} atm)$^{1/2}$ or $\sim$322, or an H_2/HT ratio of 161 after isotope exchange. This swamping out of the tritium by protium markedly reduces the tritium migration rate into the SO_3 decomposer.

From the mechanism postulated above we see that the rate-limiting steps in tritium permeation are: (1) the permeation rate of tritium as T_2O through the first Al_2O_3 barrier (T_2 permeation is negligible in comparison with T_2O for the 9/1 ratio of T_2O/T_2 in the helium stream); (2) the H_2 concentration in the gap (which swamps out the T_2 concentration) and the sweep rate of helium in the gap (this assumes an efficient gap design that permits rapid migration of tritium species along the 10-μm gap regions and into the helium purge channels); and (3) the permeation rate of tritium as HT through the second Al_2O_3 barrier and into the SO_3 decomposer.

Tritium permeation rates based on the above mechanisms are summarized in Table 7-11 with the values for rate of HT permeation into the SO_3 decomposer given in the last column. The permeation rate is calculated from the relation

$$R = K \cdot A\,(p)^{1/2}/x \text{ moles/s}, \qquad (34)$$

where the permeation rate R is in moles/s when the permeability K is in moles/cm-s-atm$^{1/2}$, the area A is in cm^2, the partial pressure p of the permeating gas is in atm, and the permeation distance x is in cm.

We find in carrying out the calculations that the permeation rate of tritium as T_2 is negligible compared with the permeation rate as T_2O through the first Al_2O_3 barrier, so that the T_2 permeation rate into the duplex-tube gap (see column 3 of Table 7-11) is fixed by the partial pressure of T_2O in the main helium stream. The estimated amount of H_2 permeating into the gap (originating from H_2O in the SO_3 decomposer) is given in column 4 of Table 7-11 based on Eqs. (33) and (34). Because this H_2 originates from the metal alloy reduction of the H_2O migrating through the Al_2O_3, we can expect a Cr_2O_3-rich oxide layer to develop at the metal-to-Al_2O_3 interface. The rate of development of this oxide layer will range from about 3 μm/year at 1000 K to 15 μm/year at 1200 K for the H_2 permeation rates shown in column 4 of Table 7-11.

By adjusting the helium purge flow in the gap to different values for each heat exchanger stage (see column 5 of Table 7-11), we maintain the H_2 partial pressure at $\sim 10^{-3}$ atm and the HT partial pressure at $\sim 10^{-5}$ atm in the 20-atm helium purge stream. A regenerative heat exchanger is used to recover heat from the purge stream exhaust, and the helium then is compressed to 50 atm and added to the input gas entering the slip-stream tritium processor. Tritium-depleted helium from the slip-stream processor is returned and heated in counter flow in the same regenerative heat exchanger used for the purge stream exhaust, and used as the input helium purge gas.

To calculate the permeation rate of HT into the SO_3 decomposer, we first calculate the partial pressure of H_2 in the duplex tubing gap. This partial pressure (in atm) is obtained from the relation

$$P_{H_2} = \frac{(\text{moles/s of } H_2)(20 \text{ atm})}{(\text{moles/s of He})} \quad . \tag{35}$$

We next need to calculate the permeation rate of H_2 through the Al_2O_3 barrier at the SO_3 decomposer interface, but this presents a problem, i.e., at the metal-to Al_2O_3 interface the amount of H_2O dissolved in the Al_2O_3 will be very low because of the reducing action of the metal alloy, whereas on the SO_3 decomposer side the amount of H_2O dissolved in the Al_2O_3 will be much higher because of the high pressure ($\sim$3 atm) of steam present. Hence, we expect a relatively low concentration of defects in the Al_2O_3 near the metal-to-Al_2O_3 interface, so that the permeation rate of H_2 should be comparable to that in H_2O-free Al_2O_3 in this region. We therefore roughly approximate the H_2 permeation rate by assuming that the effective thickness of the Al_2O_3 scale, where the low defect concentration persists, is one-tenth of the overall scale thickness, and we use Eqs. (32) and (34) to calculate the H_2 permeation rate (see column 6 of Table 7-11). We assume further that the permeation rate of H_2 through the rest of the Al_2O_3 scale is sufficiently rapid that it can be ignored compared with the low-defect region. Finally, we proportion the tritium (HT) permeation rate to the H_2 permeation rate by using the ratio (given earlier) of 161/1 for H_2 to HT in the gap region. The values thus obtained for the HT permeation rate into the SO_3 decomposer are given in column 7 of Table 7-11 and amount to a total permeation rate of 2.43×10^{-10} moles/s of HT.

To estimate the concentration of tritium in the hydrogen product of the hydrogen production plant, we compare the amount of tritium permeating into the SO_3 decomposer with the amount of hydrogen produced by the plant. Thus, taking the tritium to be in the form of T_2 for calculational purposes, the permeation rate of T_2 into the plant is $(1/2)(2.43 \times 10^{-10}) = 1.22 \times 10^{-10}$ moles/s as compared with an H_2 production rate of about 5000 moles/s. This gives a tritium (T_2) concentration of $1.22 \times 10^{-10}/5000 = 2.4 \times 10^{-14}$ moles T_2/mole H_2.

To put this tritium concentration into a proper frame of reference, we note that two studies[36,37] have analyzed hypothetical scenarios in which houses and power plants in metropolitan Los Angeles burn natural gas containing traces of tritium. If our hydrogen product were used in a comparable way to the natural gas in the above scenarios, the weighted average exposure to the general public in the Los Angeles area would be about 70 μrem/year, with a maximum individual exposure of about 400 μrem/year. This compares with a natural radiation background of 114 mrem/year for an individual in the Los Angeles area, with an additional exposure from all medical sources of 98 mrem/year. Thus, a level of tritium of 2.4×10^{-14} moles T_2/mole H_2 in the hydrogen product would increase individual exposures by an average amount of less than 0.1% above natural background if the hydrogen or hydrogen products were used directly in homes. Therefore, we have a product that we expect will have a very low tritium contamination level. However, considerable uncertainties exist in the data base used in the calculations here, and experimental studies will be needed to better substantiate the data.

7.3.3 Tritium Losses to the Environment

Tritium is mainly lost to the environment when it leaks from the blanket and coolant handling systems into the reactor hall through the piping systems, and into the cooling water through the 5-cm-thick steel shell between the blanket pod region and the magnet shields.

To prevent this type of leakage we have provided an aluminum metal shroud surrounding all of the piping system components, including both the helium and Li-Pb coolant systems, the slip-stream processor, and the heat exchangers. The aluminum shroud will be compartmentalized for isolating various components or regions, thus maintaining safety in case of leaks.

Both aluminum metal and its natural oxide scale provide highly effective barriers against tritium permeation. Extrapolating the high temperature T_2 permeability data in aluminum metal[38] to room temperature, we find $K = 7 \times 10^{-26}$ g T_2/cm-s-atm$^{1/2}$. The permeabilities of T_2 and T_2O are many orders of magnitude less in Al_2O_3 as illustrated in Eqs. (32) and (33). On the conservative side, we assume that the permeability for aluminum metal applies to the bulk material, including the surface oxide. Using an overall area of 10,000 m^2, an aluminum thickness of 0.5 mm, and a T_2 pressure of 10^{-8} atm, we calculate a T_2 permeation rate of 4×10^{-13} g/year, which is equivalent to 4 μCi/year. In case of a serious leak into the aluminum shroud from the helium piping system, the T_2 partial pressure could possibly increase to as much as 3.20×10^{-5} atm, which would raise the permeation rate through the aluminum shroud to 0.2 μCi/year. Within the slip-stream processor, a leak in the boiler could give a T_2O pressure of ∿1 atm, which, for an aluminum shroud area of 20 m^2, would raise the permeation rate to 0.1 μCi/year.

These permeation rates are all extremely low. We conclude that if an aluminum shroud is used to surround the coolant piping systems and associated equipment, tritium permeation into the reactor hall through the shroud will be insignificant as long as the shroud is leaktight. The reactor hall itself serves as secondary containment.

To estimate the permeation rate of tritium through the walls of the helium piping (made of HT-9), we first estimate values of $D = 7 \times 10^{-5}$ cm^2/s and $S = 5.8 \times 10^{-7}$ moles T_2/cm^3-atm$^{1/2}$ at 500 K, which gives $K = S \cdot D = 4.0 \times 10^{-11}$ moles T_2/cm-s-atm$^{1/2}$. For a wall area of 7330 m^2, an average wall thickness of 8 cm, and a T_2 pressure of 3.20×10^{-5} atm, this results in a tritium leakage rate of 1.3×10^{-5} g T_2/s, or an accumulative total of 400 g T_2/year. Of course, this does not add significantly to the tritium inventory because the helium purge stream in the shroud is continuously processed for tritium. Nonetheless, the 400 g T_2/year is probably too high by a factor of about 10^3 because of a natural oxide barrier on the surface of the HT-9. We therefore estimate the tritium permeation rate through the helium piping, barring leaks, as about 0.4 g T_2/year. Because the helium piping constitutes most of the surface area available for tritium permeation in the coolent transport systems, the other components do not contribute significantly, and we therefore take the total tritium permeating through the piping to be about 1 g T_2/year.

To estimate the permeation rate of tritium into the cooling water for the shield, we assume that $D = 1.6 \times 10^{-4}$ cm^2/s and $S = 3 \times 10^{-6}$ moles T_2/cm^3-atm$^{1/2}$ for tritium in HT-9 at 600 K, which gives $K = 1.4 \times 10^{-9}$ moles T_2/cm-s-atm$^{1/2}$. Now, for a surface area of 176 m^2, a wall thickness of 5 cm,

and a T_2 pressure of 1.32×10^{-7} atm, we calculate a tritium permeation rate of 1.1×10^{-6} g T_2/s, or 34 g/year. Taking into account the temperature gradient through the shield wall (water-side temperature = 438 K) reduces these values somewhat to 18 g/year, or 1.8×10^5 Ci/year.[18] Assuming a total water volume of 50,000 liters would give an accumulated tritium content of 4 Ci/liter-year. This value must be reduced even further, by perhaps three orders of magnitude, because of the permeation resistance provided by the natural surface oxide on the HT-9 at the water interface. We therefore conclude that, the tritium content of the cooling water for the shield accumulates at the rate of about 4 μCi/liter-year, which is a reasonably low value for a working plant.

Thus, as a general conclusion, we find that tritium losses to the environment are exceedingly low during normal operation of the MARS/synfuel plant.

7.3.4 Reactor Accident Issues

Although we will make a few comments here about reactor accident issues in regard to tritium, this is an area that we have not developed to any significant extent because so many of the design concepts are relatively new. Hence, this area deserves more attention in the future.

Two aspects of reactor accidents that we have looked at in a preliminary way are coolant leaks and overheating of the blanket as a consequence of an accidental loss of coolant. Another area is protection of the $U(D,T)_3$ storage unit and the slip-stream processor against any unusual incidents because they contain large inventories of tritium.

Consider first a leak in the helium coolant; the leak could occur within the blanket, into the reactor hall, or into the hydrogen plant (the SO_3 decomposer). If all of the helium coolant were released, the total tritium content would be about 10 g.

If a helium leak in one of the modules released helium into the plasma zone, it would of course quench the thermonuclear reaction and the entire reactor would then be shutdown. The helium would need to be transferred back into the helium circulating system or into the helium ballast tank, and the module would be repaired. It seems reasonable to maintain helium supply and return valving on the individual modules to be able to shut off the main helium supply in case of a major leak in a module. This type of accident would not present a safety problem or an extensive shutdown unless the helium also carried liquid Li-Pb with it into the plasma region, or if the helium were to vent into the reactor hall.

If the helium did vent into the reactor hall, enough volume would have to be present in the hall to contain the released helium if the hall were immediately sealed. Containment would be more positively assured if compartmental valving were used along the piping as well as in the reactor blanket modules. The gases in the reactor hall would then be processed for tritium recovery, and the walls and surfaces would be scrubbed down and painted. From then on, the gases present in the reactor hall would need to be periodically (or continuously) vented up a stack to prevent buildup of unacceptable levels of tritium evolving from the paint.

If helium were released into the SO_3 decomposer, both the reactor and chemical plant would need to be immediately shutdown, and the SO_3 decomposer

and the recovery units for the decomposer gases would have to be isolated, and the products in the chemical plant would be processed for tritium recovery. It should be possible to decontaminate the portions of the chemical plant exposed to tritium, but if not, those portions would need to be replaced.

If liquid Li-Pb were released into the plasma region, either by itself or carried by high pressure helium, it would quench the plasma reaction and shutdown the reactor, but would not be expected to present a safety problem. Isolation valves would again be needed on the Li-Pb coolant for each module. Cleanup could be difficult and expensive for a Li-Pb spill because even trace amounts of heavy metals in the plasma region could be detrimental to the thermonuclear reaction.

A spill of liquid Li-Pb into the reactor hall would be comparable in cleanup problems to a release of helium into the reactor hall. We do not anticipate a fire problem with the $Li_{17}Pb_{83}$ composition used, although chemical reaction will slowly take place with the air and construction materials. Again, the walls and surfaces would all have to be scrubbed and painted and the reactor hall atmosphere would need to be vented to prevent buildup of unacceptable levels of tritium.

If a coolant stoppage occurred, the reactor would have to be immediately shutdown, and if the coolant stoppage were localized, the region of coolant stoppage would need to be isolated from the rest of the system using the valves for that particular module or modules. After the afterheat effects within the module stabilized, the coolants could be released into their respective ballast tanks. Any pressure buildup from afterheat would have to be periodically released to prevent excessive buildup.

If the coolant stoppage were general throughout either or both of the coolant systems, the reactor would again have to be immediately shutdown and the pressure monitoring and coolant release procedures followed as before. If the reactor continued to operate with a coolant stoppage, the first wall would likely overheat, followed by a blowout of liquid Li-Pb into the plasma region, at which time the reactor would shut itself down. In the worst conceivable operating scenario, the first wall would heat up enough to release all of its tritium, which would be about 0.5 g of tritium per module.

If a blanket module completely ruptured and released all of its internal parts into the reactor hall, it would not be expected to increase the tritium hazard in the hall significantly more than with a more simple release. This is because most of the tritium in the blanket is entrapped in extremely inert refractory materials such as α-SiC, $MgAl_2O_4$, Fiberfrax, and HT-9. Even the $LiAlO_2$ fuel would be partially protected from reaction with the environment by containment in the α-SiC balls.

Because a large inventory of tritium fuel is stored in the form of $U(D,T)_3$, it is important that this part of the process unit be well-protected from unusual or totally unexpected events. Overheating and exposure to air or water would especially need to be protected against. Also, the slip-stream processor would need to be designed with unusual care because large amounts of tritium are handled there as well. It would seem prudent to have separate vaults for the slip-stream processor and the $U(D,T)_3$ units to reduce the possibility of accidental interactions with the rest of the reactor system. It is difficult to make more specific comments until more detailed considerations are given to the designs. We recommend further detailed analyses of accident issues as more detailed equipment designs develop.

7.3.5 Tritium Safety and Control Conclusions

Permeation barriers are very effective as a means of containing tritium, but they must be designed with care and there is some concern about their reliability at temperatures above about 1100 K. At temperatures up to about 1100 K, Al_2O_3 and Cr_2O_3 as coatings or scales on Fe and Ni alloys form effective barriers against tritium permeation, but the barriers must be carefully designed to prevent the oxides from fracturing or spalling. At or near room temperature, aluminum metal used as a shroud over piping and equipment forms an extremely effective tritium permeation barrier.

A duplex-tube heat exchanger improves the reliability of coup ıg the reactor to an SO_3 decomposer in the hydrogen production plant and reduces chances for accidental leakage of tritium into the plant. Tritium levels in the product hydrogen are expected to be about 2.3×10^{-14} moles T_2/mole H_2, which, if the hydrogen were to be burned in power plants and homes, would lead to an average individual exposure of less than 0.1% above the natural radiation background in the metropolitan Los Angeles area.

In the area of reactor accidents, we see no major problems with tritium releases. This is because the amount of tritium contained in the helium and Li-Pb coolants is very low and because valving schemes can be used to isolate blanket modules and the piping system into relatively small volumes so that leaks can be contained within the reactor hall. However, further work is needed in evaluating reactor accidents especially as desigr details on blankets and coolan.: processing methods progress.

REFERENCES

1. J. E. Shelby, "Radiation Effects in Hydrogen-Impregnated Vitreous Silica," J. Appl. Phys. 50, 3702 (1979).

2. T. Namba, H. Miyaguchi, M. Yamawaki, and M. Kanno, "Hydrogen Permeation through Vanadium and the Effect of Surface Impurity Layer on It," J. Nucl. Matls. 105, 318 (1982).

3. J. E. Shelby, "Molecular Diffusion and Solubility of Hydrogen Isotopes in Vitreous Silica," J. Appl. Phys. 48, 338 (1977).

4. J. E. Shelby, P. L. Mattern, and D. K. Ottesen, "Radiation-Induced Isotope Exchange in Vitreous Silica," J. Appl. Phys. 50, 5533 (1979).

5. J. E. Shelby, "Reaction of Hydrogen with Hydroxyl-Free Vitreous Silica, J. Appl. Phys. 51, 2589 (1980).

6. J. E. Shelby and J. Vitko, Jr., "Hydrogen Transport in a Machinable Glass-Ceramic," J. Non-Crystalline Solids 45, 83 (1981).

7. H. Kudo and K. Okuno, "Kinetic Studies of the Tritium Release Process in Neutron-Irradiated Li_2O and LiOH," J. Nucl. Matls. 101, 38 (1981).

8. H. Kudo and K. Okuno, Chemical Behavior of Tritium in CTR Blanket Materials--Tritium Release from Neutron Irradiated Li_2C_2, private communication from H. Kudo, Japan Atomic Energy Research Institute, Tokaimura, Japan (July, 1982).

9. R. A. Causey, J. D. Fowler, C. Ravanbakht, T. S. Elleman, and K. Verghese, "Hydrogen Diffusion and Solubility in Silicon Carbide," J. Amer. Ceramic Soc. 61, 221 (1978).

10. R. M. Roberts, T. S. Elleman, H. Palmour III, and K. Verghese, "Hydrogen Permeability of Sintered Aluminum Oxide," J. Amer. Ceramic Soc. 62, 495 (1979).

11. K. Verghese, L. R. Zumwalt, C. P. Feng, and T. S. Elleman, "Hydrogen Permeation through Non-Metallic Solids," J. Nucl. Matls. 85 and 86, 1161 (1979).

12. T. E. Boothe and H. J. Ache, J. Phys. Chem. 82, 1362 (1978).

13. T. E. Boothe and H. J. Ache, J. Phys. Chem. 83, 457 (1979).

14. T. E. Boothe and H. J. Ache, J. Nucl. Matls. 84, 85 (1979).

15. H. Kudo, Tritium Chemistry in Nuclear Fusion Research Program of JAERI, 1974-1982, private communication, Japan Atomic Energy Research Institute, Tokaimura, Japan, (July, 1982).

16. P. J. Jorgensen, M. E. Wadsworth, and I. B. Cutler, "The Kinetics of the Oxidation of Silicon Carbide," in Silicon Carbide, a High Temperature Semiconductor, edited by J. R. O'Connor and J. Smiltems, Pergamon Press, New York, 1960, pp 241-250.

17. F. W. Clinard, Jr., and G. F. Hurlen, "Neutron Irradiation Damage in MgO, Al_2O_3 and $MgAl_2O_4$ Ceramics," J. Nucl. Matls. 108 and 109, 655 (1982).

18. J. H. Norman et al., Retention of Tritium by a Li_2O Breeder System, private communication, GA Technologies, (May, 1983).

19. R. G. Bedford, "The Solubility of Water in Molten Silicates " J. Glass Tech. 16, 20 (1975) and private communication, Lawrence Livermore National Laboratory, Livermore, CA (August 1969).

20. N. A. Galaktionowa, Hydrogen-Metal Systems Databook, English translation revised and edited by A. Abraham (Ordentlich Publishers, Holon, Israel, 1980).

21. C. M. Griffith provided us with an experimental bulk density value for Linde 5A molecular sieve, private communication, Lawrence Livermore National Laboratory Tritium Facility, Livermore, CA (April, 1983).

22. A. E. Sherwood, private communication, Lawrence Livermore National Laboratory Tritium Facility, Livermore, CA (April, 1983).

23. J. R. Bartlit, W. H. Denton, and R. H. Sherman, "Hydrogen Isotope Distillation for the Tritium Systems Test Assembly," in Proceedings of the Third Topical Meeting on the Technology of Controlled Nuclear Fusion, May 9-11, 1978, Vol. 2, pp. 778-783, CONF-780508, 1978.

24. Metal Hydrides, edited by W. M. Mueller, J. P. Blackledge, and G. G. Libowitz (Academic Press, New York, 1968).

25. R. W. Taylor, private communication, Lawrence Livermore National Laboratory Department of Chemistry and Materials Science, Livermore, CA (May, 1983).

26. J. L. Maienschein, private communication, Lawrence Livermore National Laboratory Tritium Facility, Livermore, CA (May, 1983).

27. B. G. Logan, C. D. Henning, G. A. Carlson, et al., Mirror Advanced Reactor Study-Interim Report, Lawrence Livermore National Laboratory, Livermore, CA, UCRL-53333, (1983).

28. K. E. Plute, E. M. Larsen, L. C. Wittenberg, and D. K. Sze, "Tritium Recovery from Liquid Lithium-Lead by Vacuum Degassing," presented at the Fifth ANS Topical Meeting on the Technology of Fusion Energy, Knoxville, TN, April 26-28, 1983, University of Wisconsin, UWFDM-516 (May 1983).

29. J. Völkl and G. Alefeld, "Hydrogen Diffusion in Metals," in Diffusion in Solids, Recent Developments edited by A. S. Nowick and J. J. Burton (Academic Press, New York, 1975), pp. 231-302.

30. R. M. Alire, P. C. Souers, H. H. Miller, and S. A. Steward, "Low Permeability Materials for Tritium and Tritium Removal with Organic Materials," in The Technology of Controlled Nuclear Fusion, Proceedings of the Fourth Topical Meeting, Vol. 1, edited by F. H. Tenney and C. C. Hopkins, King of Prussia, Pennsylvania, Oct. 14-17, 1980, U. S. Department of Energy, CONF-801011, July 1981, pp. 498-501.

31. P. W. Trester and S. S. Liang, "Material Corrosion Investigations for the General Atomic Sulfur-Iodine Thermochemical Water-Splitting Cycle," in Hydrogen Energy System, Proceedings of the 2nd World Hydrogen Energy Conference, Zurich, Switzerland, August 21-24, 1978, Vol. 4, edited by T. N. Veziroglu and W. Seifritz, (Pergammon Press, Oxford, 1978), pp. 2113-2159.

32. J. D. Fowler, D. Chandra, T. S. Elleman, A. W. Payne, and K. Verghese, "Tritium Diffusion in Al_2O_3 and BeO," J. Amer. Ceram. Soc. 60, 155 (1977).

33. S. K. Roy and R. L. Coble, "Solubility of Hydrogen in Porous Polycrystalline Aluminum Oxide," J. Amer. Ceram. Soc. 50, 435 (1967).

34. C. W. Alexander, Solubility of Deuterium in Aluminum Oxide, M. S. Thesis, North Carolina State University, Raleigh, North Carolina (1976).

35. D. R. Chari, Deuterium Solubility in Aluminum Oxide Powder, M. S. Thesis, North Carolina State University, Raleigh, North Carolina (1977).

36. G. C. Werth, et al., An Analysis of Nuclear-Explosive Gas Stimulation and the Program Required for its Development, Lawrence Livermore National Laboratory, Livermore, CA, UCRL-50966 (1971).

37. R. C. Maninger and D. W. Dorn, Tritium Content in Gaseous Fuels, private communication, Lawrence Livermore National Laboratory, Livermore, CA (November 2, 1982).

38. P. A. Finn and R. G. Clemmer, "Tritium Handling Considerations for ETF and Starfire," in The Technology of Controlled Nuclear Fusion, Proceedings of the Fourth Topical Meeting, King of Prussia, Pennsylvania, Oct. 14-17, 1980, Vol. 1, edited by F. H. Tenney and C. C. Hopkins, U. S. Department of Energy, CONF-801011, (July 1981) pp. 543-554.

8 Sulfur Trioxide Fluidized Bed Composer

CONTENTS

8. The Sulfur Trioxide Fluidized-Bed Composer

8.1 INTRODUCTION

In GA Technologies' sulfur-iodine cycle for hydrogen production, the overall process can be represented by the abbreviated chemical description shown in Fig. 8-1. As can be surmised, many process engineering steps are necessary to perform the chemistry. For example, the following list of transformations is a more detailed description of the part of the cycle leading to the use of the fluidized bed decomposer:

1. $H_2O\ (l) + SO_2(g) + xI_2\ (l) \rightarrow H_2SO_4\ (sol) + 2HI_x\ (sol)$

2. $H_2SO_4\ (sol) \rightarrow H_2SO_4\ (l)$

3. $H_2SO_4\ (l) \rightarrow H_2SO_4\ (g)$*

4. $H_2SO_4\ (g) \rightarrow H_2O\ (g) + SO_3\ (g)$*

5. $SO_3\ (g) \rightarrow SO_2\ (g) + 1/2\ O_2\ (g)$*

6. $2HI_x\ (sol) \xrightarrow{H_3PO_4} 2HI\ (g) + (x - 1)\ I_2\ (l)$

7. $2HI\ (g) \rightarrow H_2\ (g) + I_2\ (g)$

8. $I_2\ (g) \rightarrow I_2\ (l)$.

The starred transformations represent the part of the process leading to the fluidized bed decomposer where the highest temperature of the thermochemical cycle occurs. In this section we discuss how we provide this high temperature, obtain good $SO_3 \rightarrow SO_2$ conversion efficiency, and design a vessel that is operable in a corrosive atmosphere, that will withstand the imposed thermal and mechanical stresses, and that can be matched energetically to the helium supply.

The temperature-enthalpy history of the starred transformations is shown in Fig. 8-2. As the figure indicates, the enthalpy requirement to decompose the SO_3 to SO_2 is 98 kJ/mol H_2. An additional 73 kJ is required as sensible heat addition for a total of 171 kJ/mol H_2. High temperature helium from the fusion reactor blanket supplies this energy to the vapor in the decomposer. Figure 8-3 illustrates the thermal energy and temperature requirements for the overall H_2SO_4 process stream (on this figure the decomposer region has been circled). The heat content of the helium is transferred to the decomposer across duplex tubing placed horizontally in the decomposer unit. The use of

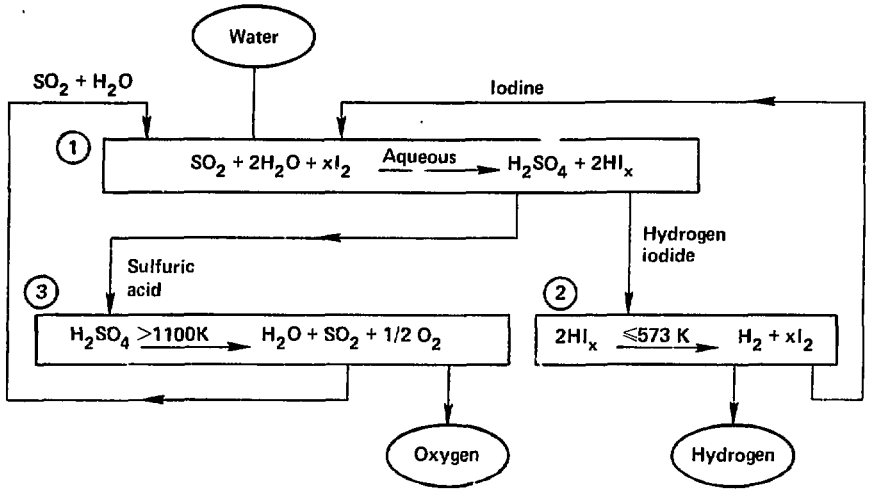

Fig. 8-1. The GA Technologies sulfur iodine cycle.

duplex tubing, with a helium gas in the gap between the tube walls, provides a means of tritium control needed to maintain the hydrogen product at the appropriate level of purity.

A highly schematic representation of a four-stage fluidized bed decomposer is shown in Fig. 8-4. This is our reference design model and is one of 10 identical units that would be used in the thermochemical plant. Nine units are required for operation and the tenth is a spare. The highest decomposition temperature that we have elected to use in this study for the reference case is 1100 K. At this temperature and a fourth-stage process pressure of approximately 6.7 atm, the conversion efficiency of SO_3 to SO_2 is 63%, as shown in Fig. 8-5. As we are able to operate at higher and higher decomposition temperatures, the conversion efficiency increases markedly. This, in turn, decreases the amount of recycle necessary in the overall process stream and raises the effectiveness of this chemical reactor. We wish to optimize this effectiveness, balancing the size and number of process units against the limits imposed on the structural components by the strength of the materials.

8.2 THE SULFUR TRIOXIDE DECOMPOSITION PROCESS STEP

Figure 8-1 shows that step 3, the decomposition of the sulfuric acid to SO_2 and O_2, is the high temperature step in the cycle.

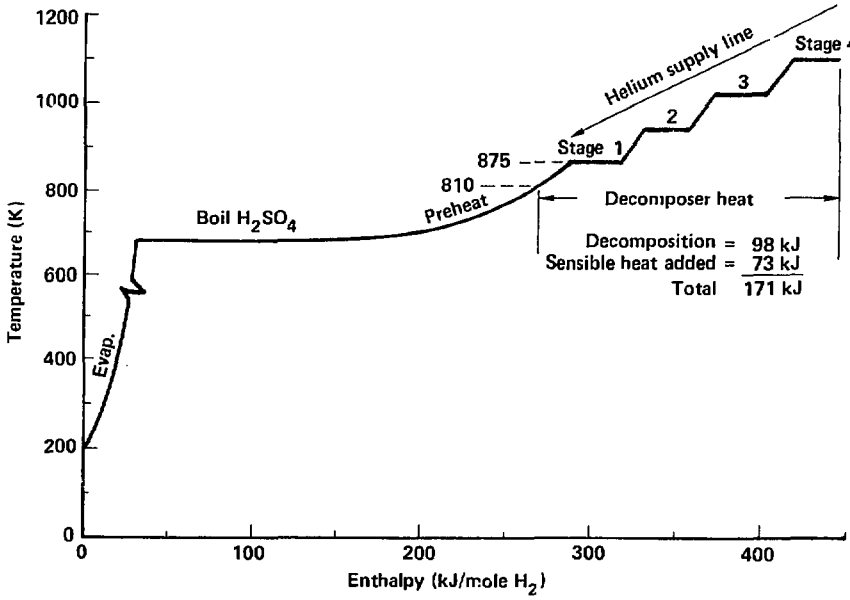

Fig. 8-2. Temperature-enthalpy curve for a four-stage fluidized-bed SO_3 decomposer.

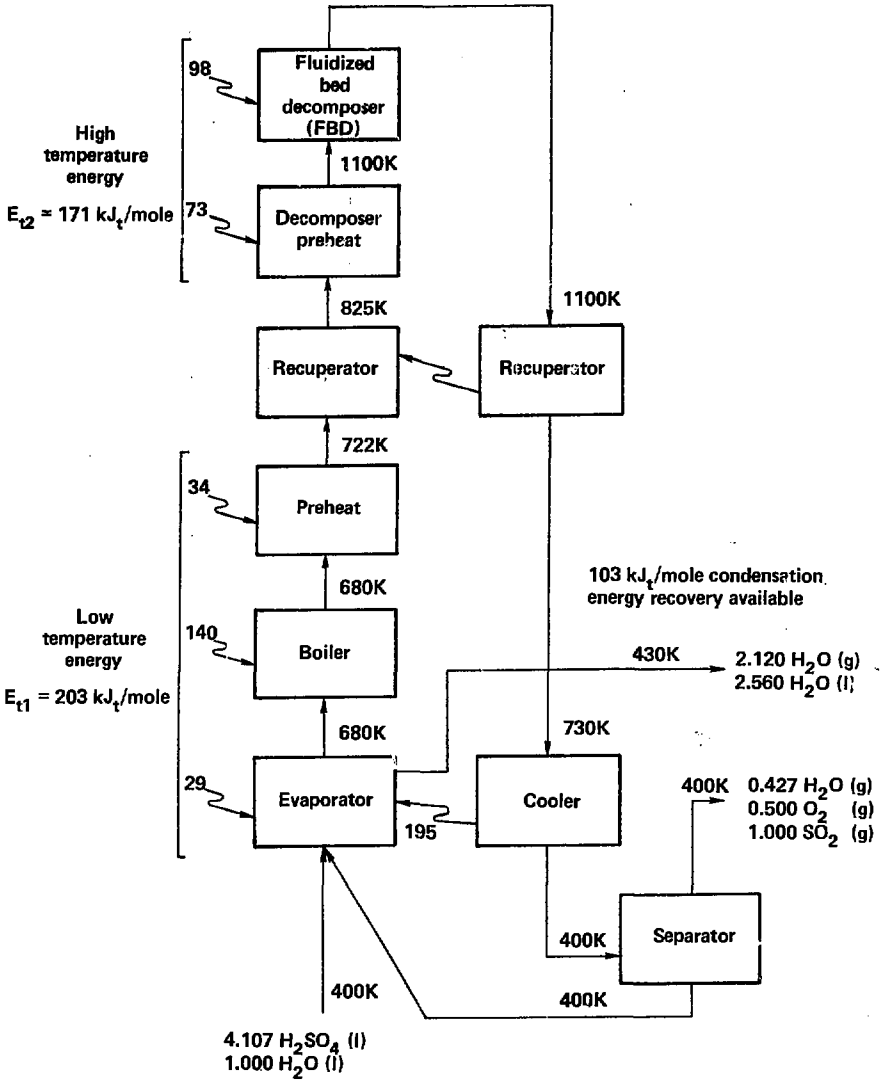

Fig. 8-3. Thermal energy and temperature requirements for H_2SO_4 process stream.

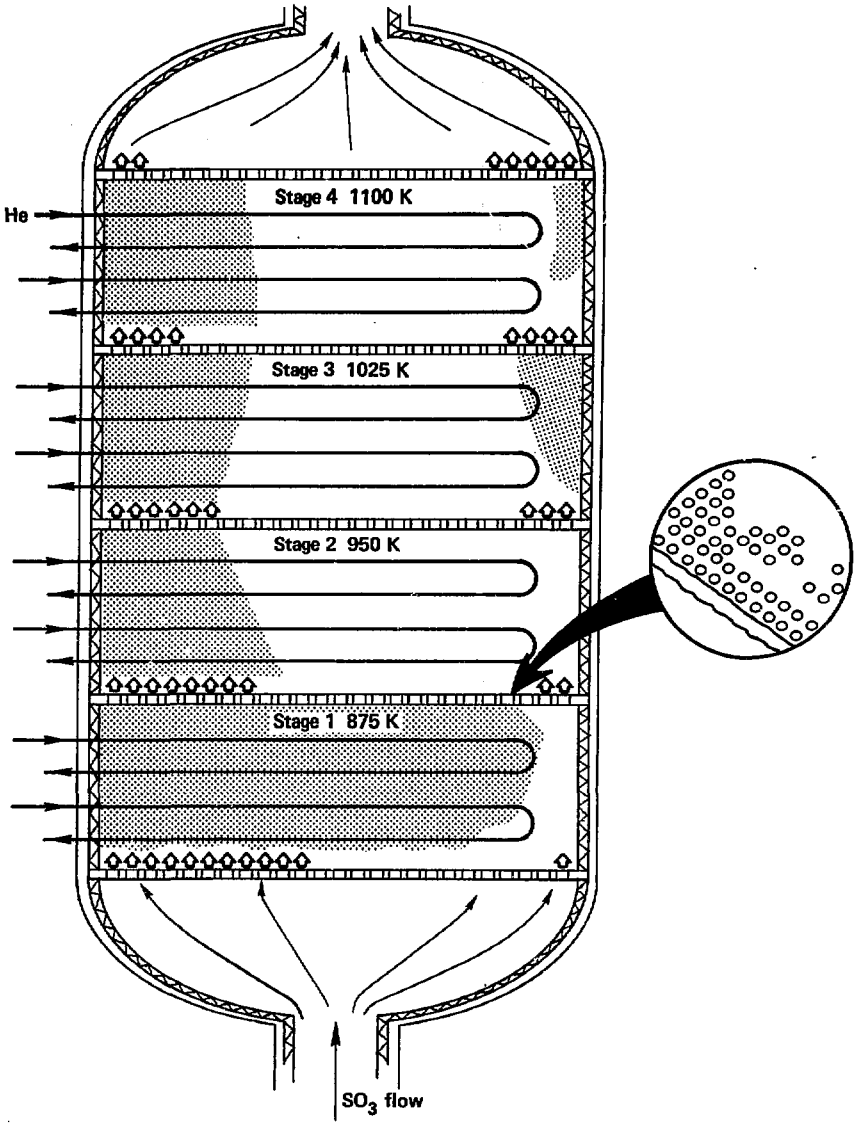

Fig. 8-4. Cross section through a four-stage fluidized bed decomposer.

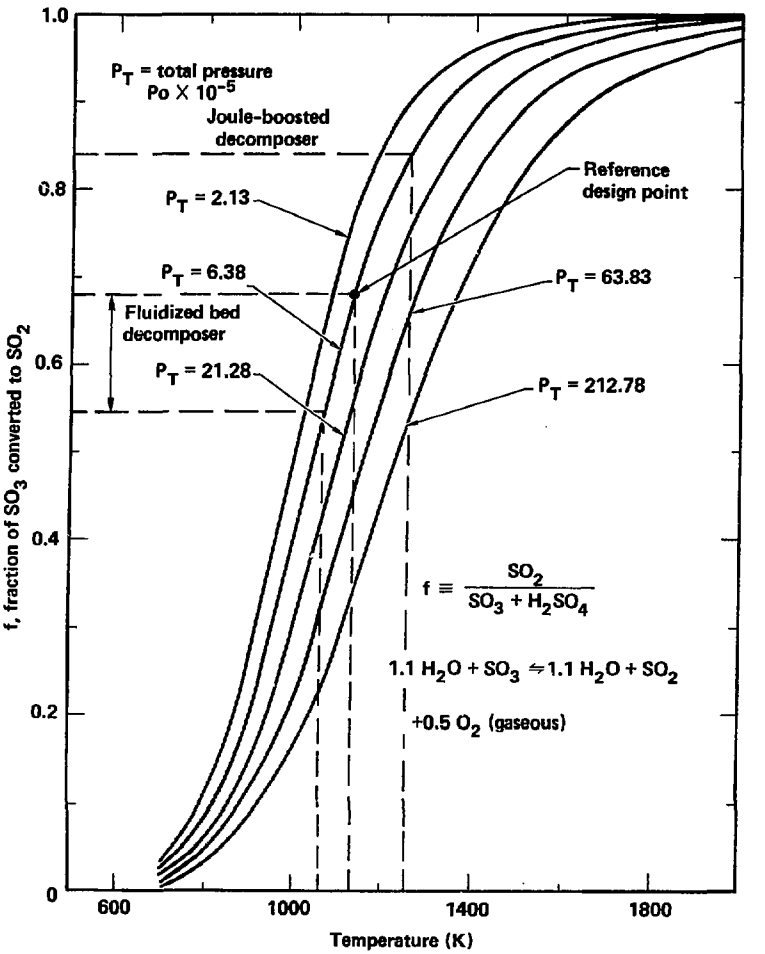

Fig. 8-5. Equilibrium curves for SO_3 decomposition.

The equilibrium for Reaction (3) in Fig. 8-1 lies to the right at temperatures above 1000 K, but catalysts are needed to attain sufficiently rapid decomposition rates below 1250 K. Numerous catalysts are available for this process. Considering cost vs effectiveness, we have chosen platinum as the catalyst for the staged, fluidized bed SO_3 decomposer used in this study.

The SO_3 decomposition reactor is a challenging unit to design, owing not only to the high temperatures required but also to the corrosive nature of the products involved. Reaction kinetics also strongly influence the design.

The overall details of the thermochemical process within which the SO_3 decomposer resides are found in Sections 4 and 5 of this volume, which discuss the thermochemical process and the thermochemical plant, respectively. In summary, the basic steps are as follows (see Fig. 8-2 for reference):

- Boiling the azeotrope. The 98 wt % azeotrope is boiled isothermally at about 7 atm and 690 K to obtain the gaseous feed for the decomposer. The gaseous species produced are H_2SO_4, SO_3, and H_2O.

- Preheating the gas. The gas from the boiler is preheated from 690 to 870 K (the temperature of the first isothermal stage of the four-stage decomposer). Molecular H_2SO_4 decomposes endothermically to SO_3 and H_2O during this preheat.

- Decomposition of SO_3. The gaseous feed from the preheater now contains SO_3 and H_2O. About 63% of the SO_3 is decomposed at 6.7 atm and 1100 K (the pressure and temperature of the last stage of the decomposer). An approximate 0.3-atm pressure drop has occurred across the decomposer stages, and SO_2 and O_2 have been formed as products.

- Cooldown of decomposition products. A recuperation is now used to cool the gaseous products from the decomposer to prevent back reaction. Energy recovered by the recuperator is then used to help preheat the incoming gases to the decomposer. See Section 6 of this volume for details.

8.3 PACKED-BED CHEMICAL REACTORS VS FLUIDIZED BED REACTORS

Without the use of catalysts, GA Technologies has shown (Ref. 1) that the conversion of SO_3 to SO_2 would only be 3% at 1050 K, and that another 200 K would be required to achieve 95% conversion efficiency at 1250 K. If it were feasible to operate at 1250 K, considering the problem of material strength, it would thus be possible to eliminate the use of catalysts. (For example, Refs. 2 and 3 discuss Joule-boosted decomposers that permit decomposition at 1250 K.) For this study we have elected not to use Joule-boosting but to use the temperature available from the high temperature stage of the TRW two-zone blanket. This temperature can be as high as 1200 K but not greater than about 1273 K. The heat transport medium is helium at 50 atm operating pressure. Considering film temperature drops, pinch points, and temperature losses across the duplex tubing that delivers the helium, we

have established the maximum temperature of the reactants in the last stage of the decomposer at 1100 K for the reference design. This temperaure can vary somewhat, as will be seen. As previously indicated, the first-stage temperature of the decomposer has been established at 870 K. The use of a catalyst is mandatory.

In a system such as this chemical reactor, two conditions must be provided:

1. Enough residence time and catalyst surface area so that reactions can go to equilibrium.

2. Sufficient heat to the reacting sites.

To obtain the required surface area, catalysts such as platinum are impregnated into porous, spherical, or other forms of particle substrates such as titania. The size of these impregnated particles may range from hundreds of microns for fluidized bed systems to tens of millimeters for packed bed systems. In either case there is a volume of particles within which the heat transfer tubes are placed. The SO_3 flows on the shell side of this chemical reactor heat exchanger. Helium flowing in the tubes provides the requisite energy to make the decomposition process proceed.

Two general classes of chemical reactors can be considered for this application: packed beds and fluidized beds. Our analysis of a packed bed reactor has shown that it is not feasible because of extremely large temperature gradients at the tube wall on the reactor side. Large temperature gradients also exist within the packed bed between adjacent tubes. If high flow velocities are used to partially offset the large temperature gradients, high pressure drops result.

Alternatively, the fluidized bed reactor is intrinsically isothermal within the volume of the particle bed, with an effective thermal conduct up to 100 times that of silver. This high rate of heat transport is due to the circulation of the solids. Heat transfer coefficients between the particles and the tube wall are also reasonably high either because the circulating particles scour the boundary layer or because of some other phenomena that enhance the heat transfer. The multi-staged fluidized bed is our design choice.

8.4 GENERAL DESCRIPTION OF A FLUIDIZED BED

For a complete treatment of fluidized beds, see Ref. 4. Fluidization is the operation by which fine solids are transformed into a fluid-like state through contact with a gas flowing upward through the volume of particles. The gas in this case is a mixture of SO_3, O_2, SO_2, and H_2O.

At low flow velocities the gas percolates through the void spaces between stationary particles. This is a fixed or packed bed. As the flow velocity is increased, a point is reached where the particles are all suspended in the upward-flowing gas. The bed is considered to be just fluidized and the velocity at which this occurs is called the minimum fluidization velocity, U_{mf}.

If the gas velocity is increased above U_{mf}, gas bubbles form and flow upward through the bed. The particles also move about in the bed propelled by the bubble motion.

With a further increase in velocity, the gas entrains the solids and they are carried out of the bed. This velocity is the terminal velocity, U_t.

The operational gas flow rate, U_o, in a fluidized bed is limited in its least value by U_{mf} and in its maximum value by the entrainment of solids.

8.4.1 Minimum Fluidization Velocity

The minimum fluidization velocity[4] may be obtained from the following equations:

for small particles,

$$U_{mf} = \frac{d_p^2 (\rho_s - \rho_g) g}{1650\ \mu} \qquad Re < 20 \ ;$$

for large particles,

$$U_{mf}^2 = \frac{d_p (\rho_s - \rho_g) g}{24.5\ \rho_g} \qquad Re > 1000 \ .$$

8.4.2 Terminal Particle Velocity

The upper limit to gas flow is approximated by the terminal, or free-fall, velocity of the particles.[4] There are three analytic expressions for this velocity as a function of the particle's Reynolds number $\left(Re_p = \frac{d_p U_t \rho_g}{\mu}\right)$:

$$U_t = \frac{g(\rho_s - \rho_g) d_p^2}{18\ \mu} \qquad Re < 0.4 \ ,$$

$$U_t = \left[\frac{4(\rho_s - \rho_g)^2 g^2}{225\ \rho_g \mu}\right]^{1/3} d_p \qquad 0.4 < Re < 500 \ ,$$

$$U_t = \left[\frac{3.1 g(\rho_s - \rho_g) d_p}{\rho_g}\right]^{1/2} \qquad 500 < Re < 200{,}000 \ .$$

8.4.3 Pressure Drop in Fluidized Beds

The pressure drop through packed beds of uniformly sized particles has been correlated by Ergun[5] using the equation

$$\frac{\Delta p}{L} = 150 \frac{(1 - \varepsilon_{mf})^2}{\varepsilon_{mf}^3} \times \frac{\mu U_o}{(\phi_s d_p)^2} + 1.75 \left(\frac{1 - \phi_{mf}}{\varepsilon_{mf}^3}\right)\left(\frac{\rho_g U_o^2}{\phi_s d_p}\right) \ .$$

Here the maximum value of Δp is slightly higher than the static pressure of the bed, as shown in Fig. 8-6. With a further increase in velocity the voidage suddenly increases, resulting in a decrease in pressure drop to the static pressure of the bed. Despite further increases in gas flow, the pressure drop remains essentially constant until entrainment begins. For this range of velocities the pressure drop is given by the equation

$$\frac{\Delta p}{L_{mf}} = (1 - \varepsilon_{mf})(\rho_s - \rho_g)g \quad ,$$

where $L_{mf} \equiv$ bed height at onset of fluidization. The range of velocity or the ratio of U_t/U_{mf} usually lies between 10:1 and 90:1, depending on the particle's Reynolds number. For our design procedure we calculate both the minimum fluidization velocity and the terminal velocity and then select some multiple of U_{mf} to determine U_o, the operating velocity, which must, of course, be less than U_t by a safe margin. Note that these velocities are all based on what is called the "superficial velocity," or the velocity one would calculate for the given mass flow rate if there were no particles in the bed; i.e., $\varepsilon = 1.0$.

The following illustrates some of the more important design steps and results.

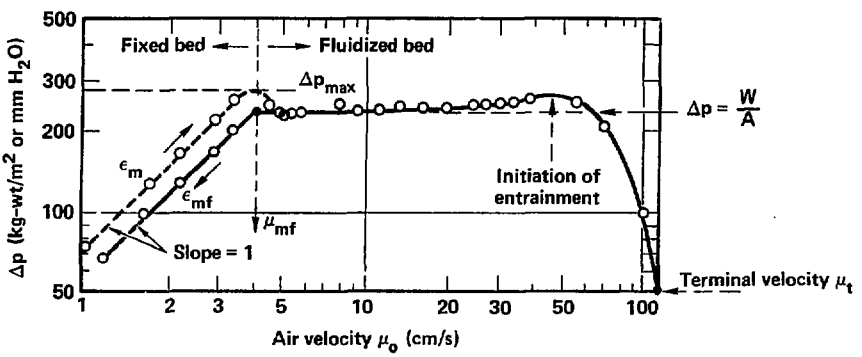

Fig. 8-6. Pressure drop vs gas velocity for a bed of uniformly sized sand particles.

8.5 PUMPING POWER REQUIREMENTS IN THE FLUIDIZED BED

Figure 8-7 illustrates the percentage of pumping power required on the SO_3 side of the fourth stage only of the decomposer as a function of catalyst particle diameter.

The strong influence of the particle diameter on the pumping power is due to the fact that although the volumetric flow rate (velocity x flow area) through the stage is constant as the velocity increases, the height of the bed H must also increase to maintain catalyst contact time. Figure 8-8

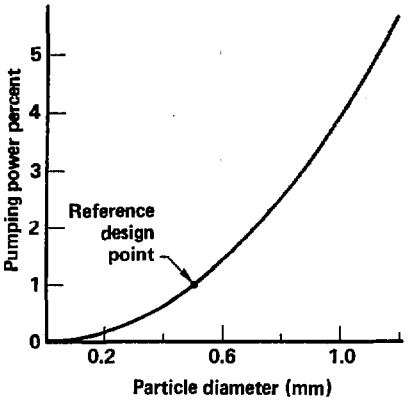

Fig. 8-7. Pumping power percentage as a function of bed particle diameter for the fourth stage of a four-stage SO_3 decomposer--SO_3 side only.

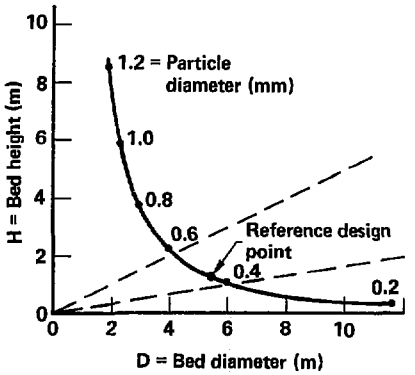

Fig. 8-8. Decomposer bed height/bed diameter relationships as a function of bed particle diameter.

illustrates this relationship for the range of particle sizes examined. The curve generated is hyperbolic, with small particles asymptotically producing large bed diameters D and short heights and large particles asymptotically producing large bed heights and small diameters. A range of particle sizes leading to a value of D between 2 H and 6 H is an implied choice, keeping reasonable pumping power limits in mind. For the reference case we selected a particle diameter of 0.5 mm for those particles in the fourth stage. This produces approximately a 1% pumping power requirement. This pumping power is somewhat high, but the choice is weighted by the need to have as high a heat transfer coefficient at the exterior wall of the tube as possible to minimize the material temperature of the tube wall, which is particularly critical in this last, highest temperature stage.

8.6 PUMPING POWER REQUIREMENTS FOR HELIUM FLOW

Figure 8-9 illustrates the percent of pumping power for the helium flow circuit as a function of surface heat flux using tubes of different inside diameters, e.g., 0.01 and 0.02 m. The data apply to the high temperature stage only. The total power handled by the nine operating decomposer units is approximately 940 MW for a 3500-MW (fusion) energy source delivering 3592 MW (thermal) and 153 MW (dc electricity) to the thermochemical plant. Thus, assuming equal energy partitioning, the last high temperature stage of any one decomposer unit handles 26 MW and the percentages in the figure are based on that value. It is not unreasonable to figure that these pumping power percentages for the last stage could be one or two percent or even higher. The reason is that in this high temperature area we are willing to pay for the higher pumping power to achieve low film temperature drops in the helium. We are also willing to accept low values of average heat flux to get the maximum material temperature down to a value that is as low as possible. This concern about material temperature is not necessary in the prior stages, and in those stages we would design for higher surface heat flux and lower pumping power.

Figure 8-10 shows how the maximum material temperature varies with both tube diameter and surface heat flux. We have selected 1200 K as a maximum material temperature. On this basis, surface heat fluxes of 2 to 3 W/cm^2 are possible using tubes with an inside diameter of 0.01 m. These are thick-walled duplex tubes and, as we will show, the stresses in the tubes are approximately 12 MPa. The 100,000-hour 1% creep stress for alloys that we can consider for this application ranges from 25 to 28 MPa at 1200 K. The strength falls off rapidly with increasing material temperature.

8.7 VOLUME REQUIREMENTS OF HELIUM COOLANT TUBES

Figure 8-11 depicts the percentage of the last stage volume occupied by the helium coolant tubes. This reinforces the selection of the small diameter tube and the average surface heat flux between 2 and 3 W/cm^2. The smaller tubes yield the lesser volume because

$$Q/\text{flux} = \pi \times \text{dia} \times \text{length} \times \text{no. tubes}$$

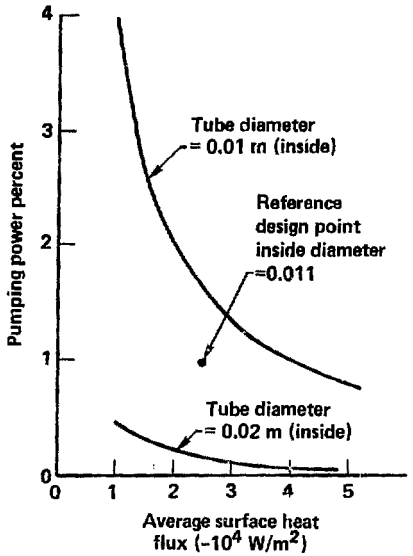

Fig. 8-9. Pumping power for helium flow as a function of surface heat flux.

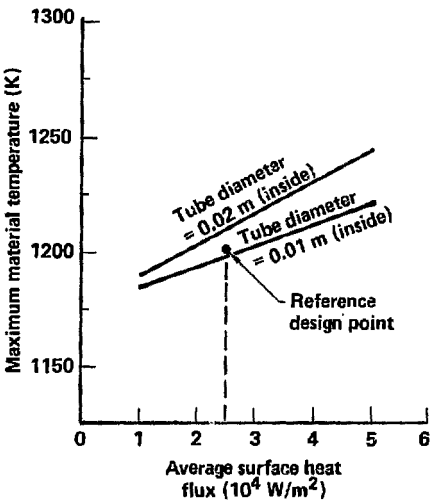

Fig. 8-10. Material temperature as a function of tube diameter and surface heat flux.

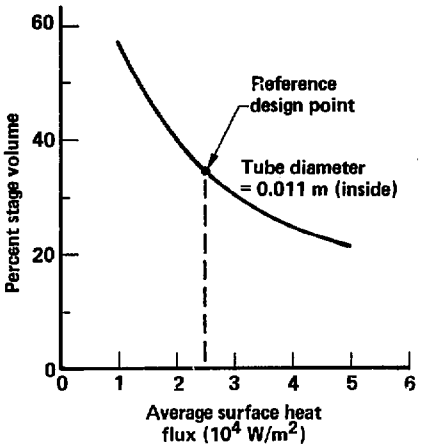

Fig. 8-11. Volume of the last stage of the decomposer unit occupied by coolant tubes.

and

$$\text{tube vol} = \pi \times (\text{dia})^2 \times \text{length} \times \text{no. tubes}.$$

Smaller tube volumes produce smaller total bed volumes and hence should be more cost effective.

8.8 STRUCTURAL MATERIALS FOR THE DECOMPOSER

In designing this decomposer as a structural unit, we assumed that the outer container of the decomposer can be an internally insulated, quasi-adiabatic shell with a relatively cool outer wall to support pressure stresses of about 7 atm because of the flowing SO_3 that is being decomposed. This type of pressure vessel is not considered to be a difficult design problem.

The tubes, on the other hand, present the following three difficult problems:

1. In the fourth (last) stage of the decomposer, tube temperatures are as high as 1200 K and the total differential pressure across the tube wall is a minimum of approximately 43 atm. Actual operating stresses will not be significantly high by ordinary standards but the allowable 100,000-hour, 1% creep strength at 1200 K is only approximately 25 to 28 MPa.

2. The SO_3 environment is corrosive and only certain metal alloys--those containing a high fraction of chrome--can be considered. The ceramic SiC has high strength at these elevated temperatures and excellent corrosion resistance, but its lack of ductility is a serious shortcoming at this stage of development. Therefore, we are deferring its use at this time.

3. The need for very tight control of the amount of tritium allowed in the hydrogen product (our criterion is 1×10^{-6} ppm) requires that duplex tubing be used with a helium purge gas in the gap between the tubes. The gap can be infinitesimal and the co-extrusion of tubes is state of the art. Nevertheless, the production of large quantities of these duplex tubes, particularly if bends are required, adds to the overall design complexity.

8.8.1 Candidate Materials

In regard to the strengths of the high temperature metal alloys considered suitable from a corrosion standpoint for the SO_3 decomposer, the creep rupture values can be summarized in equation form as follows:

Incoloy-802: $\ln \sigma = -6.3829 - 0.33874 \ln t + 1.4871\ 10^4/T$,

Waspaloy: $\ln \sigma = -3.9271 - 0.15750 \ln t + 1.1066\ 10^4/T$,

Udimet-500: $\ln \sigma = -6.0216 - 0.20110 \ln t + 1.4129\ 10^4/T$,

Udimet-710: $\ln \sigma = -4.3450 - 0.25028 \ln t + 1.2960\ 10^4/T$,

where

σ = stress (MPa),

t = time (hours),

T = temperature (Kelvin).

For the Incoloy-802, the 1% creep strength may be taken as 0.69 times the creep-rupture value and the 0.2% creep strength as 0.40 times the creep-rupture value. For the other three alloys, 0.8 times the creep rupture for the 1% creep strength and 0.65 times the creep rupture for the 0.2% creep strength are recommended. The reason that the Incoloy-802 is different from the other alloys is that it is a carbide-dispersion-strengthened alloy, while the others are a combination of gamma- and solution-strengthened alloys.

The results calculated using the four preceding creep rupture equations and the factors for 1 and 0.2% creep are given in Table 8-1 at 1200 K and 100,000 hours.

Table 8-1. Creep strengths of four alloys considered for the decomposer. Values are determined at 1200 K and 100,000 hours.

	Creep strength (MPa)		
	Creep rupture	1% creep	0.2% creep
Incoloy-802	8.2	5.7	3.3
Waspaloy	32.5	26.0	21.1
Udimet-500	21.1	24.9	20.2
Udimet-710	35.6	28.5	23.2

These data, with the exception of the Incoloy-802, involve an extrapolation in time. The creep data are extrapolated from 10,000 hours for the Waspaloy and 1000 hours for the other two. The creep data for these four alloys, as summarized by the Orr-Sherby-Dorn method, are plotted in Figs. 8-12 through 8-15.

Our design choice for this study is the Waspaloy.

8.8.2 Fabrication of the Waspaloy into Tubing

The Waspaloy is produced in sheet form by Universal-Cyclops and by Special Metals Company. It has been successfully fabricated into tube shapes by LeFiell Mfg. Co., Santa Fe Springs, CA. The sheet is first TIG-welded into tubes and then drawn down, reducing wall thicknesses in the process from 80 mils to 20 or 30 mils. At this point the weld is almost invisible, according to the manufacturer. It is likely that the material will require aging and heat treatment. The Waspaloy is considered to be resistant to hot corrosion with or without an aluminide coating.

8.8.3 Comparison of Heat Transfer Coefficients--Horizontal Tubes vs Vertical Tubes

The literature contains a wealth of material dealing with correlation equations that may be used to determine heat transfer coefficients between bundles of horizontal or vertical tubes and a gas-solid fluidized bed. (See, for example, Ref. 6, which cites 65 references to the subject.)

A review of some of this literature shows that horizontal tubes can, and generally do, produce higher heat transfer coefficients than vertical tubes. The probable reasons for this are that the vertical tubes may induce gas streaming around the tube and diminish particle-to-wall heat transfer, while

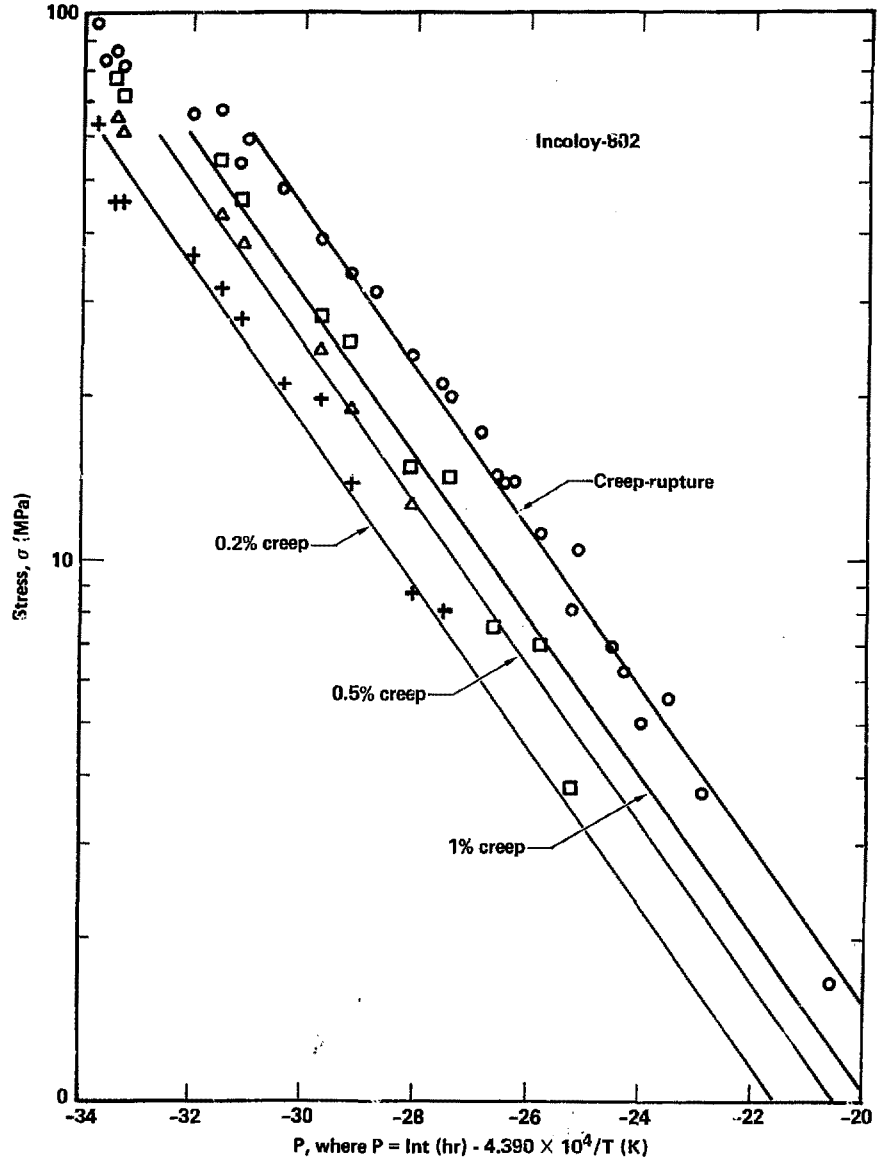

Fig. 8-12. Incoloy-802 creep rupture data.

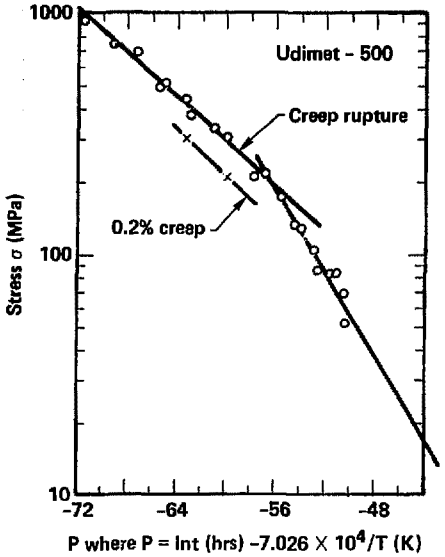

Fig. 8-13. Udimet-500 creep rupture data.

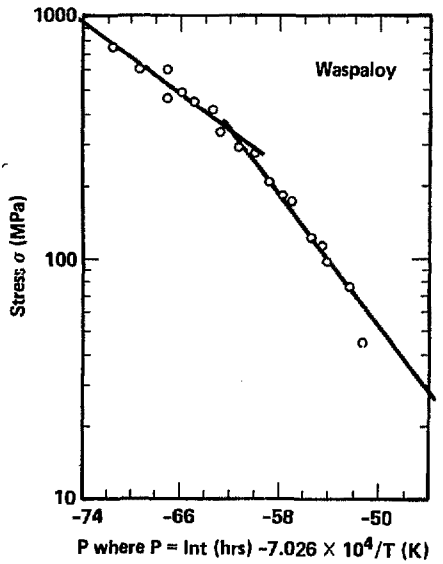

Fig. 8-14. Waspaloy creep rupture data.

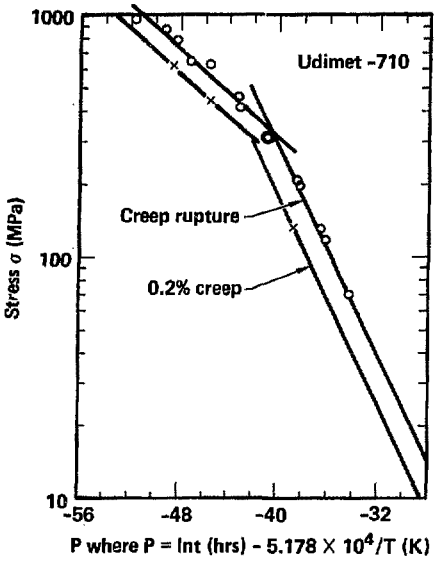

Fig. 8-15. Udimet-710 creep rupture data.

the horizontal tubes would encourage particle-to-wall interaction and at the same time buffet the particles around, causing a greater angular distribution.

Two correlation equations are representative. The first is the Vreedenberg equation (Ref. 7) for horizontal tubes, in which

$$\frac{hd}{k} = 0.66 \left(\frac{C_{pg}}{k_g}\right)^{0.3} \left[\left(\frac{d_t \rho_g U_o}{\mu}\right)\left(\frac{\rho_s}{\rho_g}\right)\left(\frac{1-\varepsilon_F}{\varepsilon_F}\right)\right]^{0.44} \quad \text{(Ref. 4)}$$

for

$$\frac{d_t \rho_p U_o}{\mu} < 2000 \ .$$

The second was developed for vertical tubes by Wender and Cooper (Ref. 8) who correlated data and experimental findings from a number of investigators to get

$$\frac{h_w d_p}{k_g} = 0.01844 \ C_R (1-\varepsilon_f)\left(\frac{C_{pg}\rho_g}{k_g}\right)^{0.43}\left(\frac{d_p \rho_g U_o}{\mu}\right)^{0.23}\left(\frac{C_{ps}}{C_{pg}}\right)^{0.8}\left(\frac{\rho_s}{\rho_g}\right)^{0.66} ,$$

for

$$\frac{d_p \rho_g U_o}{\mu} = 10^{-2} - 10^{2} \quad .$$

Notice that for the horizontal tubes the particle size is not a part of the equation but that tube diameter is instrumental in determining the film coefficient. Conversely, for the vertical tubes the tube diameter is not part of the equation and the film coefficient is determined by particle diameter. Also, for vertical tubes the quantity $(C_{pg}\rho_g/k_g)$ is not dimensionless but has units of s/m^2. Figure 8-16 compares film coefficients for horizontal and vertical tubes using these two equations. For the SO_3 decomposer we have elected to use horizontal tubes because of their superior film coefficient and because horizontal tubes give us another degree of control in establishing h. That is, h is a function of tube diameter for horizontal tubes. The design point is indicated in Fig. 8-16.

8.9 STAGING THE DECOMPOSER

From the helium side of the SO_3 decomposer it seems evident that the use of multiple stages is a thermal-hydraulic necessity. Consider, for example, a single-stage decomposer operating at some temperature T on the SO_3 side that provides some reasonable level of SO_3-to-SO_2 conversion efficiency. In our case this temperature would be 1100 K. Practically, the helium delivery temperature can be no higher than 1200 K or perhaps 1250 K. Materials and their creep strength and corrosion resistance establish this upper limit. The helium exit temperature can be no less than the 1100 K, SO_3 temperature plus some allowance for the ΔT at the pinch point, say 50 K. The single-stage system is thus constrained to have a helium bulk temperature change as small as 50 K and not more than 100 K. This temperature gradient establishes the mass flow rate of the helium. This mass flow rate is inversely proportional to the number of stages in the decomposer. The pressure drop is inversely proportional to the square of the number of stages, and the pumping power is an inverse cubic function.

In this study we have examined the mass and energy balance and flow rates for three different cases of staged decomposers:

1. A single-stage model wherein the decomposition temperature is taken to be 1100 K.

2. A two-stage model with decomposition energy equally partitioned between two isothermal stages of 1100 and 955 K.

3. A four-stage model with four isothermal stages of 1100, 1025, 950, and 870 K, also equally energy-partitioned.

As indicated, single-stage systems or even two-stage systems appear to have no utility for our particular application. Our design choice is a four-stage decomposer. The data that brought us to this conclusion are presented for all three models in Fig. 8-17. In Fig. 8-17a, if a reasonable helium temperature drop is chosen to provide the necessary energy for

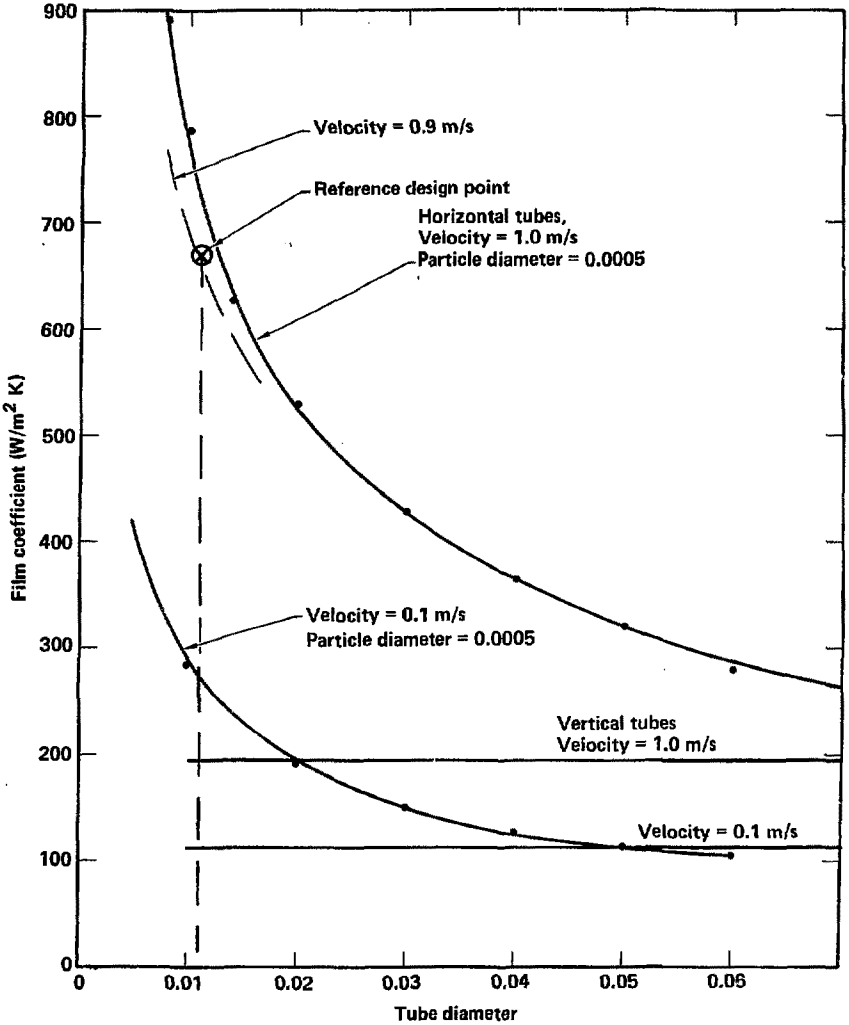

Fig. 8-16. Comparison of film coefficient of heat transfer, h, for horizontal and vertical tubes in the fluidized bed. For the horizontal tubes we use the Vreedenberg[7] correlation for $R_e < 2000$. For the vertical tubes we use Wender and Cooper's,[8] correlation for $10^{-2} < R_e < 10^2$.

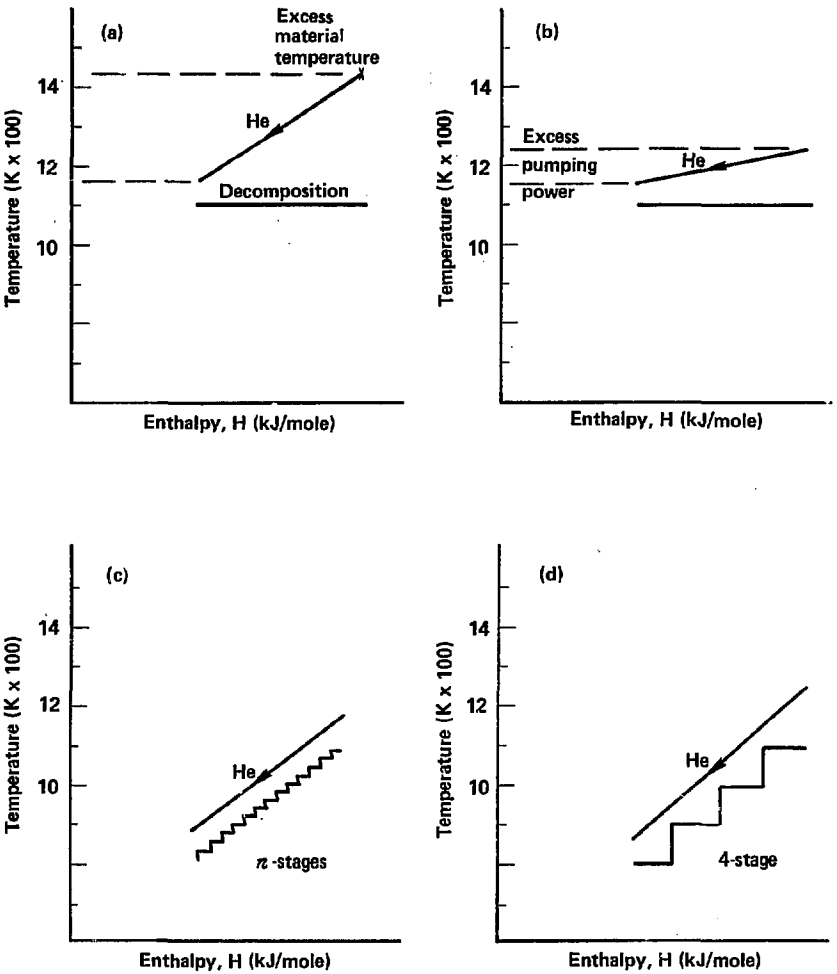

Fig. 8-17. Comparison of single-stage, four-stage and n-stage decomposers relative to temperature, pump power and load matching.

decomposition, then the resulting material temperatures become unreasonably high. On the other hand, as suggested in Fig. 8-17b, if the slope of the helium temperature gradient is decreased to accommodate the material creep strength, then the consequent increased mass flow rate of the helium leads to intolerable pressure drops and pumping powers. The benefit of having multiple stages becomes obvious in Fig. 8-17c. For successively larger numbers of stages, load lines can match and parallel supply lines, and pressure drops can be optimized against material temperatures. However, there is an economic limit on the number of possible stages. Figure 8-17d shows the four-stage decomposer, which we assume to be a practical, economic choice.

8.9.1 Process Mass and Energy Balance

This section explains the methods used for calculating the mass and energy balances for the sulfuric acid decomposition phase of GA Technologies' thermochemical hydrogen production cycle. The main purpose of these calculations is to estimate heat loads and temperature requirements for sulfuric acid decomposition and to determine those process conditions and resulting heat loads that will thermally match the TMR heat source.

This process step is the decomposition of sulfuric acid to form SO_2 and O_2. The feed acid vapor is produced by the azeotropic boiling of an acid-water mixture at 690 K and 7 atm. The highest allowable process temperature is 1100 K for this design case. Heat for the process is to be derived from a stream of hot helium at 1220 K and 50 atm (see Figs. 8-1 and 8-2). For these calculations, all flows are referenced to 1 g mole of SO_2 production, which will allow this portion of the process to be scaled by multiplying the flows and heat loads by the desired molar rate of SO_2 (or equally, the H_2 production rate in kg/s). We considered three cases as illustrated in Figs. 8-18 through 8-21: Case I used one chemical reactor stage, Case II used a two-stage reactor, and Case III used four reactors.

8.9.2 Stream Compositions

We calculated the stream compositions using the conventional thermodynamic relations for the two chemical reactions involved in this process. The first reaction is the decomposition of the sulfuric acid to sulfur trioxide and water, thus

$$H_2SO_4 \rightleftharpoons SO_3 + H_2O.$$

The second reaction is the decomposition of the sulfur trioxide to sulfur dioxide and oxygen, thus

$$SO_3 \rightleftharpoons SO_2 + 1/2\ O_2.$$

The mathematical expressions which model the chemical equilibrium for these two reactions are

$$k_1 = \frac{\left(P_{SO_3}\right)\left(P_{H_2O}\right)}{\left(P_{H_2SO_4}\right)}$$

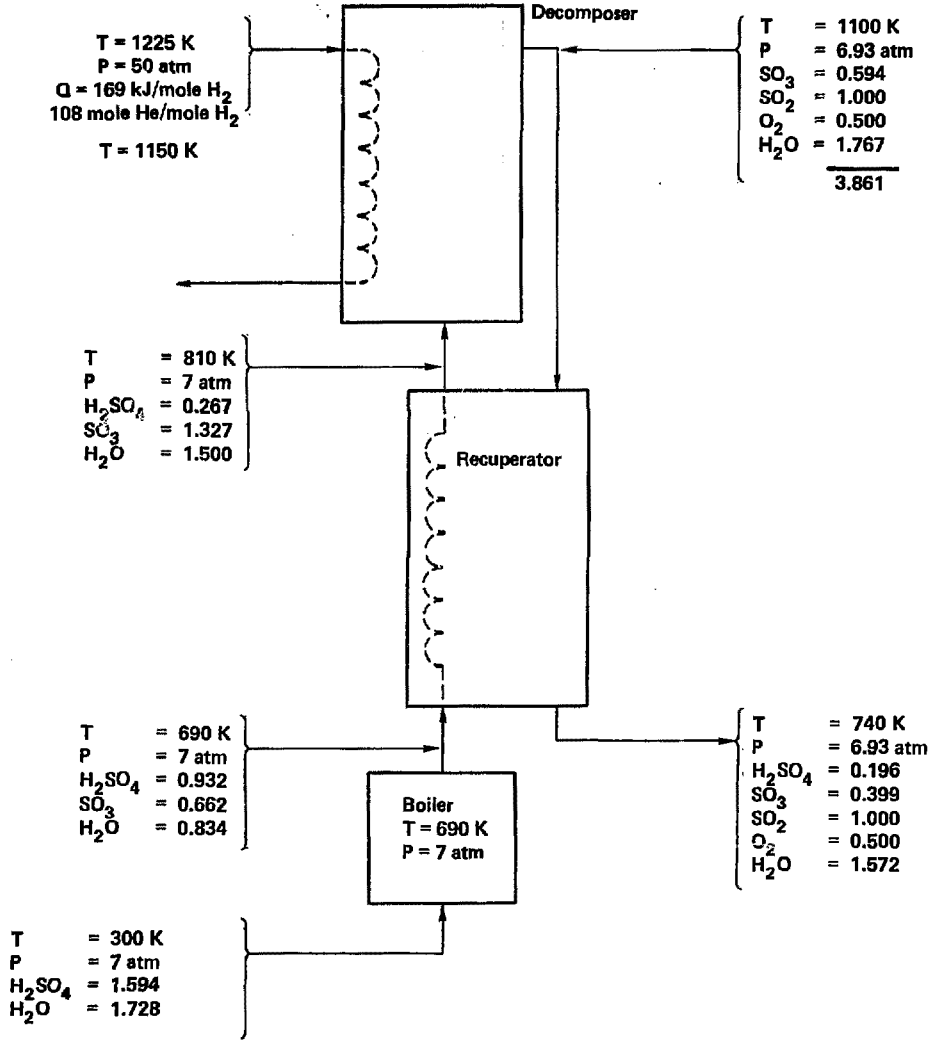

Fig. 8-18. Case I - Single-stage fluidized-bed decomposer.

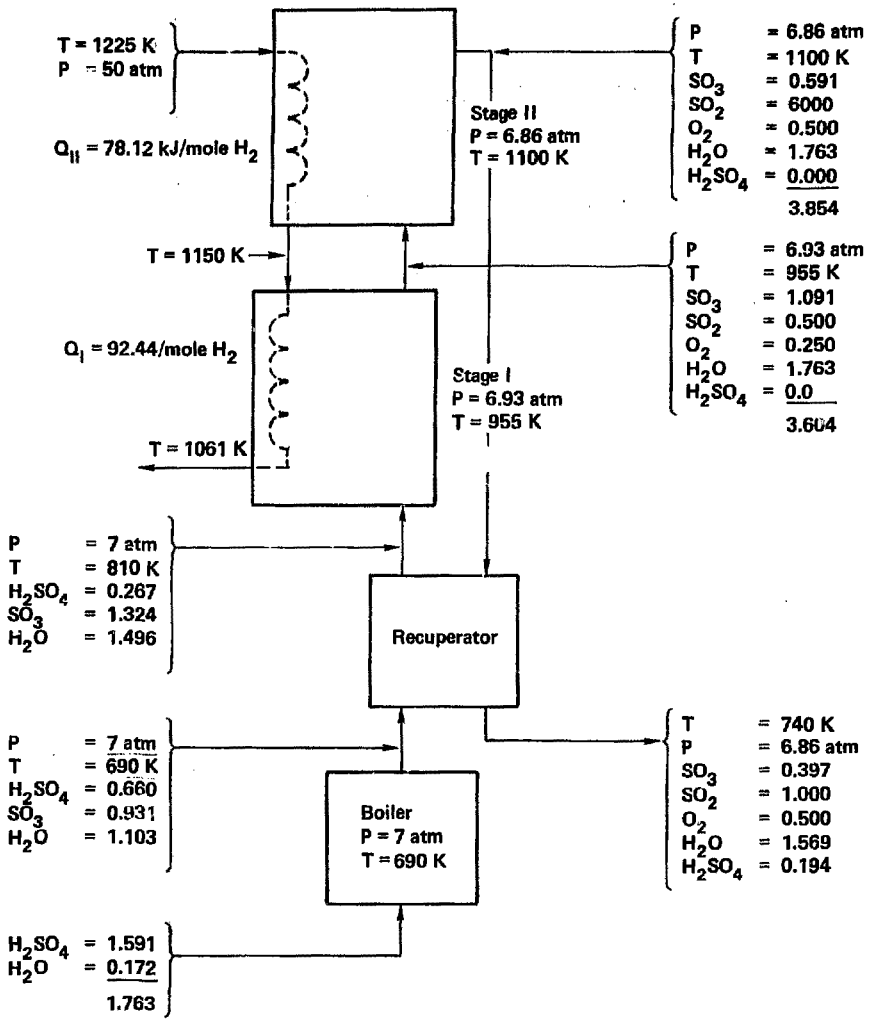

Fig. 8-19. Case II - Two-stage fluidized bed-decomposer.

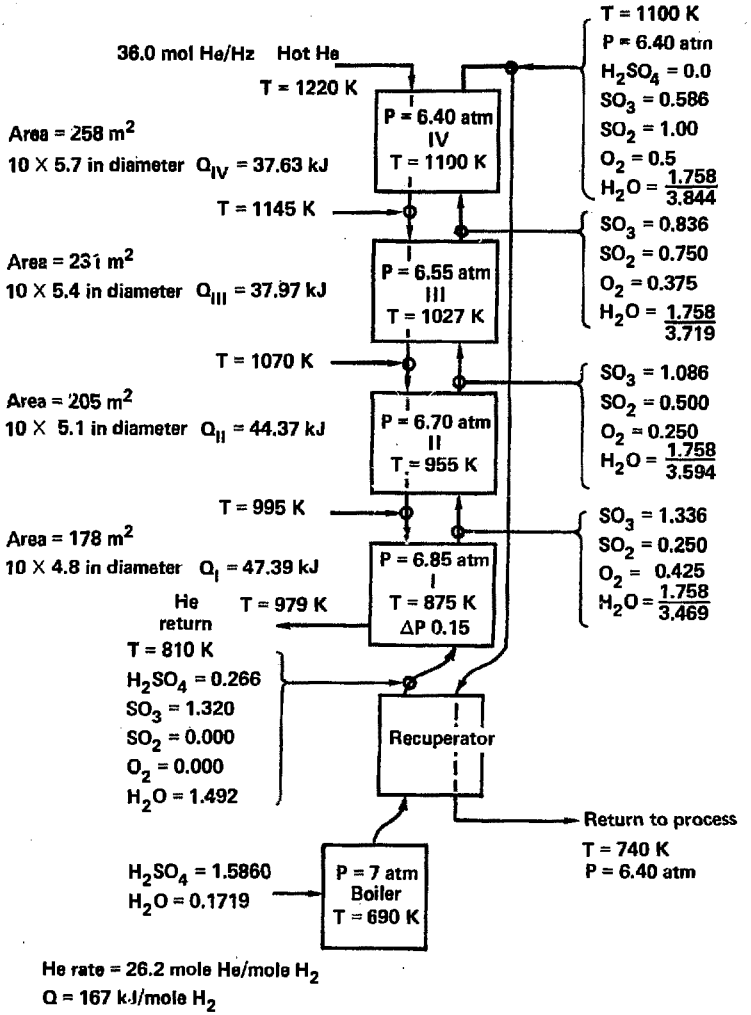

Fig. 8-20. Case III - Four-stage fluidized-bed decomposer.

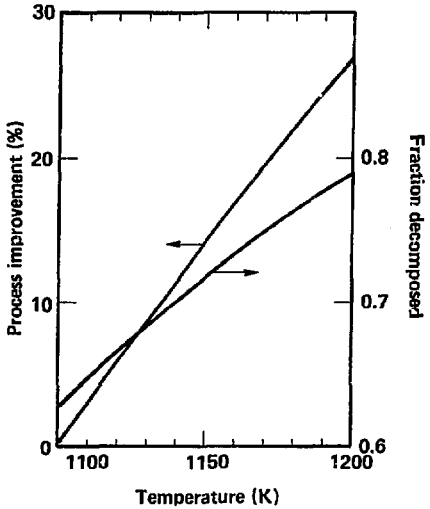

Fig. 8-21. Process improvement with final stage decomposer temperature.

for the first reaction, and

$$k_2 = \frac{\left(P_{SO_2}\right)\left(P_{O_2}\right)^{1/2}}{\left(P_{SO_3}\right)}$$

for the second reaction. Equilibrium constants k_1 and k_2 are a function of temperature and can be calculated using data from the JANAF tables.[9] The various subscripted Ps are the partial pressures of species present. These equations are solved by assuming that the partial pressure of each species is equal to the total pressure multiplied by its mole fraction. If N_o is the initial number of moles of sulfuric acid present, N_w the initial number of moles of water present, N_1 the moles reacted by the first reaction, and N_2 the moles reacted by the second reaction, then

$$k_1 = P \frac{N_1 - N_2 \; N_w - N_1}{N_o - N_1 \; N_w + N_o + N_1 + \frac{N_2}{2}}$$

and

$$k_2 = P^{1/2} \frac{\left(N_2\right)\left(\frac{N_2}{2}\right)^{1/2}}{N_1 - N_2\, N_w + N_o + N_1 + \frac{N_2}{2}^{1/2}} ,$$

where P is the total pressure. To calculate the exact composition of the process streams, it is necessary to solve these two equations simultaneously for N_1 and N_2; however, the first equation is quadratic in N_1 and the second is cubic in N_2, which makes such a solution difficult.

A good approximate solution to these equations is obtained by a simplifying assumption. At temperatures where the first reaction makes significant changes in the stream composition, the second reaction has almost no effect. And, conversely, at temperatures where the second reaction is changing the stream composition, the first reaction is essentially complete. Thus, in calculating stream compositions at lower temperatures, one solves the first equation for N_1 by setting $N_2 = 0$. At higher temperatures, N_1 is set equal to N_o and the second equation is solved for N_2. From N_1 and N_2 the stream composition is given by the relations

- moles H_2O = $N_w + N_1$,
- moles H_2SO_4 = $N_o - N_1$,
- moles SO_3 = $N_1 - N_2$,
- moles SO_2 = N_2 ,
- moles O_2 = $N_2/2$.

8.9.3 Stage Temperature Calculations

For Cases II and III it is necessary to estimate the isothermal temperatures of the reactor stages, other than the last stage, which is set at 1100 K so that helium temperature drops and heat transfer area requirements can be estimated. For Cases II and III we assumed the reaction to be equally divided among the stages. This assumption sets N_2 for each stage and by using the relationship for the second reaction, this fixes the value for k_2. Finally, the JANAF tables can help determine the stage temperature.[9]

8.9.4 Stream Enthalpies

We calculated the stream enthalpies from the stream compositions and enthalpy data given in the JANAF tables.[9] Zero enthalpy was based on the feed stream at 273 K. The enthalpy of a given stream was then calculated as the enthalpy required to heat the feed stream to the temperature in question plus the enthalpy required to react the stream to the desired composition.

8.9.5 Process Improvement and Optimization

For our initial studies, we examined the possibility of using a multiple-stage sulfuric acid decomposer. We found that as the number of stages increased, the required helium flow rate was reduced. In fact, each time the number of stages doubled, the helium rate was cut in half. This was an important finding because of the pressure drop and pumping power relationships to the helium mass flow rate.

The multiple staging of the acid decomposer is just one of several possible process design techniques that lead to an economic and efficient process. A modification of this process would involve raising the temperature of the final decomposer stage. This modification can be done in two ways and for future design studies we may wish to use both. The first way is to develop better high temperature materials, particularly the ceramics. Obviously, as stronger and more corrosion-resistant alloys and ceramics become available, the temperature of the final stage will not be as limited by the choice of available materials.

The second way is to do a more tailored fitting of energy load lines to supply lines in the final-stage region. Consider a simple example where, at our reference 1100 K stage, an additional "half-step" stage is used as illustrated in Fig. 8-22. For the half step we have retained the slope of the helium line and the pinch point criteria, and have fit in an additional isothermal stage at 1135 K without changing the maximum material temperatures. The material temperature does not change because it is determined by $T_{mat'l} = (T_{He,\,max} - \Delta T_{film,\,He})$.

At 1135 K we see from Fig. 8-5 that the conversion efficiency would increase to 69% from 63% at 1100 K, a 10% improvement. If a further "quarter step" could then be added and ~1156 K reached, one would expect a nearly 21% improvement in conversion efficiency over the 1100 K level. These improvements represent a direct reduction in the size of the equipment used in the SO_3-SO_2 process stream because of less recycle. At this time, it appears that a better temperature distribution would use smaller temperature steps as the temperature increases.

Another possible process improvement involves routing the process streams. If reversal of the decomposition reaction can be avoided, the decomposed acid stream from the last stage could be routed through heat exchanger tubes of the previous decomposition stages to help provide the high temperature heat requirement. This change would not reduce the total heat requirement because heat transferred to the decomposer stages would have to be made up at lower temperatures with the reduced recuperator performance.

8.10 ILLUSTRATIVE PARAMETERS FOR THE REFERENCE DESIGN CASE

Figure 8-23 is a computer printout of the parameters for the SO_3 decomposer heat exchanger.

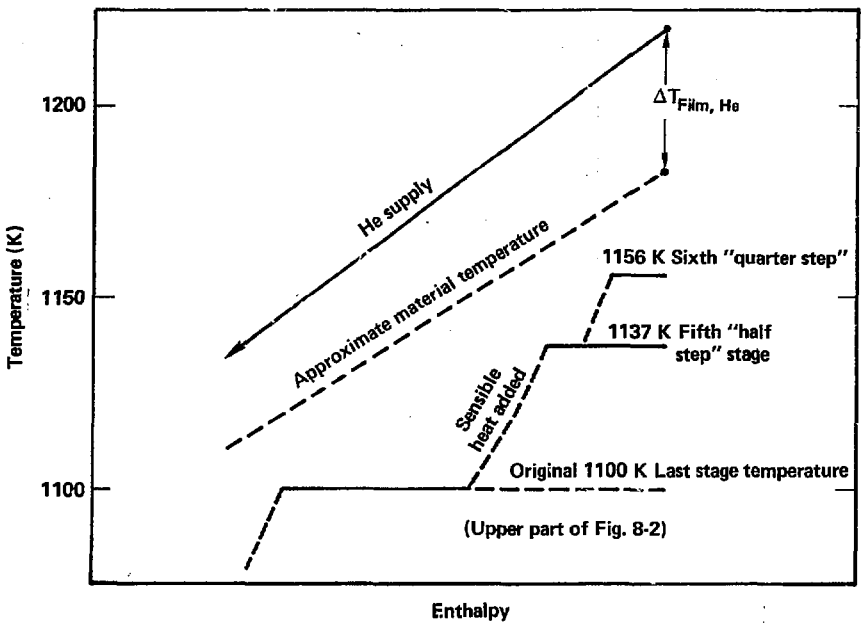

Fig. 8-22. "Half step" staging.

SO3 DECOMPOSER HEAT EXCHANGER----------
THERMAL HYDRAULIC DESIGN

OVERALL DESIGN PARAMETERS----------

NUMBER OF DECOMPOSER UNITS	9
NUMBER OF STAGES PER UNIT	4
HYDROGEN PRODUCTION RATE	5478 MOLS/S
DECOMPOSITION ENTHALPY REQD	171 KJ/MOL OF H2
ENERGY PARTITION PER STAGE=	EQUIPARTITIONED
ENERGY PER DECOMPOSER UNIT=	1.04082E+08 WATTS

TUBE SIDE (HELIUM COOLANT)

PRESSURE OF THE HELIUM	50 ATM
HELIUM PRESS IN SAP	28.5 ATM
FLOW RATE PER UNIT	66.7192 KG/S
IN. TEMP LAST STAGE	1220 K
OUTLET TEMP LAST STAGE	1145 K
NUMBER OF TUBES	10000
OD OF TUBES	.01584 M
ID OF TUBES	.011 M
FLOW VELOCITY	34.0544 M/S
REYNOLDS NUMBER	19306.7
NUSSULT NUMBER	54.1038
FILM COEFFICIENT	1475.56 W/M2-K
FRICTION FACTOR	5.97485E-03
PRESSURE DROP	2597.24 PA/M
PRESSURE DROP IN ATM	.0256257 ATM
HELIUM PUMP POWER	.253159 MW/4TH STAGE
PUMP POWER % OF STAGE PWR	.972923 %

DECOMPOSER SIDE (SO3)----------

NOMINAL SO3 PRESSURE	7 ATM
DIA. OF BED PARTICLES	5E-04 M
DENSITY OF PARTICLES	3000 KG/M3
FLUIDIZATION VELOCITY, UMF	.111201 M/S
EXCAPE VELOCITY, UT	1.97604 M/S
FLOW VELOCITY, UO	.889611 M/S
RESIDENCE TIME	.5 S
NU NO. FOR HORIZONTAL TUBES	188.544
FILM COEFFICIENT,H	952.24 W/M2-K
PRESSURE DROP, SO3 SIDE	7009.97 PA
PRESSURE DROP, SO3 SIDE, ATM	.0691639 ATM
PUMPING POWER	.109188 MW/4TH STAGE
PUMPING PWR % OF STAGE POWER	.419625 %

Fig. 8-23. Parameters for SO_3 decomposer heat exchanger.

SIZING THE DECOMPOSER----------

SO3 FLOW AREA	17.509 M2
DECOMPOSER DIAMETER	4.72156 M
DECOMP STAGE HT., W/O TUBES	.635436 M
DECOMP STAGE HT., WITH TUBES	.974415 M

VOL.FRACTION OF TUBES IN STAGE	.34788
SURFACE AREA OF TUBES	1040.82 M2
OVERALL HEAT TRANSFER COEFF.	665.259 W/M2-K
FILM TEMP DROP, HELIUM	16.9427 K
FILM TEMP DROP, SO3	18.2319 K
INNER WALL TEMP DROP	.714286 K
OUTER WALL TEMP DROP	.714286 K
HELIUM GAP TEMP DROP	.694444 K
TOTAL TEMPERATURE DROP	37.2976 K
TOTAL TEMP DROP CHECK	37.5794 K
AVERAGE SURFACE HEAT FLUX	25000 W/M2
EXCESS DELTA T AT PINCH PT.	7.42066 K
MAXIMUM MATERIAL TEMP.	1202.52 K

CALCULATION OF THE TUBE STRESSES ----------

OUTER TUBE, LONG	4.95247E+06 PA	718.374 PSI
OUTER TUBE, CIRCUM.	1.2084E+07 PA	1752.83 PSI
INNER TUBE, LONG	4.95248E+06 PA	718.376 PSI
INNER TUBE, CIRCUM.	1.20841E+07 PA	1752.84 PSI

THERMAL STRESS PA

TOTAL STRESS PA

ALLOW. 1%, 100,000 HR CREEP STRESS 25.5034 MPA

Fig. 23. (continued)

8.11 PLATINUM CATALYST REQUIREMENTS FOR THE DECOMPOSER

Figure 8-23 shows that the volume of the four decomposer stages is:

vol = 4 x (SO_3 flow area) x (stage height without tubes) x 10

= 4 x 17.509 x 0.635

= 444.7 m^3.

This assumes four equal-sized stages per unit and 10 units for the plant.

In this overall volume the fraction that is made up of the titania substrate within which the catalyst is impregnated is $(1-\epsilon)$, where ϵ is the void fraction. For our reference case the void fraction is 0.7.

The density of the titania is 4240 kg/m^3 as a solid. Because we require large amounts of surface area for the catalyst, we use approximately 0.75 x (solid density) or 3180 kg/m^3 (actually 3000 kg/m^3 is used for the computer calculations). The total amount of titania is 4.23 x 10^5 kg.

Based on data from GA Technologies,[1] we have assumed that the amount of platinum that will be required can be taken as 0.08% times the amount of the titania, or 338 kg of platinum.

The market price for platinum is about $16,000/kg, so that the material costs are $5.4 M. The labor costs may be $5 to 6 M. Overall, the cost of the platinum catalyst in place is estimated to be on the order of $10 M. This seems to be a very reasonable and low cost when considered in the context of a fusion/synfuel plant whose total cost may be $3000 or $4000 M. Furthermore, the costs should be recoverable since the platinum is not consumed.

8.12 STRESSES IN THICK-WALLED TUBING

We have made three assumptions in the calculation for tube stresses arising from the differential pressure between the helium flow and the SO_3:

1. Duplex tubing is used and the pressure in the infinitesimally small gap between the coaxial tubes can be set at any value desired. We used the average pressure between the helium and the SO_3, i.e., 28.5 atm in all the cases studied.

2. The thicknesses of the tube walls, t_i and t_o, are not equal but calculated so that the stresses in the inner and outer tube are equal.

3. The tubes, as assembled in the decomposer, are unrestrained, horizontally oriented, made in the form of a U, and supported at frequent intervals along the length of the U.

The equations used are the following[10] (see also Fig. 8-24):

$$\sigma_1 = \frac{qb^2}{a^2 - b^2} \quad ,$$

$$\sigma_2 = \frac{qb^2(a^2 + r^2)}{r^2(a^2 - b^2)} \qquad \max \sigma_2 = q\,\frac{a^2 + b^2}{a^2 - b^2} \quad \text{at } r = b \quad ,$$

$$\sigma_3 = \frac{-qb^2(a^2 - r^2)}{r^2(a^2 - b^2)} \qquad \max \sigma_3 = -q \quad \text{at } r = b \quad .$$

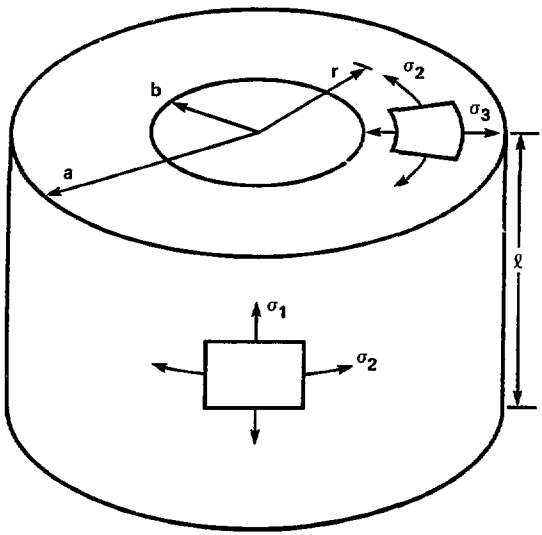

Fig. 8-24. Determining stresses in thick-walled tubing.

8.13 CONCLUSIONS

We believe that the multi-stage fluidized-bed SO_3 decomposer, as a chemical reactor, provides an excellent means for satisfying the high

temperature step of GA Technologies' thermochemical cycle. It provides several advantages:

- Ability to have a number of isothermal stages. Each stage can be incremented in temperature from the prior stage, permitting us to tailor the energy demand line to the energy supply line.

- Maximum calculated material temperatures of approximately 1200 K. These temperatures are in no way trivial, but stress levels, at the same time, are well below the 100,000-hour 1% creep by factors of two or three.

- Use of horizontal tubes for the helium flow. This provides very reasonable values of heat transfer coefficients on both the helium side and the SO_3 side. We typically obtained values greater than 1000 W/m^2-K.

- Estimated cost of $10 M for the platinum catalyst for the decomposer units. This figure appears to be quite reasonable.

- State-of-the-art decomposer vessel (the outer shell).

The use of duplex tubing for the helium flow is an accepted technology but it clearly increases cost and complexity. This area needs further study, particularly to determine if the use of duplex tubing can genuinely provide the control of tritium required.

To date we have focused our analytical attention on only the last, highest temperature stage based on the theory that if the last stage can be designed, the lower temperature stages will follow. The next level of development will be to do the more difficult, integrated analysis.

REFERENCES

1. J. Norman, GA Technologies, private communication.

2. R. L. Werner, O. H. Krikorian, F. L. Ribe et al., Conceptual Design Study FY1981, Synfuels from Fusion--Using the Tandem Mirror Reactor and a Thermochemical Cycle to Produce Hydrogen, Lawrence Livermore National Laboratory, Livermore, CA, UCRL-19311 (1982).

3. R. L. Werner, F. L. Ribe et al., Synfuels from Fusion--Using the Tandem Mirror Reactor and a Thermochemical Cycle to Produce Hydrogen, Lawrence Livermore National Laboratory, Livermore, CA, UCRL-19609 (1982).

4. Kunii and Levenspiel, Fluidization Engineering (John Wiley & Sons, New York, 1969).

5. S. Ergren, Chemical Engineering Progr., 48 and 89 (1952).

6. N. S. Grewal and S. C. Saxena, "Exp. Studies of Heat Transfer Between Bundles of Horizontal Tubes and a Gas-Solid Fluidized Bed," ASME 80-HI-119.

7. S.H.A. Vreedenberg, J. Appl. Chem 2, Suppl. 1, S26 (1952); Chem. Eng. Sci. 9 (52) (1958) and 11 (274) (1960).

8. L. Wender and G. T. Cooper, AICHE Journal 4 (15) (1958).

9. D. R. Stull and H. Prophet, JANAF Thermodynamic Tables, Second Edition, U. S. National Bureau of Standards, Washington, D.C. (1971), with supplements through December 31, 1979, from M. B. Chase, Project Director, The Dow Chemical Company, Midland, MI.

10. R. J. Roark and W. C. Young, Formulas for Stress and Strain (McGraw-Hill Book Company, New York, 1975).

9 Preliminary Cost Estimates

CONTENTS

9. Preliminary Cost Estimates

We have estimated installed equipment costs and direct operating costs for the chemical plant as matched to the MARS blanket. The plant is based on a TMR with a two-temperature zoned blanket and a fluidized bed decomposer.

9.1 THE ECONOMIC BASIS

We present costs based on constant, July 1980 dollars, and use currently available chemical plant technology. Because the chemical portion of the plant will be manpower-intensive and cannot be operated with as few people or as little supplies or maintenance as in an electric power plant, we have used chemical plant experience[1] in estimating all labor costs.

9.2 COSTING PROCEDURES

The chemical industry has developed considerable expertise in estimating the capital cost as well as the projected operating costs of their respective plants. We have determined costs for the chemical plant and the power system interface using standard chemical engineering costing techniques. These costing techniques are based on the use of actual construction experience from many chemical plants to predict capital and operating costs from freight-on-board (FOB) equipment costs. We used the new reference work by Peters and Timmerhaus[1] to augment the older Guthrie methods,[2,3] both for estimating the FOB costs of equipment and for deriving, from the FOB cost estimates, the installed direct capital cost, the total plant investment, and the operating cost. Where standard works could not provide capital costs, as in most of Section II and the power recovery systems, we used vendor estimates or other special sources of FOB cost data. The industry standard, Marshall and Swift (M&S),[4] equipment cost index was used to reduce all costs to the same (July 1980) basis.

We recognize that some of the best costing techniques are maintained as proprietary by A&E and chemical and oil companies. A proprietary costing method, available at GA Technologies, was used to spot check costs for a representative number of items. We did not find any overall bias, although we did note variations between different types of equipment.

We believe that our cost estimates are well within our goal of $\pm$ 30% accuracy.

9.3 PRELIMINARY CAPITAL COST

9.3.1 Section I: Main Solution Reaction Step

The simplified schematic of Section I is presented in Fig. 5-2 of this volume. Table 9-1 presents a detailed list of the equipment required for performing the main solution reaction step, together with size and cost data. With the exception of the heat exchanger reactor (R-101), all items have been costed by the Guthrie method.[2,3]

The structural material used throughout Section I is mild steel. If other than dry SO_2, oxygen, and/or water are present, the steel must be

Table 9-1. Preliminary capital costs for Section I[a] (M$ July 1980).

	Item No.	Parallel units	Diameter (M)	Length (M)	Equivalent mild steel FOB cost	Actual FOB cost plus adders	Installed direct capital cost	Total plant investment basis
C101	Primary scrubbing reactor	6	3.8	9.0	0.334	1.388[b]	2.267	3.009
C102	Lower phase SO_2 scrubber	6	5.1	19.5	0.869	3.967[b]	6.252	8.232
C103	Boost reactor	6	5.1	19.5	0.869	3.967[b]	6.252	8.232
C104	Secondary scrubbing reactor	6	4.5	8.6	0.391	1.693[b]	2.721	3.597
S101	High pressure flash drum	6	3.6	13.5	0.501	1.787[b]	3.004	4.057
S102	Low pressure flash drum	6	4.2	12.0	0.464	1.735[b]	2.948	3.947
S104	Primary water knockout drum	6	3.0	3.9	0.116	0.116	0.346	0.518
S105	Secondary water knockout drum	1	3.0	3.9	0.019	0.019	0.057	0.086
R101	Heat exchanger reactor	6	1.8	7.5	1.205	20.686	22.772	27.194
E101	SO_2 heat exchanger	6	1.7	12.0	0.731	1.112	2.075	3.020
E102	Section III water heat exchanger	2	1.1	12.0	0.178	0.178	0.413	0.631
E103	Section II water heat exchanger	3	1.2	12.0	0.282	0.282	0.654	0.997
P101	Water feed pump	6+1	-	-	0.002	0.002	0.008	0.012
P103	Reactor feed pump from C101	6+1	-	-	0.009	0.017	0.032	0.043
P104	Iodine feed pump	6+1	-	-	0.018	0.037	0.067	0.092
P105	Reactor feed pump from C103	6+1	-	-	0.034	0.068	0.121	0.167
P106	Reactor feed pump from C104	6+1	-	-	0.047	0.094	0.173	0.239
TE101	O_2 power recovery turbine	1	-	-	0.996	0.996	2.148	3.238
TE103	Iodine power recovery turbine	1	-	-	0.058	0.169	0.250	0.329
Total capital cost					7.123	38.313	52.560	67.640

[a] Based on a hydrogen plant producing 5025 mole/s.

[b] Adders include the field installation of liner.

protected by an appropriate coating or lining. Although spray-on hydrocarbon-based coatings are adequate when moist SO_2 is present, liners of bulk fluorocarbon are specified when H_2SO_4, HI, or I_2 are present. The installed cost of fluorocarbon linings is estimated to be $\$1100/m^2$.

The heat exchanger reactor is unique because of the material involved, which is niobium. The \$220/kg cost of the niobium tubing dominates the reactor cost. Added to the \$15.8 M cost of the tubing is an appropriate amount for installing the tubing (\$3.2 M), plus the FOB cost of the equivalent mild steel heat exchangers (\$1.2 M), giving an FOB cost of \$20.2 M. We estimated the installation cost from the cost of the equivalent mild steel heat exchanger since niobium is required only for the heat transfer surfaces.

The Guthrie method allows us to specify the piping materials separately from the construction materials for the equipment. Either mild steel or standard fluorocarbon-lined mild steel piping is specified as appropriate. The pumps are either cast iron for water or cast iron with a molded fluorocarbon liner for corrosive solutions.

Because Section I operates essentially as six parallel systems, 83% of production capacity may be maintained if any one system is down for repairs. Pumps are cross-connected so that one installed spare backs up the active six. The power recovery turbines do not have a spare; they can be bypassed.

The column labeled "Total Plant Investment Basis" in Table 9-1 indicates that the major unit costs of Section I are associated with the heat exchanger reactor (R-101). The cost of R-101 may be decreased if more of the heat load is shifted to water-based heat exchangers. If the power-bottoming cycle were eliminated, the cost of R-101 would be significantly decreased because of the much larger differential temperatures across the exchanger.

9.3.2 Section II: Sulfuric Acid Processing Step

The simplified schematic for the sulfuric acid processing step is presented in Fig. 5-2 of this volume. Detailed lists of the equipment required for H_2SO_4 concentration and decomposition together with cost data are shown in Table 9-2. All cost estimates were made using Guthrie's techniques.[2,3]

The major costs in Section II are associated with heat transfer equipment. Silicon carbide is the material of choice for heat transfer surfaces where liquid-gas interfaces occur. Silicon carbide is used for all heat transfer involving concentrated H_2SO_4 except in the recuperator/decomposer preheater. Incoloy-800H is used in the recuperator/decomposer preheater because only gases exist at the temperatures encountered.

Vessels are fabricated from fluorocarbon-lined mild steel; this fluorocarbon lining is thermally insulated from the process by an acid brick lining.

The costs of SiC and vessel liners are treated as adders to the base carbon steel equipment costs. Silicon carbide U-tube costs are estimated to be \$32.7/M for the 5-cm-diameter tubes specified for the H_2SO_4 vaporizer,[5] and we used this cost to estimate the rest of the SiC heat exchangers.

Table 9-2. Preliminary capital costs for Section II.[a]

Item No.		Parallel units	Diameter (M)	Length (M)	Equivalent mild steel FOB cost	Actual FOB cost plus adders[b]	Installed direct capital cost	Total plant investment basis
C201	Isobaric concentrator vessel	2	5.0	30.0	0.615	2.184	3.634	4.658
C202	Low pressure distillation column	2	4.5	12.0	0.462	0.953	1.572	1.980
R201	Decomposer vessel	8	6.0	12.0	0.900	15.829	18.659	22.159
S201	Condensate separator on C201	2	1.4	2.4	0.035	0.073	0.156	0.208
S202	Condensate separator on C202	2						
S203	Intermediate flash separator	2x2	3.6	4.8	0.155	0.650	1.016	1.290
S204	Secondary condensate separator	2x2	1.4	2.4	0.070	0.146	0.312	0.416
S205	Acid knock-out drum	2x5	3.6	3.0	0.211	0.854	1.352	1.719
E201	Concentrator heat exchangers	-	-	-	1.394	5.808	9.449	11.995
E202	Distillation column heat exchangers	-	-	-	0.745	1.804	3.750	4.916
E203	Partial condenser on C201	2	1.0	6.0	0.103	0.103	0.236	0.351
E204	Partial condenser on C202	2	1.2	6.0	0.116	0.116	0.264	0.398
E206	Vaporizer preheater	4	3.0	7.2	0.478	1.955	3.173	4.034
E207	Vaporizer	16	3.0	10.0	2.361	10.670	16.736	21.147
E208	Decomposer preheater	32	3.0	9.0	2.622	25.969	39.696	47.298
E209	Decomposer heat exchanger tubes	-	-	-	2.683	16.095	25.480	31.475
E210	Feed preheater to C201	6	3.0	7.2	0.732	3.995	3.995	7.348
E211	Partial condenser on inter. flash	2x2	1.2	6.0	0.238	0.238	0.543	0.817
E212	Total condenser on inter. flash	2x2	1.5	6.0	0.293	0.293	0.669	1.006
E213	Total condenser on C201	8	2.0	6.0	0.857	0.857	1.794	2.757
E214	Total condenser on C202	4	2.0	6.0	0.457	0.457	1.043	1.569
P201	Dilute acid feed pump	6+1	-	-	0.434	1.306	2.415	3.140
P202	Vaporizer feed pump	6+1	-	-	0.145	0.435	0.805	1.047
P203	Distillation column overhead pump	6+1	-	-	0.027	0.027	0.063	0.096
TE201	Liquid expander from H.P. conc.	1	-	-	0.180	0.180	0.427	0.642
TE202	Liquid expander from inter. flash	1	-	-	0.053	0.053	0.125	0.189
Total capital cost					16.066	91.050	137.364	172.655

[a] Based on a hydrogen plant producing 5025 mole/s

[b] Adders include installation of SiC tubing, acid brick, and fluorocarbon lining.

9.3.3 Section III: Hydrogen-Iodide Concentration Step

Capital costs for Section III are presented in Table 9-3. The simplified flow diagram for this section is presented in Fig. 5.6 of this volume. The construction materials and costing techniques are similar to those used for Section I. Where fluorocarbon linings are not acceptable because of thermal or mechanical limitations, we have used Hastelloy-C.

The HI concentration step is the most capital-intensive portion of the chemical plant. Although significant costs are associated with I_2 knockout and HI distillation, the largest costs are associated with H_3PO_4 concentration.

The high cost components of the H_3PO_4 concentration system are the steam compressors and heat exchangers. The compressor costs are based on vendor estimates[6] and reduced to the 1980 base using the M&S[4] cost index. These compressor costs appear to be fixed unless future developments bring down the relative cost of turbine compressors. Flowsheet modifications have the potential for reducing the heat transfer costs, particularly if direct contact heat transfer is used between immiscible streams in Sections I and III and between Sections III and IV. The large amount of rotating machinery in the H_3PO_4 concentration system makes this part of the process a potential source of downtime. The compressors in the third evaporation stage were deliberately oversized to make them identical to the first and second stage units. If any one of the 15 units is down, intermediate pressures may be shifted to permit operation at 93% of capacity with only a slight overall loss of efficiency.

9.3.4 Section IV: Hydrogen-Iodide Decomposition Step

The HI decomposition step has the lowest flow rates and lowest costs of the four chemical process steps. The costs are as high as they are given in Table 9-4 only because of the high pressures involved. The simplified flowsheet for Section IV is given in Fig. 5-7 of this volume.

9.4 CHEMICAL PLANT OPERATING COSTS

Preliminary estimates of the operating and maintenance costs of chemical plants may be calculated from the FOB costs of the capital equipment. According to Guthrie,[3] the yearly operating and maintenance cost is 20% of the direct capital cost, assuming mild steel construction.

Assuming the cost of the mild steel plant is 248.2% of the FOB cost of the equivalent mild steel equipment,[5] the yearly operating cost of the chemical plant is $48.6 M as indicated in Table 9-5.

Table 9-3. Preliminary capital costs for Section III[a] (M$, July 1980).

	Item No.	Parallel units	Diameter (M)	Length (M)	Equivalent mild steel FOB cost	Actual FOB cost plus adders	Installed direct capital cost	Total plant investment basis
C301	Iodine wash column	3	4.5	18.0	0.348	2.769[bc]	3.346	4.139
C302	Iodine knockout column	10	7.7	24.0	3.137	29.26[bc]	34.476	42.272
C303	HI distillation	3	6.9	21.6	0.912	22.194[b]	25.016	29.478
S301	Surge drum--C303 reflux	3	2.7	10.2	0.128	0.128	0.756	0.969
S303	Flash drum--first H_3PO_4 stage	6	6.0	9.0	0.499	1.660[c]	2.949	3.780
S304	Flash drum--second H_3PO_4 stage	5	3.6	16.2	0.357	1.192[c]	2.114	2.708
S305	Flash drum--third H_3PO_4 stage	4	6.6	10.7	0.463	3.237	5.797	7.027
S306	S-H_3PO_4 separator	3	5.9	22.2	0.558	3.907	6.789	8.242
E302	Intermediate condenser on C303	3	1.6	12.0	0.148	1.496	2.081	2.513
E303	Reboiler on C303	6	1.1	12.0	0.903	3.951	5.110	6.608
E304	Condenser on C303	6	1.6	12.0	0.820	4.063	5.480	6.967
E305	Iodine cooler	1	1.4	12.0	0.102	1.023	1.423	1.719
E306	Heater--first H_3PO_4 stage	65	1.5	12.0	3.229	25.696	34.975	42.920
E307	Heater--second H_3PO_4 stage	50	1.5	12.0	2.639	21.417	29.262	35.789
E308	Heater--third H_3PO_4 stage	49	1.5	12.0	1.774	13.083	17.720	21.812
E309	Concentrated H_3PO_4 cooler	6	1.8	12.0	2.148	21.701	30.168	36.434
E310	Water cooler--first H_3PO_4 stage	1	1.7	12.0	0.239	1.763	2.386	2.938
E311	Water cooler--second H_3PO_4 stage	1	1.8	12.0	0.224	1.647	2.229	2.643
E312	Water cooler--third H_3PO_4 stage	1	1.7	12.0	0.160	1.181	1.600	1.970
P301	Lower phase feed pump	10+1	-	-	0.212	0.425	0.814	1.112
P302	Iodine wash water pump	3+1	-	-	0.006	0.006	0.013	0.021
P304	Feed pump--C303	10+1	-	-	0.742	1.486	2.721	3.749
P305	Concentrated H_3PO_4 pump	10+1	-	-	0.478	0.956	1.750	2.406
TE302	First H_3PO_4 stage PR turbine	1	-	-	0.398	0.398	0.741	1.092
TE303	Second H_3PO_4 stage PR turbine	1	-	-	0.257	0.257	0.562	0.892
TE304	Third H_3PO_4 stage PR turbine	1	-	-	0.240	0.240	0.516	0.757
TE305	Iodine power recovery turbine	1	-	-	0.087	0.171	0.291	0.396
TC301	First H_3PO_4 stage steam comp.	6	-	-	17.321	17.321	37.378	61.467
TC302	Second H_3PO_4 stage steam comp.	5	-	-	14.434	19.562	31.149	46.949
TC303	Third H_3PO_4 stage steam comp.	4	-	-	11.547	11.547	24.919	37.559
	Total capital cost				64.610	214.038	314.531	417.328

[a] Based on a hydrogen plant producing 5025 mole/s.

[b] Adder includes field installation of packing.

[c] Adder includes field installation of liner.

Table 9-4. Preliminary capital costs for Section IV[a] (M$, July 1980).

	Item no.	Parallel units	Diameter (m)	Length (m)	Equivalent mild steel FOB cost	Actual FOB cost plus adders	Installed direct capital cost	Total plant investment basis
C401	HI-I_2 distillation column	1	4.7	15.0	0.174	1.794[b]	2.198	2.663
C402	HI absorber	6	4.1	9.6	1.077	1.342[bc]	4.411	5.850
C403	H_2S scrubber	2	3.8	27.3	0.718	1.049[bc]	2.900	4.083
S401	Reactor effluent V-L separator	1	2.9	13.2	0.166	0.300[c]	0.728	1.009
S402	H2-HI vapor liquid separator	1	2.4	9.6	0.124	0.206[c]	0.527	0.735
D401	Reflux surge drum--C401	1	3.3	15.0	0.077	0.254[c]	0.373	0.510
R401	HI decomposition reactor	4	4.5	27.0	1.795	3.782[bc]	8.411	11.532
E400	Misc. integrated heat exchangers	13	-	-	1.333	6.626	9.457	12.100
E4XX[d]	Absorption refrigeration unit	1	-	-	1.732	1.732	2.891	4.678
P401	Reactor feed pump	4+1	-	-	0.654	1.892	2.980	3.975
P402	HI recycle feed pump	1+1	-	-	0.294	1.442	2.272	3.029
P403	Reflux pump--C401	1+1	-	-	0.013	0.038	0.059	0.077
P404	Make-up water feed pump	6+1	-	-	0.021	0.021	0.049	0.074
P405	Recycle pump--C402	6+1	-	-	0.025	0.071	0.112	0.149
P406	SO_2-H_2O pump to C403	6+1	-	-	0.018	0.018	0.043	0.065
P407	Recycle pump--C403	2+1	-	-	0.015	0.015	0.036	0.053
TE401	HI-I_2 power recovery turbine	1	-	-	0.357	1.033	1.521	2.048
TE402	Hydrogen power recovery turbine	1	-	-	1.666	1.666	3.596	3.421
	Total capital cost				10.259	23.281	42.564	58.051

[a] Based on a hydrogen plant producing 5025 mole/s.

[b] Adder includes field installation of packing.

[c] Adder includes field installation of liners.

[d] The absorption refrigerator includes heat exchangers E408, E410, and E411.

Table 9-5. Estimated operating costs of chemical plant (M$ July 1980).

Section	Equivalent mild steel FOB cost	Total plant investment based on mild steel[a]	Yearly operating cost[b]
I	7.123	17.679	3.536
II	16.066	39.727	7.945
III	64.610	160.362	32.072
IV	10.259	25.463	5.093
Total	98.058	243.231	48.646

[a] 248.2% of FOB equipment cost.

[b] 20% of total plant investment.

REFERENCES

1. M. S. Peters and K. D. Timmerhaus, Plant Design and Economics for Chemical Engineers, (McGraw-Hill, New York) 1980.

2. K. M. Guthrie, "Capital Cost Estimating," Chemical Engineering, 76, (6), 114-142 (1969).

3. K. M. Guthrie, "Capital and Operating Costs for 54 Chemical Processes," Chemical Engineering, 77, (13), 140-156 (1970).

4. Marshall and Swift, Los Angeles, Equipment Cost Index, compiled quarterly for 47 different industries and reported regularly in Chemical Engineering (McGraw Hill, New York).

5. J. Smelko, Union Carbide Company, Cleveland, OH, private communication to T. Galloway of Lawrence Livermore National Laboratory, Livermore, CA, (June 1981).

6. D. Stanwich, Ingersol Rand Company, Philipsburg, MA, private communication, (August 1982).

10 Fuels Beyond Hydrogen

10. Fuels Beyond Hydrogen

10.1 INTRODUCTION

Hydrogen can be a fuel in its own right. This is the assumption we have made in this study and in our prior work on fusion/synfuels. We have followed this course because we wished to focus attention on the main question of how to fit a fusion reactor to a thermochemical process. We have answered this satisfactorily and conclude that the idea has merit.

Figure 10-1 illustrates our raw materials, the processes we can use, and the products to be obtained in progressing to a synfuel economy using the fusion reactor as the driver.

In the long view or in studies of larger scope, hydrogen may better serve as a feedstock to produce the more complex fuels shown on this figure. We do not know what the best product might be but we have chosen methanol to illustrate that its synthesis from hydrogen and oxygen is a reasonable choice, particularly in a transition period when a fusion economy is just emerging and our coal resource has not yet been depleted.

10.2 MARS/SYNFUEL METHANOL PLANT

The MARS/synfuel methanol plant is designed to use the hydrogen and oxygen produced by GA Technologies' sulfur-iodine cycle, together with a source of carbon, such as coal, to manufacture methanol. The reasons for selecting methanol as the first synfuel other than hydrogen are:

- It is easily stored because it is liquid;
- It is considered as a universal substitute fuel for natural gas and crude oil, and can be used in automobiles, industrial and utility turbines, and boilers;
- It can be synthesized from hydrogen, oxygen, and coal using technology that is commercially available today.

We have developed the concept of a coal-based methanol plant coupled to the fusion-driven sulfur-iodine cycle. The thermal efficiency of the plant is calculated to be 44% and is comparable to coal-to-methanol plant efficiency. The fusion-driven process has the advantage of using less coal and discharging less CO_2 into the atmosphere.

10.3 PROCESS CHARACTERISTICS

The methanol plant has been sized to use the entire amount of hydrogen produced by the 3500-MW_f TMR and the sulfur-iodine cycle, an amount equivalent to ~1480 MW. Based on this hydrogen use, methanol production of 9852 tons per day (TPD) would also use 64% of the oxygen produced from the sulfur-iodine cycle.

The main process steps are:

- Coal preparation, which involves crushing the coal to 3/8 in. or less, drying it to 8% moisture, and storing it;

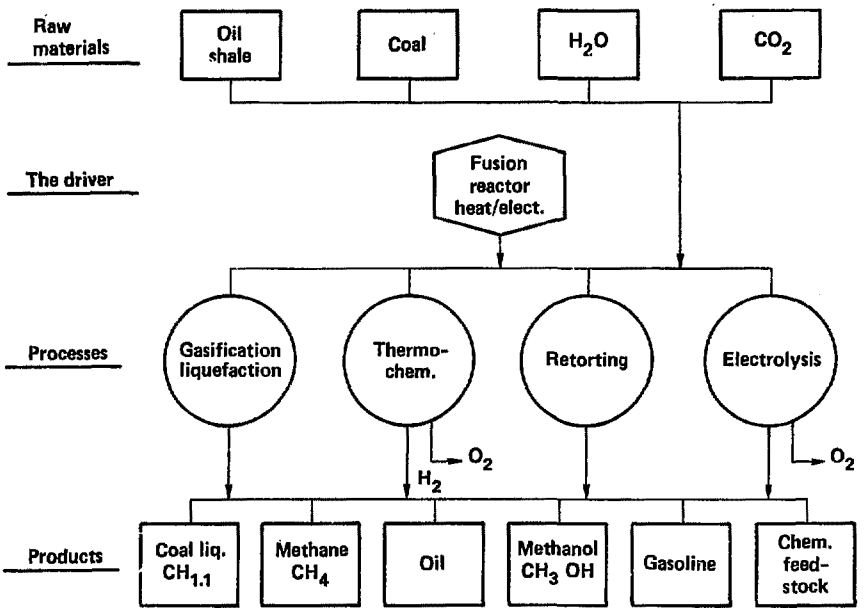

Fig. 10-1. Intermediate step for processing hydrogen as a fuel.

- Coal gasification using oxygen (from the sulfur-iodine cycle) and steam;
- Methanol synthesis gas preparation;
- Methanol synthesis and purification.

We have chosen the Winkler gasifier for this process. It is available commercially and has been used in 22 plants around the world since 1926, with five plants still operating as of 1980.

To synthesize methanol, the amounts of carbon monoxide, carbon dioxide, and hydrogen must be in certain proportions. The gasifier product gas does not have the right proportion of these gases, being too rich in carbon monoxide and too poor in hydrogen. Therefore, it has to be sent to the feed gas preparation step, which adjusts the ratio of the gases to the proper level by adding hydrogen and removing carbon dioxide. Furthermore, the gasifier product gas contains small amounts of sulfur-bearing gases that have to be removed in the feed-gas preparation step because they act as poisons to the methanol catalyst.

Currently, the two processes that dominate the world methanol market are the low pressure ICI process and the low pressure Lurgi process. The ICI process was developed earlier and accounts for more than 50% of the world's methanol capacity. Our conceptual design of the methanol synthesis loop is based on the ICI process.

10.4 PROCESS DESCRIPTION

Process flowsheets for synthesis gas preparation and for methanol production are shown in Figs. 10-2 and 10-3, respectively. Wyoming sub-bituminous run-of-mine coal is received by rail, unloaded, and stored in 15-day-capacity storage piles. Coal to be used for gasification is crushed to 3/8 in., dried to 8% moisture, and sent to active closed storage, ready to be transferred to the gasification section.

The heart of the gasification section is the 12 fluid bed gasifiers. Oxygen from the surfur-iodine cycle, which is available at 60°F and 14.5 psia, is compressed to the gasification pressure of 90 psia and heated to the gasification temperature of 450°F before being sent to the gasifier. Coal is fed to the gasifiers by means of a lock hopper system. During gasification, coal reacts with steam and oxygen to form a raw product gas that consists of 33.9% CO, 11.2% CO_2, 25% H_2, 2.9% CH_4, 1% N_2 and sulfides, and 25.9% H_2O by volume. This product gas exits the gasifiers at a temperature of 2100°F. Ordinarily, these hot effluent gases would be used to generate saturated and superheated steam in a heat exchanger, design-limited to metal temperatures of 600°F (as shown in Fig. 10-1). For our purposes, we assume that this 2100°F stream can be sent back to the sulfur-iodine cycle as a source of high temperature heat for the decomposition of H_2SO_4; however, this coupling step has not been worked into the hydrogen process design at this time. Next, the raw product gas is cleaned of particulates and sent to the gas preparation area so that a gas suitable for methanol synthesis can be produced.

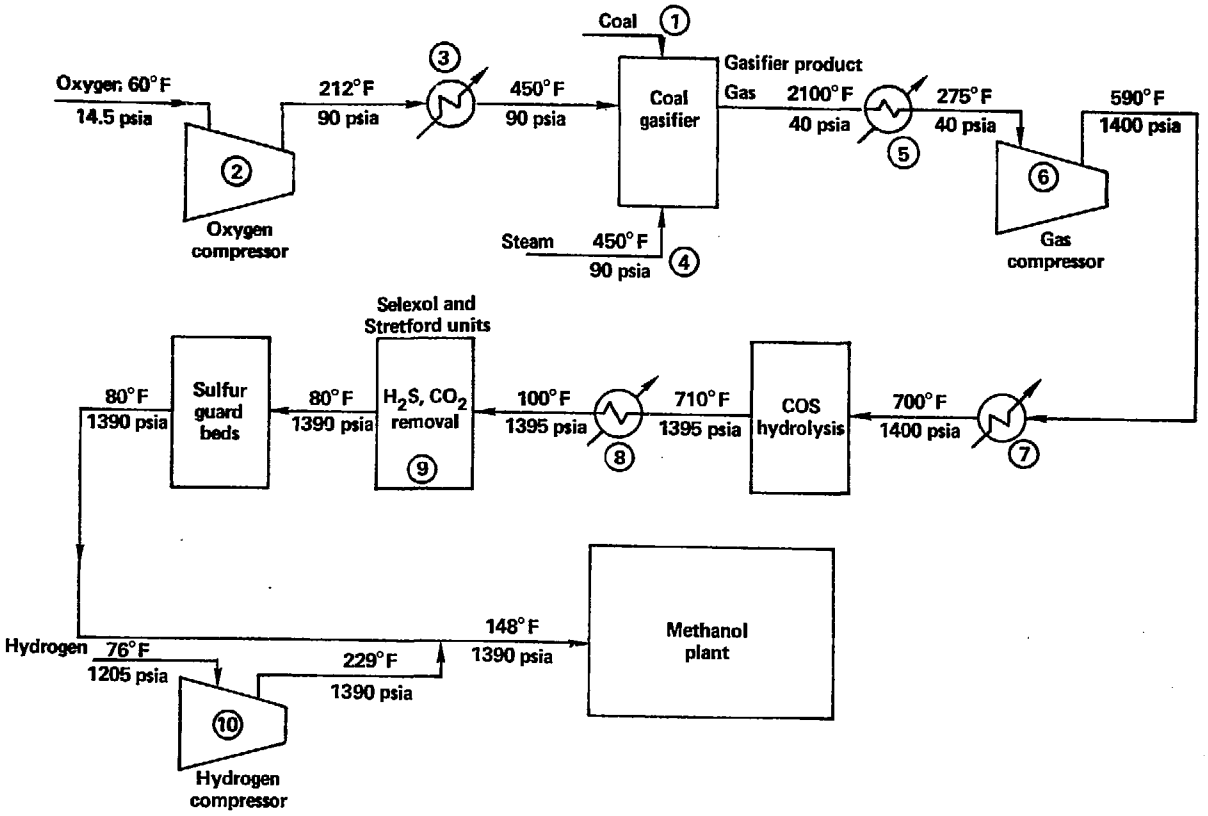

Fig. 10-2. Preparation of gas synthesized for methanol production.

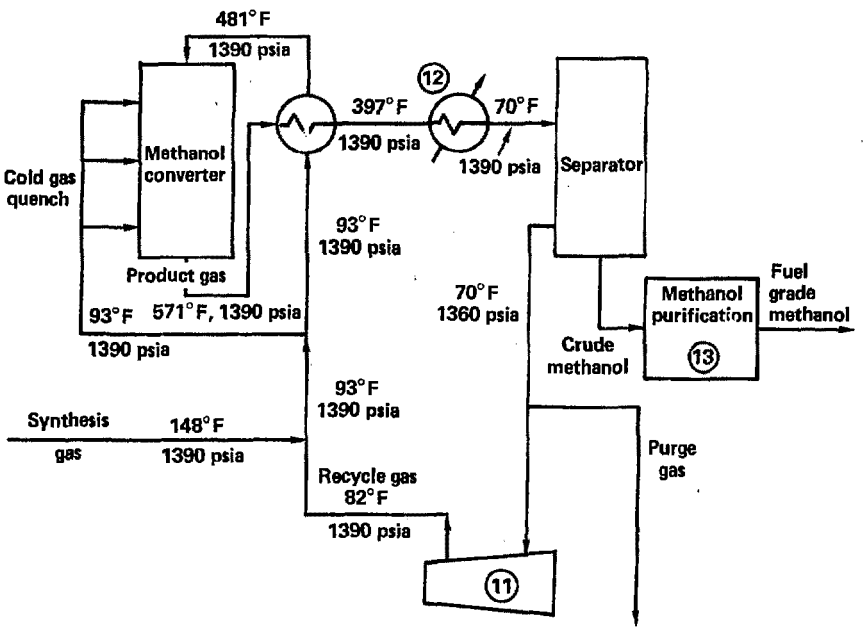

Fig. 10-3. Methanol synthesis and purification.

The gas preparation area consists of four parallel trains of processing equipment. The first step is compression of the gas to 1400 psia, which is approximately the pressure required for methanol synthesis.

Methanol is synthesized through the following reactions:

$$CO + 2H_2 \rightleftharpoons CH_3OH \quad ,$$

$$CO_2 + 3H_2 \rightleftharpoons CH_3OH + H_2O \quad .$$

Efficient synthesis of methanol requires the feed gas to have a ratio of CO, CO_2, and H_2 corresponding to the stoichiometric equation

$$\frac{H_2}{2CO + 3CO_2} = 1.0 \quad .$$

In practice, for kinetic reasons, this ratio is kept at a slightly higher value of 1.05. The raw product gas from the gasifier does not have the proper composition, being too rich in CO_2 and too poor in H_2. Furthermore, it contains carbonyl sulfide (COS), which can act as a poison to the methanol catalyst. Thus, the first step in adjusting the composition of the methanol feed gas is hydrolysis of COS to CO_2 and hydrogen sulfide (H_2S), which can be controlled more effectively in the acid gas removal unit. The raw product gas is thus heated to the COS hydrolysis temperature of 700°F and passed through packed beds of catalyst where the COS is hydrolyzed.

The exit gas stream from the COS hydrolysis unit is cooled to 100 °F to facilitate acid gas absorption in the Selexol unit. The purpose of the Selexol unit is to remove H_2S and adjust the CO_2 level in the gas to the minimum amount required to maintain catalyst stability during methanol synthesis. The H_2S is removed from the raw gas in the first absorber and CO_2 is removed in the second. Because the organic solvent is recirculated, it must be continually regenerated by stripping. The absorbers and strippers are packed columns in which the gas streams are contacted with liquid solvent. The purge gas stream leaving the H_2S stripper is sent to the Stretford unit for sulfur recovery. The gas leaving the CO_2 stripper contains mostly CO_2 and hence is simply vented. The synthesis gas leaving the Selexol unit contains only trace levels of H_2S and COS and has the proper amount of CO and CO_2. Guard beds are provided to remove trace sulfur compounds.

The final stage in this preparation area is the addition of hydrogen from the sulfur-iodine cycle. The hydrogen is compressed to 1390 psia and added to the gas stream from the sulfur guard beds to adjust its composition to that required for methanol synthesis.

The methanol synthesis area consists of four synthesis loop trains. Here, the syngas is first combined with recycle gas, which is gas that has passed through the methanol converter but has not reacted. This combined gas stream is then split into two parts. One part is heated to the reaction temperature of 481°F, whereas the other part is sent to the reactor cold, at a temperature of 93°F.

Methanol synthesis is highly exothermic, releasing heat in the amount of 36,344 Btu/lb mole CO converted and 23,616 Btu/lb mole CO_2 converted. In the ICI process, this heat of reaction is removed and the reactor temperature

is controlled within a narrow range by injecting cold feed gas at appropriate levels directly into the catalyst bed, using a specifically developed distributor. We have calculated the material and energy balance around the methanol converter assuming a 20% per pass conversion of both CO and CO_2.

The effluent gas stream from the converter is first used to heat part of the feed gas and is then cooled to 70 °F, releasing both sensible heat and the latent heat of vaporization of methanol, which is used to raise steam. We have assumed that more than 97% of the methanol is condensed and separated from the unreacted gas. To give this level of methanol recovery, the separator has to be operated at 1360 psia.

The crude methanol is then sent to the purification area where it is distilled in a one-column distillation system to fuel grade purity.

Part of the unreacted gas from the separator is purged from the process. The other part is recompressed to reaction pressure and recycled back to the methanol converter. The purge is required to prevent the buildup of inert gases such as methane (CH_4) in the synthesis loop. We have assumed a maximum of 25% CH_4 in the synthesis loop in the calculation of the purge stream volume. The purge stream consists of 48% H_2 and 25% CH_4 and can be used as a fuel. The heating value of the purge stream has been credited to the process.

10.5 ENERGY BALANCE AND THERMAL EFFICIENCY

The process of converting coal, hydrogen, and oxygen to methanol inevitably involves energy changes. Certain process steps require the addition of energy and other process steps recover energy from the process. The difference between the energy added and the energy recovered from the process is the net energy consumed by the process.

Devices or process steps that involve energy changes are marked with a circle in Figs. 10-2 and 10-3. Only those energy changes in a typical coal-to-methanol plant are shown.

The quantities of the energy changes are given in Table 10-1. A positive number indicates that energy is required by that step; a negative number indicates that energy is released by that step. Units of energy are given in both millions (MM) of Btu/hour as well as MW. For the purpose of calculating the energy requirements of steam-turbine-driven compressors, a heat rate of 3393 Btu/hp-hour has been assumed, to take into account the efficiency--75%--of converting heat to mechanical energy.

Table 10-1 indicates that the most energy consuming process steps are:

1. Raw gas compression to methanol synthesis pressure; and

2. Reboiler heat duty for methanol distillation in the purification step.

The most energy is recovered from the high-temperature raw product gas exiting the gasifier and the product gas exiting the methanol converter.

Adding up all the process energy requirements results in a total of 911 MW, whereas adding up all the process energy outputs results in a total energy recovery of 872 MW. Assuming that all the energy recovered can be fed back into the process, the net energy required by the process is 39 MW.

Table 10-1. Energy balance for the MARS coal-to-methanol process. Energy available = 2976 MM Btu/hour (872 MW); energy required = 3109 MM Btu/hour (911 MW); net energy required = 133 MM Btu/hour (39 MW).

	Device/process step	Δ energy[a] Heat MM Btu/hour	Heat MW	Energy for driving turbines[b] MM Btu/hour	Energy for driving turbines[b] MW
1.	Coal drying and crushing	144.44	42.32	15.44	4.53
2.	Oxygen compressor			48.91	14.33
3.	Oxygen heater	23.65	6.93		
4.	Steam generation	422.70	123.85		
5.	Waste heat recovery	-1161.1	-340.20		
6.	Raw gas compression to synthesis pressure			693.13	203.09
7.	Raw gas heating to COS hydrolysis unit	72.23	21.16		
8.	Heat recovery before Selexol unit	-714.60	-209.38		
9.	Selexol & Stretford	Negligible	Negligible		
10.	H_2 compression			12.90	3.78
11.	Recycle compressor			71.60	20.98
12.	Methanol product gas heat recovery	-1140.0	-322.30		
13.	Methanol purification	1604.4	470.09		

[a]Positive, energy required; negative, energy output.
[b]Assumes heat rate of 3393 Btu/hp-hour.

The total energy input to the coal-to-methanol plant consists of the higher heating value of coal, which amounts to 2068 MW, and the higher heating value of hydrogen, which amounts to 1481 MW. The energy output from the methanol plant consists of the higher heating value of methanol, 2348 MW, the higher heating value of the purge gas, 435 MW, and process output, -39 MW. (The negative sign indicates that energy is required by the process.) These energy flows are shown in Fig. 10-4.

If we define the thermal efficiency of the coal-to-methanol plant as the total plant energy output divided by the total plant energy input, we obtain

$$\text{thermal efficiency of coal-to-methanol plant} = \frac{HHV_{methanol} + HHV_{purge} + P}{HHV_{coal} + HHV_{hydrogen}} \times 100 = 77\% \quad ,$$

where HHV is the higher heating value and P is the process output.

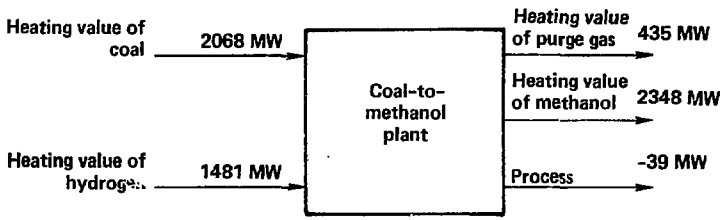

Fig. 10-4. Thermal efficiency of the MARS/synfuel methanol plant.

We can similarly define an overall thermal efficiency of methanol production from fusion power by taking into account an efficiency (36% is assumed) in converting fusion power to hydrogen heating value. Thus,

$$\text{overall thermal efficiency} = \frac{HHV_{methanol} + HHV_{purge} + P}{HHV_{coal} + \frac{HHV_{hydrogen}}{0.36}} = 44\% \quad .$$

This is slightly lower than the overall thermal efficiency of 46% for a stand-alone coal-to-methanol plant. However, the MARS methanol plant has the advantage of using 25% less coal than the stand-alone plant, and coal, being a nonrenewable resource that is available in limited amounts, is worth conserving. The MARS methanol plant has the further advantage of decreasing the amount of CO_2 vented to the atmosphere.

CONTENTS

Work performed under the auspices of
the U.S. Department of Energy by the
Lawrence Livermore National Laboratory
under contract number W-7405-ENG-48.

United States Government Printing Office: 787-002/A-4058-9/84